THE UNIVERSITY OF CHICAGO

SEARCH FOR PAIR PRODUCTION OF HIGGS BOSONS IN THE FOUR BOTTOM QUARK FINAL STATE USING PROTON-PROTON COLLISIONS AT $\sqrt{S} = 13$ TEV WITH THE ATLAS DETECTOR

A DISSERTATION SUBMITTED TO
THE FACULTY OF THE DIVISION OF THE PHYSICAL SCIENCES
IN CANDIDACY FOR THE DEGREE OF
DOCTOR OF PHILOSOPHY

DEPARTMENT OF PHYSICS

BY
PATRICK BRYANT

CHICAGO, ILLINOIS
DECEMBER 2018

This thesis is dedicated to my friends and family – the people who make life and the pursuit of knowledge joyous.

Table of Contents

List of Figures

List of Tables

ACKNOWLEDGMENTS

This thesis is the work product directly and indirectly of an enormous number of physicists, administrators, staff, friends and family. First I would like to thank the thousands of people who dedicated significant fractions of their lives to the development and operation of the Large Hadron Collider, the ATLAS detector and the technologies which made them both possible.

To my parents who encouraged my mathematical and scientific interests from the very beginning, thank you. I learn more every day about how fortunate I have been to have parents capable and willing to endlessly discuss mathematical, technical and philosophical subtleties of the world in which we find ourselves. I had the privilege of a father who built everything he could himself and loved to help me with projects ranging from pine wood derby cars to hand soldered telephone kits. At the same time I had a mother who taught me the principles of calculus when I was ready and the public school system was not. When my middle school ran out of math for me she made sure I could be driven to the local high school, and when my high school ran out she made sure I could attend college lectures. She forced the high school to allow me the opportunity to test out of entry level science courses, a practice they had abandoned when too many kids entered AP courses unprepared. And to my sister, thank you for tolerating the chaos of a continually bored younger brother. Many of my fondest childhood memories consist of the time we spent building K'Nex contraptions and Rube Goldberg machines.

To my advisor Mel, thank you for five years of guidance and support. I still remember the day he came into my office to suggest I work on diHiggs to four b-jets. I was beyond excited to finally begin contributing directly to ATLAS physics results, a goal I had held for half of my life. One of my proudest moments was after a presentation I gave to the Exotics group on my work and he commented that I had mastered my subject. Hearing this from my advisor

and force for good in high energy physics made me feel that I could make unique and valuable contributions to science. In addition to being a wonderful mentor Mel also ensured I was well funded; I want to thank him for nominating me for the Grainger Graduate Fellowship and Nathan Sugarman award which funded my last year.

To my first postdoc, John Alison, thank you for providing excellent tools and a clear goal oriented approach to physics. With some help from Karol Krizka, John taught me almost everything I know about the day to day in particle physics. I'm now looking forward to the next couple years working with John as his first postdoc!

To the brilliant electronics engineer Mircea Bogdan, it has been an absolute pleasure bring the auxiliary cards to life with you. In addition to his infinite patience and engineering mentorship, he also frequently provided me and my friends and family with free aquarium tickets; nothing takes your mind off the stresses of graduate student life like watching jelly fish waft by.

To my informal co-advisor, Young-Kee Kim, thank you for your constant joy in physics and life. Young-Kee has been a continual source of inspiration and support. I aspire to one day be as generous with my time and bring as much art and culture into the lives of those around me.

To Lauren Tomkins, thank you for getting me started on that very first prototype AUX card and your mentorship and friendship over the years. Lauren kept me functional as a team player and provided useful career advice and recommendation letters.

To David Wardrope, Michael Kagan, Baojia Tong, Jana Schaarschmidt and Stephane Willocq, with whom I worked most closely on this thesis topic aside from Mel and John, thank you for years of work, enjoyable physics discussions, and fruitful arguments.

To my other committee members – Carlos Wagner, Guy Savard and David Schmitz – thank

you for your lessons, questions and time.

Finally to the many others who made my time at the University of Chicago possible and enjoyable, thank you all!

Rui Zou	Yasu Okumura	Andy Mehta
Jordan Webster	Max Swiatlowski	Chris Pollard
Yangyang Cheng	Tova Holmes	Georges Aad
Gabe Facini	Todd Seiss	Raymond Brock
Jamie Saxon	Lesya Hoyrn	Eric Torrence
Jim Pilcher	Amy Schulz	David Strom
Mary Heintz	David Reid	Alex Tuna
Holly Jaffey	Shadla Cycholl	Tomo Lazovich
Sandy Heinz	Autym Henderson	Massimiliano Bellomo

Kieran Murphy and Gus Downs

ABSTRACT

A search for Higgs boson pair production in the $b\bar{b}b\bar{b}$ final state is carried out with up to 36.1 fb^{-1} of LHC proton–proton collision data collected at $\sqrt{s} = 13\,\text{TeV}$ with the ATLAS detector in 2015 and 2016. Three benchmark signals are studied: a spin-2 graviton decaying into a Higgs boson pair, a scalar resonance decaying into a Higgs boson pair, and Standard Model non-resonant Higgs boson pair production. This thesis presents a search in events with four individually resolved b-tagged jets. Higgs bosons produced with large momenta are reconstructed as single large radius jets with substructure. The analysis of this topology is presented in [197]. The two analyses are statistically combined and upper limits on the production cross section of Higgs boson pairs times branching ratio to $b\bar{b}b\bar{b}$ are set in each model. The combined result searches for resonance masses in the range 260-3000 GeV. No significant excess is observed; the largest deviation of data over prediction is found at a mass of 280 GeV, corresponding to 2.3 standard deviations globally. The observed 95% confidence level upper limit on the non-resonant production is 13 times the Standard Model prediction.

Chapter 1

EXECUTIVE SUMMARY

This thesis consists roughly of three parts:

1. Chapters 2-5 introduce the theory motivating our study and an exposition of the experimental apparatus.
2. Chapters 6-13 explain the data and analysis methods.
3. Chapter 14 shows the results and Chapter 15 considers the future of the thesis topic.

In 2012 a new particle was discovered at the Large Hadron Collider (LHC, Chapter 3) which thus far appears to be consistent with the Standard Model (SM, Chapter 2) Higgs boson. The Higgs is the final piece of the SM and plays the crucial role of providing masses to the fundamental particles and setting the range of the weak nuclear force which powers the stars.

Having discovered the Higgs like particle, we must now measure its most salient properties to confirm or refute as many predictions of the SM as possible. This thesis presents a general search for processes producing two Higgs bosons (diHiggs) in proton collisions at the LHC using the ATLAS detector (Chapter 4). The motivation to search for diHiggs production is provided in Chapter 5.

Chapter 6 briefly introduces the data and simulated data samples and Chapter 7 defines the basic reconstructed physics objects. In Chapter 8 we describe and motivate the selection applied to the data. Chapter 9 details the trigger strategy and corresponding modeling uncertainty.

The background modeling, perhaps the most challenging aspect of this thesis, is explained in Chapter 10. Chapter 11 explains the systematic uncertainties of both the signal and

background models. This is followed by Chapter 12 shows the results in dedicated validation regions of the data where no significant signal contribution is expected.

Chapter 13 introduces the principles of statistical analysis and the procedure used in the search presented in this thesis. We conclude this thesis with Chapters 14 and 15 which present the results of the search and a brief discussion of the future of diHiggs physics respectively.

Chapter 2

THE STANDARD MODEL OF PARTICLE PHYSICS

> *Dass die Gesamtheit der Sinneserlebnisse so beschaffen ist, dass sie durch das Denken geordnet werden können, ist eine Tatsache, über die wir nur staunen, die wir aber niemals werden begreifen können.*
>
> *The very fact that the totality of our sense experiences is such that by means of thinking it can be put in order, this fact is one which leaves us in awe, but which we shall never understand.*
>
> – Albert Einstein, translation by Jean Piccard [94]

Einstein is often wildly misquoted; the above excerpt from his 1936 article *Physik und Realität* is usually paraphrased as, "The most incomprehensible thing about the Universe is that it is comprehensible". This certainly rolls off the tongue more easily but misses the central thesis of his article. Einstein was struggling with the emerging trend that as physicists found success in modeling more physical phenomena with fewer independent laws, the resulting laws became further removed from human intuition.

He gives the equivalence principle of General Relativity (GR) as an example which explains the observed equality of inertial and gravitational mass. Einstein's brilliance was two-fold: First he took this observed equality seriously and postulated that acceleration and gravitation are locally indistinguishable. Second, he was able to work out the complex mathematics of the curved dynamic spacetime manifold his postulate required. He had succeeded in explaining a more diverse set of phenomena with fewer underlying principles while requiring substantially more time and thought to understand the explanations.

The story is similar for quantum field theory (QFT), the mathematical framework underlying

the Standard Model of particle physics (SM). We believe all phenomena in nature can in principle be described by an appropriately chosen QFT[1] with some small but currently unknown set of axioms.

Regarding the early development of QFT, Einstein wrote [94],

> *Although the attempts so far made are restricted to linear equations, which, as we know from the results of the general theory of relativity, are insufficient, the complications met up to now by the very ingenious attempts are already terrifying.*

For the remainder of this chapter, we will attempt to outline the complications which Einstein and others – including the author of this thesis – found to be so terrifying.

The union of Special Relativity (SR) with quantum mechanics (QM) places significant constraints on the possible degrees of freedom of nature and their interactions. Any completed description of physical law must recover SR and QM in the appropriate limits.[2] It is important to consider some of the implications of QM and SR separately before describing their union. Sections 2.1 and 2.2 briefly introduce the foundations of QM and SR. Section 2.3 outlines some of the properties of their union – relativistic quantum field theory. For the remainder of this thesis QFT will refer to the relativistic variety unless otherwise stated.

We introduce the first QFT – Quantum Electrodynamics (QED) – to make contact with experimental results in section 2.4. In section 2.5 we describe how QFT is able to model the strong nuclear force and accommodate the hadronic particle zoo with Quantum Chromody-

[1] Worded in this way gravity is included! The interactions of gravity can be calculated in QFT with the caveat that in a perturbative expansion, the number of terms which must be renormalized grows without bound as a function of the interaction energy. This means perturbative gravity as formulated in QFT cannot *predict* the dynamics at high energies but it can model experimental results. It is an interesting speculative possibility that gravity as a QFT may be non-perturbatively renormalizable with finitely many relevant operators. This possibility was first considered by Steven Weinberg in 1977 [198] and is called Asymptotically Safe Gravity.

[2] And similarly for GR, where the story is far from settled.

namics (QCD). Section 2.6 introduces the final piece of the SM which unifies electromagnetism and the weak nuclear force while providing a mechanism to generate the observed fundamental particle masses. Finally in section 2.7 we summarize the SM and some of its most pressing experimental and theoretical issues.

2.1 Quantum Mechanics

In QM, the usual degrees of freedom of particles like position or angular momentum are promoted to differential operators acting on vectors in the space of all possible states. The state space is called a **Hilbert space** $\mathcal{H}$ and particle states are defined by vectors $|\Psi\rangle \in \mathcal{H}$. The observable quantities of the system are encoded in the direction of the state vector $|\Psi\rangle$ relative to some basis of the vector space but, are independent of the normalization of $|\Psi\rangle$. We are then free to normalize $|\Psi\rangle$ to a unit vector.

The key axiom of QM is that the motion of $|\Psi\rangle$ through $\mathcal{H}$ in time is **unitary** – the inner product between any two vectors in $\mathcal{H}$ is constant in time. This has the important consequence of ensuring the reversibility of time evolution in QM; no information is lost because, two different states cannot evolve to the same state after any amount of time.

Proof. Let $|a\rangle$ and $|b\rangle$ be unequal unit state vectors in $\mathcal{H}$, ie. $\langle a|a\rangle = \langle b|b\rangle = 1$ and $\langle a|b\rangle \neq 1$. Let U denote a unitary time evolution operator which takes state $|a\rangle$ to state $|c\rangle$: $U|a\rangle = |c\rangle$. Since U is unitary it preserves the inner product of any state with itself $\Rightarrow \langle c|c\rangle = 1$. Assume U also takes a different starting state $|b\rangle$ to $|c\rangle$: $U|b\rangle = |c\rangle$. Again, because U is unitary it preserves the inner product between $|a\rangle$ and $|b\rangle$ so $\langle a|b\rangle = \langle c|c\rangle$. By contradiction $U|b\rangle \neq |c\rangle$. □

When considering states describing multiple identical particles, the axiom of unitarity allows

for two categories of particles. Let $|\Psi_1, \Psi_2\rangle \in \mathcal{H} \otimes \mathcal{H}$ describe a system with two identical particles.[3] Suppose that these two particles are able to swap places in $\mathcal{H} \otimes \mathcal{H}$ after some amount of time. Then there exists a unitary operator U such that

$$U\,|\Psi_1, \Psi_2\rangle = |\Psi_2, \Psi_1\rangle$$

Applying U twice switches the particles back and we return to the initial two particle state

$$U^2\,|\Psi_1, \Psi_2\rangle = |\Psi_1, \Psi_2\rangle$$

Since the particles are identical you might expect that $|\Psi_1, \Psi_2\rangle = |\Psi_2, \Psi_1\rangle$. Inspecting this more carefully, the relationship we actually have is that U is its own inverse: $UU = I$. If $U\,|\Psi_1, \Psi_2\rangle = \lambda\,|\Psi_1, \Psi_2\rangle$ for some eigenvalue λ then $\lambda^2 = 1 \Rightarrow \lambda = \pm 1$.

It turns out that the value of λ depends on the type of particles being exchanged, specifically on their **spin**. Spin is the expectation value of angular momentum for particle states with zero momentum. The intrinsic angular momentum of quantum mechanical particles emerges automatically from their description in QFT and is maintained in the non-relativistic limit.

It is an observational fact that particles have either integer or half integer multiples of angular momentum in units of Plank's constant $\hbar$, regardless of the chosen axis of projection! In QM we accommodate experimental observation by adding the axiom that states with identical particles of integer spin (**bosons**) are symmetric under particle exchange while states of identical particles of half integer spin (**fermions**) are antisymmetric under particle exchange.

The symmetry or antisymmetry of a system of many identical particles determines the statis-

[3] $\mathcal{H} \otimes \mathcal{H}$ is the tensor product of two copies of the Hilbert space $\mathcal{H}$ describing the state space of a single particle. The tensor product produces a space with dimension given by the product of the dimensions of the constituents. There are states in the tensor product space which cannot be written as the product of states in the constituent spaces. Such states are said to be "entangled". Much of the weirdness of quantum mechanics is a consequence of the non-intuitive nature of the tensor product.

tical distribution of individual particle locations and momenta. Correspondingly this axiom is called the spin-statistics axiom. The relationship between particle spin and exchange statistics is axiomatic in QM while it can be derived from deeper principles in QFT.

Most crucially for our own existence, the antisymmetry of identical fermion exchange gives rise to the Pauli exclusion principle: Two identical fermions cannot occupy the same quantum state.

Proof. Suppose we have a system of two identical fermions $|\Psi_1, \Psi_2\rangle \in \mathcal{H} \otimes \mathcal{H}$ in some unit normalized initial state $\langle \Psi_1, \Psi_2 | \Psi_1, \Psi_2 \rangle = 1$. Assume there is a unitary time evolution operator U such that $U |\Psi_1, \Psi_2\rangle = |\Psi_3, \Psi_3\rangle$. The particles are identical fermions so $|\Psi_3, \Psi_3\rangle = - |\Psi_3, \Psi_3\rangle \Rightarrow \langle \Psi_3, \Psi_3 | \Psi_3, \Psi_3 \rangle = 0$. This means U did not preserve the inner product of the initial state with itself. By contradiction U is not unitary and cannot result from time evolution. □

The Pauli exclusion principle is what allows macroscopic objects to exist in forms other than gas, black holes or more exotic quantum states like Bose-Einstein condensates.

2.2 Classical Field Theory and Special Relativity

Classical field theory is the study of the dynamics of continuous media called fields. **Fields** are just a collection of numbers at every point on some manifold. Examples include the height of water at every point on the surface of a lake or the pressure and velocity of air at every point in the atmosphere. The collections of numbers at each point are called **tensors** and they must respect the algebraic structure of the symmetries of the host manifold. This thesis is not targeted to group theorists so we will take some time to explain the previous sentence.

For a thorough and rigorous explanation see Peter Woit's excellent book, *Quantum Theory, Groups and Representations* [205]. We have attempted in the next few sections to motivate the need for relativistic quantum field theory in a more qualitative way, but have followed Woit's notation in most cases where equations are needed.

2.2.1 Representations and $SO(3)$

Continuing with the intuitive example of air, consider taking a chunk of atmosphere and rotating it. After the rotation the chunk would support the same pressure waves and wind flow dynamics. Our chunk of air has a spatial symmetry described by the group of rotations of a sphere called the special orthogonal group in three dimensions or $SO(3)$ for short. Let T be a tensor field set of degrees of freedom describing some dynamic property of air. Given any two rotations R_1, $R_2 \in SO(3)$, there must exist a map ρ from $SO(3)$ to the space of linear transformations acting T such that that $\rho(R_1)\rho(R_2)T = \rho(R_1R_2)T$. Such maps between groups are called **homomorphisms**.

In other words, if we apply two rotations to our coordinate system it should be equivalent to instead apply two "rotations" to the tensor at each point. The existence of a homomorphism ensures symmetry transformations of space can be applied equivalently to space itself or the degrees of freedom on it. Tensors for which a homomorphism exists are said to transform **covariantly** under the symmetry transformations of the host manifold.

Let $x \in \mathbb{R}^3$ denote a point on the manifold and $T(x)$ be a tensor degree of freedom at that point. Now suppose we translate and rotate the coordinate system such that

$$x \to x' = Rx + a \tag{2.1}$$

for $a \in \mathbb{R}^3$. The tensor degree of freedom at the original point x in terms of the new

coordinate system becomes

$$T(x) \to T'(x) = \rho(R)T(R^{-1}(x' - a)).$$

We have applied the appropriate "rotation" $\rho(R)$ to the tensor at the original point x. In the transformed coordinate system x is given by the inverse of the map in equation 2.1. The purpose of these transformation gymnastics is simply to describe the same physical configuration of a tensor field in terms of a different arbitrary choice of space coordinate orientation.

In the above sketch of the notion of covariant tensors we acted on T from the left with a homomorphism of the symmetry transformation. There is also the notion of a **contravariant** tensor which transforms under the action of a homomorphism of the symmetry transformation on the right. This distinction is somewhat arbitrary and we say the contravariant tensors are elements of a **dual** space to the original covariant tensor. There is an operation called the **Hermetian conjugate** denoted with a † which swaps these spaces.

In the case where the tensor transformation can be represented by real matrices the Hermetian conjugate is simply the transpose: A real matrix acting on a column vector from the left is dual to the transpose matrix acting on a row vector from the right.

$$\begin{aligned} T^\dagger(x) \to T'^\dagger(x) &= [\rho(R)T(R^{-1}(x' - a))]^\dagger \\ &= T^\dagger(R^{-1}(x' - a))\rho(R)^\dagger \end{aligned} \tag{2.2}$$

A homomorphism ρ of a group G is said to be **unitary** if $\rho(g)^\dagger\rho(g) = I$ for all $g \in G$.

For degrees of freedom like pressure ρ is the trivial homomorphism: $\rho(R) = 1$ for all $R \in SO(3)$. When a tensor field transforms under the trivial homomorphism we say it is a **scalar** under such transformations. T could also be a three dimensional field like wind, in which

case ρ is the identity homomorphism: $\rho(R) = R$ for all $R \in SO(3)$. These tensors transform as **vectors**.

Higher dimensional target spaces of ρ are allowed, but do not show up in models of airflow. The macroscopic degrees of freedom of air are emergent from the thermal properties of ideal gases which do not support shear stress or other more structured interactions. Disordered solids like glass have $SO(3)$ symmetry and can support shear stress. Shear and pressure can be described by 3 by 3 symmetric matrices. The component proportional to the identity matrix can again be represented by the trivial homomorphism. The remaining five components can be expressed as a linear combination of five 3×3 traceless symmetric matrices. Rotations of the glass coordinate system are equivalent to rotations in this 5 dimensional space for shear stress and a 1 dimensional space for pressure.

A **representation** of dimension n of a group is a homomorphism to the space of $n \times n$ matrices. Irreducible representations are those for which there exists no basis such that every matrix corresponding to every group element is block diagonalized. It turns out that there is an irreducible representation of $SO(3)$ in all odd dimensions n and we have given explicit physical examples which can be represented in 1, 3 and 5 dimensions.

Remarkably there is another symmetry group with the same representations in odd dimensions as $SO(3)$ that in a generalized sense (which will be made explicit at the end of this section) also has irreducible representations in *even* dimensions. In some ways this other group is even more natural to consider than $SO(3)$.

2.2.2 *The Quaternions and the Relationship Between $SU(2)$ and $SO(3)$*

The mathematician Sir William Hamilton discovered a new division algebra[4] on the 16th of October 1843 and was so excited he engraved its defining properties into the stones of a nearby bridge. He had been struggling for years to generalize the geometric interpretation of the division algebra of the complex numbers as translations, rotations and scalings of the plane to the same in three dimensions.[5]

Hamilton's breakthrough was to instead consider rotations in four dimensions and then study three dimensions by projection along the extra dimension. He had discovered the quaternions $\mathbb{H}$ which are 4-$\mathbb{R}$-dimensional numbers $a + b\epsilon_x + c\epsilon_y + d\epsilon_z \in \mathbb{H}$ where $a, b, c, d \in \mathbb{R}$ and

$$\begin{gathered} \epsilon_x^2 = \epsilon_y^2 = \epsilon_z^2 = \epsilon_x\epsilon_y\epsilon_z = -1 \\ \Rightarrow \epsilon_x\epsilon_y = -\epsilon_y\epsilon_x = \epsilon_z, \quad \epsilon_y\epsilon_z = -\epsilon_y\epsilon_z = \epsilon_x, \quad \epsilon_z\epsilon_x = -\epsilon_x\epsilon_z = \epsilon_y \end{gathered}$$

This complicated looking algebra can be interpreted as containing the symmetries of 3D space by restricting our attention to the "complex" component $b\epsilon_x + c\epsilon_y + d\epsilon_z$. The familiar 3D vector dot and cross products are given by the symmetric and antisymmetric bilinear forms

$$\begin{aligned} u \cdot v &\equiv \frac{1}{2}(\tilde{u}v + \tilde{v}u) = u_x v_x + u_y v_y + u_z v_z \\ u \times v &\equiv \frac{1}{2}(uv - \widetilde{uv}) = (u_y v_z - u_z v_y)\epsilon_x - (u_x v_z - u_z v_x)\epsilon_y + (u_x u_y - u_y u_x)\epsilon_z \end{aligned} \tag{2.3}$$

where u, $v \in \mathbb{H}$ are of the form $u_x\epsilon_x + u_y\epsilon_y + u_z\epsilon_z$. The tilde's denote the quaternionic

[4] A division algebra is just a space where the notions of addition, subtraction, multiplication and division are all well defined. The real numbers $\mathbb{R}$ and the complex plane $\mathbb{C}$ are the most familiar examples.

[5] He was doomed to failure by topology. There is no way to arrange a unit vector field everywhere tangent to a sphere (as can be done easily for a circle). This is called the hairy ball theorem and it prevents a global definition of the Lie algebra $\mathfrak{so}(n)$ for infinitesimal $SO(n)$ rotations away from an arbitrary rotation $R \in SO(n)$ when n is 3,5,6,7,9 or higher. Correspondingly there are only division algebras in 1,2,4, and 8 dimensions [175]

conjugate which flips the sign of ϵ_x, ϵ_y and ϵ_z, and the order of multiplication: $\widetilde{\tilde{u}v} = \tilde{v}u$.[6] The typical ad hoc justifications for the vector dot and cross products are thus seen to arise uniquely from the algebraic structure of the quaternions.

Furthermore, the Pauli matrices multiplied by a factor $-i \in \mathbb{C}$

$$-i\sigma_x \equiv \tau_x = \begin{pmatrix} 0 & -i \\ -i & 0 \end{pmatrix} \quad -i\sigma_y \equiv \tau_y = \begin{pmatrix} 0 & -1 \\ 1 & 0 \end{pmatrix} \quad -i\sigma_z \equiv \tau_z = \begin{pmatrix} -i & 0 \\ 0 & i \end{pmatrix}$$

have the same algebraic properties as the quaternions

$$\tau_x^2 = \tau_y^2 = \tau_z^2 = \tau_x\tau_y\tau_z = -I$$

$$\Rightarrow \tau_x\tau_y = -\tau_y\tau_x = \tau_z, \quad \tau_y\tau_z = -\tau_y\tau_z = \tau_x, \quad \tau_z\tau_x = -\tau_x\tau_z = \tau_y$$

Thus the symmetry group of the unit quaternions ($a + b\epsilon_x + c\epsilon_y + d\epsilon_z \in \mathbb{H}$ subject to $a^2 + b^2 + c^2 + d^2 = 1$) under multiplication – denoted $Sp(1)$ – is isomorphic[7] to the group generated by the Pauli matrices: 2×2 unitary matrices with unit determinant ($SU(2) \simeq Sp(1)$).

We can write any vector $v \in \mathbb{R}^3$ as a purely complex quaternion $b\epsilon_x + c\epsilon_y + d\epsilon_z \in \mathbb{H}$. Then for any unit quaternion $u \in Sp(1)$, the action $v \to uvu^{-1}$ is equivalent to a rotation in

[6] The order of multiplication must be switched to ensure consistency with the algebra: $\epsilon_x\tilde{\epsilon}_y = -\epsilon_x\epsilon_y = -\epsilon_z$ and $\epsilon_y\tilde{\epsilon}_x = -\epsilon_y\epsilon_x = k \Rightarrow \widetilde{\epsilon_x\tilde{\epsilon}_y} = \epsilon_y\tilde{\epsilon}_x$.

[7] Isomorphisms are bijective homomorphisms. A bijection is a map where each element in the target corresponds to a unique element in the input, ie. one to one and onto.

$SO(3)$. Take for example $u = \epsilon_x$ and $v = v_x\epsilon_x + v_y\epsilon_y + v_z\epsilon_z$:

$$\begin{aligned} uvu^{-1} &= \epsilon_x(v_x\epsilon_x + v_y\epsilon_y + v_z\epsilon_z)(-\epsilon_x) \\ &= v_x\epsilon_x + v_y\epsilon_x\epsilon_y(-\epsilon_x) + v_z\epsilon_x\epsilon_z(-\epsilon_x) \\ &= v_x\epsilon_x + v_y\epsilon_z(-\epsilon_x) + v_z(-\epsilon_y)(-\epsilon_x) \\ &= v_x\epsilon_x - v_y\epsilon_y - v_z\epsilon_z \end{aligned}$$

Conjugation by ϵ_x rotates v by 180° around the x axis. Notice that $v \to uvu^{-1} = (-u)v(-u)^{-1}$ so the action of u and $-u$ is the same. This means that for every element in $SO(3)$ this homomorphism has two preimages in $Sp(1)$. $Sp(1)$ is called a "double cover" of $SO(3)$ for this reason.

Digression: Nearly all texts only discuss the relationship of $SU(2)$ to $SO(3)$ without introducing the quaternions. This would be equivalent to learning the complex numbers with a 2×2 real matrix representation:

$$1 \equiv \begin{pmatrix} 1 & 0 \\ 0 & 1 \end{pmatrix}, \quad i \equiv \begin{pmatrix} 0 & 1 \\ -1 & 0 \end{pmatrix}$$

Complex analysis would be extraordinarily clunky! For example, imagine proving Euler's Identity:

$$e^{i\theta} = \cos\theta + i\sin\theta \tag{2.4}$$

The Euler identity can trivially be generalized beyond the complex plane when students are armed with the quaternion algebra. Let $u = u_x\epsilon_x + u_y\epsilon_y + u_z\epsilon_z \in Sp(1)$ be a purely imaginary unit quaternion (just like i is one of two purely imaginary unit

complex numbers). Then u^2 is simply

$$\begin{aligned} u^2 &= (u_x\epsilon_x + u_y\epsilon_y + u_z\epsilon_z)^2 \\ &= \cancelto{-1}{(-u_x^2 - u_y^2 - u_z^2)} + [\cancelto{0}{(u_x u_y \epsilon_x\epsilon_y + u_y u_x \epsilon_y\epsilon_x)} + (\text{cyclic permutations})] \\ &= -1 \end{aligned}$$

Therefore we can exponentiate $u\theta$ with the usual Taylor expansions for e^x and recover the expansions for $\cos x$ and $\sin x$:

$$\begin{aligned} e^{u\theta} &= \sum_{n=0}^{\infty} u^n \frac{\theta^n}{n!} \\ &= \sum_{n=0}^{\infty} u^{2n} \frac{\theta^{2n}}{(2n)!} + u^{2n+1}\frac{\theta^{2n+1}}{(2n+1)!} \\ &= \sum_{n=0}^{\infty} (-1)^n \frac{\theta^{2n}}{(2n)!} + u(-1)^n \frac{\theta^{2n+1}}{(2n+1)!} \\ &= \cos\theta + u\sin\theta \end{aligned}$$

which is more intuitive than the more common identity using Pauli matrices:

$$e^{i\theta\vec{u}\cdot\vec{\sigma}} = I\cos\theta + i\vec{\sigma}\cdot\vec{u}\sin\theta$$

Because there are two elements in $Sp(1)$ for each element in $SO(3)$, if we try to define a homomorphism $\rho : SO(3) \to Sp(1)$ we are forced to make a choice. We can only define ρ up to a sign ambiguity: $\rho(R_1)\rho(R_2) = \pm\rho(R_1R_2) \in Sp(1)$ where R_1, $R_2 \in SO(3)$. Under projection along the real numbers, this is a true homomorphism so we call it a "projective homomorphism".

We can define a true homomorphism $\rho : SO(3) \to Sp(1)/\mathbb{R} \simeq \mathbf{RP}^3$ where $\mathbf{RP}^3$ is the real projective space of three dimensions given by the space of lines through the origin in

$\mathbb{R}^4$. $Sp(1)/\mathbb{R}$ is the group of elements in Sp(1) where we are interested in elements modulo multiplication by a real number.

In principle then, our dynamic tensors at each point of our $SO(3)$ symmetric manifold may also covariantly transform in representations of $Sp(1)$ so long as observable quantities do not depend on the normalization of the tensor.

The one dimensional representation of $Sp(1)$ is the trivial representation: $\rho(u) = 1$ for all $u \in Sp(1)$. Using the identity homomorphism we get a four dimensional representation: $\rho(u) = u$ for all $u \in Sp(1)$. If we want to have a dynamic tensor field with local degrees of freedom $v \in \mathbb{H}$ where the host manifold is invariant under rotations of $SO(3)$ we must define a multi-valued map $\Phi : R \in SO(3) \rightarrow \Phi(R) = \pm u \in Sp(1)$ and then remove the dependence of observables on the scalar magnitude of the tensor field. Degrees of freedom which transform in this way are called **spinors**.

Spinor degrees of freedom live in $\mathbb{C}^2 \simeq \mathbb{H}$ and transform under $SU(2) \simeq Sp(1)$. Spinors are allowed in QM with $SO(3)$ symmetric space because observables are independent of the state normalization. In QFT the symmetry group of spacetime is not just $SO(3)$ with space and time translations. The true symmetry group of spacetime implies subtle changes in the allowed structure of field theory with radical consequences for relativistic quantum theories of fields.

2.2.3 Special Relativity

Special Relativity is nothing more than the hypothesis that spacetime is symmetric under the action of a specific symmetry group called the Poincaré group $\mathcal{P}$. This group contains the four symmetries of space and time translations, the three symmetries of space rotations, and three symmetries called boosts for a total of ten continuous symmetries.

Boosts are linear transformations which mix space and time coordinates. The existence of boost symmetries requires a constant c which relates units of space and time such that they can be mixed consistently. In SI units $c \equiv 299,792,458\,\mathrm{m/s}$ which defines the ratio of meters to seconds. This is analogous to the way rotations can mix coordinates of width, length and height. Space coordinates must be expressible in equal units for rotations to make sense. Setting $c = 1$ amounts to a choice of a common unit for space and time coordinates.

The combined group of rotations and boosts (and the discrete symmetries of reflections and time reversal) is called the Lorentz group and is denoted $O(3,1)$.[8] The action of the Lorentz group preserves the following indefinite inner product between spacetime points $a, b \in \mathbb{R}^4$:[9]

$$a_\mu b_\mu = -a_t b_t + a_x b_x + a_y b_y + a_z b_z \tag{2.5}$$

Note: We can map a_μ to the space of 2×2 complex matrices

$$(a_t,\, a_x,\, a_y,\, a_z) \to \begin{pmatrix} a_t + a_z & a_x - i a_y \\ a_x + i a_y & a_t - a_z \end{pmatrix}$$

and the determinant

$$\begin{vmatrix} a_t + a_z & a_x - i a_y \\ a_x + i a_y & a_t - a_z \end{vmatrix} = a_t^2 - a_x^2 - a_y^2 - a_z^2$$

is equivalent to $-a_\mu a_\mu$. Multiplying the matrix representation of a_μ by any 2×2

[8] The notation $O(3,1)$ refers to the sign pattern in the preserved inner product. The group $O(2,2)$ preserves the product $a_\mu b_\mu = -a_0 b_0 - a_1 b_1 + a_2 b_2 + a_3 b_3$ for example. Restricting to the positive or negative subspace of $O(m,n)$ one recovers the more familiar groups $O(n)$ or $O(m)$ respectively.

[9] For $a, b \in \mathbb{H}$, the inner product $\frac{1}{2}[ab + \widetilde{a}b]$ is the same as equation 2.5 up to an overall sign. The transformation group of the quaternions preserving this symmetric bilinear form is therefore the Lorentz group. Remarkably, Hamilton set out to construct a division algebra containing $O(3)$ and was forced instead to find an algebra containing the Lorentz group and the spinor group. This was 62 years before Einstein recognized $O(3,1)$ as the structure of flat spacetime and 81 years before Pauli conjectured $Sp(1)$ as the symmetry group of intrinsic electron angular momentum! The connections between the SM and the four division algebras is a fascinating and growing area of research. See [107, 106].

complex matrix with unit determinant (matrices in $SL(2,\mathbb{C})$) will not change the determinant. It is not hard to show that $SL(2,\mathbb{C})$ is a double cover of $SO^+(1,3)$ and therefore the relativistic version of the spinor representation $Sp(1)$ from section 2.2.2.

Restricting our attention to the subgroup of transformations preserving $a_x b_x + a_y b_y + a_z b_z$ we have the familiar set of rotations and reflections $O(3)$. If instead we consider the subgroup preserving $-a_t b_t + a_i b_i$ for $i \in x, y, z$ we have the group $O(1,1)$ which are the symmetries of the hyperbola

$$1 = \cosh^2\eta - \sinh^2\eta = \begin{vmatrix} \cosh\eta & \sinh\eta \\ \sinh\eta & \cosh\eta \end{vmatrix}$$

rather than the circle

$$1 = \cos^2\theta + \sin^2\theta = \begin{vmatrix} \cos\theta & \sin\theta \\ -\sin\theta & \cos\theta \end{vmatrix}$$

The transformation matrices for the $SO(1,1)$ and $SO(2)$ subgroups of the Lorentz group can be remembered as the matrices whose determinant gives the hyperbolic and trigonometric identities as shown.

The three hyperbolic symmetries preserving $-a_t b_t + a_i b_i$ for $i \in x, y, z$ are the boosts of the Poincaré group. They can be thought of as rotations through an "angle" η called **rapidity** which is related to the relative velocity v between the initial and final coordinate systems:

$$\tanh\eta = \beta \equiv \frac{v}{c} \tag{2.6}$$

An important constraint on the possible dynamics of field theories comes from the principle of **causality**:

Observables at one point in spacetime can only effect observables at a later point if the speed of the propagating mode which couples the observables can reach the later

point within the time separation of the points

$$(\Delta x)^2 + (\Delta y)^2 + (\Delta z)^2 \leq (v\Delta t)^2$$

where v is the speed of the mode.

Furthermore, this must be true for all coordinate systems which are equivalent up to a symmetry transformation. Because Poincaré transformations preserve the inner product 2.5, they also preserve the interval

$$(\Delta x)^2 + (\Delta y)^2 + (\Delta z)^2 - (c\Delta t)^2$$

where c is the constant for space-time unit conversion required by the boost symmetries. For the remainder of this thesis we will set $c = 1$.

In differential form, the sphere of causality depends only on the fastest possible propagating mode which is given by

$$\mathrm{d}x^2 + \mathrm{d}y^2 + \mathrm{d}z^2 = \mathrm{d}t^2$$

Dynamic field theories which respect this differential form are said to be **local**:

The correlation between differentially separated fluctuations of coupled tensor fields cannot exceed the expected random correlation from thermal fluctuations unless

$$\mathrm{d}x^2 + \mathrm{d}y^2 + \mathrm{d}z^2 - \mathrm{d}t^2 = 0$$

$\mathcal{P}$ can be decomposed as the semi-direct product of $\mathbb{R}^4$ (spacetime translations) and $O(3,1)$

(rotations, boosts and space and time inversions):

$$\mathcal{P} \simeq \mathbb{R}^4 \ltimes O(3,1)$$

Poincaré transformations can be expressed in terms of a spacetime translation $a \in \mathbb{R}^4$ and a Lorentz transformation Λ which can be represented as a 4×4 real matrix. It is a semi-direct product rather than a direct product because of the way Poincaré transformations are composed:

$$\begin{aligned}(a_2,\, \Lambda_2)((a_1,\, \Lambda_1)(x)) &= \Lambda_2(\Lambda_1 x + a_1) + a_2 \\ &= \Lambda_2\Lambda_1 x + \Lambda_2 a_1 + a_2 \\ = (\Lambda_2 a_1 + a_2,\, \Lambda_1\Lambda_2)(x)\end{aligned}$$

In words, the Lorentz transformation of the second Poincaré transformation must be applied to the spacetime translation of the first but not vice versa.

One way to ensure observables are consistent and do not violate causality is to compute them relative to quantities which are the same in all coordinate systems generated by Poincaré transformations. Lorentz scalars constructed by contracting covariant and contravariant tensors at each spacetime point have this property. We can construct Lorentz scalars from tensors if they transform under a unitary representation of the Lorentz group:

$$T^\dagger(x)T(x) \to T^\dagger(x)\rho(\Lambda)^\dagger\rho(\Lambda)T(x) = T^\dagger(x)T(x)$$

Here is where we hit a road block and we find our first radical departure from the usual notions of particle mechanics as alluded to at the end of the previous subsection. The *only* finite dimensional irreducible unitary representation of the Lorentz group is the scalar repre-

sentation.[10] Known particles like the electron are well described in the non-relativistic limit as transforming under the unitary representation $SU(2) \simeq Sp(1)$. These representations must either become infinite dimensional, reducible or non-unitary when extended to the full symmetry group of spacetime!

2.3 Quantum Field Theory

In the previous section we explained that tensor degrees of freedom defined at every point in spacetime must respect the algebraic structure of the symmetry group of spacetime. We then looked for representations of symmetry groups with the same algebraic structure as the original group which act on the tensor degrees of freedom instead of spacetime itself. We needed these representations to exist so that physical configurations of the tensor fields could be equivalently described in all coordinate systems related by spacetime symmetry.

Next we attempted to construct spacetime symmetry independent quantities from covariant and contravariant tensors. At this stage in order to accommodate the observation of electrons and other seemingly fundamental particles of a non-scalar nature, we were forced to abandon either the finite dimensionality, irreducibility or unitarity of non-relativistic physics.

Fortunately, quantum mechanics offers a clue for how to resolve this: In QM, it is equivalent to require the operator valued degrees of freedom to be unitary or, for their action on the Hilbert space to be unitary. By promoting our tensor fields to be operators acting on some infinite dimensional state space we can hope it will be possible to construct unitary irreducible representations of the Lorentz group in terms of their action on the state space.

Furthermore, this promotion of tensor fields to operator fields leads naturally to field degrees of freedom transforming under representations of the richer symmetry group $SL(2, \mathbb{C})$:

[10] We will not attempt to prove this here. For more see Chapter 35 of [205].

Observables constructed from the Hermetian inner product of state vectors automatically project $Sp(1)$ onto its double cover of $SO(3)$.

In the non-relativistic limit $c \to \infty$, the symmetry group of spacetime becomes

$$\mathbb{R}^4 \ltimes O(3)$$

and the state space of single particles will transform under representations of $Sp(1)$. In this picture, all of the weirdness of QM is a consequence of our lack of intuition for the unitary structure of Poincaré invariant state spaces. A sentient being whose natural units place c and $\hbar$ near unity would find all of this much easier to follow!

2.3.1 Unitary Representations of Poincaré

Formally defining a state space which transforms unitarily under Poincaré transformations turns out to be exceedingly difficult, if not impossible in all but a few cases. What we *do* understand are the so called "free" field theories in which the state space of a given Lorentz representation consists of an infinite tensor product of single particle states called a **Fock space**: $\otimes^{\infty}\mathcal{H}$.

The single particle states are solutions to the free wave equation

$$\mathcal{D}T(x) = \lambda T(x) \tag{2.7}$$

where $\mathcal{D}$ is a differential operator which commutes with the Lorentz representation of the tensor field T at every spacetime point x and λ is a constant.[11] We choose $\mathcal{D}$ to commute

[11] In contrast to interacting theories, this equation is linear, meaning a linear combination of solutions is also a solution. Linearity is what allows the formal definition of the Fock space as a vector space. It is not obvious how to extend this notion to theories defined by nonlinear equations.

with the action of Lorentz on T so that Poincaré transformations preserve the solution space. In this way the non-unitary action of the Poincaré group on the field operators induces a unitary transformation on physical observables. We will drop the spacetime labels for fields for the remainder of this chapter, ie. $T(x) \equiv T$.

Infinite dimensional unitary representations of the Poincaré group therefore exist if such a differential operator on T can be found. Schrödinger understood this but could only find the d'Alembertian operator $\partial^2 \equiv \partial_\mu \partial_\mu$[12] where the sum over indices is the same as the Lorentz invariant inner product 2.5:

$$\partial^2 \phi = (-\partial_t^2 + \partial_x^2 + \partial_y^2 + \partial_z^2)\phi = m^2 \phi \tag{2.8}$$

This is called the Klein-Gordon equation and its solution space is trivially Lorentz invariant because the inner product $\partial_\mu \partial_\mu$ is a Lorentz scalar.

Dirac's genius was to recognize that the Klein-Gordon operator $\partial^2 - m^2$ can be factored in terms of 4×4 matrices generating a Clifford algebra. We will not delve into such complexities here, instead we will start with the massless wave equation

$$-\partial^2 \Psi(x) = 0 \tag{2.9}$$

and factor the d'Alembertian over $\mathbb{C} \otimes \mathbb{H}$.[13] Numbers in $\mathbb{C} \otimes \mathbb{H}$ can be conjugated in three ways, there is the regular complex conjugate $* : i \to -i$, the quaternionic conjugate $\tilde{}: \epsilon_i \to -\epsilon_i \; i \in x, y, z$ and finally the Hermetian conjugate $\dagger$ which does both. Note that the quaternionic and Hermetian conjugates must flip the order of multiplication of the quaternion generators to respect the quaternion algebra.

[12] $\partial_\mu \equiv (\frac{\partial}{\partial t}, \frac{\partial}{\partial x}, \frac{\partial}{\partial y}, \frac{\partial}{\partial z}) \equiv (\partial_t, \partial_x, \partial_y, \partial_z)$

[13] This is isomorphic to linear combinations of the Pauli matrices with complex coefficients.

To factor ∂^2 it will suffice to find a Hermetian differential operator with coefficients in $\mathbb{C}\otimes\mathbb{H}$ such that

$$(q_t\partial_t + q_x\partial_x + q_y\partial_y + q_z\partial_z)^*(q_t\partial_t + q_x\partial_x + q_y\partial_y + q_z\partial_z) = \partial_t^2 - \partial_x^2 - \partial_y^2 - \partial_z^2 \equiv -\partial^2$$

It is easy to check that $\partial_\dagger \equiv \partial_t + i\epsilon_x\partial_x + i\epsilon_y\partial_y + i\epsilon_z\partial_z$ is a solution:

$$\partial_\dagger^*\partial_\dagger = -\partial^2$$

where the $_\dagger$ reflects the fact that $\partial_\dagger$, and $\partial_\dagger^*$ are Hermetian: $\partial_\dagger = \partial_\dagger^\dagger$.

Then any fields Ψ_L, $\Psi_R \in \mathbb{C}\otimes\mathbb{H}$ satisfying the **Weyl wave equations**

$$\begin{aligned}\partial_\dagger^*\Psi_L &= 0\\ \partial_\dagger\Psi_R &= 0\end{aligned} \tag{2.10}$$

are independent spinor solutions to the massless wave equation 2.9. These independent solutions are called **Weyl spinors** and as can be seen from equation 2.10 the solution spaces are related by complex conjugation.[14]

Returning to the case $\lambda \neq 0$, all nontrivial simultaneous solutions to both Weyl equations violate Lorentz covariance.

Proof. Suppose there exists a nonzero spinor field such that $\partial_\dagger^*\Psi = \partial_\dagger\Psi = im\Psi$ where $(im)^2 = -\lambda$ with $m \neq 0$. Then we can add the Weyl equations together

$$(\partial_\dagger^* + \partial_\dagger)\Psi = 2\partial_t\Psi = 2im\Psi.$$

[14] As explained in 3.5.3 of [107], this representation in $\mathbb{C}\otimes\mathbb{H}$ gives a simpler relationship between left and right Weyl spinors than the usual representation using Pauli matrices because the complex conjugate flips the sign of the basis vectors $i\epsilon_x, i\epsilon_y, i\epsilon_z \in \mathbb{C}\otimes\mathbb{H}$ *and* the complex components of their coefficients. The construction of Dirac spinors is explained further in [106].

We can also subtract the Weyl equations

$$(\partial_\dagger - \partial_\dagger^*)\Psi = 2i(\epsilon_x\partial_x + \epsilon_y\partial_y + \epsilon_z\partial_z) = 0.$$

The wave equation becomes

$$\partial^2\Psi = -\partial_t^2\Psi = m^2\Psi$$

which cannot be invariant under boosts unless $\Psi = 0$. □

We can however solve the coupled equations

$$\begin{aligned} \partial_\dagger^*\Psi_L &= im\Psi_R \\ \partial_\dagger\Psi_R &= im\Psi_L \end{aligned} \tag{2.11}$$

in a Lorentz covariant way. The set $(\Psi_L,\ \Psi_R)$ solves the wave equation for $\lambda = m^2 \neq 0$:

$$\begin{aligned} \partial^2\Psi_L &= m^2\Psi_L \\ \partial^2\Psi_R &= m^2\Psi_R \end{aligned}$$

A coupled pair of Weyl spinors which solve the wave equation in this way is called a **Dirac spinor**.

While we are unable to define classical field theories that transform under unitary representations of the Poincaré group[15] we are able to define infinite dimensional state spaces for massive and massless scalar and spinor fields which transform unitarily. In the next section we consider how to formulate nontrivial dynamics resulting from interactions between fields.

[15] Other than scalar fields or infinite dimensional fields.

2.3.2 Variational Mechanics and the Lagrangian

The universe appears to be the ultimate calculating machine. Set up any kind of complicated mechanism and the universe will evolve all the moving parts forward in time in some self consistent way. Pendula swing, chemicals react and particles collide all without contradiction. Dynamic variables such as the angle of a pendulum, the distance between chemical reactants or the quantized values of fields are examples of the general notion of a degree of freedom. Degrees of freedom can be ascribed values and rates of change in some appropriately chosen coordinate system. As the system evolves, the degrees of freedom trace out paths in the collective coordinate space of instantaneous values and rates of change called "phase space". Nature it seems, picks out special paths in phase space based on some underlying and possibly unchanging rules.

The goal of fundamental physics is to find out if these rules exist and if they do, to find their explicit form.[16] This requires finding the correct set of degrees of freedom, path selection rules and computational tools to make predictions.

Appendix A introduces the calculus of variations and classical Lagrangian mechanics for readers that are not already familiar with the topic. The central idea in the application of the calculus of variations to physics is that nature has a consistent way of picking paths, so there should also exist a function over phase space which picks the same paths.

The phase space of fields is infinite dimensional, with each space point tracing out its own path in time. We define the Lagrangian density over spacetime as a function of each tensor

[16] We can never know for certain if this goal has been reached, but we can know if we haven't reached it! Our current model of the universe appears to be mathematically inconsistent when extrapolated to some extreme corner cases and there are observed physical phenomena which cannot be accounted for with the known particles and forces. See Section 2.7.1 for more.

field T_i and their spacetime gradients $\partial_\mu T_i$:

$$\mathcal{L}(T_i,\, \partial_\mu T_i) \tag{2.12}$$

We can then integrate the Lagrangian density over a spacetime region Ω with boundary Σ to get the action

$$S[\gamma_i] = \int_\Omega \mathrm{d}^4x\, \mathcal{L}(T_i,\, \partial_\mu T_i) \tag{2.13}$$

which is a functional of field configurations γ_i.

Next we can ask for field configurations about which the action is stationary by computing the first order change to the action under a perturbation of the field. Let $T_i' = T_i + \epsilon t_i$ where t_i is some field configuration that is zero on Σ. We can compute the variation of the action as a function of ϵ, set $\epsilon = 0$ and find stationary solutions for T_i:

$$\begin{aligned}
0 &= \frac{\mathrm{d}S}{\mathrm{d}\epsilon}\Big|_{\epsilon=0} \\
&= \int_\Omega \mathrm{d}^4x\, \frac{\mathrm{d}\mathcal{L}(T_i',\, \partial_\mu T_i')}{\mathrm{d}\epsilon}\Big|_{\epsilon=0} \\
&= \int_\Omega \mathrm{d}^4x \left[\frac{\mathrm{d}T_i'}{\mathrm{d}\epsilon}\frac{\partial\mathcal{L}}{\partial T_i'}\Big|_{\epsilon=0} + \frac{\mathrm{d}(\partial_\mu T_i')}{\mathrm{d}\epsilon}\frac{\partial\mathcal{L}}{\partial(\partial_\mu T_i')}\Big|_{\epsilon=0}\right] \\
&= \int_\Omega \mathrm{d}^4x \left[t_i\frac{\partial\mathcal{L}}{\partial T_i} + (\partial_\mu t_i)\frac{\partial\mathcal{L}}{\partial(\partial_\mu T_i)}\right]
\end{aligned}$$

Integrate the second term in the last line by parts:

$$0 = \int_\Omega \mathrm{d}^4x \left[t_i\frac{\partial\mathcal{L}}{\partial T_i} - t_i\partial_\mu\frac{\partial\mathcal{L}}{\partial(\partial_\mu T_i)} + \partial_\mu\left(t_i\frac{\partial\mathcal{L}}{\partial(\partial_\mu T_i)}\right)\right] \tag{2.14}$$

The integral over the total derivative term is zero because we set $t_i(x) = 0$ for $x \in \Sigma$. Then

for the action to be stationary for all t_i the Euler-Lagrange equation must hold:

$$0 = \frac{\partial \mathcal{L}}{\partial T_i} - \partial_\mu \frac{\partial \mathcal{L}}{\partial(\partial_\mu T_i)} \tag{2.15}$$

If we hypothesize that physical dynamics should be independent of some continuous symmetries which deform the fields T_i in the direction of t_i, we can require that the action be unchanged. The total derivative term in equation 2.14 must be zero if t_i corresponds to a change of T_i generated by a symmetry transformation.

For any physically unobservable family of continuous deformations of the fields, there is a corresponding conserved current which ensures the action is invariant:

$$\partial_\mu \left(t_i \frac{\partial \mathcal{L}}{\partial(\partial_\mu T_i)} \right) = 0 \tag{2.16}$$

More generally, if the applied symmetry also transforms spacetime, the action integration region Ω and integration measure d^4x may also change. The conserved current picks up an additional term from the divergence of the change in spacetime coordinates times the Lagrangian density:

$$\partial_\mu \left(\delta T_i \frac{\partial \mathcal{L}}{\partial(\partial_\mu T_i)} + \delta x_\mu \mathcal{L} \right) = 0 \tag{2.17}$$

where the variation of the field δT_i includes deformations from field symmetries and the change in spacetime coordinates δx_μ. When δx_μ corresponds to spacetime translations the conserved currents are energy and momentum and when δx_μ corresponds to rotations the currents are angular momentum. The conserved currents associated to boosts are more abstract but qualitatively correspond to the center of mass.

Equations 2.16 and 2.17 are special cases of **Noether's theorem** [158] which gives the general conserved quantities associated to field theories where even the spacetime measure

d^4x may depend on x. In particular, Noether's theorem explicitly shows that the stress energy tensor in GR is *not* a globally conserved quantity. This revelation demoted the notion of conservation to a local property with at best globally *approximate* conservation laws! Ed Witten wrote a fascinating article [204] discussing a modern interpretation of global symmetry which we recommend to the interested reader.

2.3.3 Scattering and Feynman Diagrams

The Euler-Lagrange equations allow us to calculate *classical* paths but we would like to calculate quantum mechanical **scattering amplitudes**. The idea here is to associate complex numbers with processes where some free particles come in to an interaction region, scatter, and transition to some generally different set of outgoing free particles. This defines a **scattering matrix** (or S-matrix for short) which in contrast to free theories allows for nonzero overlap between distinct free particle states. We then require the scattering matrix to be Poincaré invariant, local, and unitary despite the fact that the state space of the interacting theory may be ill-defined.

There are some beautiful techniques for computing scattering amplitudes which capitalize on generalized notions of unitarity, the analytical structure of the amplitude over complexified inputs and the linearization of hidden symmetries of the amplitude. For an introduction to these topics we recommend H. Elvang and Y. Huang's book [96].

The most broadly used method for calculating scattering amplitudes uses Richard Feynman's formulation in terms of a **path integral**.[17] Feynman's idea [100] was to formulate quantum mechanics, not in terms of the unitary time evolution of particle states as in Hamiltonian mechanics, but in terms of a sum over all possible paths between in and out states.

[17] S. Tominaga [134] and J. Schwinger [183] independently found a different formulation around the same time. For more on this see Section 2.4

This method can obscure the unitarity of the S-matrix but, each path contains only local interactions and is manifestly Lorentz covariant.

There should exist a suitable measure for the sum over paths such that the total probability (given by the magnitude of the amplitude sum) is one for an input state to go to any output state consistent with conservation laws. The probability should also be exactly zero for any output state inconsistent with those same laws.

For free theories all paths γ between input and output field configurations are weighted equally with complex phase given by the action in units of $\hbar$. The total overlap between input and output field configuration is then

$$\langle \mathrm{Out} | \, \mathrm{S} \, | \mathrm{In} \rangle = \int_{\gamma_{\mathrm{In}}}^{\gamma_{\mathrm{Out}}} \left[\mathcal{D}\gamma \right] e^{iS[\gamma]/\hbar}$$

where the "integral" measure $\mathcal{D}\gamma$ is a functional measure over the space of paths. The functional measure must be carefully defined to enforce the unitarity of the S-matrix.

In this picture $\hbar$ can be interpreted as the constant which converts between units of energy and frequency. For the remainder of this discussion we choose units such that $\hbar = 1$. It is important to note that in these units the action represents a complex phase and must be dimensionless. The spacetime measure d^4x has units $[E]^{-4}$ so every term in the Lagrangian density must have dimension $[E]^4$. This has important consequences for the coefficients for interaction terms called **couplings** and their scale dependence which we describe in Section 2.3.4.

We can split a general S-matrix into a sum of the identity matrix I and a transition matrix T as $\mathrm{S} = I + iT$. For free theories what goes in is what comes out and $\mathrm{S}_{\mathrm{free}} = I$. If an interaction term is added to the free field Lagrangian density, we can compute S-matrix

elements in a perturbative expansion we illustrate schematically as

$$\begin{aligned}\langle \text{Out}|\, \text{S}\, |\text{In}\rangle &= \int_{\gamma_{\text{In}}}^{\gamma_{\text{Out}}} \big[\mathcal{D}\gamma\big] \exp\Big\{ i \int \mathrm{d}^4x [\mathcal{L}_{\text{free}} + g\mathcal{L}_{\text{int.}}] \Big\} \\ &= \int_{\gamma_{\text{In}}}^{\gamma_{\text{Out}}} \big[\mathcal{D}\gamma\big] e^{iS_{\text{free}}[\gamma]} \big(1 + ig\mathcal{L}_{\text{int.}} - \frac{g^2}{2}\mathcal{L}^2_{\text{int.}} - \frac{ig^3}{3!}\mathcal{L}^3_{\text{int.}} + ...\big)\end{aligned}$$

where g is a small coupling parameter which determines how much the nonzero interaction points contribute to the action. The terms $\mathcal{L}^n_{\text{int.}}$ are the interaction term evaluated at n spacetime points.

Subtracting off the trivial part of the scattering matrix gives

$$i\,\langle \text{Out}|\, T\, |\text{In}\rangle = \int_{\gamma_{\text{In}}}^{\gamma_{\text{Out}}} \big[\mathcal{D}\gamma\big] e^{iS_{\text{free}}[\gamma]} \big(ig\mathcal{L}_{\text{int.}} - \frac{g^2}{2}\mathcal{L}^2_{\text{int.}} - \frac{ig^3}{3!}\mathcal{L}^3_{\text{int.}} + ...\big)$$

thereby only considering paths making use of the interaction term.

Feynman represented this expansion as a sum of integrals over d^4x where each integral could be represented with a diagram [101]. External particles coming in from the left and going out on the right are free theory states while internal lines represent free field propagators[18] and vertices represent exchanges between fields. Each vertex is accompanied by delta distributions with support only over the total incoming values of each conserved Noether current. The diagram is then integrated over all internal degrees of freedom to get the corresponding partial amplitude.

Diagrams with n vertices are suppressed by g^n so that successive orders in the expansion contribute less to the total amplitude. Eventually however, the expansion will diverge be-

[18] Free field propagators are simply the inverse of the corresponding wave equation operator. For instance, in momentum space (ignoring subtleties of analytic continuation from 4D euclidean space) the Klein-Gordon propagator is $-i/(p_\mu p_\mu - m^2)$.

cause the number of contributing diagrams grows factorially in n.[19] Fortunately there is a notion of "Borel summation" which allows such divergent expansions to provide excellent approximations up to a finite order where the divergence takes over. For more on this issue and related analysis problems we recommend J. Baez' enjoyable article *Struggles with the Continuum* [49] and the lecture notes from M. Florey et al. *How I Learned to Stop Worrying and Love QFT* [103].

Feynman diagram integrals are generally easier to compute in momentum space as this linearizes the energy-momentum conserving delta distributions. We can perform a spacetime Fourier transform to convert the tensor fields over spacetime $T(x_\mu)$ to an equivalent description over momentum space $T(p_\mu)$:

$$T(p_\mu) = \int \mathrm{d}^4x\, T(x_\mu) e^{-ip_\mu x_\mu}$$

If we assume $T(x_\mu)$ goes to zero at infinity this change of variables diagonalizes the ∂_μ operator:

$$\begin{aligned}
\partial_\mu T(x_\mu) &= \int \mathrm{d}^4x \left(\partial_\mu T(x_\mu)\right) e^{-ip_\mu x_\mu} \\
&= \cancelto{0}{\int \mathrm{d}^4x\, \partial_\mu \left(T(x_\mu) e^{-ip_\mu x_\mu}\right)} - \int \mathrm{d}^4x\, T(x_\mu) \partial_\mu e^{-ip_\mu x_\mu} \\
&= ip_\mu \int \mathrm{d}^4x\, T(x_\mu) e^{-ip_\mu x_\mu} \\
&= ip_\mu T(p_\mu)
\end{aligned}$$

In this way vertices represent exchanges between fields not at points in spacetime but, at points in momentum space.

[19] There are some special, highly symmetric interacting theories where this series does converge but they are the exception that makes the rule. In such theories the usual Feynman diagram approach is sub-optimal or even impossible as is the case for $\mathcal{N} = 4$ SYM which has no known off-shell super-space formulation [96].

Consider the Lagrangian density for a massless Dirac fermion Ψ coupled to a massless real scalar field ϕ:[20]

$$\mathcal{L} = i\bar{\Psi}\partial\!\!\!/\Psi - \frac{1}{2}\partial_\mu\phi\partial_\mu\phi + g\phi\bar{\Psi}\Psi$$

For g sufficiently small this theory is well described by free massless Dirac fermions and scalars with interactions mediated by the trivalent vertex $\phi\bar{\Psi}\Psi$. We can compute $\Psi\Psi \to \Psi\Psi$ scattering with a sum of diagrams:

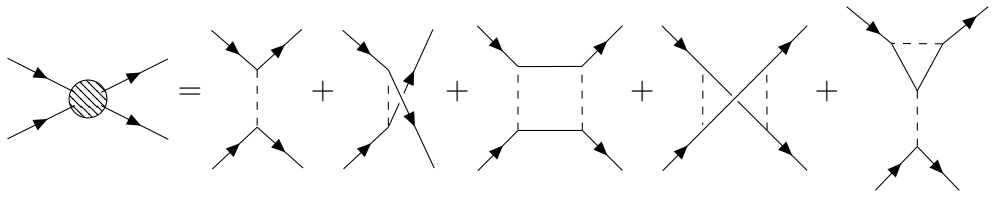

(2.18)

First, notice that with only trivalent vertices the interaction term must be evaluated an even number of times. An odd number of $\phi\bar{\Psi}\Psi$ vertices would create outgoing scalars which are not included in the output state.

The two leading order diagrams contributing to this process are at order g^2. The second and fourth diagrams in the expansion are required by the fact that these are identical fermions so we must include scalar exchanges which swap the fermions. All topologically in-equivalent diagrams at each order in g must be included.[21]

The first two diagrams are known as **tree diagrams** because they contain no loops. Tree amplitude integrals are fully "localized" by the Noether current conserving delta distributions.

[20] The $\partial\!\!\!/$ operator denotes $\gamma_\mu\partial_\mu$ where γ_μ are 4 by 4 anti-commuting matrices which generate the Clifford algebra $Cl(3,1)$ which Dirac used to factor the Klein-Gordon operator: $\partial^2 - m^2 = (\partial\!\!\!/ - mI)(\partial\!\!\!/ + mI)$ where I is the 4 by 4 identity matrix.

[21] In general it is extremely difficult to know if two diagrams are topologically equivalent! Physicists interested in pushing the limits of amplitude calculations often use the "planar limit" which restricts the set of diagrams to consider as those which can be drawn on a plane without any lines crossing.

The first two diagrams are

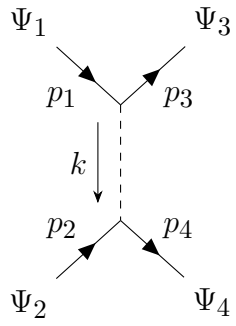

$$= \bar{\Psi}_4\bar{\Psi}_3 \int \frac{\mathrm{d}^4k}{(2\pi)^4}\,(ig)^2 \frac{-i\delta^4(p_1-p_3-k)}{k^2}\Psi_1\Psi_2 = \frac{ig^2}{(2\pi)^4}\frac{(\bar{\Psi}_3\Psi_1)(\bar{\Psi}_4\Psi_2)}{(p_1-p_3)^2}$$

and

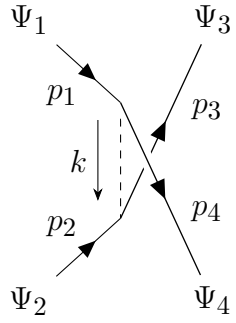

$$= \bar{\Psi}_3\bar{\Psi}_4 \int \frac{\mathrm{d}^4k}{(2\pi)^4}\,(ig)^2 \frac{-i\delta^4(p_1-p_4-k)}{k^2}\Psi_1\Psi_2 = \frac{ig^2}{(2\pi)^4}\frac{(\bar{\Psi}_4\Psi_1)(\bar{\Psi}_3\Psi_2)}{(p_1-p_4)^2}$$

where spacetime and spinor indices are implied.

Then in Mandelstam variables[22] the tree level amplitude for $\Psi\Psi \to \Psi\Psi$ scattering in this model is

$$A_{\text{tree}} = \frac{ig^2}{(2\pi)^4}\left(\frac{(\bar{\Psi}_3\Psi_1)(\bar{\Psi}_4\Psi_2)}{t} + \frac{(\bar{\Psi}_4\Psi_1)(\bar{\Psi}_3\Psi_2)}{u}\right)$$

For the polynomial expansion in g expressed in the diagrammatic sum 2.18 to give a unitary S-matrix, each order in g must be independently unitary. This gives a nice way to check for errors in each diagrammatic sum at order g^n. Conversely, if any scattering process at any order allowed by a theory is found *not* to be unitary there must be terms missing from the Lagrangian. The existence of both the charm quark and the Higgs boson was predicted by

[22] In two to two scattering $1,2 \to 3,4$ Mandelstam variables are defined as $s = (p_1+p_2)^2 = (p_3+p_4)^2$, $t = (p_1-p_3)^2 = (p_2-p_4)^2$, and $u = (p_1-p_4)^2 = (p_2-p_3)^2$ where $p^2 = p_\mu p_\mu$ as in equation 2.5.

adding the simplest possible terms to the known Lagrangian which recovered unitarity.

2.3.4 Loop Integrals: Regularization and Renormalization

A problem arises when trying to compute the last diagram in equation 2.18 – the integral over the unconstrained loop momentum is divergent:

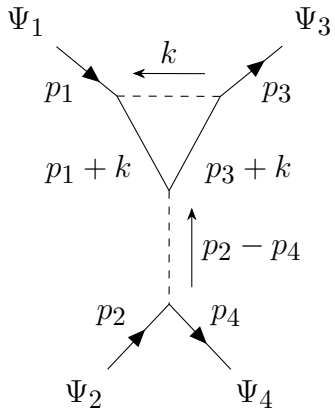

$$\propto \frac{g^3}{2} \int \frac{\mathrm{d}^4 k}{(2\pi)^4} \frac{(\not{p}_3 + \not{k})(\not{p}_1 + \not{k})}{(p_3 + k)^2 k^2 (p_1 + k)^2} \tag{2.19}$$

We can compute the loop integral in Figure 2.19 by utilizing a couple of clever tricks. First we combine the denominators by writing the integrand in terms of an integral over "Feynman parameters" using the following identity [194]:

$$\frac{1}{A_1 \ldots A_n} = (n-1)! \int_0^1 \mathrm{d}a_1 \ldots \mathrm{d}a_n \frac{\delta(1 - \sum_{i=1}^n a_i)}{(a_1 A_1 + \ldots + a_n A_n)^n}$$

If we define $q \equiv k + a_1 p_1 + a_3 p_3$ then we have

$$\begin{aligned} \mathrm{N} &\equiv (\not{p}_3 + \not{k})(\not{p}_1 + \not{k}) \\ &= ([1 - a_3]\not{p}_3 - a_1 \not{p}_1 + \not{q})([1 - a_1]\not{p}_1 - a_3 \not{p}_3 + \not{q}) \end{aligned}$$

and

$$\frac{\mathrm{N}}{(p_3+k)^2k^2(p_1+k)^2} = 2\int_0^1\int_0^1 \mathrm{d}a_1\mathrm{d}a_3\,\frac{\mathrm{N}}{\big(a_1(p_1+k)^2+(1-a_1-a_3)k^2+a_3(p_3+k)^2\big)^3}$$

$$= 2\int \mathrm{dF}\,\frac{\mathrm{N}}{(q^2+\mathrm{D})^3}$$

$$\text{where } \mathrm{D} \equiv a_1(1-a_1)p_1^2 + a_3(1-a_3)p_3^2 - 2a_1a_3p_1p_3$$

$$\text{and } \int \mathrm{dF} \equiv \int_0^1\int_0^1 \mathrm{d}a_1\mathrm{d}a_3$$

Now we can swap the order of integration to do the momentum space integral before the Feynman parameter integral. We can replace $\mathrm{d}^4k \to \mathrm{d}^4q$ because the Jacobian for this transformation is trivial. By adding mass terms and a small complex deformation to the propagators we can define a **Wick rotated** integral replacing $t \to it$ such that the Minkowski metric of spacetime becomes Euclidean. Let $\bar{q}$ denote the Wick rotated four momentum.

Expanding N in orders of $\bar{q}$ we have $N \equiv \bar{q}^2 + \mathcal{O}(\bar{q}) + \mathcal{O}(\bar{q}^0)$. The terms linear in $\bar{q}$ integrate to zero while the $\mathcal{O}(\bar{q}^0)$ gives a finite piece. The following integral identity will allow us to explicitly evaluate the divergent part of the loop integral [194]:

$$\int \frac{\mathrm{d}^d\bar{q}}{(2\pi)^d}\,\frac{(\bar{q}^2)^a}{(\bar{q}^2+D)^b} = \frac{\Gamma(b-a-d/2)\Gamma(a+d/2)}{(4\pi)^{d/2}\Gamma(b)\Gamma(d/2)}\,D^{-(b-a-d/2)}$$

Taking $a=1$, $b=3$ and the Euclidean spacetime dimension to be $d = 4+2\epsilon$ for $\epsilon \ll 1$ the divergent part of the loop integral is[23]

$$\approx \frac{(g\tilde{\mu}^\epsilon)^3}{(4\pi)^2}\int \mathrm{dF}\,\frac{1}{\epsilon}\left(\frac{1}{D}\right)^\epsilon$$

[23] This process of regularizing divergent integrals by introducing a non-integer spacetime dimension is known as **dimensional regularization**. It was first described by Juan José Giambiagi and Carlos Guido Bollini [59] and discovered independently by Gerard 't Hooft and Martin Veltman where they used it to renormalize nonabelian gauge interactions [128]. The story [57] of Giambiagi and Bollini's work in a tumultuous Argentina is little known and incredible.

where we have introduced the arbitrary dimensionful parameter $\tilde{\mu}$ such that $g\tilde{\mu}^\epsilon$ is dimensionless in d dimensions.

Using the fact that $A^\epsilon \approx 1 + \epsilon \log A$ and $\int 1\mathrm{dF} = 1$ the divergence simplifies to

$$\approx \frac{g^3}{(4\pi)^2}\left(\frac{1}{\epsilon} + \int \mathrm{dF}\ \log\frac{\tilde{\mu}^3}{D}\right)$$

This quantity diverges in the limit $d \to 4$ because we calculated it with free field propagators between states which are only well defined in the free theory. Fortunately, many interacting theories defined in this way can be **renormalized** whereby a finite number of divergences can be absorbed by the field normalizations and the free parameters in the Lagrangian density.

In the process of renormalization we often find we are forced to introduce arbitrary scale parameters such as $\tilde{\mu}$. These parameters have no impact on physical observables. We can measure the physical coupling g_{phys} in a $\Psi\Psi$ collider at some collision energy and renormalize the theory to match. Next we can predict what we would measure for the coupling at a different collision energy.

In each experiment we are free to add or subtract logarithms of our arbitrary scale $\tilde{\mu}$ when defining g_{phys}. By choosing $\tilde{\mu} \approx \sqrt{s}$ we minimize the contributions from the logarithms of $\tilde{\mu}$ at a given experimental energy scale $\sqrt{s}$ while fixing the functional dependence of g_{phys} on $\sqrt{s}$.

Interacting QFTs cannot predict the physical values of Lagrangian parameters but, they *can* predict the measured change in those parameters as a function of the experimental energy scale. This scale dependence of the free parameters of a QFT is called the **Renormalization Group** (RG) despite not being a group in the mathematical sense.[24] The RG of a theory

[24] The change in parameters as a function of scale is not always an invertible flow. Many low energy theories can flow to the same high energy theory for example.

is encapsulated in the **beta functions** of the theory which give the rate of change of the couplings with respect to the reference energy scale.

$$\beta(\mu) = \frac{\mathrm{d}g}{\mathrm{d}\log\mu}$$

By measuring the couplings of the SM at some experimental scale we can compute their expected values at another scale. The result of this calculation is shown in Figure 2.3. In the following sections we will explain the origin and flow of these parameters as we construct the SM from the tools described above.

2.4 Quantum Electrodynamics

Einstein showed in 1905 that any successful description of light interacting with matter must be both quantum mechanical [92] (unitary) and Lorentz invariant [93] (local). Maxwell's 1865 classical field theory of electromagnetism [144] already described light in a Lorentz invariant manner but, was far from a quantum mechanical description.

Dirac found a fermionic wave equation in 1928 [87] which he interpreted semi-classically by computing the first order energy levels of hydrogen. He arrived at his wave equation by factoring the Klein-Gordon operator (equation 2.8) in terms of 4 by 4 complex anti-commuting matrices. Dirac then used his new found wave equation to compute the Hamiltonian governing the time evolution of spinor fields in a classical background electromagnetic field.

Prior to this work the experimentally observed "duplexity" of intrinsic electron angular momentum (the Stern-Gerlach experiment [109] is the canonical example) had been empirically added to models of the atom by Pauli [166] and Darwin[25]. The solutions to the

[25] Charles Galton Darwin, grandson of Charles Darwin.

Dirac equation offered a relativistic explanation for this phenomenon at least in a first order approximation.

Dirac was concerned that his equations applied equally well to electrons of positive or negative charge and initially took this to be a nonphysical artifact of his equation. Only four years later however, Carl Anderson and Seth Neddermeyer observed particle tracks in their cloud chamber experiments which appeared consistent with positively charged electrons which became known as positrons. This was the first observation of antimatter.

It was becoming clear there was deep truth hiding in the Dirac equation but, attempts to perform more precise and fully quantum mechanical calculations with it were running into the divergences of Section 2.3.4. Rather than finding smaller and smaller corrections at succeeding orders in perturbation theory, second order calculations gave infinite corrections.

In 1947 while riding a train to a conference, Hans Bethe realized he could absorb these infinities into the definition of the free parameters of the theory by fixing a small number of observables to their experimentally determined values. Once this was done he was able to compute finite higher order corrections to other observables. Bethe successfully applied his technique to extract the Lamb shift[26] from a fully quantum mechanical treatment of the Dirac equation [56].

Only a year later Tominaga [134] and Schwinger [183] independently arrived at a fully quantized description of electromagnetism and fermions which could be applied beyond leading order using a technique. Their approach became known as canonical or "second" quantization. Schwinger famously found the magnetic dipole moment of the electron received a correction from the quantum mechanical treatment of the electromagnetic field known today

[26] The splitting of hydrogen energy levels due to the orbital angular momentum of the electron interacting with the proton's magnetic field.

as the **anomalous magnetic moment** given by

$$\frac{\alpha}{2\pi} \approx 0.00116$$

where $\alpha \approx \frac{1}{137}$ is the "fine structure" constant.

In the same year Feynman took a radically different approach, first reformulating non-relativistic quantum mechanics in terms of path integrals, and then applying his techniques, inspired by Bethe's success with renormalization to higher order corrections in quantum electrodynamics (QED) [101]. Dyson soon showed that the two formulations of QED were physically equivalent [90] and clarified the foundational concepts.

Feynman's formulation based on Lagrangian mechanics and the path integral has the favorable quality of manifestly preserving the Lorentz invariance of electrodynamics. The QED Lagrangian density

$$\begin{aligned} \mathcal{L} &= \bar{\psi}(i\not{D} - m)\psi - \frac{1}{4}(F_{\mu\nu})^2 \\ \text{where } D_\mu &\equiv \partial_\mu + ig_1 A_\mu \\ \text{and } F_{\mu\nu} &\equiv \partial_\mu A_\nu - \partial_\nu A_\mu \end{aligned} \tag{2.20}$$

is a Lorentz scalar by construction. The coupling g_1 between Maxwell's vector field A_μ and the Dirac spinor field ψ is a free parameter which must be renormalized and matched to experiment at some reference scale. The solid red line in Figure 2.3 shows the RG flow for this parameter within the SM. In the low energy limit we fix g_1 with the observed fine structure constant $\alpha \equiv \lim_{\mu\to 0} \frac{g_1^2}{4\pi}$.

A remarkable realization given the QED Lagrangian is that the gauge redundancy of the solution space for A_μ to Maxwell's equations is mathematically equivalent to the choice of

complex phase at each point in spacetime for the spinor field ψ. A spinor field redefinition

$$\psi \to e^{ia(x)}\psi$$

for an arbitrary real function over spacetime $a(x)$ is equivalent to a vector field gauge transformation:

$$A_\mu \to A_\mu + i\partial_\mu a(x)$$

It is not hard to show that the QED Lagrangian is invariant under equal and opposite transformations of ψ and A_μ:

$$\psi \to e^{ia(x)}\psi$$
$$A_\mu \to A_\mu - i\partial_\mu a(x)$$

Combined gauge and complex phase transformations are collectively referred to as $U(1)$ gauge transformations. A straightforward application of Noether's theorem shows that the $U(1)$ gauge symmetry of QED corresponds to the conservation of electric charge current.

2.5 Quantum Chromodynamics

It is natural to ask if the notion of gauge symmetry can be generalized to include more complex Lie groups than $U(1)$. Heisenberg noticed in 1932 that the strong nuclear force seemed to act on protons and neutrons in the same way [123]. This apparent symmetry became known as "isotopic spin" symmetry where proton and neutrons were seen as different isotopic spin states of some two component spinor object. In this model isotopic spin symmetry corresponds to local $SU(2)$ transformations of the proton-neutron spinor rather than $U(1)$ rotations.

Defining a QFT invariant under local isotopic spin transformations motivated Yang and Mills in 1954 [207] to generalize gauge invariance to arbitrary Lie groups. The field strength tensor $F_{\mu\nu}$ is gauge invariant because it emerges from the commutator of the covariant derivative D_μ with itself:

$$\begin{aligned} F_{\mu\nu} &= \frac{1}{ig}[D_\mu, D_\nu] \\ &= \frac{1}{ig}\big(\cancelto{0}{[\partial_\mu, \partial_\nu]} + ig(\partial_\mu A_\nu - \partial_\nu A_\mu) + (ig)^2[A_\mu, A_\nu]\big) \\ &= \partial_\mu A_\nu - \partial_\nu A_\mu + ig[A_\mu, A_\nu] \end{aligned}$$

In the $U(1)$ case the gauge field A_μ emerges from the gradient of the local phase rotations of ψ given by $e^{ia(x)}$. If instead ψ transforms under a more complex Lie group the local transformations will be described by $e^{i\tau_i a_i(x)}$ where τ_i are the generators of the Lie group and $a_i(x)$ are independent functions over spacetime for each group generator.

A general gauge field A_μ can be expanded as a linear combination of components, one for each group generator:

$$A_\mu \equiv A_{\mu,i}\tau_i$$

The $ig[A_\mu, A_\nu]$ term of the field strength tensor cannot be neglected if $[\tau_i, \tau_j] \neq 0$ as is the case for nonabelian (non-commutative) groups. Remarkably this implies that nonabelian gauge fields have interactions between the components corresponding to different group generators.

A true isotopic spin symmetry for fundamental proton and neutron fields implies the existence of three massless vector bosons, one neutral like the photon and two with equal and opposite charge. To escape experimental detection these new particles would have to be more massive than the pions thus motivating the study of approximate or broken symmetries to provide vector boson mass terms.

In 1964 Gell-Mann [108] and Zweig [209] proposed the strong nuclear force may result from

a broken $SU(3)$ symmetry with three new fundamental fermion fields called up, down and strange (u,d and s) **quarks**. $SU(3)$ has eight generators which seemed to explain the "eight-fold way" of the observed baryons and mesons.

In a remarkable twist this turned out to be the correct Lie group proposed for the wrong reasons. We now understand the "eight-fold way" of light baryons and mesons to emerge from the approximate "isospin" symmetry between the three lightest quarks. If there had been a larger mass splitting between any two of these quarks Gell-Mann and Zweig would have had no motivation to propose $SU(3)$ as the gauge group of the strong force. Similarly, had there been a larger mass splitting between the up and down quarks, Yang and Mills would have had little reason to formulate nonabelian gauge theory in the first place.

It wasn't until 1972 after a fourth quark was proposed to preserve unitarity in weak interactions that Fritzsch, Gell-Mann and Leutwyler correctly formulated the strong interactions in terms of fermions with independent $SU(3)$ symmetries [104] which they called **color charge**. In analogy to quantum electrodynamics the theory became known as quantum chromodynamics (QCD).

They proposed that all observed strongly interacting particles (**hadrons**) were singlets under $SU(3)$ transformations or "color neutral" but, could not yet explain why particles with color charge like the quarks and the $SU(3)$ gauge bosons called **gluons** had not been directly observed. Furthermore, Bjorken had previously derived scaling rules for electromagnetic and weak scattering off of hadrons in high and low momentum transfer limits relying only on the local nature of the electromagnetic and weak currents [79]. Fritzsch, Gell-Mann and Leutwyler could only speculate on how their model might be consistent with Bjorken's scaling rules.

In 1973 Gross, Wilczek [120] and Politzer [172] explained both issues by calculating the one

loop beta function of the $SU(3)$ gauge coupling g_3:

$$\frac{\mathrm{d}g_3}{\mathrm{d}\log\mu} \approx \frac{g_3^3}{(4\pi)^2} \times \left(\frac{2}{3}n_f - \frac{11}{3}N\right)$$

N is the group index for $SU(N)$ and n_f is the number of fermions coupled to $SU(N)$.[27] For $SU(3)$, the one loop beta function is negative if $n_f \leq 16$ as is the case in the SM.

As the renormalization scale approaches infinity, g_3 approaches zero becoming **asymptotically free**. The asymptotic freedom of QCD ensures the validity of the perturbative calculations at sufficiently high scales. In the low energy limit however, g_3 must become large, eventually invalidating the perturbative calculation used to compute the beta function. We denote the scale at which this occurs by Λ_{QCD}. The RG flow of g_3 in the SM is shown by the blue dashed line in Figure 2.3.

It is an unproven conjecture that Yang-Mills theories are confined, meaning physical states are singlets under gauge transformations and that they exhibit a "mass gap": The lightest physical state has a non-zero mass. Anyone who proves or finds a counter example to this conjecture will win one million dollars from the Clay Mathematics Institute which lists it as one of six unsolved *Millennium Prize Problems*.[28]

Asymptotic freedom is a double edged sword, guaranteeing the validity of perturbative calculations at high energies while simultaneously invalidating all known analytical techniques to determine the physical particle spectrum.

In 1974 Wilson provided the first well defined formulation of non-perturbative QCD – known as lattice QCD – by discretizing spacetime and recovering QCD in the continuum limit [202].

[27] This is for fermions in the fundamental representation of $SU(N)$. Fermions in the adjoint representation like vector like quarks or gluinos would contribute differently as would fundamental scalars.

[28] The Poincaré conjecture is the only Millennium Problem with a known solution and was proven by Grigoriy Perelman just under a century after its formulation.

Today we use supercomputers to numerically evaluate the behaviour field theories on finite spacetime lattices. Exascale computing is expected to allow many problems in QCD to be precisely estimated with this technique [58]. Many important first principles calculations in QCD will likely remain intractable for classical computers and quantum computers could someday prove invaluable to our understanding of strongly coupled theories [174, 131].

2.6 Electroweak Unification and the Higgs Mechanism

It is challenging to tell a linear story for this final piece of the SM. The formulation of the electroweak force and the required symmetry breaking provided by the Higgs mechanism proceeded chaotically and along multiple channels from 1930 to 1970. It is only with the power of hindsight that we can see how all the pieces fit together, leading inevitably to the current formulation of the SM.

Roughly speaking there were three major hurdles preventing an understanding of the weak nuclear force:

1. The high scale of Fermi's constant: In 1934 it was already clear that the characteristic energy scale of the weak nuclear force was at least a hundred times the proton mass. Collider experiments capable of directly probing this scale would not be developed for fifty years. Meanwhile dozens of hadrons were being discovered with no clear underlying theoretical description.

2. Nonabelian gauge theory: In 1954 Yang and Mills generalized gauge symmetry to general Lie groups using $SU(2)$ as an example. Calculations using their theory remain technically challenging today. At the time it was already clear they were missing something crucial as there was no way to provide the predicted massless gauge bosons with gauge invariant mass terms to avoid experimental limits. The confinement of

quarks due to the nonabelian interactions of QCD further complicated attempts to understand the relationship between hadrons and leptons.

3. Spontaneous symmetry breaking in gauge theory: Studies of superconductivity in condensed matter physics lead to the technical developments required to understand the phenomenology of field theories whose physical spectrum violated the symmetry of the underlying theory. Extending this phenomenology to relativistic nonabelian gauge theory finally allowed Yang and Mill's original $SU(2)$ to be applied to the weak interactions.

2.6.1 Fermi's Constant and Weak Interactions

In 1936 Anderson and Neddermeyer noticed particle tracks in their argon cloud chamber whose charge to mass ratio was larger than any known nucleus but much smaller than that of an electron or positron [17]. They were concerned this discrepancy could have been caused by multiple scattering in the argon. They conservatively assumed these strange tracks originated from protons. Only a year later Street and Stevenson managed to perform a more precise determination of this new particle's mass showing definitively that it was between the electron and proton [195] masses.

The race was on to better understand the properties of the particle which had become known as the "mesotron". Rasetti used an absorber block of iron and coincidence detectors to select incoming mesotrons and then required no prompt detection in the coincidence detector on the opposite side of the block to select mesotrons which had been stopped by the iron. For about half of the stopped mesotrons a high energy positron was observed a few microseconds later emerging from the absorber. Rasetti used this to claim that positively charged mesotrons decay to positrons while negatively charged mesotrons react in some way with the iron. He also performed the first direct measurement of the mesotron lifetime which was found to be

consistent with indirect atmospheric absorption measurements [178].

Yukawa had predicted the existence of a new scalar particle [208] with approximately the mesotron mass which he called the meson. When it became clear that the mesotron was not Yukawa's meson, the mesotron name went out of favor. The name **muon** was eventually adopted to distinguish it from the emerging zoo of strongly interacting mesons which more closely matching Yukawa's prediction.

Prior to all the excitement over the muon (which was looking more and more like a heavy version of electrons and positrons) Pauli had expressed deep concerns about the phenomenon of nuclear beta decay. The decay products seemed to badly violate the conservation of momentum which Noether had previously shown would reject the hypothesis that physical law is invariant under translations. Pauli proposed that beta decay must also produce an electrically neutral particle which he called a neutron. Two years later what we know today as the neutron was discovered and was much too heavy to be a candidate for Pauli's proposed particle. Pauli's neutron became known as the **neutrino** meaning "small neutron".

In 1934 Fermi quantified Pauli's proposal by analogy to the process of excited atoms emitting photons [201]. As a local theory, Fermi realized that for beta decay to allow a single fermion to decay into three other fermions, dimensional analysis required a beta decay constant with units of $[E]^{-2}$. He estimated the order of magnitude of this new constant at $4 \times 10^{-50}\text{cm}^3\,\text{erg} \approx (500\,\text{GeV})^{-2}$. Today's precision measurements put the true value of Fermi's constant at $G_F \approx (293\,\text{GeV})^{-2}$ so the man famous for his order of magnitude estimates was right on the money.

Fermi's theory also offered and explanation for the muon lifetime while suggesting the existence of multiple types of neutrino which had yet to be observed directly. More than a quarter century after Pauli's proposal, an experiment by Cowan, Reines, Harrison, Kruse and McGuire used reactor neutrinos to observe protons absorbing neutrinos and being converted

to a neutron and a positron [75].

2.6.2 Hints of broken SU(2)

Yang and Mills first studied $SU(2)$ gauge theory as a model for the approximate symmetry between protons and neutrons [207]. This attempt predicted the existence of new massless vector bosons which had not been observed but, offered a mechanism for beta decay and muon decay in terms of a charged current carried by the two charged vector bosons. It also predicted the existence of a neutral current weak interaction allowing neutrinos to transfer momentum to weakly interacting fermions. To avoid experimental detection these new vector bosons had to have large masses which seemed to violate the gauge symmetry from which they were derived.

It was known that the half integer spin of fermions, when projected along the direction of their momentum could take one of two values: $\pm\hbar/2$. If the projection is positive the fermion is said to have positive or "right handed" **helicity** while "left handed" helicity corresponds to fermions with negative spin projection. **Parity** (P) was an assumed symmetry of physical interactions which flips the sign of the spatial spacetime coordinates: $P(t, x, y, z) = (t, -x, -y, -z)$. In particular, P flips the sign of momentum but preserves the sign of angular momentum.[29] Thus P symmetry implies all physical interactions should treat left and right handed fermions equally.

Parity had been taken for granted for decades since by a change of inertial reference frame one can flip the direction of momentum of a massive particle and therefore flip its handedness or **chirality**. This is the reason the Dirac equation requires both left and right handed

[29] Classically this is obvious because both the momentum vector and displacement vectors change signs. For quantum mechanical spin, where there is no notion of a displacement vector, the parity operation flips the field spatial coordinates and the sign of the spin operator to maintain the consistency of the representation.

components to describe a Lorentz covariant massive fermion field. Parity symmetry had been extensively tested for both electromagnetic and strong nuclear interactions but not weak interactions. In 1956 Lee and Yang concluded that weak interactions could violate Parity [139]. They realized that the most general Lagrangian terms allowing four fermion interactions as in Fermi's theory could be written in Lorentz invariant ways while violating parity.

Only a year later Wu, Ambler, Hayward, Hoppes and Hudson performed a beautiful experiment as proposed by Lee and Yang to check for parity violation in beta decays. By polarizing the nuclear spins of a thin sample of cobalt-60, they could check for an angular bias in the beta emission direction relative to the nuclear polarization. They found [206] that beta decays violated parity by at least 70% which according to Lee and Yang also implied a violation of **charge conjugation** (C) symmetry (C exchanges particles for their antimatter counterparts). It was left as an open question as to whether weak interactions also violated **time reversal** symmetry (T).[30]

This revelation also explained the observation of hadrons which appeared to have identical masses and lifetimes but whose decay modes had different signs under the parity transformation. What had been seen were the same particles undergoing different decay processes, one where parity was violated and one where it was not.

Salam and Ward finally hit upon the correct symmetry space which gives rise to both electromagnetic and weak interactions in 1958 [181]. They combined $U(1)$ and $SU(2)$ gauge interactions into a single "charge space" to explain both the parity violation of the weak interactions and the parity conservation of the electromagnetic interactions.

Glashow then successfully parametrized the symmetry breaking required to give gauge boson

[30] In 1954 Bell proved in his Ph.D. thesis [53] that local unitary QFTs respect the combined action of charge conjugation, parity and time reversal or CPT as an exact symmetry. Under the assumption that nature is described by such a theory T violation is equivalent to CP violation.

masses by enforcing the renormalizability of the electroweak interactions [113, 112]. His result explained the observed selection rules for hadron decays involving the new quantum number "strangeness". Furthermore, he showed that to maintain consistency in the limit of zero gauge boson mass the more familiar 1954 Yang-Mills gauge theory was recovered.

The predicted parity violating charged and neutral currents carried by massive $W^{\pm}$ and Z vector bosons were directly observed at CERN in 1973 with the Gargamelle bubble chamber [153].[31] The UA1 and UA2 experiments at the Super Proton Synchroton (SPS)[32] directly observed the decays of $W^{\pm}$ and Z bosons ten years later (1983) [98, 162, 19, 50].

2.6.3 Fermion Generations

In 1957 Pontecorvo proposed that neutrinos could oscillate to their antimatter partner [173] which is possible because they are electrically neutral. The validity of this proposal remains one of the most important open questions in the SM. He was also lead to speculate that a new quantum property of neutrinos, in analogy to "strangeness" for hadrons, could be the only quantity which physically distinguishes neutrinos from their antimatter counterparts.

Five years later (1962) Danby et al. demonstrated the existence of at least two different "flavors" of neutrino using a beam of neutrinos created by muonic pion decays. They found that neutrinos produced in association with muons when absorbed by their detector produced muons but never electrons [82]. As this experiment was being performed, Maki, Nakagawa and Sakata proposed the existence of two flavors of neutrino to explain the leptonic decay rates of hadrons. They also explained the small difference in the value of Fermi's constant as measured in muon decays versus beta decay [142]. Their model contained a 2 by 2 unitary

[31] The chamber is now on display at CERN just outside my old office in Building 4.

[32] This accelerator remains in use as part of the injector chain for the Large Hadron Collider (LHC). See Chapter 3 for more.

matrix which parametrized the mixing between the proposed neutrino flavors. Their matrix became known as the Pontecorvo-Maki-Nakagawa-Sakata (PMNS) matrix.

In 1963 Cabibbo explained strangeness violating hadron decays and the different branching ratios for different mesons decaying to the same leptons. He defined a mixing angle between down and strange quarks [65] to allow these decays. The inclusion of the Cabibbo angle further improved agreement between determinations of Fermi's constant in muon decays versus leptonic hadron decays.

Wu et al. had left as an open question whether weak interactions might violate the combined symmetry action of CP. Such a process would not be possible with a 2 by 2 unitary mixing matrix and would require Cabibbo's matrix and the PMNS matrix to be extended. To the surprise of much of the physics community, Cronin, Fitch, Christenson and Turlay observed CP violation in 1964 using rare decays of strange mesons called kaons [69].

Then in 1968 Davis, Harmer and Hoffman observed a large deficit in the total solar neutrino flux [83]. Gribov and Pontecorvo explained the deficit by suggesting the two known neutrinos could mix during their trip from the sun to the earth [119] and acknowledged that more neutrino flavors may exist.

As the quark model gained traction in our understanding of the strong interactions, the combined electromagnetic and weak interactions between fundamental fermions suggested charged and neutral leptons with up and down type quarks must be bundled into groups called generations to preserve unitarity. Glashow, Iliopolis and Maiani formalized this argument which became known as the GIM mechanism. Their mechanism predicted a down type quark partner to the strange quark which they called "charm" [111].[33]

A bound state of charm and anti-charm quarks called the J/ψ was discovered simultaneously

[33] Glashow and Bjorken first speculated about this possibility in 1964.

in 1974 by the Stanford/Berkeley group using the SPEAR storage ring [48] and by the MIT/Brookhaven group [47].[34] Combined with the deep inelastic scattering experiments at the Stanford Linear Accelerator Center (SLAC) which showed the proton was composite, and Gross, Wilczek and Politzer's demonstration that QCD was consistent with Bjorken's scaling rules, the discovery of the J/ψ cemented the quark model of strongly interacting fermions.

The observation of CP violation combined with the quark model and the preservation of unitarity via the GIM mechanism required at least one more full generation of fermions. The PMNS matrix was extended to three generations and Cabibbo's mixing angle was extended by Kobayashi and Maskawa [135] to the Cabibbo-Kobayashi-Maskawa (CKM) matrix.

The third generation charged lepton which became known as the τ was discovered using the SPEAR storage ring between 1974 and 1977 [169, 170]. The third generation down type quark ("bottom" or sometimes "beauty") was found in 1977 at Fermilab with the E288 experiment [124].

It took another eighteen years to find the third generation up type quark ("top" or sometimes "truth") due to its enormous mass of 173 GeV. A new proton-antiproton collider with beam energies a thousand times greater than the proton rest mass was constructed at Fermilab to search for both the top quark and Higgs boson (introduced in the next section). In 1995 the CDF and DØ collaborations announced their discovery of the top quark [164, 184].

Finally in 2001 the DONUT collaboration, also at Fermilab, announced their discovery of the third generation neutral lepton, the tau neutrino [136].

[34] Unfortunately the two groups gave the particle different names and today we call it by both.

2.6.4 Spontaneous Symmetry Breaking and Gauge Theory

At the end of the 1950's Salam, Ward and Glashow had found the weak and electromagnetic interactions could be neatly explained as emerging together from a local $U(1) \times SU(2)$ gauge symmetry. The $SU(2)$ piece only acted on left handed components of fermions and right handed components of antifermions to explain the maximal parity violation of the weak interactions. Unfortunately their model required Dirac fermion mass terms (coupling left and right handed components) which seemed to be $SU(2)$ gauge dependent. Furthermore, the S-matrix for massive $W^{\pm}$ boson scattering in their model violated unitarity at sufficiently high energies. The solution to both of these problems originated in the study of condensed matter systems – a testament to the value of interdisciplinary research.

In 1957 Bardeen, Cooper and Schrieffer (BCS) explained superconductivity as resulting from interactions between quantized mechanical waves (phonons) and electrons in a metal [52]. They showed that electron wave functions in momentum space are pulled together by the exchange of virtual phonons so long as the energy difference between the electrons is less than the exchanged phonon modes. This attractive force, no matter how small, changes the electronic ground state of the metal in the zero temperature limit to one which violates local $U(1)$ gauge invariance.

BCS theory showed that it is possible to have a locally gauge invariant theory with physical properties that depend on the gradient of the gauge. At the start of the 1960's Nambu and Jona-Lasinio became interested in applying ideas from BCS theory to particle physics [156, 154, 155]. They suspected that gauge dependent mass terms could arise from a mechanism analogous to BCS.

Goldstone, Salam and Weinberg poked a serious hole in this program in 1962 by proving massless scalar bosons must exist for any theory where the Lagrangian is $SU(2)$ invariant

but the physical spectrum is not [116]. These massless scalar bosons would have created a new long range force which was clearly not observed so it seemed spontaneously broken symmetry could not explain the required weak boson masses.

Fortunately Goldstone, Salam and Weinberg's proof had a loophole which applied specifically to the case of spontaneously broken gauge symmetries as explained by Anderson a few months later [18].[35] While Anderson's result was published where particle physicists would see it, his paper primarily concerned non-relativistic condensed matter systems which were not familiar to many particle physicists at the time. The next year, three papers were published using Anderson's mechanism to generate gauge boson masses without massless scalars but, only the paper by Higgs [127] recognized Anderson's work. Englert and Brout [97], and Guralnik, Haken and Kibble [121] had independently found Anderson's mechanism and applied it to relativistic gauge theory.

We can illustrate the Higgs mechanism with the simple Lagrangian

$$\begin{aligned} \mathcal{L} &= \frac{1}{2}(D_\mu\phi)^*(D_\mu\phi) - \frac{1}{4}(F_{\mu\nu})^2 - V(\phi^*\phi) \\ \text{where } V(\phi^*\phi) &= -\frac{1}{2}m^2\phi^*\phi + \frac{1}{4}\lambda(\phi^*\phi)^2 \end{aligned} \tag{2.21}$$

with complex scalar field ϕ and $U(1)$ gauge field A_μ. The $U(1)$ covariant derivative D_μ and field strength tensor $F_{\mu\nu}$ are taken from Equation 2.20. The scalar potential $V(\phi^*\phi)$ has a "Mexican hat" shape as illustrated by Figure 2.1. We can express ϕ in terms of a magnitude and phase $\phi \equiv |\phi|e^{i\theta}$ where the minimum of the potential is at $|\phi_0|e^{i\theta}$ for all θ. Then the vacuum state of ϕ will have a nonzero expectation value (VEV) at $v \equiv |\phi_0|$. The physical spectrum will be most naturally expressed in terms of quantized fluctuations around the

[35] Ed Witten wrote an excellent summary [203] of Anderson's work and the historical and scientific context in which it came about that we recommend to the interested reader.

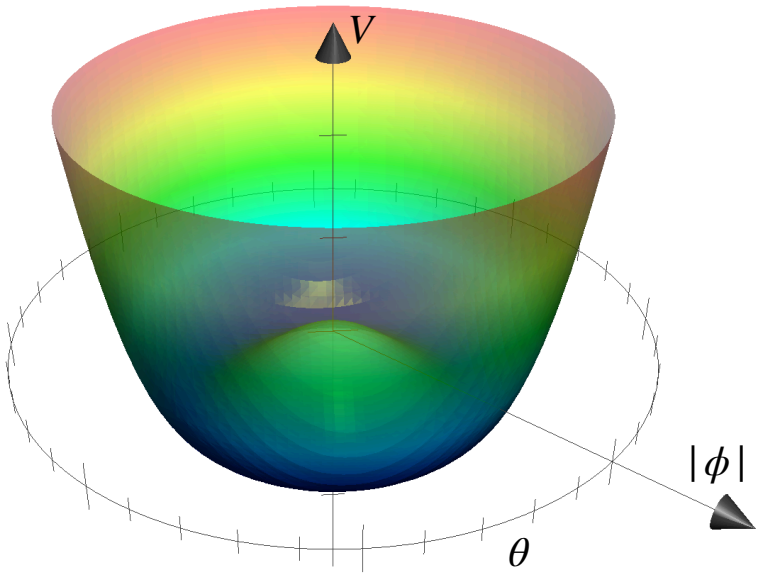

Figure 2.1: The Mexican hat scalar potential $V(\phi^*\phi)$ with $\phi \equiv |\phi|e^{i\theta}$ from Equation 2.21. Notice that the minimum of the potential is a circle with $|\phi| \neq 0$. The vacuum expectation value (VEV) of ϕ spontaneously selects a $U(1)$ gauge as a result of the degenerate minimum.

VEV rather than the origin **spontaneously breaking** the local $U(1)$ symmetry of ϕ:

$$|\phi|e^{i\theta} \equiv (v+h)e^{i\theta} \text{ where } h \text{ is the } \textbf{Higgs field}.$$

$$\begin{aligned}
\Rightarrow V(h) &= -\frac{1}{2}m^2(v+h)^2 + \frac{1}{4!}\lambda(v+h)^4 \\
&= \mathcal{O}(h^0) + (\frac{\lambda v^3}{3!} - m^2 v)\,h + (\frac{\lambda v^2}{4} - \frac{m^2}{2})h^2 + \frac{1}{3!}\lambda v h^3 + \frac{1}{4!}\lambda h^4 \quad (\to 0) \\
&= \mathcal{O}(h^0) + \frac{1}{2}m_h^2 h^2 + \frac{1}{3!}\lambda v h^3 + \frac{1}{4!}\lambda h^4 \text{ where } m_h = \sqrt{2}m
\end{aligned}$$

In the penultimate line we used the fact that $\frac{\mathrm{d}V}{\mathrm{d}h}\Big|_{h=0}$ by definition to set $\lambda = 6\frac{m^2}{v^2}$. We can drop the constant term which adds a constant shift to the action and only changes the path integral by an overall phase.

The covariant derivative acting on the redefined fields gives

$$\begin{aligned} D_\mu\phi &= \big[\partial_\mu(v+h)\big]e^{i\theta} + (v+h)\partial_\mu e^{i\theta} + igA_\mu(v+h)e^{i\theta} \\ &= \big[\partial_\mu h + ig(v+h)(A_\mu + \frac{1}{g}\partial_\mu\theta)\big]e^{i\theta} \end{aligned}$$

Redefining the vector field as $B_\mu \equiv A_\mu + \frac{1}{g}\partial_\mu\theta$ we have

$$\frac{1}{2}(D_\mu\phi)^*(D_\mu\phi) = \frac{1}{2}(\partial_\mu h)^2 + \frac{1}{2}m_B^2 B_\mu^2 + 2g^2 vhB_\mu^2 + g^2h^2B_\mu^2$$

where $m_B \equiv g^2v^2$. The $2g^2vhB_\mu^2$ and $g^2h^2B_\mu^2$ terms provide Higgs couplings to the new massive vector field B_μ.

Finally, the field strength tensor simply switches over to the new B_μ field:

$$\begin{aligned} F_{\mu\nu} &= \partial_\mu(B_\nu - \frac{1}{g}\partial_\nu\theta) - \partial_\nu(B_\mu - \frac{1}{g}\partial_\mu\theta) \\ &= \partial_\mu B_\nu - \partial_\nu B_\mu + \frac{1}{g}\cancelto{0}{(\partial_\nu\partial_\mu\theta - \partial_\mu\partial_\nu\theta)} \end{aligned}$$

The massless scalar boson one expects from the $e^{i\theta}$ component of the complex scalar field was absorbed into the physical spectrum of the vector field, providing a longitudinal degree of freedom and corresponding vector boson mass.

In 1967 Weinberg published his *Model of Leptons* [199] which showed that the Higgs mechanism could be applied to break the $U(1) \times SU(2)$ gauge group which had been phenomenologically applied to the electromagnetic and weak interactions. In this case the scalar field is a complex scalar doublet in the fundamental representation of $U(1) \times SU(2)$ and is thus four real dimensional. Three of these scalar field degrees of freedom provide transverse polarizations to the $SU(2)$ gauge fields and the fourth becomes a massive scalar field which we call the Higgs.

Weinberg suspected that this theory should be renormalizable but did not prove it. In 1972 t'Hooft and Veltman [128] used the dimensional regularization technique pioneered by Juan José Giambiagi and Carlos Guido Bollini [59] to explicitly renormalize Yang-Mills theories.

At sufficiently high reference scales the VEV becomes negligible and the SM $SU(2)$ gauge coupling g_2 becomes asymptotically free. The green dashed line in Figure 2.3 shows the RG flow of g_2. The pink dashed, cyan dashed and orange dashed lines show the RG flow of the top quark, bottom quark and tau lepton Yukawa couplings respectively. These are the fermions with the largest mass in the SM and therefore the largest Yukawa couplings. Finally the black dashed line shows the RG flow of the Higgs quartic coupling which becomes negative around 10^{11} GeV implying the SM vacuum state is metastable.

The issues of gauge dependence and unitarity mentioned at the start of this section had been solved. Dirac fermion mass terms emerge from Yukawa couplings to the original symmetric scalar field definition. Schematically

$$y\phi\bar{\psi}\psi \rightarrow yv\bar{\psi}\psi + yh\bar{\psi}\psi$$

where y is a dimensionless Yukawa coupling and $yv = m_\psi$. Meanwhile, the Higgs couplings to the massive $W^\pm$ and Z vector bosons enforce unitarity of the vector boson scattering matrix.

2.7 Summary

The Standard Model is the simplest possible quantum field theory which can describe electromagnetism, the strong and weak nuclear forces and the observed particle masses summarized in Figure 2.2. A summary of the discoveries leading to the formulation of the SM is presented in Figure 2.5.

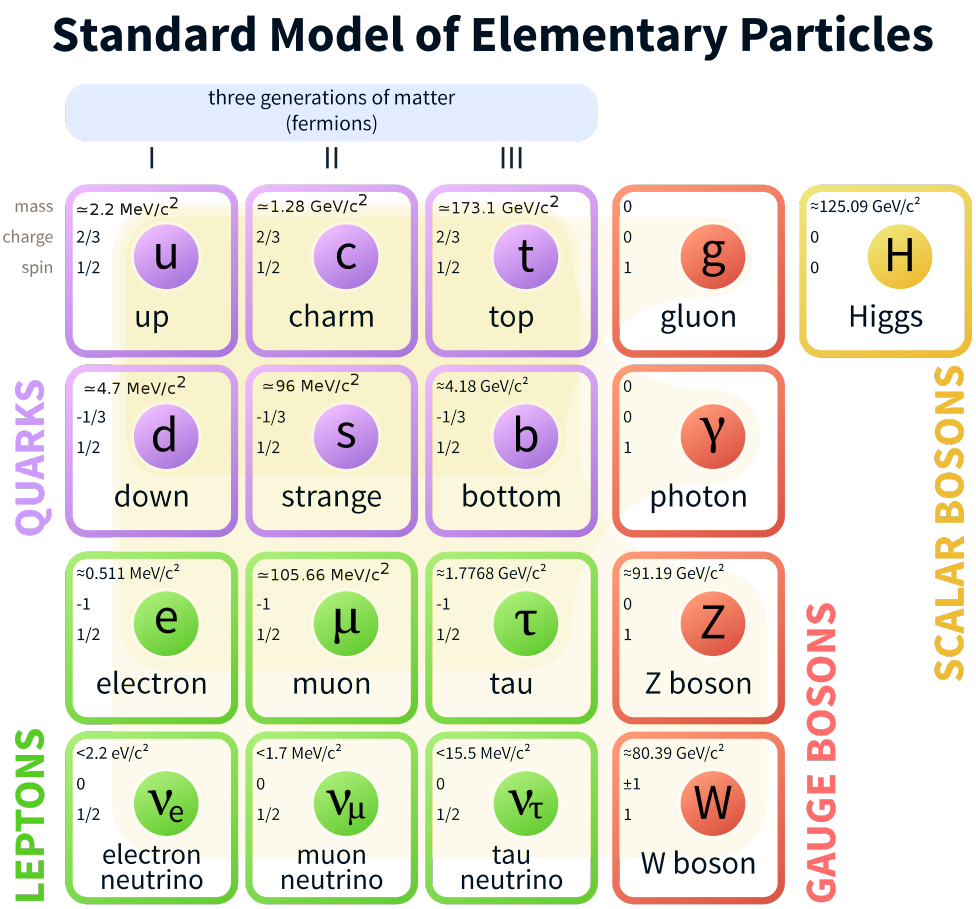

Figure 2.2: The fundamental fermions and bosons of the SM [167].

In the modern Wilsonian interpretation of the renormalization group, we view the interactions of the SM as dependent on a reference scale and use perturbative methods to compute this scale dependence. The calculation is consistent from a scale of a few hundred MeV (Limited by Λ_{QCD} below which non-perturbative methods are required) to at least the Plank mass $M_{Pl} = \sqrt{\hbar c/8\pi G_N} \approx 10^{18}$ GeV as shown in Figure 2.3.

This description has been successful over its domain of applicability, predicting scattering cross sections for a huge variety of processes spanning 14 orders of magnitude with no observed significant deviations from the theory (Figure 2.4).

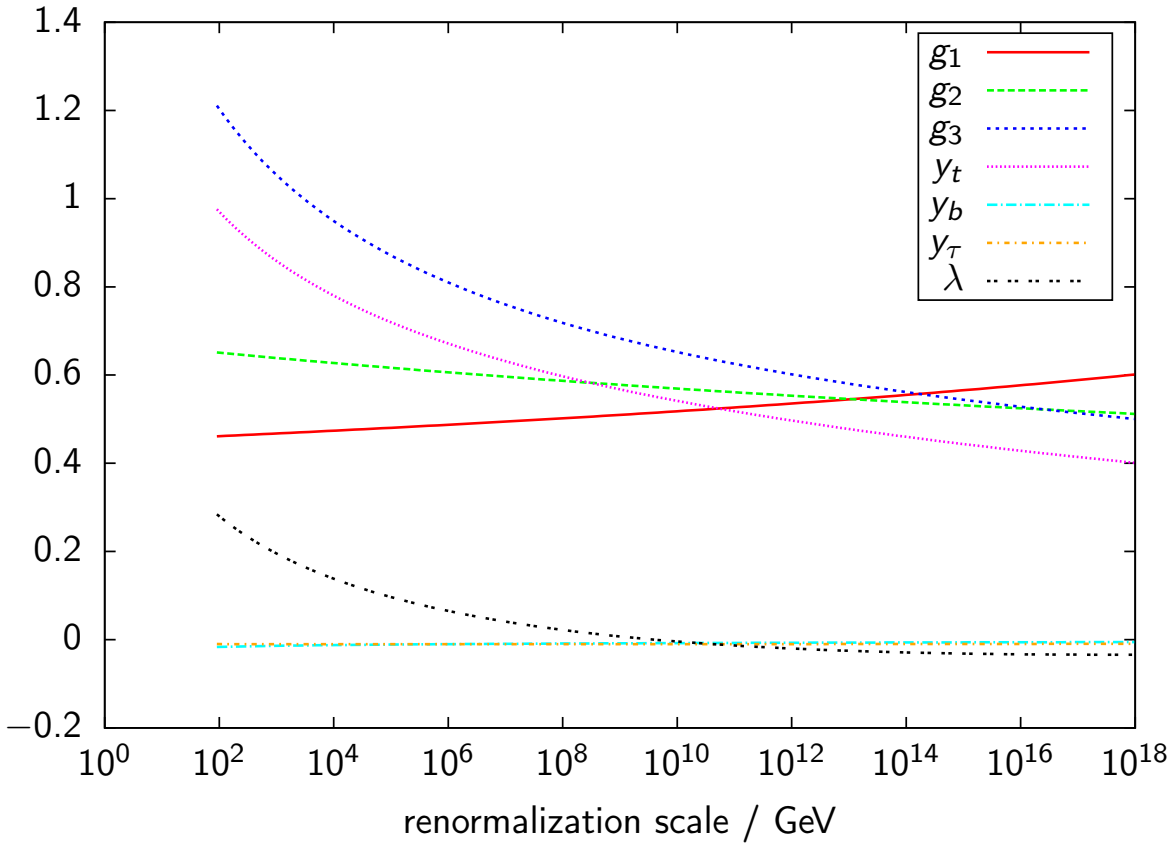

Figure 2.3: The RG flow [1] of some of the free coupling parameters of the SM calculated at 3-loop precision for the scale μ and 2-loop precision for the Higgs VEV with the FlexibleSUSY package [20]. The parameters g_1, g_2 and g_3 are the gauge couplings of the unbroken $U(1)$, $SU(2)_L$ and $SU(3)_c$ groups respectively. The y_t, y_b, and y_τ are the three largest Yukawa couplings in the SM and λ is the Higgs self coupling.

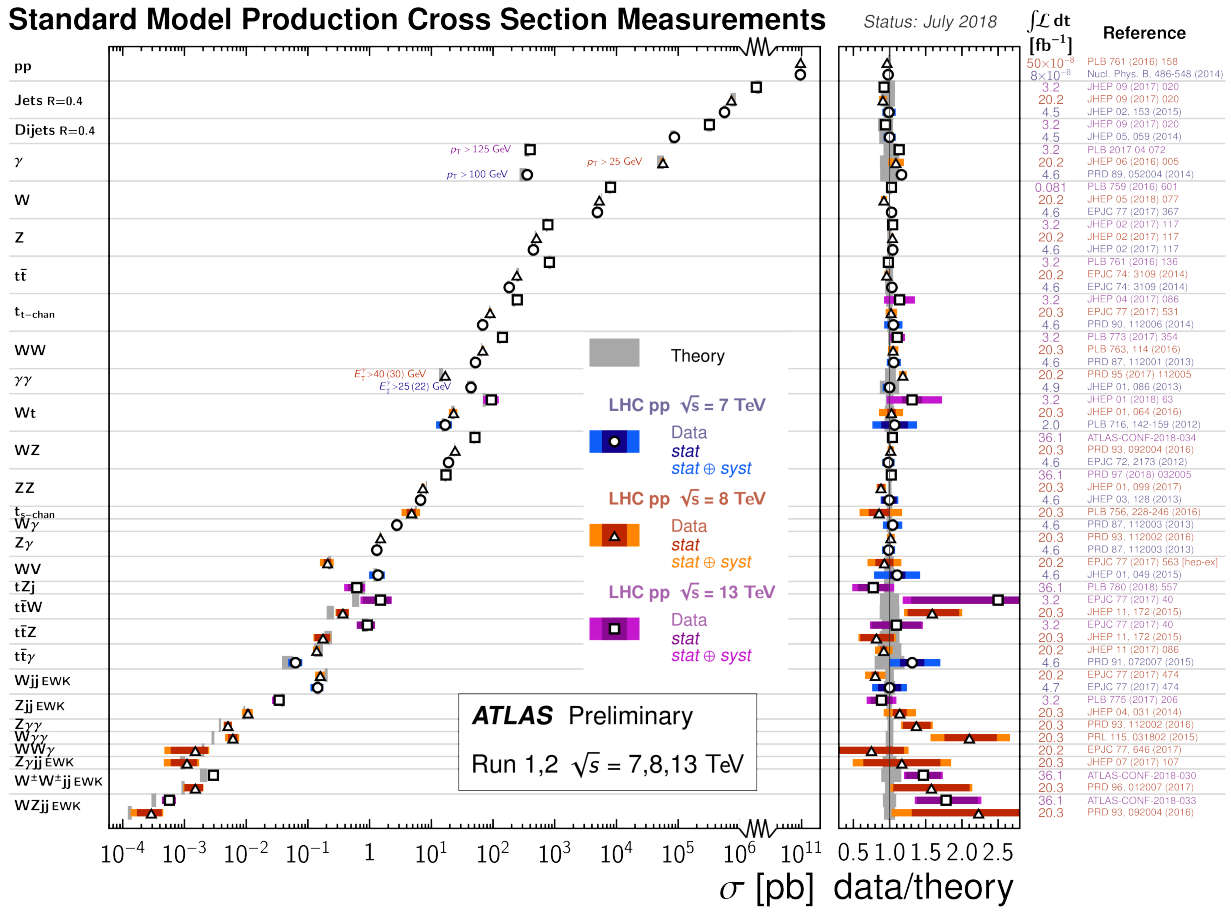

Figure 2.4: A summary of scattering processes observed by ATLAS (Chapter 4) from proton collisions generated by the LHC (Chapter 3).

One of the most precise single predictions from the SM which involves contributions from all the gauge forces is the electron anomalous magnetic moment a_e (introduced in Section 2.4). When a torque is applied to a gyroscope the spin axis will precess at a rate inversely proportional to its moment of inertia. Analogously, the spin of an electron precesses under an applied magnetic field in proportion to its gyromagnetic ratio. Charged particles also move in circular paths in uniform magnetic fields with a constant frequency known as the cyclotron frequency.

Both the precession and cyclotron frequencies are proportional to the applied magnetic field and electron charge to mass ratio. The cyclotron frequency is a classical property while the precession frequency is purely quantum mechanical and is proportional to a_e. The two frequencies can be compared with precision better than one part per trillion as demonstrated in a 2008 measurement [122], and compared with the SM expectation (using measurements of Rubidium atoms to set the fine structure constant [110]):

$$\text{Measured: } a_e = 0.001\,159\,652\,180\,91 \pm 26 \times 10^{-14}$$

$$\text{Predicted: } a_e = 0.001\,159\,652\,181\,78 \pm 76 \times 10^{-14}$$

2.7.1 Open Questions

The Standard Model is incomplete as a description underlying all physical phenomena. Our remaining questions about fundamental physics can be roughly lumped into four categories:

1. **Disagreement with Experiment:** These imply new physical phenomena or a mistake on the part of the theoretical or experimental communities, and sometimes both. Today, such discrepancies are rare, generally small and, difficult to interpret with many possible sources of error.

- The muon anomalous magnetic moment a_μ is 3.7σ [132] larger than the theoretical prediction. The Fermilab muon $g-2$ experiment is currently taking data to improve the experimental precision of a_μ [115]. Combined with improved theoretical predictions we should soon know if this discrepancy is here to stay.
- There are hints of lepton flavor universality violation in leptonic decays of mesons containing bottom quarks. This suggests in addition to the Higgs Yukawa couplings something interacts more strongly with some leptons than others. Global fits to several measurements suggest a 4σ deviation from SM predictions [81].
- Nothing in the SM can account for the phenomenological success of cold dark matter (CDM) in explaining cosmological observations. Dark matter may be made up of a new particle sector which interacts extremely weakly with the SM particles. In the worst case scenario for experimental detection dark matter may only interact with the SM gravitationally.
- Neutrinos have mass but the precise nature of the mechanism which provides that mass is unknown. If their mass comes from couplings to the Higgs field the corresponding Yukawa couplings are bizarrely small (this falls in category four) and a fifth type of fermion known as a sterile neutrino must be added to the SM. If their masses come from a dimension five or higher operator a new scale is implied by the dimensionful coupling which is typically around $10^{14}\,\text{GeV}$ [117].
- The observed amount of CP violation is insufficient to explain the large amount of matter in the universe if we assume the universe began with equal amounts of energy in matter and antimatter. This is addressed further in Chapter 5.2.1.

2. **Theoretical Consistency:** Descriptions of fundamental physics are often found to be internally inconsistent, leading to contradictory or ill defined predictions for observable quantities. In some cases issues arise from poorly defined observables. In others the

theory must be treated as "effective" over some domain of applicability rather than fundamental and applying to all physical phenomena.

3. **Challenging Calculations:** High order perturbative corrections are becoming increasingly important as the boundaries of experimental precision are pressed. The dynamics of strongly coupled theories and non-perturbative dynamics remain deeply mysterious. Simulations of many body systems from large atoms to cosmological structure formation are needed to test various aspects of fundamental physics.

4. **Philosophical Questions:** Many properties of fundamental physics seem to emerge from deep foundational principles such as unitarity, locality, renormalizability and symmetry while many others seem ad hoc or finely tuned without explanation. Examples include:

    - Why three generations of fermions?
    - Why $SU(3) \times SU(2) \times U(1)$?[36]
    - Why do the CKM and PMNS matrices have the observed values?
    - Why doesn't the strong force violate CP?
    - Why do the fermion Yukawa couplings span six orders of magnitude?
    - Why is the electroweak scale sixteen orders of magnitude smaller than the Plank scale?
    - Why is the cosmological constant small?

All open questions in fundamental physics have aspects relating to each of these four categories. Perhaps most glaringly, as Einstein stated in the second quote in the introduction to

[36] The true gauge group of the SM is actually $(SU(3) \times SU(2) \times U(1))$ modulo $\mathbb{Z}/6$ because the $U(1)$ hypercharge of the fermions can be rotated by a sixth root of unity with no impact on the resulting dynamics. This may be an important clue to the question of why this gauge group describes the SM [107, 106, 88, 89].

this chapter, it is not clear how gravity and quantum mechanics can emerge together from a single theoretical framework.

The smallness and dimension of Fermi's constant $G_F = (293\,\mathrm{GeV})^{-2}$ in combination with the hypothesis of perturbative renormalizability implied the existence of new particles at the scale $G_F^{-1/2}$. This turned out to be the W, Z and Higgs bosons. This lesson does not apply directly to the gravitational coupling constant G_N which also has dimension $[E]^{-2}$ where $M_{Pl} \equiv G_N^{-1/2}$. In a series of papers in 1967 DeWitt showed [85] how to treat gravity in both canonical and path integral quantization and found that it was most likely not perturbatively renormalizable.

Even more dramatically Almheiri, Marolf, Polchinski and Sully conjectured in 2013 that the notions of unitarity, locality and the equivalence principle of GR are mutually inconsistent [16]. Their conjecture remains controversial today but, if true suggests that fundamental principles of relativistic quantum field theory, GR or both are deeply flawed.

A better understanding of physics at the Plank scale will likely pull primarily from the last three categories of questions. Experimental surprises in cosmology, gravitational wave physics and potentially even particle physics may someday contribute. Speculative studies assuming gravity to be non-perturbatively renormalizable (the asymptotic safety scenario) have interesting consequences for the SM couplings in the low energy limit [91].

Quantum field theories exhibiting asymptotic safety have only recently been explicitly constructed [141] and further study of this class of QFTs is warranted. The vast majority of QFTs must be treated as effective theories rather than fundamental theories due to divergences in the RG flow of their couplings at finite scales. Asymptotically free theories and highly symmetric theories known as conformal theories do not constitute the full suite of fundamental QFTs (well defined at all scales).

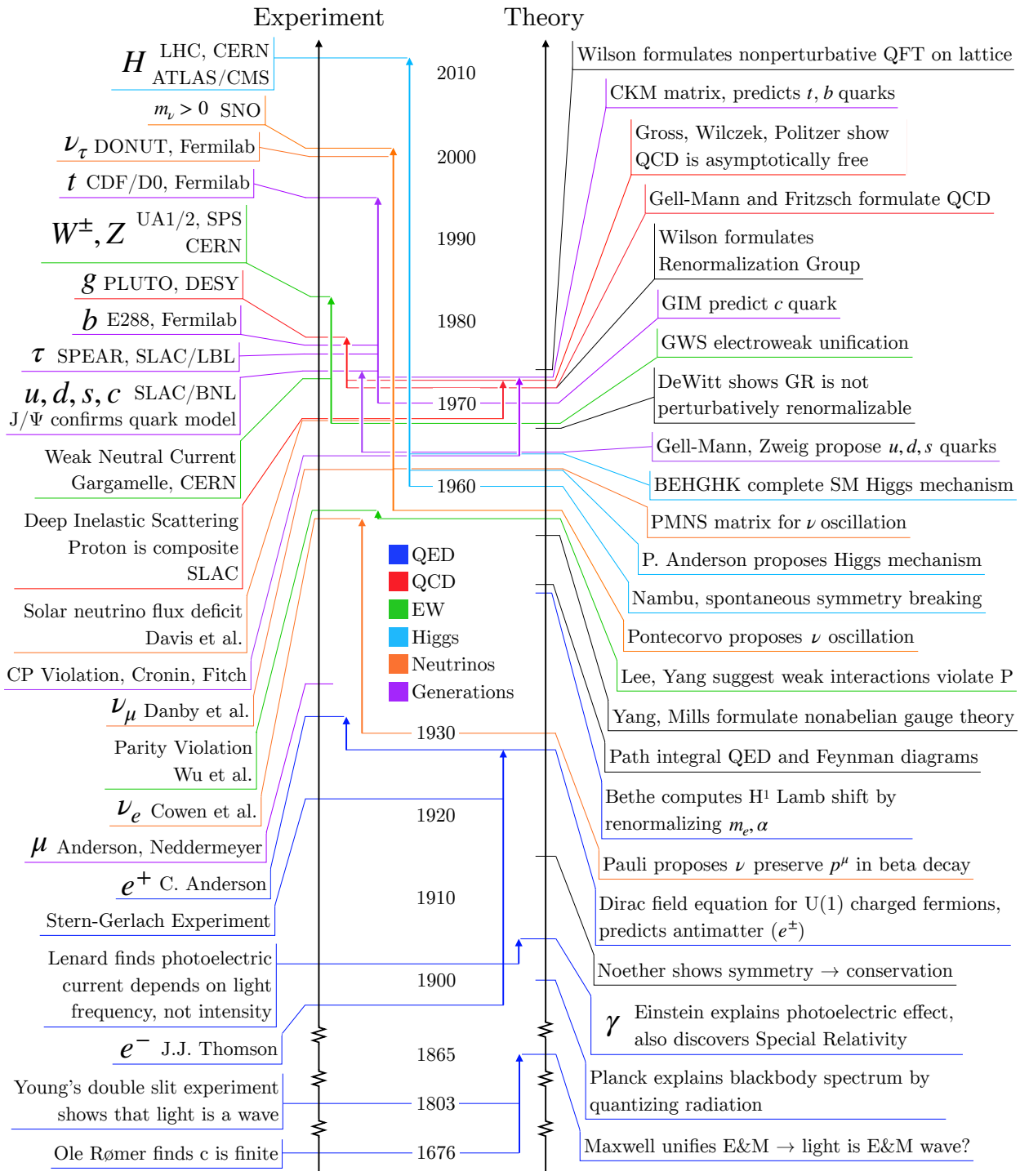

Figure 2.5: A summary of the experimental (left) and theoretical (right) milestones in the development of QFT and the SM. Colors and arrows show the interplay between experimental and theoretical development particularly in the period of rapid development from 1955 to 1975.

Chapter 3

THE LARGE HADRON COLLIDER

The Large Hadron Collider (LHC) is arguably the largest machine ever built[1]. It occupies the tunnel originally built for the Large Electron Positron collider (LEP). The LEP tunnel was optimized for the storage of $50 - 100\,\mathrm{GeV}$ electron beams where the primary concern is the energy loss from synchrotron radiation:

$$E_{\mathrm{loss}} \propto \frac{e^2}{m^4} \frac{E_{\mathrm{beam}}^4}{r} \tag{3.1}$$

where e and m are the particle charge and mass respectively and r is the bending radius of the particle path. Straight sections of the tunnel containing acceleration cavities are needed to replace energy lost to synchrotron radiation. If larger sections of the tunnel circumference are made straight to accommodate acceleration cavities, the regions which are dedicated to bending must compensate with a tighter bending radius. The LEP tunnel dimensions were thus determined by the acceleration cavity technology available in the 1980's, the acceleration power budget of around 100 MW, and the desired beam energy. The result was a 27 km tunnel with more than 2 km of straight sections for acceleration. The tunnel was routed an average of 100 m underground, straddling the French-Swiss border outside of Geneva as shown in Figure 3.1. LEP was removed from the tunnel at the end of 2000 to make room for the LHC.

The LHC is designed to accelerate and store two counter-rotating beams of strongly interacting particles (hadrons), specifically protons and heavy ions like lead and xenon. The proton mass is approximately two thousand times larger than the electron mass. Synchrotron losses

[1] One could argue the United States electrical grid is the largest machine ever built but we contend that such systems are better defined as a large collection of much smaller machines. The LHC cannot analogously be broken up into independently functioning sub-units.

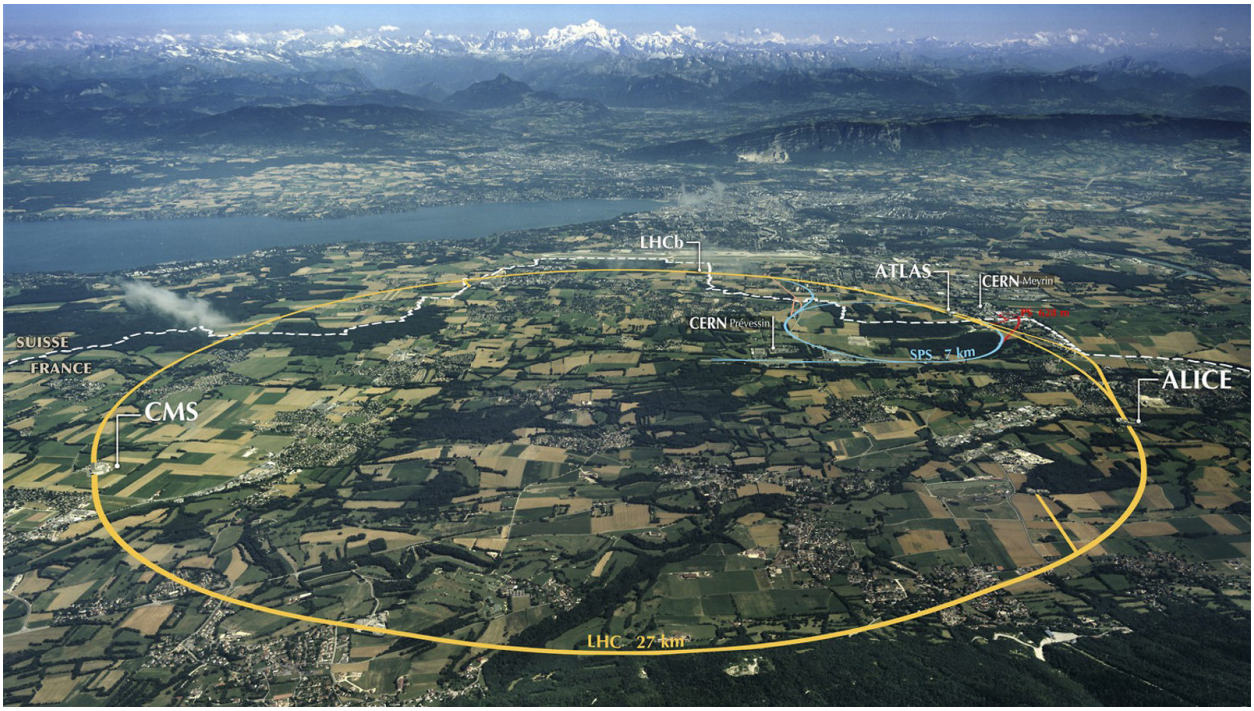

Figure 3.1: In this figure [68] by Maximilien Brice, the 27 km Large Hadron Collider (LHC), its four main experiments and the 7 km Super Proton Synchrotron (SPS) are shown in geographic context. The French Alps are visible on the horizon with Mont Blanc in the center. The Jura mountain range starts at the bottom of the image.

for proton beams in the same tunnel therefore become important for beam energies above $\approx 50\,\text{TeV}$.[2] Unfortunately, the magnetic field needed to bend the beams along a given radius of curvature is proportional to the beam energy. As a result, the LHC beam energy is limited by the field strength of high field superconducting magnets. The LHC uses 1,232 dipole magnets based on niobium titanium (Nb-Ti) superconducting wire operated at 1.9 K. Each dipole is 15 m long and weighs 30 tonnes. The magnets are designed to carry 14 kA of current and generate 8.3 T fields with less than 0.01% variation between any two magnets. Additionally, they must maintain this level of variation across the 15× dynamic range required to ramp the beam up from injection energy to the maximum of 7 TeV per beam. Each dipole magnet stores 7 MJ of energy, enough to melt 30 kg of copper. For a detailed description of the LHC magnets, see reference [180].

Before entering the LHC, protons are accelerated in stages by a sequence of four accelerators starting with the LINAC2, a 50 MeV linear accelerator. Next, the protons enter a synchrotron called the PS Booster which brings them to 1.4 GeV at which point they are injected into the Proton Synchrotron (PS). The PS further boosts the protons up to 26 GeV before injecting them into the Super Proton Synchrotron (SPS). The 7 km SPS, an engineering marvel in its own right, finally injects the protons into the LHC at an energy of 450 GeV. For reference, the rest mass of a proton in these units is approximately 1 GeV. When the LHC beams are full, they each contain 2808 bunches of protons with roughly 10^{11} protons per bunch. At the maximum design energy of 7 TeV per proton per beam this corresponds to a total of 720 MJ of kinetic energy - equivalent to a 1600 tonne freight train moving at 30 m/s!

The LHC beams intersect to produce collisions at four interaction points. A Toroidal LHC ApparatuS (ATLAS) is located closest to the primary CERN campus in Meyrin at access

[2] Nb-Ti superconducting wire has an extremely low heat capacity at 1.9 K allowing even small amounts of synchrotron radiation to become problematic as it heats the magnets. For the LHC, this is handled with dedicated synchrotron radiation heat sinks which can dissipate the $\approx 200\,\text{mW/m}$ of synchrotron radiation at peak beam energy. They are operated between 5-20 K.

point 1. The Compact Muon Solenoid (CMS) - optimized to study the same physical processes as ATLAS - is located in France at access point 5.[3] LHCb (LHC beauty, so named for the quark it is optimized to study, also known as the bottom quark) and ALICE (A Large Ion Collider Experiment) are located at the two remaining interaction points on either side of ATLAS. The LHC uses most of the available beam time for proton-proton collisions with a few weeks per year reserved for special runs and heavy ion collisions.

For a complete description of the LHC see reference [63].

3.1 The 2008 Quench Incident

When the current in the LHC magnets is ramped up, the magnetic fields produce huge internal stresses on the magnet structure. This can cause components to shift, generating small amounts of heat. These shifts can cause sections of the superconducting cables to exceed the superconducting critical temperature. When this happens, dedicated current dump circuits are activated to prevent all of the stored energy from being dissipated by the region of cable which became a regular conductor in a process called a quench.[4] The magnets must be ramped up and quenched many times to enable stable operation at their design current. This process, called "training", can take weeks or months and must be repeated every time the magnets are cooled down from room temperature.

At the end of the LHC commissioning process in 2008, one of the quench circuits failed when an electrical short formed in the connection between two adjacent dipole magnets.

[3] The numbers associated to the interaction points are larger than the total number of interaction points because there are additional access points for cooling infrastructure and maintenance.

[4] Due to the 104 s time constant of the enormous inductance of the dipole magnets, the only way to quickly transfer the current out of the magnet is to heat it up above the critical temperature while simultaneously opening a bypass circuit through a thick copper bar. This process allows the magnet current to be transferred to the bypass copper bus bar in 1 s.

The short created an arc which generated 2-6 MW of heat, vaporizing the nearby region of the beam pipe and breaking the ultra high vacuum within. The heat also vaporized large amounts of liquid helium, causing the pressure inside the magnet cryostat to reach 8 bar - far beyond the maximum design pressure of 1.5 bar. The spike in pressure forced up to 20 kg/s of liquid helium and debris into 3 km of the beam pipe until the pressure inside the cryostat generated around 56 tonnes of force between the two dipoles. The ensuing explosion pushed the magnets apart displacing more than a dozen of the 30 tonne dipole magnets. Six tonnes of helium were lost and 53 magnets were damaged with 37 ultimately needing to be replaced. The first LHC run was delayed by more than a year while repairs were made and the magnets were modified to allow faster helium venting in the event of a similar incident. To read more about this quench incident see section 6 of reference [180].

3.2 LHC Performance

In November of 2009 the first run (Run-1) of the LHC began at a reduced beam energy to prevent further delays. Data was collected at center of mass collision energies[5] of $\sqrt{s}$ =7 and then 8 TeV until 2012 when the first scheduled long shutdown (LS-1) began. On July 4, 2012 the ATLAS and CMS collaborations jointly announced [138] the discovery of a new boson with a mass of 125 GeV consistent with the predicted SM Higgs boson.

During LS-1 the joints between the dipole magnets were modified to allow the magnets to be safely ramped up to their design current. Each experiment took advantage of the down time to perform upgrades and implement improved data taking systems using the lessons learned in Run-1. In particular, the ATLAS collaboration installed a new tracking layer (see

[5] The center of mass of a collision is commonly denoted $\sqrt{s}$ where s is the Mandelstam variable given by the square of the sum of the colliding particle four vectors. For colinear colliding beams of equal energy $\sqrt{s} = 2E_{\text{beam}}$.

Chapter 4.1) and optimized the software trigger system (see Chapter 8.5). In 2015 after LS-1, the LHC began Run-2, now at 13 TeV, closer to the original design energy of 14 TeV.[6]

Figure 3.2 summarizes the LHC's proton-proton collision production performance as measured by the ATLAS detector. Particle collision dataset sizes are measured in units of inverse area because the relative probability for specific collision process to occur is measured in units of area. In this way the expected number of events where a given process occurred in a dataset is just the product of the dataset size and the process "cross section". For example, the total cross section of a proton[7] is approximately $\pi r_p^2 \approx \pi(1 \times 10^{-15}\,\mathrm{m})^2 = \pi\,\mathrm{fm}^2$. A unit of area that is commonly used is the "barn" which is approximately the cross section of a uranium nucleus and is defined to be $10^{-28}\,\mathrm{m}^2 = 10^{-24}\,\mathrm{cm}^2 = 100\,\mathrm{fm}^2$. The cross section of the proton in these units is approximately 0.03 barns or 30 millibarns (mb).

When composite particles collide the total cross section increases with the collision energy. This can be understood qualitatively by analogy with the International Space Station: At the enormous relative velocities present in low Earth orbit even a small paint chip can leave a large dent, while at low relative velocity the impact would not even be noticed. This analogy is surprisingly apt since what we mean by a particle "collision" depends on the size of the deflection one wishes to measure: The elastic cross section for protons passing each other to be deflected by small angles is larger than the cross section for inelastic collisions where the protons fragment. For collisions at $\sqrt{s} = 13\,\mathrm{TeV}$ the inelastic proton-proton cross section is measured to be $78.1 \pm 2.9\,\mathrm{mb}$ [146]. The dataset used in this thesis is 27.5 inverse femtobarns (fb^{-1}) which means it was generated by roughly $78 \times 10^{-3}\,\mathrm{b} \times 27.5 \times 10^{15}\,\mathrm{b}^{-1} = 2,145$ trillion

[6] Discussions are ongoing to determine when to attempt running at the full 14 TeV.

[7] Measuring the "radius" of a particle depends somewhat on one's definition of where to define the edge of smeared blob. Hadrons like protons are not fundamental particles in the sense that they have multiple degrees of freedom at high energies. This allows one to model the charge distribution with a sphere and take the best fit sphere radius to describe electron scattering or finite nucleus size effects on atomic energy levels. The proton charge radius is measured to be $\approx 0.8 \times 10^{-15}\,\mathrm{m} \approx 1\,\mathrm{fm}$ with some disagreement among different measurement techniques which remains to be explained [3].

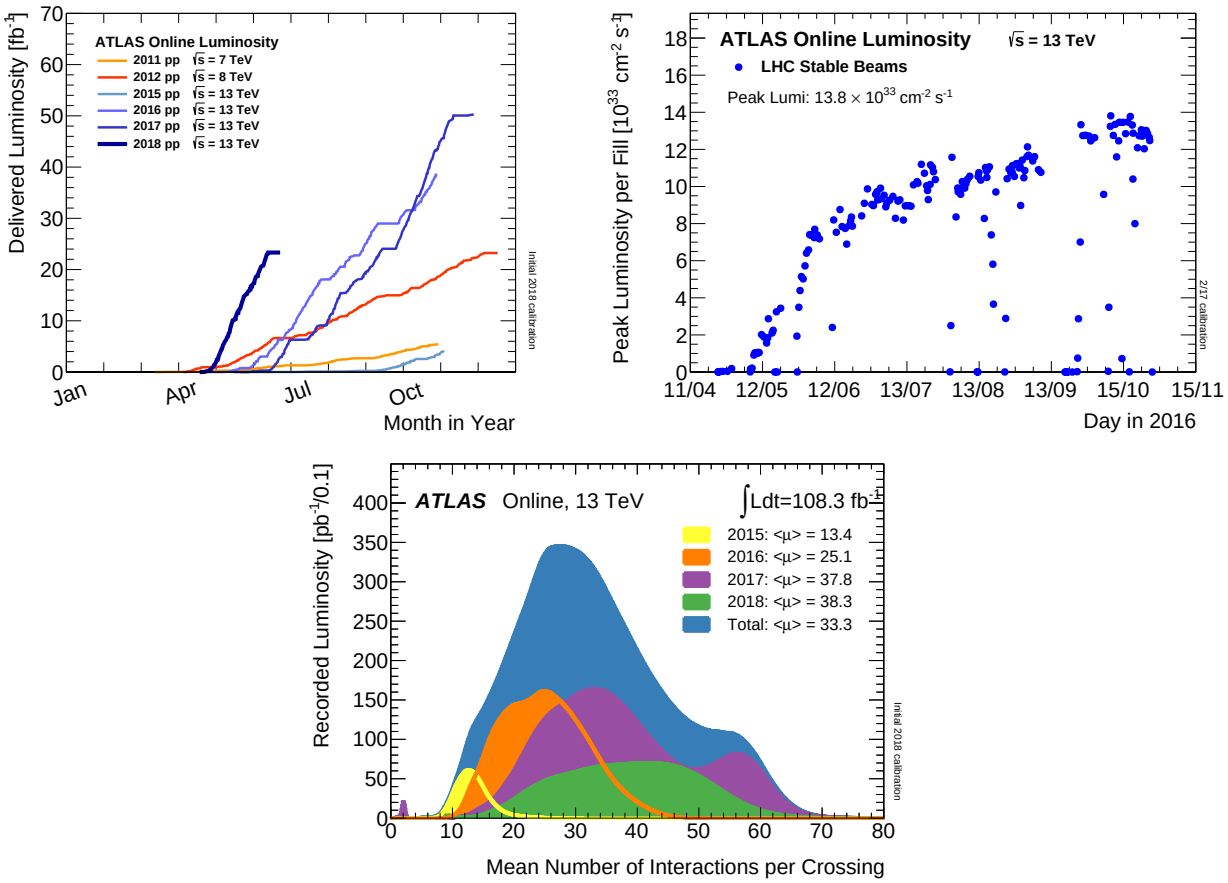

Figure 3.2: LHC performance as measured by ATLAS. Top Left: Integrated luminosity for each year of data taking. The 2018 run is ongoing. This thesis uses the datasets taken in 2015 and 2016. Top Right: Peak luminosity labelled by the corresponding LHC beam fill. The peak luminosity in 2016 of $\approx 1.4 \times 10^{34}\,\mathrm{cm}^{-2}\mathrm{s}^{-1}$ exceeded the design goal of the LHC of $1 \times 10^{34}\,\mathrm{cm}^{-2}\mathrm{s}^{-1}$. Bottom: The average number of proton-proton interactions per bunch crossing split by year. This thesis uses the 2015 and 2016 datasets shown in yellow and orange.

inelastic proton-proton collisions.[8]

We say that the "integrated luminosity" of our dataset is $27.4\,\text{fb}^{-1}$. The luminosity (denoted $\mathcal{L}$) is proportional to the proton collision rate at a given point in time so by integrating the luminosity over time we get a number which is proportional to the total number of collisions: $\int \mathcal{L}\,dt$. The proportionality constant is the cross section of the type of proton collision one wishes to count. For example, the cross section $\sigma(pp \to H)$ times the integrated luminosity gives the number of Higgs bosons we expect to be produced. As a warning the word "integrated" is often not explicitly stated when quoting the integrated luminosity so the meaning of "luminosity" must be interpreted from the units and context.

The top two plots in Figure 3.2 show the integrated luminosity as a function of time in the year for each year of ATLAS data taking up to now, and the peak luminosity for each proton-proton physics LHC beam fill in 2016. In particular, note that the peak luminosity observed by ATLAS often exceeded $1 \times 10^{34}\,\text{cm}^{-2}\text{s}^{-1} = 10^{-5}\,\text{fb}^{-1}\text{s}^{-1}$ which was the design goal luminosity for the LHC. This has enabled more than half an inverse femtobarn to be collected in a single day - a remarkable achievement.

The LHC instantaneous luminosity can be increased in two ways; by increasing the bunch[9] crossing frequency, or by increasing the number of collisions per bunch crossing. The LHC bunch spacing was 25 ns for the majority of the data used in this thesis. A few early runs in 2015 used 50 ns bunch spacing. Using spacings smaller than 25 ns would require significant changes to detector readout strategies. Nonlinear interactions between bunches and electron cloud build up in the beam pipe would also create challenges for controlling and containing the beams. Increasing the number of collisions per bunch crossing or "pile-up" primarily

[8] The recorded data set only contains roughly 1 in 400,000 of these collision events. This is explained in Chapter 8.5.

[9] As a reminder, a bunch is just a group of particles which were injected into the LHC together. The LHC is designed to have 2808 bunches of protons per beam, each with roughly one hundred billion protons. Since the total ring circumference is 27 km, the 2808 bunches are an average distance of 9.6 m apart.

creates challenges for the experiments which have to handle the increased detector occupancy. This can reduce measurement precisions and dramatically increase the computation time needed to process each event. The bottom plot in Figure 3.2 shows the mean number of proton-proton interactions per bunch crossing for each year of data taking.

Chapter 4

THE ATLAS DETECTOR

The goal of the ATLAS (A Toroidal LHC ApparatuS) Detector is to measure the momentum, energy and charge of every particle produced in the collisions provided by the LHC. This is accomplished with an onion-like detector geometry with layers that are designed to either detect the passage of a particle, or absorb particle energy. The ratio of the momentum over the electric charge of a particle can be determined from the curvature of the particle's path in a magnetic field. The energy of a particle can be estimated by sampling how its energy propagates through layers of absorbing material like lead and iron.

Strongly coupled particles like quarks and gluons form bound states called hadrons in $\mathcal{O}(10^{-23}\,\mathrm{s})$ and as such are never directly observed in the detector. Instead, high energy quarks and gluons hadronize in collimated sprays of particles which can be algorithmically clustered to form observables called "jets". The jet definition used in this thesis is described in Chapter 7.

The ATLAS detector is approximately cylindrically symmetric with the axis of symmetry along the beam line. A 3D Cartesian coordinate system is defined with the z-axis pointing along the beam line counter clockwise when viewed from above, the x-axis points towards the center of the LHC, and the y-axis points upwards. The x, y plane defines the transverse plane. Transverse momentum is the component of a momentum vector contained in the transverse plane. Longitudinal momentum is the component of a momentum vector along the z-axis. The more natural cylindrical coordinate system is then defined by taking the azimuthal angle ϕ increasing from the positive x-axis towards the positive y-axis. The polar

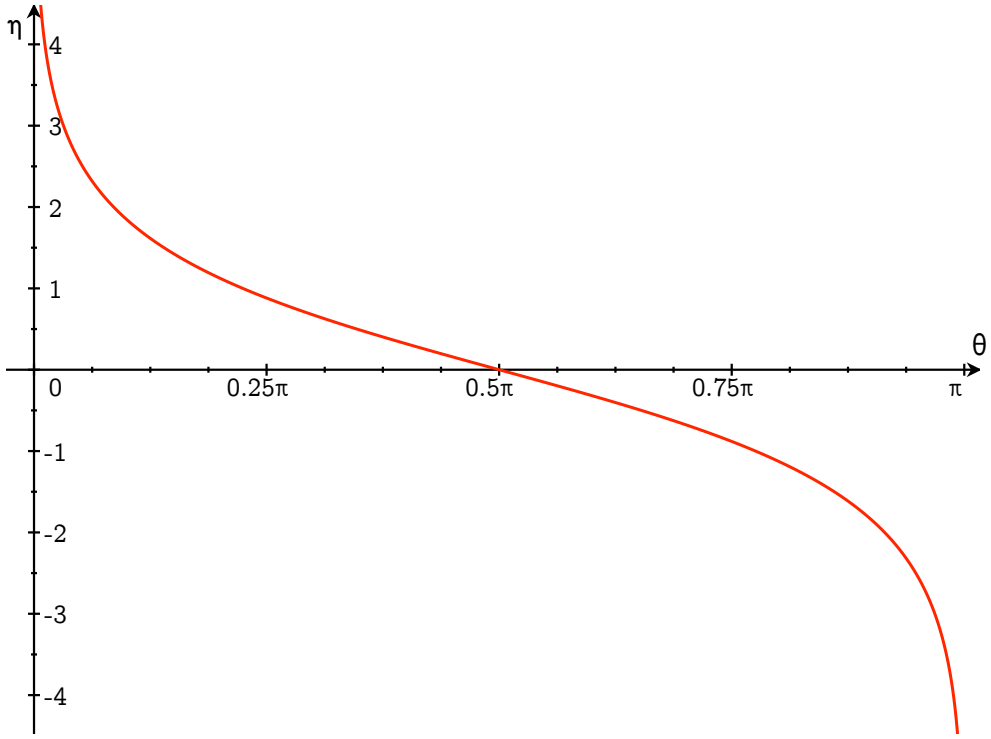

Figure 4.1: The red line shows the pseudorapidity (eqn. 4.1) η as a function of the polar angle θ.

angle θ is used to define the pseudorapidity η:

$$\eta = -\ln[\tan(\theta/2)] \tag{4.1}$$

This function is plotted in figure 4.1.

In electron-positron head-on collisions with equal beam energy, the total momentum of the colliding system is zero. The same is true for head-on collisions of proton beams with equal energy but is generally not true of the colliding partons (fundamental parts of protons eg. quarks or gluons). The probability for a type of parton to carry a given fraction of the total proton momentum is given by the proton Parton Distribution Function or PDF (not to be confused with the more general term "probability distribution function"). The z component

of the momentum exchange in collisions between two partons is generally poorly constrained because large amounts of the proton momenta continue along the beam-line going undetected. Pseudorapidity is the natural polar coordinate for collisions of composite particles because the difference in pseudorapidity between particle four-momenta $\Delta\eta$ is independent of the longitudinal momentum of the system. This means the distribution of $\Delta\eta$ of the decay products of a particle is independent of the longitudinal momentum imbalance of the partons which participated in the hard scatter collision.

The ATLAS detector systems can be broken into four major categories, listed here in radial order, starting closest to the beam pipe and moving outwards:

1. **Inner Detector (ID):** Measures particle tracks in a uniform longitudinal magnetic field. See Section 4.1.

2. **Electromagnetic (EM) Calorimeter:** Measures the energies of photons and electrons. See Section 4.2.1.

3. **Hadronic Calorimeter:** Measures the energy of hadrons which make it through the EM calorimeter. See Section 4.2.2.

4. **Muon Spectrometer (MS):** Measures the tracks of charged particles which make it through the Hadronic Calorimeter. These are predominantly muons. See Section 4.3.

Many types of particles decay before they reach the detector, so their properties must be inferred from the properties of their decay products using conservation laws. The production of a Z boson ($m_Z \approx 91\,\text{GeV}$), for example, may be inferred with high probability from the presence of two oppositely charged electrons whose four-vector sum gives an invariant mass near m_Z. Conversely, sufficiently long lived particles which are not charged under the electromagnetic or strong nuclear forces such as neutrinos or hypothesized dark matter

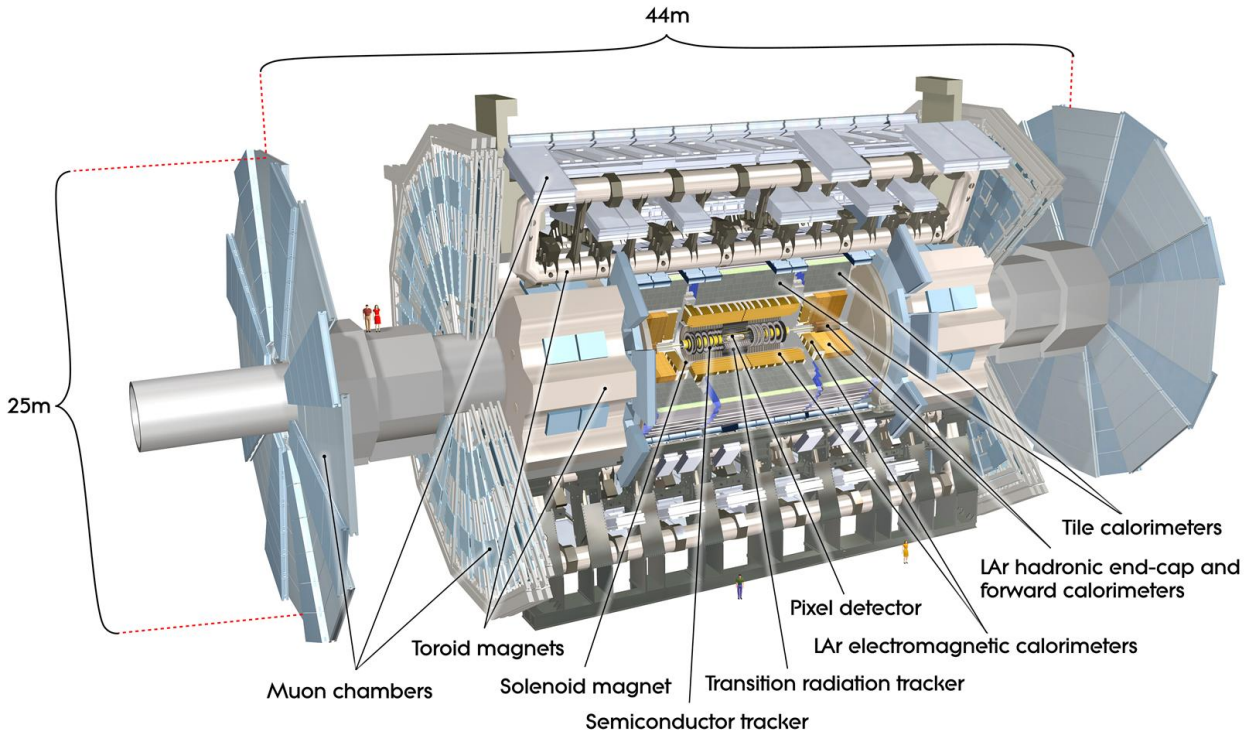

Figure 4.2: A diagram of the ATLAS detector with all major detector subsystems labeled. Humans for scale, standing in the shown locations without personal protective equipment is not recommended. The ID (Figure 4.3) consists of the insertable b-layer (IBL, not shown), pixel detector (PIX), semiconductor tracker (SCT), transition radiation tracker (TRT) and the solenoid magnet. The calorimeter (Figure 4.4) consists of the liquid argon (LAr) EM calorimeter, the tile calorimeter and the LAr hadronic end-cap/forward calorimeters. The muon spectrometer (MS) (Figure 4.7) consists of the muon chambers and the toroid magnets.

will fly through the detector without being measured. The production of such particles is inferred from the apparent violation of transverse momentum conservation.

An illustration of the ATLAS detector is shown in Figure 4.2.

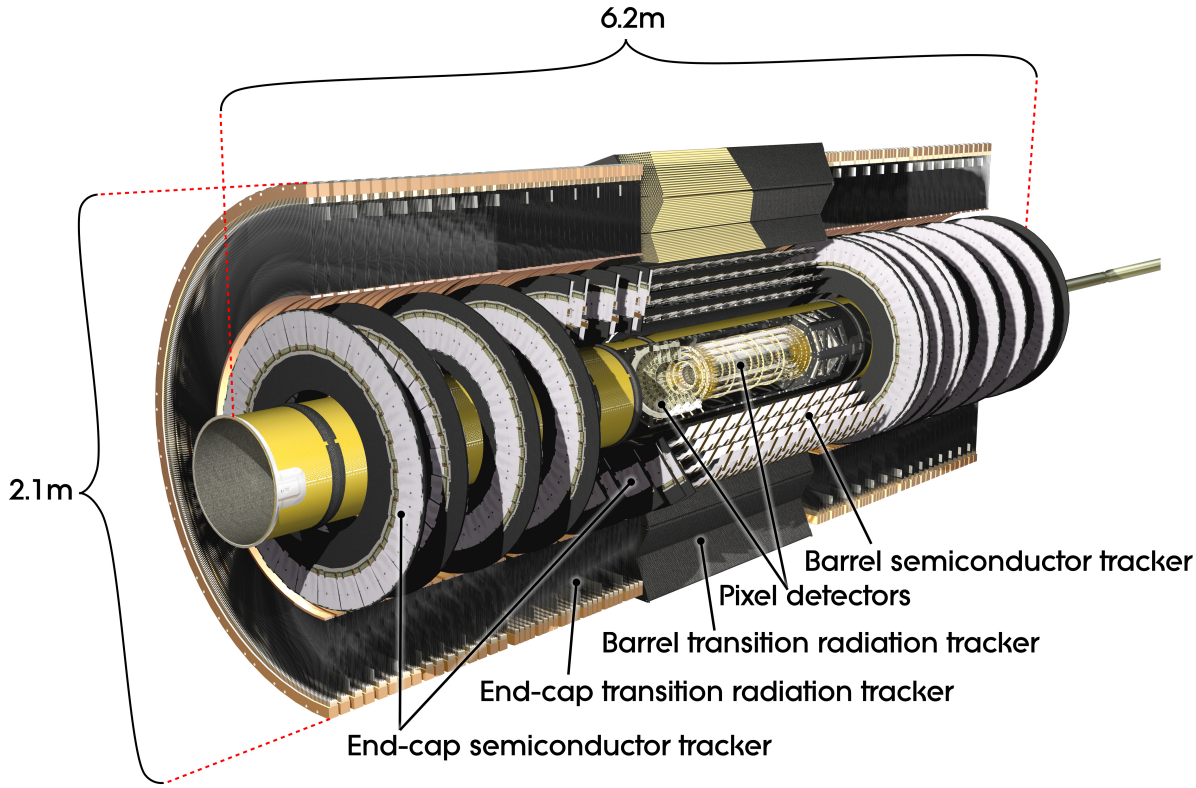

Figure 4.3: A diagram of the inner detector (ID) with all major detector subsystems labeled excluding the insertable b-layer (IBL).

4.1 Tracking

When a relativistic charged particle passes through a material it will kick some of the electrons in the material to an excited state. If an electric field is applied across the material, these electrons can be collected by an electrode and the corresponding charge spike can be measured. In silicon, electrons are kicked out of an insulating band into the conduction band, and the corresponding electron-hole pair drift apart under the applied field. The ATLAS Inner Detector (ID) uses silicon pixels and strips with bias voltages between 100-300 V. In gas, atoms are ionized and the electron and ions drift in opposite directions. The silicon tracker is surrounded by layers of 4 mm diameter tubes filled with xenon gas which make up the Transition Radiation Tracker (TRT). An electric field is applied by placing bias voltages in the range 1400-2000 V between the inner walls of the tubes and gold wires running down their centers.

The ID design utilizes these two basic technologies to balance constraints from cost, data rate, radiation hardness, track parameter resolution, particle identification performance, and total material between the collisions and the calorimeter systems which causes energy loss and multiple scattering thereby reducing the energy measurement precision of the calorimeter systems. The general principle is to use most of the cost, material, and data rate budgets in the instrumented regions closest to the collisions, moving to more sparsely instrumented detectors at larger distances from the proton collision region. The particle flux falls off roughly as $1/r$ for $r < 100$ mm (due to the extent of the collision region in z) and as $1/r^2$ for $r > 100$ mm. The tracker is optimized for resolution in the transverse plane since the initial momentum of the colliding system in the transverse plane is near zero while the momentum along the beam direction is poorly constrained. Figure 4.3 illustrates the geometry and layout of these detector systems.

The inner detector tracking system is contained inside a solenoid magnet which produces a

uniform 2 Tesla (T) magnetic field parallel to the beam axis. Charged particles in a uniform magnetic field follow helical paths where the radius of curvature is known as the cyclotron radius:

$$r_{\text{cyclotron}} = \frac{p_\perp}{|q|B} \tag{4.2}$$

where $p_\perp$ is the momentum transverse to the magnetic field, q is the particle charge, and B is the magnetic field strength. The sign of the charge determines the direction of the curvature and most charged particles of concern have charge ± 1 in units of the electron charge. By sampling the charged particle's helical paths in at least three places, one can recover the transverse momentum and charge. Additional sample points improve the momentum measurement precision and reduces ambiguity when there are many tracks.

The ID subsystems are split into "barrel" and "end-cap" regions. The barrel regions consist of concentric cylinders while the end-cap regions are made up of disks. The ideal detector would use concentric ellipsoid layers such that the angle of incidence of average particle tracks was normal to the surface of the detector. The barrel/end-cap geometry provides a compromise between the ideal geometry and feasibility of construction with flat/linear components.

The innermost four layers of the barrel consist of silicon pixel detectors. The pixels are small rectangular sections of silicon which are individually read out. As charged particles pass through the silicon, they excite electrons into the conduction band in multiple nearby pixels. The amount of charge collected in each pixel and the shape of the cluster is used to infer 2D coordinates of particle tracks in each layer with better precision than the size of individual pixels. The first pixel layer is physically attached to a new beam pipe which was installed during the first LHC long shutdown in 2014. The aptly named Insertable B-Layer (IBL) is wrapped around the new beam pipe with an 8 mm smaller diameter such that the instrumented pipe could fit inside the previous innermost pixel layer. The IBL samples

particle tracks at $r = 25.7\,\text{mm}$ while the next pixel layer is at 50.5 mm. This substantially improves the 3D resolution of points from which multiple tracks originate known as vertices, as well as the 3D impact parameter resolution of individual tracks. The impact parameter is the distance of closest approach of a track from the primary vertex of a given proton-proton collision. This is particularly important for correctly associating tracks to vertices and the identification of bottom quark (B) hadrons which typically travel a few millimeters away from the primary vertex before decaying. This is the origin of the B in IBL and the reason the previous innermost pixel layer is called the B-layer. There are also three pixel end-cap disks on each side of the barrel providing pixel coverage up to $|\eta| < 2.5$.

Moving away from the beam line, the expected particle flux decreases and the high cost and data volume of pixel detectors becomes sub-optimal. To reduce cost and data readout bandwidth, the next four layers in the central region are built from long silicon strips which measure a single coordinate. Each layer is built from two sub-layers of silicon where the strips are glued at a 40 mrad (2.3 degree) angle with respect to each other. In this way a 2D coordinate can be extracted with excellent resolution in the ϕ coordinate and larger resolution in the z coordinate. The system of silicon strips is called the Semiconductor Tracker (SCT)[1]. There are nine SCT end-cap disks on either side of the barrel, again such that the system has coverage up to $|\eta| < 2.5$.

Surrounding the SCT is the Transition Radiation Tracker (TRT). Transition radiation refers to the process which generates photons when a relativistic charged particle transitions between two mediums of different indices of refraction. The number of photons produced is directly proportional to the particle's relativistic γ factor. This means that for a given momentum, particles with a lower mass will produce more transition radiation. The TRT is built from densely stacked 4 mm diameter coaxial tubes (straws) filled with xenon gas.

[1] The pixel systems are also composed of semiconductors. Perhaps a better name would have been "Silicon Strip tracker (SST)".

The space between the straws is filled with polypropylene-polyethylene fibers with an average diameter of 15 μm. This provides passing charged particles with a large number of transitions between the index of refraction of the fibers and that of the surrounding CO_2 atmosphere. The transition radiation photons of interest fall in the x-ray spectrum and produce large charge spikes in the straw readouts while passing charged particles ionize relatively few xenon atoms giving small charge spikes. By counting the number of spikes passing corresponding high and low[2] thresholds, one can estimate the relativistic γ factor of each charged particle track through the TRT. In addition to the momentum measurement provided by the track curvature, this allows for an estimate of the charged particle mass. In particular, one can differentiate between electrons and charged hadrons whose masses are at least 250 times larger. The 4 mm straw diameter was chosen to balance signal collection speed and response. A larger diameter would give a larger ionization signal per particle but the average drift time of the electrons would be larger resulting in more overlap of signals from consecutive proton bunch crossings (out of time pileup).

Table 4.1 gives a brief summary of some of the basic properties of the ID subsystems. For a detailed description of the ID, see the ID technical design reports [41, 42] and the IBL technical design report [43].

4.2 Calorimetry

Calorimetry refers to the measurement of energy. A calorie[3] is the amount of energy it takes to heat 1 gram of water by 1 degree Celsius. The typical energy scale being measured in the ATLAS calorimeters is around 100 GeV or 4 nanocalories. Measuring these relatively tiny

[2] The number of pulses passing the low threshold is not counted, rather the time between the first and last low threshold pulse is measured.

[3] In the United States our food is labeled by how many calories it produces when it is burned though they cheat and divide by 1000 without changing the units to kilocalories.

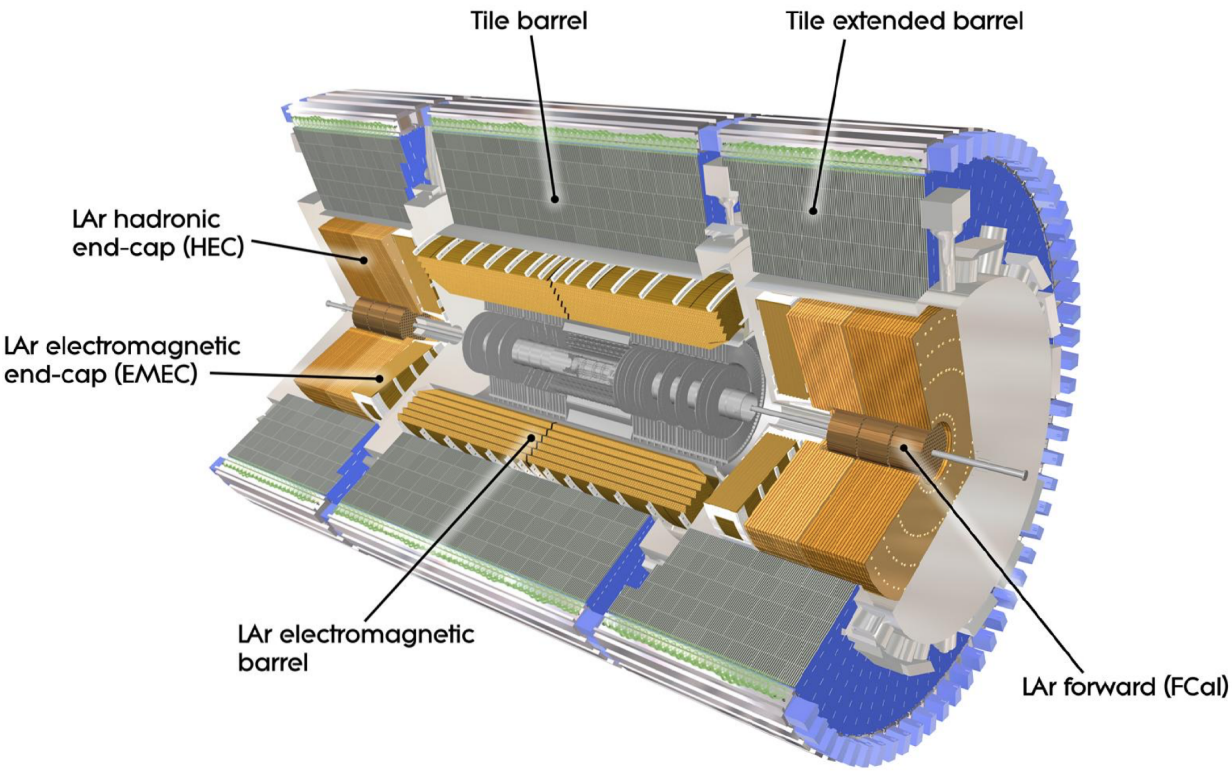

Figure 4.4: A diagram [14] of the calorimeter with all major detector subsystems labeled.

	Pixels (IBL)	SCT	TRT
Unit	Pixel	Strip	Straw
Unit Size	$50 \times 400\,\mu\text{m}^2$ ($50 \times 250\,\mu\text{m}^2$)	$80\,\mu\text{m} \times 12.6\,\text{cm}$	$4\,\text{mm} \times 144\,\text{cm}$
Resolution	$10 \times 120\,\mu\text{m}^2$ ($10 \times 60\,\mu\text{m}^2$)	$17 \times 580\,\mu\text{m}^2$	$\approx 30\,\mu\text{m}$ in r, ϕ with 35 hits
Channels	80M total (6M)	6M	350k
Coverage	$1.7\,\text{m}^2$	$60\,\text{m}^2$	$12\,\text{m}^3$
Barrel r [mm]	26, 51, 89, 123	299, 371, 443, 514	563-1066
$\lvert\eta\rvert$ Range	< 2.5	< 2.5	< 2.0
X_0	0.15, 0.8	0.12, 0.3	0.2, 0.8

Table 4.1: A summary of general tracker system specifications. Hit resolutions are approximate and depend on the exact location, particle trajectory and nearby activity. In the pixel column, items specific to the Insertable B-Layer (IBL) are specified in parentheses. The quoted radiation lengths (X_0) are averaged over ϕ and the η ranges $|\eta| < 0.6$, $|\eta| > 0.6$. Support structure cooling infrastructure contribute another 1.5-2× the total radiation length for $|\eta| > 1$

energies with percent level accuracy hundreds of millions of times per second requires some clever physics, engineering and electronics.

The general principle used by ATLAS is to stack alternating layers of absorber material and sampling material. As high energy particles pass through the absorber material they scatter and produce additional particles, either through electromagnetic interactions or nuclear interactions. This process continues until the particles in the developing shower fall below the energy threshold for e^+e^- pair production or they make it through the calorimeter. When the shower passes through the sampling material, atoms can get ionized, Cherenkov radiation can be produced or scintillating molecules can be excited. In the first case a bias voltage is used to drift the charge carriers (electrons and ions) to electrodes. In the latter two cases, photons are produced and then guided to collection fibers where they can be routed to photomultiplier tubes (PMTs) to be counted. In some cases the initially produced photons are

at wavelengths which cannot be efficiently detected by the PMTs, so a wavelength shifting material is used in the fibers.

The statistical uncertainty in calorimeter energy measurements is proportional to the square root of the number of ionizing particles produced in the shower which is in turn proportional to the shower energy. For this reason, the fractional uncertainty on sampling calorimeter measurements contains a term which is proportional to $1/\sqrt{E}$. There are also small terms proportional to $1/E$ which result from detector and electronics noise and constant terms due to detector inhomogeneities and energy leakage from gaps or broken modules. As such the calorimeter uncertainty is generally parametrized in three terms:

$$\frac{\Delta E}{E} = \frac{a}{\sqrt{E/\text{GeV}}} \oplus \frac{b}{E} \oplus c \tag{4.3}$$

The constants a and c are dimensionless and can be expressed as a percentage while b is in units of energy and describes a constant absolute uncertainty.

In the low energy regime where the a and b terms dominate the uncertainty, calorimeter energy measurements can be augmented with tracking information. Of particular relevance to this thesis, tracking information can be used to identify jets originating from $b-$hadrons which hadronize in subtly different ways from light quark or gluon jets. Additionally, muons from semileptonic $b-$hadron decays can be measured with the MS system (Section 4.3) allowing their component of the total $b-$hadron energy to be included with high precision. For these reasons, dedicated b-jet energy calibrations using tracking information are currently under study and may significantly improve the energy resolution for calorimeter deposits originating from heavy flavor quarks, particularly at low energies. For this thesis we simply add the energy from muons found in close proximity to b-jets.

Measuring the energy which is *not* deposited in the calorimeters is equally as important as

measuring the energy which is deposited. Neutrinos and muons are the only known particles which are not expected to deposit significant fractions of their energy in the calorimeter. If new stable or metastable particles are produced which are not charged under the electromagnetic or nuclear forces they will escape the calorimeter without being directly observed. By having nearly complete coverage over the 4π solid angle subtended by a sphere, the production of non-interacting particles can be inferred from energy imbalances in the transverse plane. Energy is a scalar quantity so there is no simple analogue to the notion of missing transverse momentum. Confusingly, "Missing transverse energy" or $E_{\mathrm{T}}^{\mathrm{miss}}$ is defined as the negative vector sum of the transverse *momenta* of all the observed particles in an event. Neutral hadron and photon momenta cannot be measured directly by the tracking system. Instead, their respective 3-momentum can be inferred from the direction and energy of the shower they generate in the calorimeters. When a particle's energy is much greater than it's mass, the energy is nearly equivalent to the magnitude of the 3-momentum. This approximation is almost always valid for the purposes of ATLAS and CMS which is why more effort is not made to use more precise terminology.

4.2.1 Electromagnetic Calorimeter

The innermost calorimeter system is the liquid argon (LAr) electromagnetic (EM) calorimeter. All known particles besides neutrinos and muons will deposit significant fractions of their energy in the EM calorimeter but photons and electrons deposit most or all of their energy at this stage. The EM calorimeter is composed of alternating layers of steel cladded lead absorbers and electrodes filled with liquid argon. In the barrel these layers are stacked in the ϕ direction and are accordion shaped such that particles traveling radially outward pass through many layers as shown in Figure 4.5. This geometry makes the detector modular and symmetric in ϕ which makes construction relatively cheap and simple compared

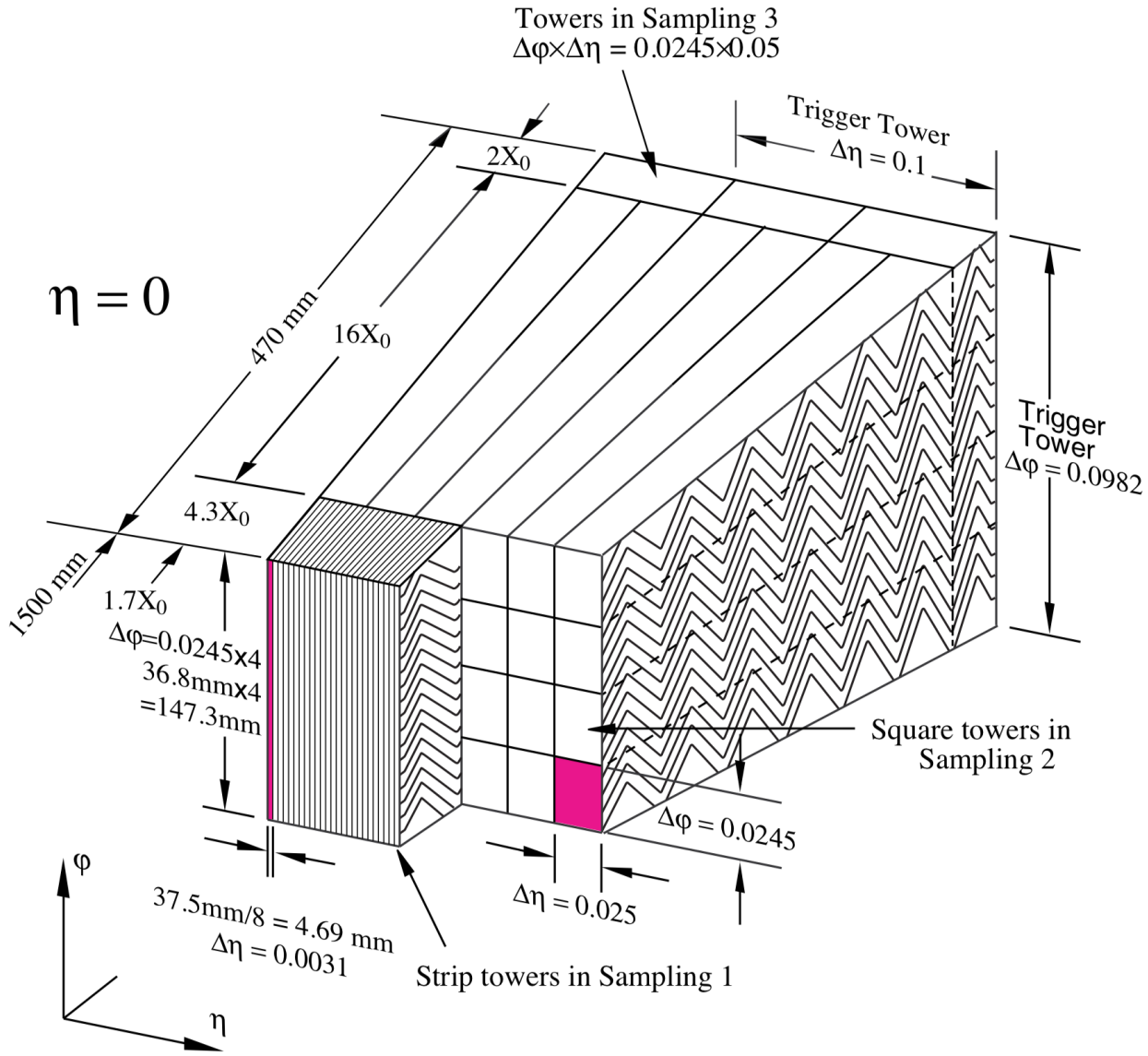

Figure 4.5: A diagram [44] of the barrel LAr EM calorimeter geometry illustrating the accordion layer structure and detector segmentation.

to a geometry where layers would be stacked radially. In the end-caps the layers are disks stacked longitudinally. The electrodes use a 2000 V bias voltage resulting in a charge drift time of 450 ns. This means the charge depositions from as many as 18 proton bunch crossings will be drifting simultaneously due to the 25 ns bunch spacing used for most of the data in this thesis. Fortunately, the signal shape from the charge readout sharply peaks and then falls off linearly to zero. Pulse shaping electronics are able to create peaks with full width at half maximum of about 70 ns which then fall below zero such that superimposed peaks from nearby bunch crossings can be well separated. Large energy deposits from consecutive bunch crossings are unlikely to overlap in the same calorimeter segments which further reduces the out of time pileup effects. The amount of current generated by particle showers is proportional to the shower energy with currents on the order of 3μA/GeV per cell.

The LAr calorimeter system is designed to have a fractional uncertainty as a function of energy less than

$$\frac{\Delta E}{E} \leq \frac{0.11}{\sqrt{E/\mathrm{GeV}}} \oplus \frac{0.4\,\mathrm{GeV}}{E} \oplus 0.0007 \tag{4.4}$$

which gives an uncertainty of $\pm 8\%$ for a 10 GeV electron which falls off rapidly to $\pm 2\%$ at 100 GeV.

Electrons, photons and pions are discriminated by checking for isolated tracks pointing to the given EM calorimeter deposit, by the shower shape, and by the fraction of energy deposited in the first and last layers of the EM calorimeter and in the hadronic calorimeter.

For a detailed description of the LAr calorimeter systems see reference [44].

4.2.2 Hadronic Calorimeter

LAr calorimeters have the added benefit of being extremely radiation hard because the active material is a liquid which can easily be replaced. For this reason the forward hadronic

calorimeters which are exposed to high levels of radiation from inelastic proton-proton scattering also use LAr. The full calorimeter system provides coverage up to $|\eta| < 4.95$ with the high η coverage being provided by the LAr end-caps and the LAr Forward calorimeters shown in Figure 4.4.

The bulk of the hadronic calorimeter is called the Tile Calorimeter and uses alternating layers of iron and scintillating plastic broken into $\Delta\eta \times \Delta\phi = 0.1 \times 0.1$ tiles. The tile layout is illustrated in Figure 4.6.

The tile calorimeter system is designed to have a fractional uncertainty as a function of energy less than

$$\frac{\Delta E}{E} \leq \frac{0.5}{\sqrt{E/\text{GeV}}} \oplus 0.02 \tag{4.5}$$

which gives an uncertainty of $\pm 10\%$ for a 40 GeV jet which falls off to $\pm 4\%$ at 500 GeV which is the range of hadronic jet energy scales relevant to this thesis.

For a detailed description of the tile calorimeter system, see reference [46].

4.3 Muon Spectrometer

The size of the ATLAS detector is in large part determined by the desired muon momentum measurement precision. Precise muon measurements require a clean environment, so the calorimeters must be deep enough to stop all other charged particles. Muon momentum is determined from path curvature in magnetic fields, so the momentum resolution can be improved by increasing the magnetic field strength or by sampling a larger section of the path to give a longer lever arm. Muon paths are bent in the transverse plane with a solenoid field in the ID, and then bent in the longitudinal plane with a toroidal field in the Muon Spectrometer (MS). This 90 degree twist in the bending direction gives a larger total path

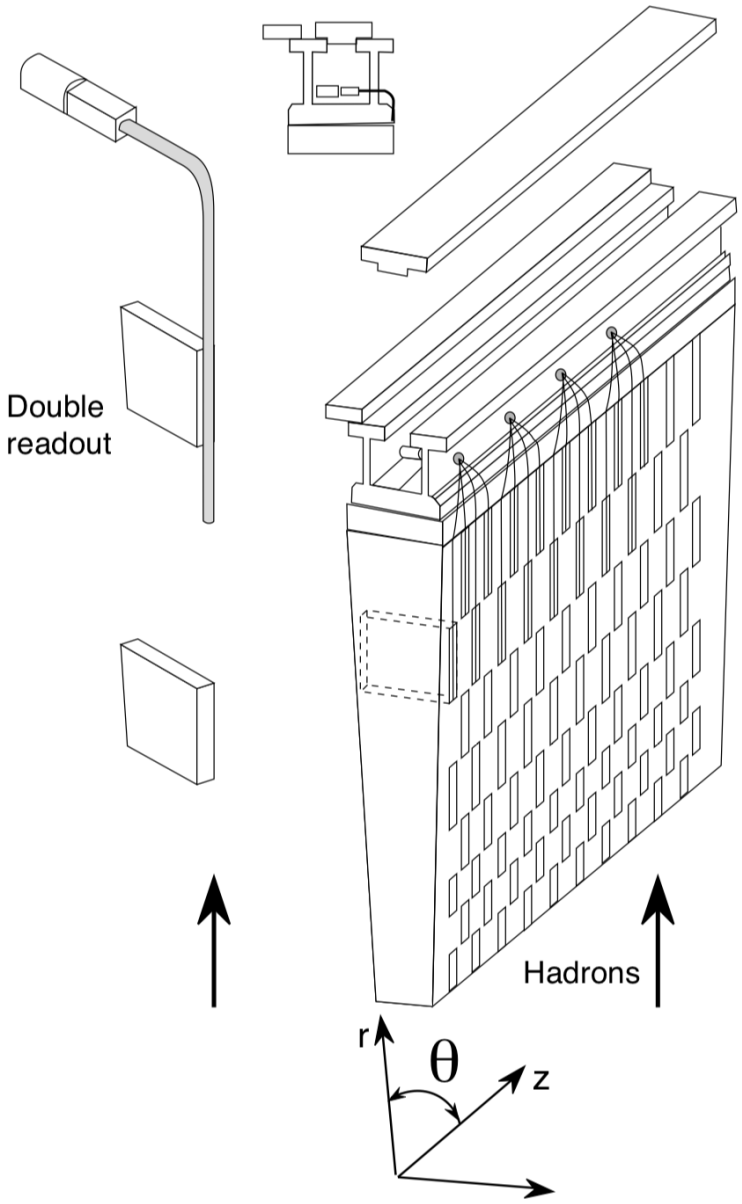

Figure 4.6: A diagram [46] of a Tile Calorimeter slice showing the scintillator layout and detector modularity.

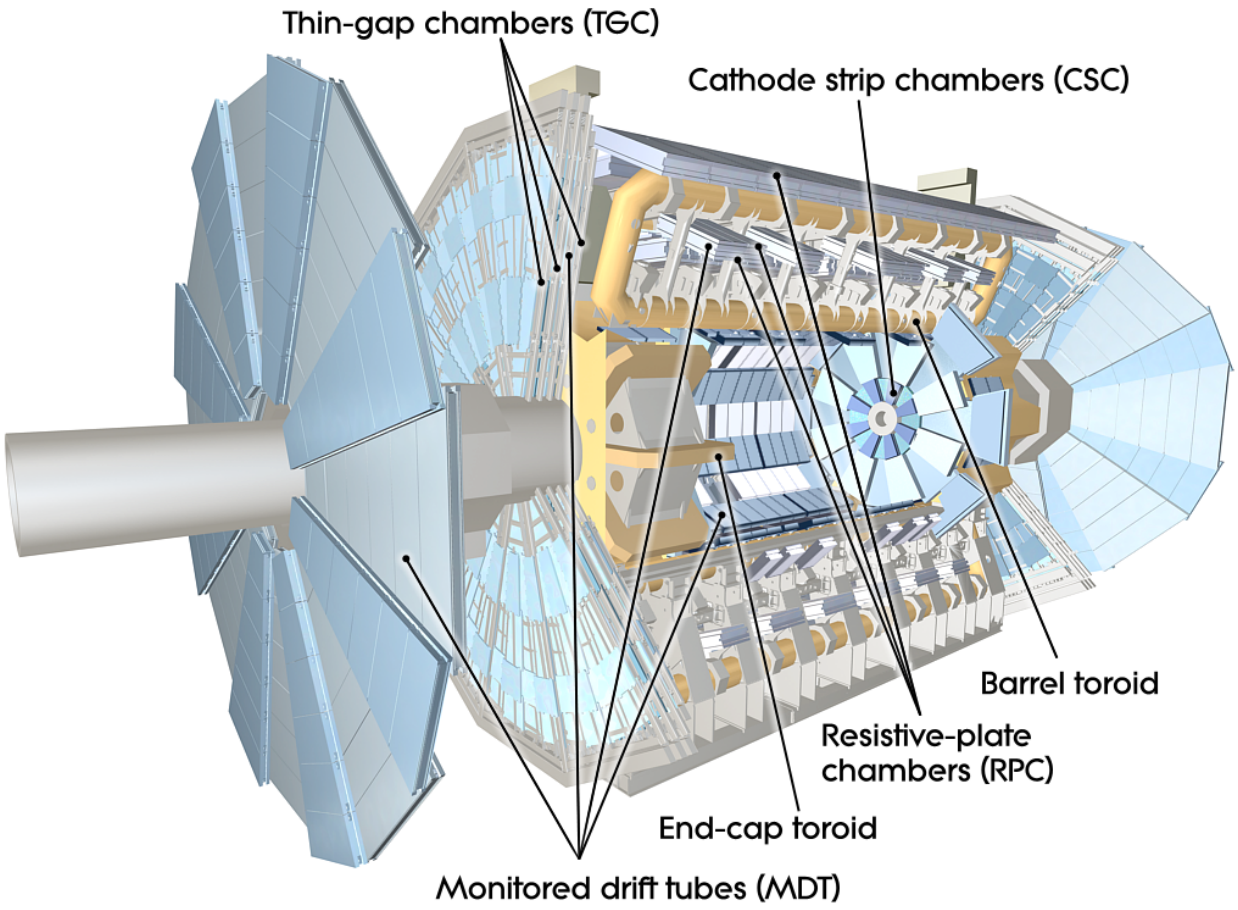

Figure 4.7: A diagram [86] of the muon spectrometer (MS) with all major detector subsystems labeled.

deflection than would be obtained from alternating solenoidal fields of equivalent magnitude[4]. The ATLAS detector was designed such that even if every other system failed, the Higgs boson could be discovered using only the MS with Higgs decays to four muons. This requires the MS to be capable of triggering on muons with $p_{\mathrm{T}} \approx 10 - 20\,\mathrm{GeV}$ and to have coverage for $|\eta| < 3.0$[5].

For low energy muons, the momentum uncertainty (a few percent) is dominated by the momentum loss in the calorimeter and multiple scattering elsewhere in the detector and magnets. Fortunately the Tile Calorimeter was designed to give some muon identification ability such that energy loss in the calorimeter could be corrected. To obtain the desired muon momentum resolution of a few percent for momenta up to a few hundred GeV given the size and field strength (0.5-1 T) of the ATLAS toroids, muon tracks need to be sampled at three points with 50 μm accuracy. To obtain three sample points over the enormous volume of the ATLAS MS, more than $5000\,\mathrm{m}^2$ needed to be instrumented making silicon detectors prohibitively expensive.

The ATLAS MS (Figure 4.7) is based on four different detection and tracking technologies which collect charge from gas ionized by passing muons:

1. **Resistive Plate Chambers (RPCs):** Designed to detect muons with a space×time resolution of 1 cm × 1 ns. They consist of resistive plates on either side of a 2 mm gap filled with $C_2H_2F_4$ gas which is ionized by passing muons. The initial ionization electrons are multiplied into a detectable avalanche by the large 8900 V potential between the two plates. The resulting charge pulse ($\approx 0.5\,\mathrm{pC}$) is detected by capacitively coupled strips which are placed in orthogonal arrays on either side of the detector. 2D

[4] The CMS (Compact Muon Solenoid) detector uses a single solenoid with return yokes to produce an alternating transverse magnetic field. This design is simpler and allows for a larger magnetic field strength resulting in comparatively compact detector, hence the name.

[5] Trigger coverage for $|\eta| < 2.4$ was found to be sufficient since only one or two of the four muons are needed to trigger the recording of an event.

coordinates can be inferred by assuming coincident signals in the strips oriented along the η and ϕ directions. In total the RPC system has 380,000 readout channels.

2. **Thin Gap Chambers (TPCs):** Also designed for fast time response, a signal from passing muons is detected within 25 ns with 99% efficiency. In particular the TGCs have a low sensitivity to the muon incident angle making them well suited for fast detection in the end-cap disks. The TGCs consist of 2.8 mm gaps filled with CO_2 and n-C_5H_12 which in contrast to the other three systems, is highly flammable in environments with oxygen. Gold plated tungsten anode wires run down the middle of the gaps every 1.8 mm and on either side of the gap there are cathode readout strips routed orthogonally to the anode wires. The readout strips are much wider than the anode wire spacing at 14-50 mm. A 3100 V potential is used to collect drifting electrons with 4 to 20 anode wires grouped together into single trigger readout channels. In total the TGC system has 440,000 readout channels.

3. **Monitored Drift Tubes (MDTs):** Made up of aluminum tubes with a 30 mm diameter with a tungsten rhenium (W-Re) wire down the middle. Lengths vary between 70 cm and 630 cm. The tubes contain a mixture of 91% argon, 5% methane and 4% nitrogen. A bias voltage between the tube walls and the wire of 3300 V is used resulting in a maximum electron drift time of 480 ns. The radial position of hits in individual tubes is measured using the drift time with an 80 μm resolution. In total there are 372,000 MDTs which are read out on individual channels. The MDTs are arranged in panels with two groups of three layers such that passing muons are sampled up to six times. The positions of the panels are monitored with laser systems to ensure good detector alignment even if parts shift over time. The MDTs provide precision measurements in the primary bending direction of the toroid fields. The MDTs cover 5500 m^2.

4. **Cathode Strip Chambers (CSCs):** CSCs are used at high η because they offer low neutron sensitivity and precision for high occupancy events. They consist of a gas chamber supported by a honeycomb structure on top of a layer of anode wires routed orthogonally to cathode strips operated at a bias voltage of 2600 V. Hit times are determined from the charge arrival time at the anode wires while hit position is determined by a segmented cathode readout. The wires are 2.54 mm apart while the cathode strips are spaced at 5.08 mm intervals. Single hit positions can be measured with 60 μm precision by interpolating the charge signal over adjacent wires. The electron drift times are less than 30 ns and the timing resolution is better than 7 ns. The low neutron sensitivity is achieved by using a gas mixture of 30% argon, 50% CO_2 and 20% CF_4 which contains no hydrogen. In total there are 61,440 cathode readout channels.

The RPCs and TPCs are used for the muon trigger system because of their fast response times. They are segmented such that muons above the desired trigger threshold will give coincidence detections within a maximum angular deflection defined by the magnetic field and momentum threshold. Additionally, they provide the muon track coordinate in the ϕ direction while the MDTs and CSCs give coordinates in the r, z plane.

For a detailed description of the MS system, see reference [45].

4.4 Triggering and Online Reconstruction

The ATLAS detector is in principle an 88 megapixel high speed 3D camera where each "image" it takes is only 1.5 megabytes (MB). For comparison, the Hasselblad H6D-100c digital camera takes 100 megapixel images which in their raw format each consume 120 MB of storage space. This difference comes down to sensor occupancy. The Hasselblad image

sensor is typically fully illuminated by the scene being photographed. If instead it was used to photograph the night sky, one could use a threshold to suppress the readout of pixels which were imaging nothing but the vacuum of space. Additionally one could fit a point spread function to the pixels which are above threshold allowing for a more accurate determination of star position than given by the pixel resolution.

The ATLAS detector works in the same way, applying reasonable thresholds to the readout channels to suppress most of the data volume without sacrificing image fidelity. Unfortunately channel thresholding does not reduce the data volume enough to record every image taken by ATLAS due to the enormous frame rate. The ATLAS frame rate is set by the LHC proton bunch spacing of 25 ns corresponding to a bunch crossing rate of 40 MHz. This means the ATLAS output data stream bandwidth is 60 terabytes per second (TB/s). Today's fastest solid state drives (SSDs) are capable of writing about 500 MB/s and can hold 256 gigabytes (GB). It would take 120,000 of these SSDs operating simultaneously to keep up with the ATLAS output and they would all have to be swapped out every 8 minutes. At $100 a piece, this would cost $1B per 12 hour LHC beam fill. With that kind of budget you could buy a new LHC every ten days.

Clearly a more reasonable approach is needed. The vast majority of proton collision events are low energy, uninteresting glancing blows called peripheral scattering events. ATLAS uses a multistage triggering scheme to discard the majority of these events. The goal is to maximize the probability to store events in which the rarest processes occur while still sampling the more common processes. This ensures sufficient but not excessive statistics for the study of a broad range of known and unknown physical interactions.

In the first stage of the ATLAS trigger, specialized hardware systems search for large localized energy deposits in the calorimeters or angular coincidence detections in the muon spectrometer (Section 4.3). These custom hardware triggers are collectively referred to as

the Level 1 trigger (L1). The L1 trigger selects approximately 1 in 400 events; reducing the event rate from 40 MHz to 100kHz. About one third of that rate is used by the muon trigger, another third by the EM calorimeter trigger, and the remaining third by hadronic calorimeter triggers or combined objects like a muon trigger plus an EM calorimeter deposit.

The events which satisfy the L1 trigger are then passed on to the software based High Level Trigger (HLT). The HLT operates on a large computing farm containing more than 20,000 processors. Most of the trigger algorithms operate in a two stage process where a first pass rough reconstruction is performed to eliminate the majority of events before a more complex reconstruction is used. This process is called "online" reconstruction because we only get one chance to do it right. If there is a bug in the algorithm or a system malfunctions, data is lost permanently[6]. This is to be contrasted with "offline" reconstruction which is applied to events in permanent storage and is periodically redone as algorithms are adapted and improved. The HLT is the first stage where information from the ID is incorporated allowing for electron/photon discrimination, jet flavour tagging, track based missing transverse momentum terms, global sequential jet calibration (see Chapter 11.2) and more. Track reconstruction is either done in small Regions of Interest (ROIs) near the corresponding calorimeter activity or globally depending on the needs of the specific trigger type. The HLT selects roughly 1 in 100 events passing the L1 trigger for permanent storage. About 30% of the 1 kHz HLT bandwidth is used for electron and muon triggers, about 20% for hadronic triggers, 15% for missing transverse energy triggers and about 5% each for photon, tau lepton and B-physics triggers.

A disproportionate amount of the HLT compute time is used by the b-jet trigger menu needed for this thesis. This is because b-tagging relies heavily on precise primary vertex finding and track reconstruction which is computationally expensive. A hardware based

[6] This sentence may be considered some light foreshadowing. As a spoiler: Nearly 30% of the data used in this thesis had to be discarded due to a bug in the online reconstruction needed for our final state.

track finder called the Fast TracKer (FTK) is being commissioned now which will lift most of the tracking burden from the HLT farm by finding and computing track parameters for more than 90% of the tracks in every event passing the L1 trigger.

For a detailed description of the ATLAS trigger in Run-2 see References [40, 30].

Chapter 5

MOTIVATION AND PHENOMENOLOGY OF HH PRODUCTION

In this chapter we motivate searches for HH production, describing the relevant experimental signatures, physical models and their consequences and current experimental constraints. In Section 5.1 we summarize the phenomenology of the SM Higgs boson and the current measurements and constraints. Section 5.2 describes the phenomenology of HH production, starting with the SM before moving to BSM models. This chapter ends with Section 5.3 where the most recent experimental limits on HH production are discussed and compared.

5.1 Higgs Boson Phenomenology

The Higgs field interacts at tree level (leading order in perturbation theory) with every massive particle in the SM.[1] At the one loop level (next to leading order in perturbation theory) it interacts with all of the remaining SM degrees of freedom, in this case, photons and gluons, the only massless fields in the SM.[2] The result is an incredibly rich phenomenology, with several production mechanisms and a vast list of possible decay channels. Figure 5.1 shows leading order Feynman diagrams for the dominant Higgs production processes and their SM cross sections at the LHC. Figure 5.2 shows the primary Higgs boson branching ratios as a function of the Higgs boson mass. Note that the observed mass $m_H = 125\,\text{GeV}$ is in a phenomenologically rich region: If the Higgs boson been $\gtrapprox 10\,\text{GeV}$ lighter the bosonic

[1] With the possible exception of the neutrinos.

[2] Again with the exception of the neutrinos, which we know to have mass but may get it from a different mechanism: Neutrinos may get their mass from a dimension 6 operator which is suppressed by a high mass "see-saw" partner thereby explaining the small neutrino masses. The open questions surrounding the neutrino masses may be resolved in the next decade or so by neutrino experiments and searches for neutrinoless double beta decay.

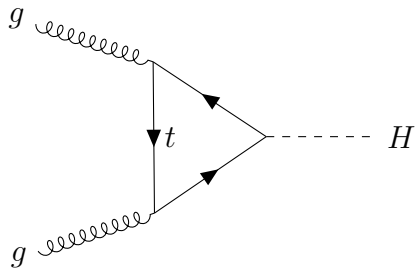

(a) Gluon fusion (ggF): $\sigma = 49\,\text{pb}$

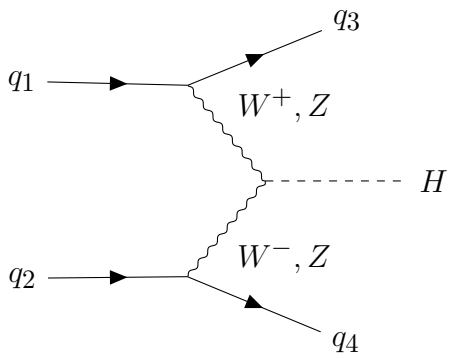

(b) Vector boson fusion (VBF): $\sigma = 3.8\,\text{pb}$

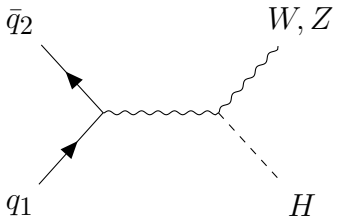

(c) Vector boson associated (VH): $\sigma = 1.4,\ 0.88\,\text{pb}$ for WH and ZH respectively.

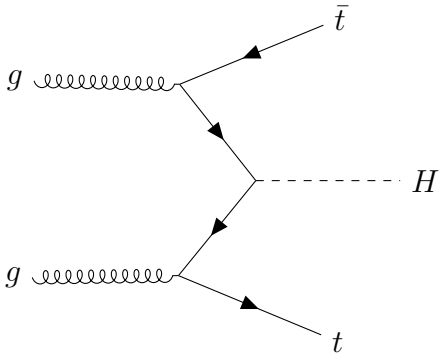

(d) $t\bar{t}$ associated ($t\bar{t}H$): $\sigma = 0.51\,\text{pb}$

Figure 5.1: Higgs production mechanisms and their cross sections for $\sqrt{s} = 13\,\text{TeV}$ and $m_H = 125\,\text{GeV}$. For each diagram incoming particles are on the left and outgoing particles are on the right. Diagrams drawn using TikZ-Feynman [95].

decay channels would have been suppressed while if it had been $\gtrapprox 10\,\text{GeV}$ heavier the fermionic decay channels would have been suppressed.

To date the Higgs Boson has been observed in decays to $\gamma\gamma$ (ATLAS [6], CMS [147]), WW^* (ATLAS [145], CMS [148]), ZZ^* (ATLAS [150], CMS [149])[3], $\tau^+\tau^-$ (ATLAS [78], CMS [163])[4] and most recently $b\bar{b}$ (ATLAS [7], CMS [161]). Each of these final states can be

[3] For the WW^* and ZZ^* decays the * denotes the fact that one of the vector bosons must be virtual or off-shell, because the Higgs mass is less than twice the vector boson mass.

[4] This observation is of historical importance as it represents the first observation of a fundamental interaction which is not mediated by a gauge force like the electroweak or strong forces. In particular the decay

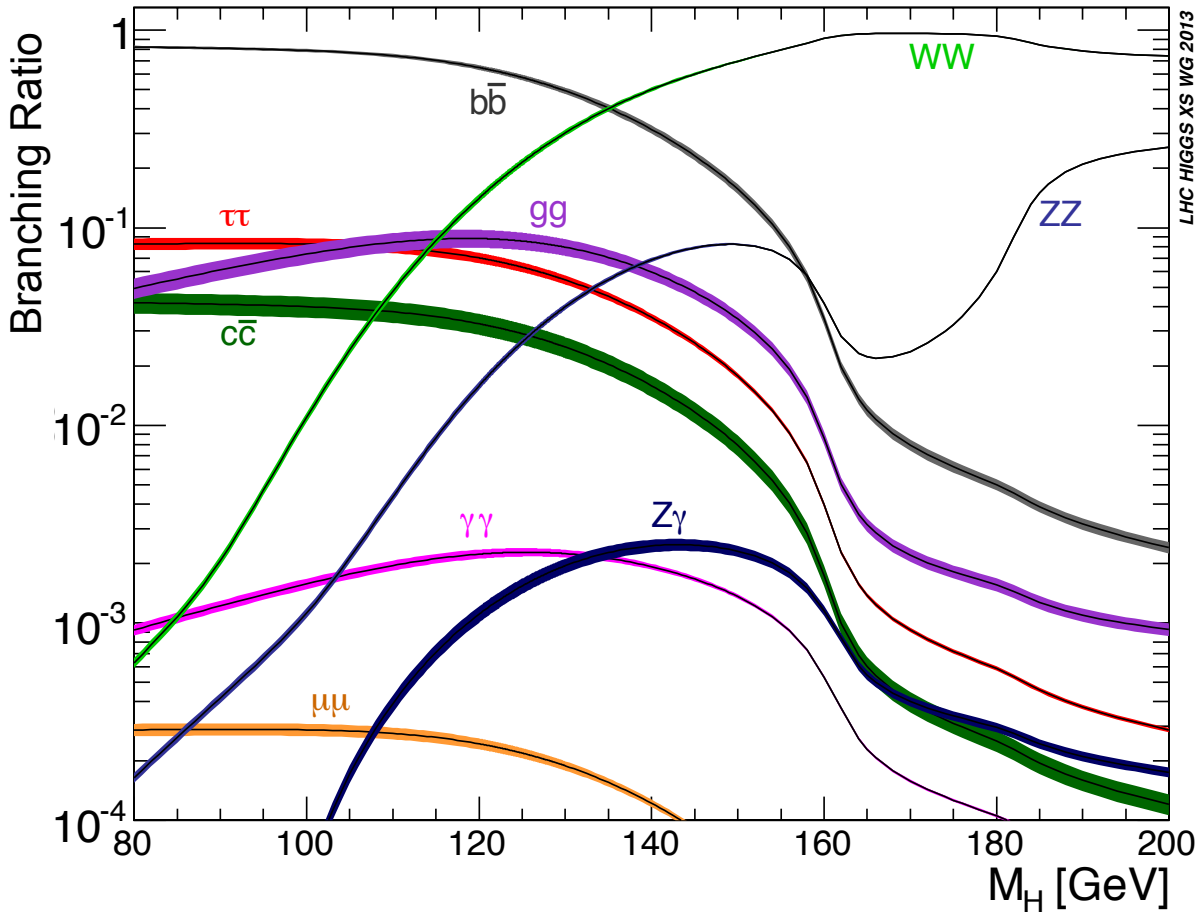

Figure 5.2: Higgs boson branching ratios as a function of its mass [151] where the line width represents the total theoretical uncertainty.

observed with additional objects that would help classify the Higgs production mechanism. For vector boson fusion (VBF) production one or two forward jets are expected from the outgoing quarks shown in Figure 5.1b. For vector boson associated (VH) production 5.1c or top quark associated production ($t\bar{t}H$) 5.1d additional hadronically or leptonically decaying W or Z bosons or top quarks are expected. By designing dedicated selection criteria to produce signal regions enriched in each production process and decay, one can constrain the relative rates of the production mechanisms and compare with the SM expectation as shown in Figure 5.3. So far, all the observed decay rates and production mechanisms are consistent with the SM expectation [73], including the recently observed $t\bar{t}H$ process (ATLAS [8], CMS [160]). This observation is a remarkable technical achievement given the complexity of the final state and the rarity of the process. No single channel was sufficient to claim observation, rather a combination of final states using all of the above Higgs decay channels in addition to the recently observed [7, 161] $H \to b\bar{b}$ decay.

Critically for this thesis, the $t\bar{t}H$, $H \to b\bar{b}$ searches add to the growing body of evidence that the observed 125 GeV scalar boson does indeed decay to bottom quark pairs as expected from the SM Higgs boson.[5] Due to the enormous hadronic backgrounds produced by hadron colliders, it is hopeless to consider observing $H \to b\bar{b}$ at the LHC without additional objects produced in association. The most sensitive searches for this decay channel use the VH production process. Simultaneously, VH, $H \to b\bar{b}$ happens to offer the best sensitivity to the VH production process due to the small cross section $\sigma(pp \to \mathrm{VH})$ combined with the hadronic background suppression from the leptonically decaying vector bosons. Evidence for this process has been found at the 4.8 σ level by CMS [161] and ATLAS recently claimed 4.9 σ evidence for the VH $H \to b\bar{b}$ process alone. Observation of both the VH production process

$H \to \tau^+\tau^-$ is mediated by a Yukawa coupling.

[5] The ATLAS $t\bar{t}H$, $H \to b\bar{b}$ search finds $> 1\sigma$ evidence while the CMS search finds $\approx 2\sigma$ evidence. Additionally CMS performed a dedicated analysis looking for $H \to b\bar{b}$ where the Higgs system has a large transverse Lorentz boost and finds 1.5σ evidence [188]. This search was validated by using the same techniques to observe $Z \to b\bar{b}$ at 5.1σ significance.

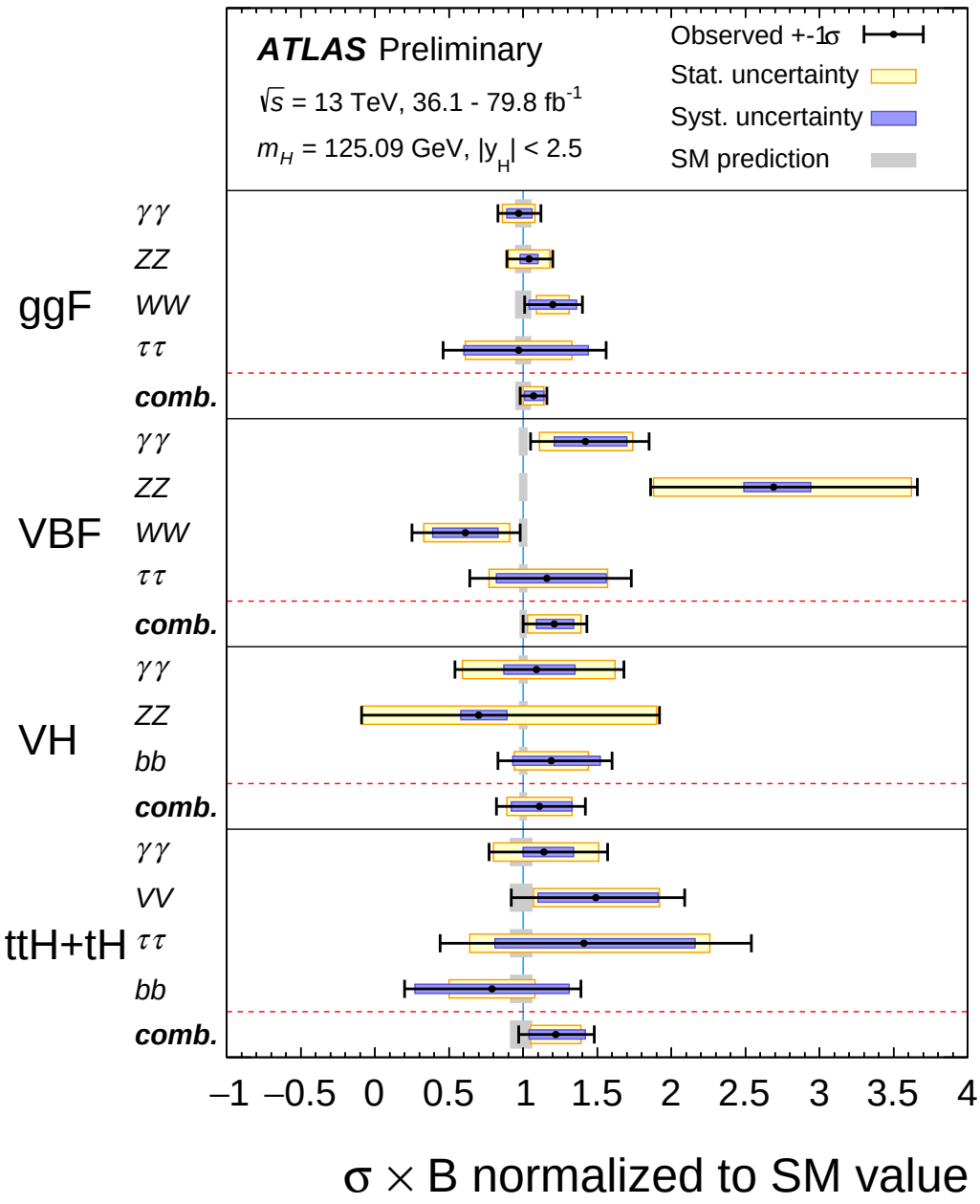

Figure 5.3: The result [73] of a combined fit to data for all available Higgs production and decay modes with m_H fixed to 125.09 GeV. Shown are the cross sections times branching ratios normalized to their SM expectation. This is the first combination plot with $> 5\sigma$ observation of all four primary Higgs production modes.

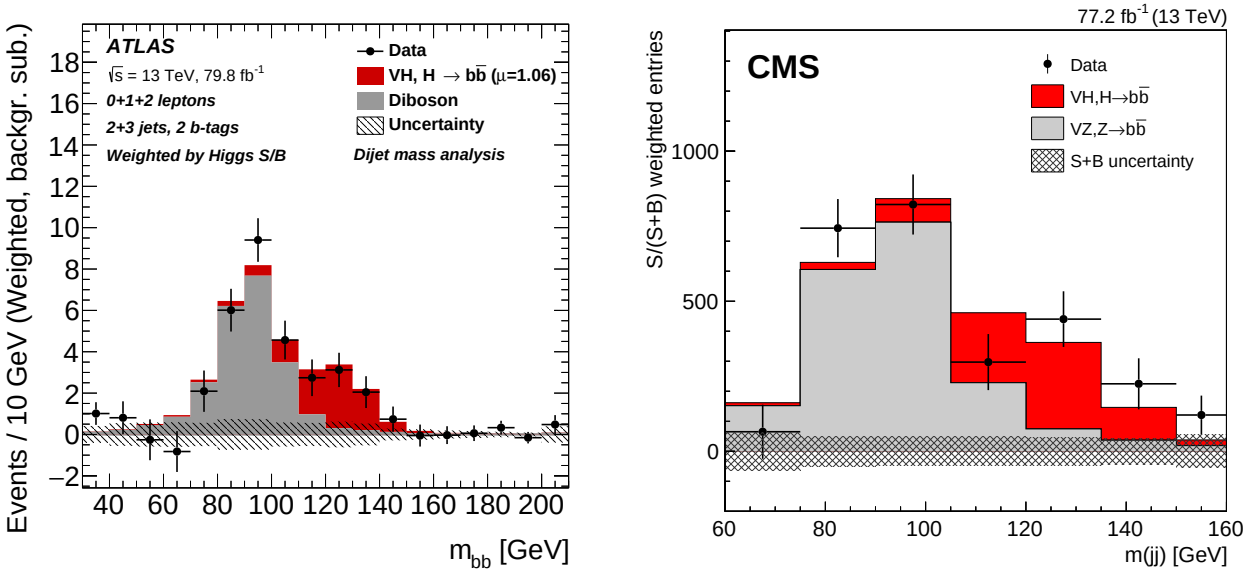

Figure 5.4: Plots from ATLAS [7] (left) and CMS [161] (right) illustrating the significance of the observed bump in the invariant mass spectrum of the Higgs candidate decay products. All the backgrounds have been subtracted except for the diboson background VZ, $Z \to b\bar{b}$. The events are weighted by signal to background (+signal in the CMS plot) ratio using the best fit signal yield. The CMS plot is then normalized to match the total best fit signal yield which is why the y-axis range is larger than for the ATLAS plot.

and $H \to b\bar{b}$ decay at greater than 5σ significance was achieved by combining additional Higgs decays in the VH search and additional Higgs production mechanisms in the $H \to b\bar{b}$ search [7]. Figure 5.4 shows the corresponding excesses after subtracting the expected backgrounds.

5.2 HH Models

Within the SM, HH production proceeds at leading order in perturbation theory via two families of diagrams as shown in Figure 5.5. In both diagrams effective Higgs couplings to gluons are generated by loops of strongly coupled fermions, most importantly the top quark. Figure 5.5a contains four top quark propagators where the two outgoing Higgs bosons come from vertices with the top quark propagators. This component of the amplitude therefore

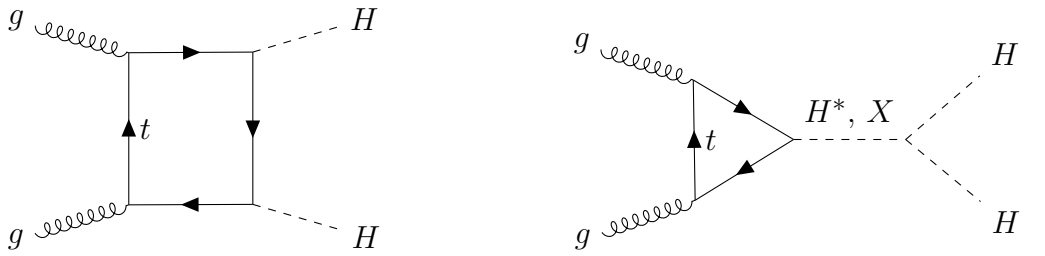

(a) Top quark box

(b) Higgs self coupling or new resonance X

Figure 5.5: ggF HH production leading order diagrams. For each diagram incoming particles are on the left and outgoing particles are on the right. Diagrams drawn using TikZ-Feynman [95].

depends on the top quark Yukawa coupling which is directly constrained by $t\bar{t}H$ production. It is also indirectly constrained by the relative rates of ggF and VBF production and by the decay rate to two photons.

In diagram 5.5b, the outgoing Higgs bosons come from a far off-shell Higgs boson propagator H^* or a new scalar or tensor degree of freedom X. If the propagator is from the SM Higgs field, it must be far off-shell due to the final state invariant mass being at least $2m_H$. The triple Higgs vertex coupling parameter is determined by the cubic component of the Higgs potential in a Taylor expansion about the vacuum expectation value (VEV) which in the SM is the degenerate global minimum of the Mexican hat potential (Chapter 2.6.4).

Each fermion propagator contributes a relative minus sign to the component amplitude of a given Feynman diagram. Because the box diagram has one additional fermion propagator compared to the triangle diagram, the two partially cancel resulting in the minuscule production cross section $\sigma(pp \to HH) \approx 34\,\text{fb}$. The leading order cross section was first computed in 1987 [114] before the top quark and Higgs discoveries. Computing the ggF SM HH production amplitude beyond leading order is challenging, but the task can be simplified by taking the limit $m_t \to \infty$; an approximation known as Higgs Effective Field Theory

or HEFT. Today $\sigma(gg \to HH)$ has been computed to second order (NLO[6]) in QCD using the exact case with a finite top mass [60, 61] and approximate NNLO corrections have been added using HEFT and applying finite top mass corrections [118].

Higgs boson pairs may also be produced via VBF, top or bottom quark associated production, or in vector boson associated production. Dedicated searches taking advantage of the additional final state objects to improve sensitivity are currently under investigation.

5.2.1 The Electroweak Phase Transition and Baryogenesis

Within the SM, the small HH production cross section and m_{HH} spectrum is determined by a delicate cancellation between amplitudes controlled by the Higgs coupling to the top quark and to itself. In the absence of new physics a measurement of the m_{HH} spectrum amounts to a measurement of the shape of the Higgs potential in the vicinity of the VEV at third order. Such a measurement would tell us a great deal about the dynamics of the early universe, specifically the phase transition which occurred when the Higgs VEV became nonzero and the SM particles acquired mass.

All of the quantum field theory calculations discussed thus far have been in the limit of zero temperature. It turns out that in the large ambient temperatures which were found in the early universe and are found today in the brief moments of heavy ion collisions at the LHC, QFT calculations must include thermal fluctuations on top of the usual "vacuum fluctuations". Temperature is related to energy by Boltzmann's constant k_B simply by the statement that for a system in thermodynamic equilibrium at temperature T, each degree

[6] For historical reasons perturbative calculations are labeled by how far removed they are from leading order (LO) by adding a "next to", eg. next to leading order or NLO. This has the unfortunate side effect of producing papers with titles like $\lambda\phi^4$ *Theory I: The Symmetric Phase Beyond NNNNNNNNLO* [187]. Many authors have taken to exponentiating the N which looks nice but can be confusing since leading order is often referred to as first order rather than zeroth order.

of freedom of the system carries an average energy $E = \frac{1}{2}k_B T$.[7] This is known as the equipartition theorem and it is a fundamental result of classical statistical mechanics. In quantum field theory the same principle applies, only now the degrees of freedom are relativistic quantum fields. These thermal fluctuations generate an "effective potential" for the Higgs field which depends on the temperature of the surrounding environment. Importantly, at very high temperatures electroweak symmetry is restored and the Higgs VEV is zero. This implies that there is some critical temperature T_c where the minimum of the Higgs potential becomes degenerate and the VEV moves away from zero. This can happen in two qualitatively different ways:

1. **First Order Phase Transition:** Figure 5.6a. In this case at the critical temperature T_c, there is bump in the potential between the minimum at the origin and the new degenerate minima away from the origin. As the temperature falls, regions of spacetime tunnel to the new ground state creating bubbles of spacetime where the SM fields have mass. This system is out of equilibrium during the phase transition. A "strong" first order phase transition is one where the bump is large relative to T_c.

2. **Second Order Phase Transition:** Figure 5.6b. At $T = T_c$ there is no potential barrier preventing the VEV from smoothly moving away from zero. The vacuum smoothly transitions to the VEV we see today. The system is close to equilibrium during the phase transition.

[7] k_B is typically quoted in units of Joules per degree Kelvin (or Celsius). In these units it is 1.4×10^{-23} J/K. In particle physics we like to define units in the simplest way possible which is to set all arbitrary unit conversion factors to 1, in particular the speed of light (defines conversion between units of distance and time), Plank's constant (defines conversion between units of energy and frequency) and Boltzmann's constant (defines conversion between units of energy and temperature). In these units mass, momentum, frequency, and temperature all have units of energy while distance and time have units of inverse energy. To convert back to more conventional temperature scales it is useful to know k_B in units of electron volts per Kelvin, $k_B \approx 8.6 \times 10^{-5}$ eV/K. Room temperature is therefore about 2 meV. The critical temperature of the electroweak phase transition on the other hand is about 10^{15} on your favorite human temperature scale. What's a few factors of two and absolute shifts of 273.15 between friends?

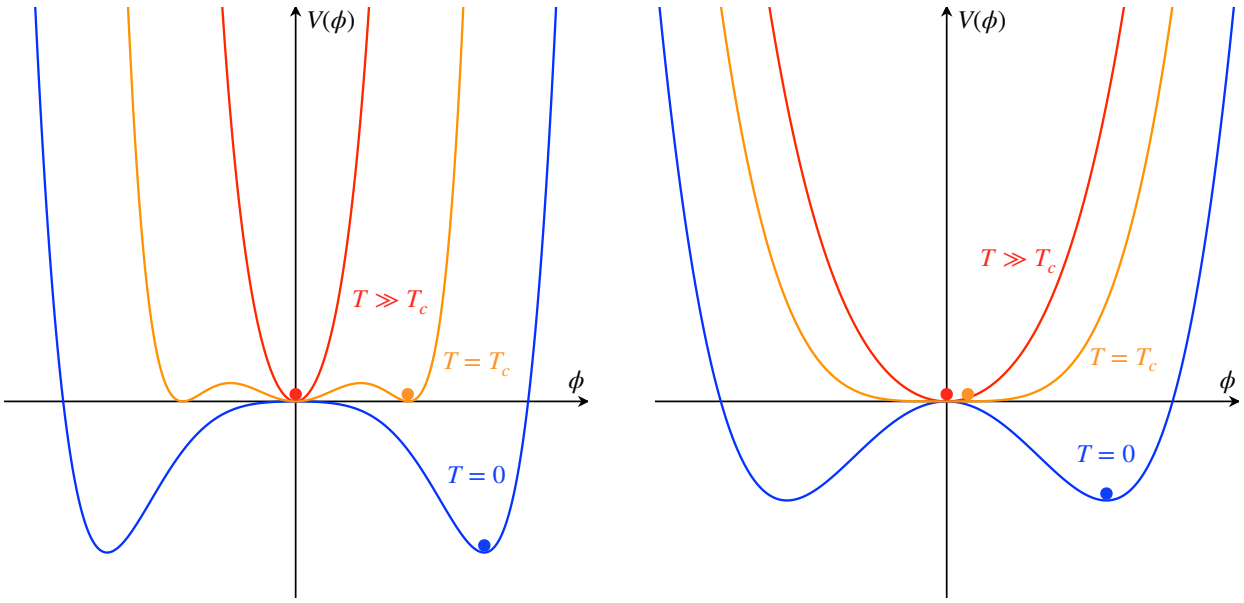

(a) First Order

(b) Second Order

Figure 5.6: Illustration of the Higgs potential $V(\phi)$ as a function of temperature showing the qualitative difference between first and second order phase transitions. The phase transitions begin when the temperature T falls below the critical temperature T_c. Colored dots illustrate the Higgs VEV before (red), during (orange) and after the phase transition (blue).

The critical temperature of the electroweak phase transition is $\mathcal{O}(100\,\text{GeV})$, below which thermal fluctuations of the electroweak fields become suppressed by the spontaneously generated masses. Assuming the SM with the observed Higgs mass, the electroweak phase transition would have been a second order transition and would have occurred approximately $10^{-12}\,\text{s}$ after the big bang [55].

One of the outstanding challenges in fundamental physics is to explain how we ended up in a universe with large amounts of matter, specifically baryons. If the early universe was sufficiently hot to have large thermal fluctuations in all available quantum fields, one would expect all that thermal energy to be nearly perfectly divided between matter, antimatter and radiation as dictated by the equipartition theorem. Then as the universe cooled, the matter and antimatter would clump under the influence of gravity where it would annihilate leaving a universe with very little matter and a lot of radiation.

If the universe did indeed start out in this way, there had to be a mechanism to preferentially produce matter over antimatter as the universe cooled. This process is called baryogenesis and for it to occur, a set of three criteria known as the Sakharov conditions [80] must be met:

1. At least one process must exist which locally generates baryons (or antibaryons). There is a known mechanism for this within the SM which is non-perturbative called the sphaleron process [152].

2. Charge (C) conjugation violation and charge-parity (CP) conjugation violation. There must be processes which are not the same if every particle is swapped with its antiparticle (C) and where both C is applied and the space coordinate reflection operation (parity) is applied whereby $\vec{x} \to -\vec{x}$ (P). The weak interaction in the SM violates C and small amounts of CP violation have been observed in rare hadron decays, though this is insufficient. There is some hope that there is maximal CP violation in the

neutrino sector [72] but this remains to be confirmed.

3. The above interactions must occur far from equilibrium. Thermal processes in equilibrium will wash out any generated excess of baryons. If the electroweak phase transition was strongly first order, it could have generated the necessary out of equilibrium dynamics. Other phase transitions may also have occurred at much higher energy scales which could have frozen in a matter antimatter asymmetry but this regime will not be practical to probe directly at colliders. For a hilarious and eye opening description of what it would take to build a $\sqrt{s} = 10^{15}$ GeV collider I encourage you to read this paper by Francis Bursa [64].

The Sakharov conditions and their viability within the SM are summarized nicely by Dennis Perepelitsa in [168].

For baryogenesis to have occurred during the electroweak phase transition, there must have been a strong first order transition. By inspection of Figure 5.6a, the effective Higgs potential at $T = T_c$ must contain terms up to sixth degree in the scalar field (three zeros of the potential, all with multiplicity ≥ 2). Various models have been proposed to generate a modified Higgs potential at the critical temperature [129, 67, 130] with this property. These modifications would also change the shape of the potential at $T = 0$, resulting in a modified Higgs cubic coupling contributing to diagram 5.5b. Because of the delicate cancellation between this diagram and the top quark box diagram 5.5a, any modification of the Higgs cubic coupling could substantially enhance the HH cross section at the LHC.

Interestingly, the effects of such a modification of the Higgs potential may also be observable by future space based gravitational wave observatories. Depending on the vacuum tunneling rate, the rapidly expanding bubbles of spacetime in the broken phase of the electroweak symmetry may have collided and produced a low frequency stochastic background of gravitational waves. The observation of such a stochastic background would be a direct observation

of gravitational radiation from $\approx 10^{-12}$ s after the big bang! The production and spectrum of these waves is discussed in [200, 137] and their relationship to enhanced HH production is discussed in [130].

5.2.2 Supersymmetry

Higgs boson pairs may also be produced within supersymmetric (SUSY) extensions of the SM. Supersymmetry extends the SM by extending the underlying Poincaré symmetries of spacetime to include additional symmetries which would imply the existence of a large number of new particles. The new symmetries act on the particles of the SM by lowering their spin by 1/2, thus producing fermionic superpartners for bosons and scalar superpartners for fermions. In these models the scalar sector of the SM must also be extended which motivates the phenomenology of two Higgs doublet models (2HDM) which are described further in Section 5.2.3. SUSY extensions of the SM contain Higgsinos, fermionic super partners of the Higgs boson. Higgsinos may be pair produced in LHC collisions and each decay to a Higgs boson and the lightest stable supersymmetric particle (LSP). The LSP would be a natural dark matter candidate. See [143] for more information on these models. A dedicated search for Higgsino pair production has been performed using the same event selection described in this thesis (Chapter 8) together with a selection optimized for events with large missing energy carried by the two LSP produced in the decay [186].

5.2.3 Resonant HH Production

In addition to the potential for non-resonant enhancement of the HH cross section as described in the previous section, there may also be new massive particles which in their decay would resonantly produce two Higgs bosons.

Digression for non-physicists: The terms particle and resonance are often used interchangeably in high energy physics. This conflation of classically unrelated concepts can be visualized nicely through analogy to music: When a violinist draws their bow across a string, the rubbing action of the bow drives the string at a broad range of frequencies. Only the driving frequencies which are near integer multiples of the note being played can transfer energy from the bow to the string. The frequencies which "resonate" are determined by the geometry and material properties of the instrument. If one wishes to learn about the properties of an instrument, one only needs to drive it at a broad range of frequencies and measure the spectrum of the sound that results.

The colliding beams of the LHC apply this principle to produce particles, both known and potentially unknown: The beams are at a fixed energy but the colliding partons may come together at any energy between zero and twice the beam energy. If there is a degree of freedom of nature which is coupled to the partons in the protons, it will "resonate" at a characteristic energy given by its mass. Such a resonance increases the probability of energy transfer from the proton beam to massive quanta of the resonating quantum field. These excitations then decay and the outgoing decay products preserve the mass information of the resonance. Resonances can then be seen as "bumps" in the invariant mass spectrum of a combination of final state objects.

Spin-1 particles (vector bosons) cannot decay to two identical scalars by the Landau-Yang theorem. This can be seen from the fact that rotating the initial spin-1 particle by 180 degrees flips the sign of the angular momentum while the final state of two scalars is identical after the rotation. In terms of Bose statistics this is simply the statement that a spin-1 particle cannot decay to a system with even total angular momentum and a system of two scalars can only have even total angular momentum.

Massive Spin-2 particles (tensor bosons) on the other hand can be in a state with zero

total angular momentum along the decay axis and in this state the angular momentum component of the wave function is even under 180 degree rotations. Massive Spin-0 particles (scalar bosons) trivially respect the conservation of angular momentum in their decay to two scalar bosons. This means any observed resonance decaying to HH must be either a scalar itself or a massive spin-2 particle.

Scalar Models - The canonical models for a new massive scalar decaying to HH are the two Higgs doublet models (2HDM). These models contain additional CP even and odd scalars. In the standard scenario we would find ourselves in the so called "alignment limit" in which one CP even scalar mimics the SM Higgs and is lighter than the other new scalars. In this limit the new heavy scalars decouple from the observed Higgs boson and as such they would not be seen as HH resonances. Small deviations from the alignment limit are still possible given the current precision of Higgs measurements. For a summary of 2HDM models and limits see [133, 125].

Tensor Models - Massive spin-2 bosons arise generally in models with large extra dimensions. We know from observations of gravitational lensing that the graviton responsible for gravity must be exactly massless.[8] In the presence of at least one extra spatial dimension, it is possible to have infinite towers of increasingly massive spin-2 states called Kaluza-Klein modes. For a summary and history of the development of Kaluza-Klein theory see [182]. In 1999, Lisa Randall and Raman Sundrum proposed a way to generate a large separation of scales between the Plank mass and the Higgs mass in two models with extra dimensions

[8] The number of degrees of freedom of a boson with spin changes discontinuously when the mass is increased from zero. Identically massless particles cannot have longitudinal spin polarizations because they must always travel at exactly the speed of light The amount of gravitational lensing generated by massless gravitons is 25% less than that generated by massive gravitons because of the different physical degrees of freedom, no matter how small the mass. The only known mechanism to avoid this constraint, the Vainshtein mechanism was recently shown to be mathematically inconsistent on scales less than $\approx 10^6$ km [54]. That said, there are also direct upper limits on the graviton mass, most recently from the combined observation of a neutron star merger via its gravitational wave radiation and electromagnetic radiation. The relative arrival time of these signals requires the graviton mass to be less than 10^{-22} eV [196].

and that those extra dimensions did not need to be compact to replicate Newtonian gravity in three spatial dimensions [177, 176]. These Randall-Sundrum (RS) models also produce Kaluza-Klein modes of the graviton. For a summary of how these massive gravitons could be produced and how they can decay to HH see [102].

5.3 Current Limits on HH Production

Single Higgs production has a rich phenomenology due to the large number of accessible final states. In principle, double Higgs or "diHiggs" production squares this number of final states, but without significant cross section enhancement from beyond the SM (BSM) physics the majority of these final states will be inaccessible at the LHC. Three final states have been shown to have comparable sensitivity to both SM HH and BSM HH production, all of which capitalize on the large SM Higgs branching ratio to bottom quarks:

1. $\text{BR}(HH \to b\bar{b}\gamma\gamma) = 2 \times 0.58 \times 0.0023 = 0.0027$
2. $\text{BR}(HH \to b\bar{b}\tau^+\tau^-) = 2 \times 0.58 \times 0.063 = 0.073$
3. $\text{BR}(HH \to b\bar{b}b\bar{b}) = 0.58^2 = 0.34$

Searches using the $b\bar{b}\gamma\gamma$ final state have by far the smallest and simplest SM backgrounds but the tiny 0.27% signal branching ratio severely limits the sensitivity.

Searches in the other two channels must contend with inferior mass resolution and substantially larger backgrounds which are more challenging to model. The $b\bar{b}\tau^+\tau^-$ final state contains the same objects as leptonically decaying $t\bar{t}$ pairs requiring the exploitation of kinematic differences to cut back the $t\bar{t}$ background. Additionally, one must consider how the tau leptons decay: Hadronic tau decays only produce one neutrino but are more challenging

to distinguish from jets produced by quarks or gluons. Leptonic tau decays produce two neutrinos resulting in more unmeasured energy giving worse mass resolution, but they also produce electrons or muons which can be used to trigger the storage of an event (Chapter 8.5).

The $b\bar{b}b\bar{b}$ final state captures the plurality of the HH signal with more than a third of the events. Unfortunately, the total cross section $\sigma(pp \to b\bar{b}b\bar{b})$ is at least three orders of magnitude larger than $\sigma(pp \to HH \to b\bar{b}b\bar{b})$. Theoretical predictions for two to four scattering in QCD are extremely challenging and there are currently no reliable simulated samples of this process. This forces searches in the $b\bar{b}b\bar{b}$ final state to use "data driven" background techniques whereby a background model is generated directly from recorded data.

Searches with both the $b\bar{b}b\bar{b}$ and $b\bar{b}\tau^+\tau^-$ final states will soon be able to use the significantly larger SM ZZ production cross section to directly validate the analysis procedures and constrain systematic uncertainties (See Chapter 15 for a more detailed discussion). The Z boson similarly provided a standard candle signal for the VH, $H \to b\bar{b}$ searches where the analysis was validated by first observing the more common VZ, $Z \to b\bar{b}$ process [161, 159].

Each of these three final states offer their own advantages and disadvantages making them difficult to compare directly. As a rough benchmark, we consider the achieved sensitivities to the predicted SM HH process. Table 5.1 lists the six most recent HH search results, ordered by their expected 95% CL limit on the signal strength μ.[9] As a spoiler, this thesis (and corresponding paper [35]) and the recent ATLAS $b\bar{b}\tau^+\tau^-$ [4] search offer the strongest observed limits on μ, followed closely by the recent CMS search using the $b\bar{b}\gamma\gamma$ final state [190] which benefited from a larger dataset.

[9] This is a somewhat unphysical benchmark since a BSM modification to $\sigma(pp \to HH)$ would be unlikely to simply scale up the SM HH differential cross section, but would be expected to alter the kinematics in some way.

Channel	Result	Luminosity	μ Obs. (Exp.) Limit
$b\bar{b}\tau^+\tau^-$	ATLAS [4]	$36.1\,\text{fb}^{-1}$	13 (15)
$b\bar{b}\gamma\gamma$	CMS [190]	$35.9\,\text{fb}^{-1}$	24 (19)
$b\bar{b}b\bar{b}$	ATLAS: **This Thesis** and [35]	$27.5\,\text{fb}^{-1}$	13 (21)
$b\bar{b}\tau^+\tau^-$	CMS [189]	$35.9\,\text{fb}^{-1}$	30 (25)
$b\bar{b}\gamma\gamma$	ATLAS [9]	$36.1\,\text{fb}^{-1}$	22 (28)
$b\bar{b}b\bar{b}$	CMS [185]	$35.9\,\text{fb}^{-1}$	74 (37)

Table 5.1: The five most recent results in the search of HH production ordered by their expected limit on the signal strength μ of the SM HH process. For a deeper discussion and comparison of these results see Chapter 15. In particular, we believe the substantially weaker limit from the CMS $b\bar{b}b\bar{b}$ result is a consequence of the low statistical power of their background modeling technique, lower trigger efficiency and larger combinatoric background from their Higgs candidate construction algorithm (see Chapter 8.1).

In searches for resonant HH production, the signal cross section generally falls off steeply as a function of the mass of the hypothesized new particle. Near the kinematic threshold of $2m_H = 250\,\text{GeV}$, all three of these final states offer similar sensitivity with the strongest limits coming from $b\bar{b}\gamma\gamma$. Above about 1 TeV the $b\bar{b}b\bar{b}$ final state dominates the sensitivity as the $b\bar{b}\gamma\gamma$ and $b\bar{b}\tau^+\tau^-$ statistics run out. As a rough benchmark of sensitivity as a function of the diHiggs mass m_{HH}, one can consider the sensitivity to a narrow width scalar resonance decaying to HH. The expected limits on narrow width scalar resonances for four of the most recent results are shown in Figure 5.7.

There are also various searches which do not rely on $H \to b\bar{b}$ but they tend to be an order of magnitude less sensitive. CMS has public results [191] using the $b\bar{b}\text{VV}^* \to \text{bb}\bar{\ell}\nu\ell\nu$ channel where VV^* are WW^* or ZZ^* and ATLAS has a public result [71] using the $WW^*\gamma\gamma \to \ell\nu jj\gamma\gamma$ decay channel and many more final states are under study.

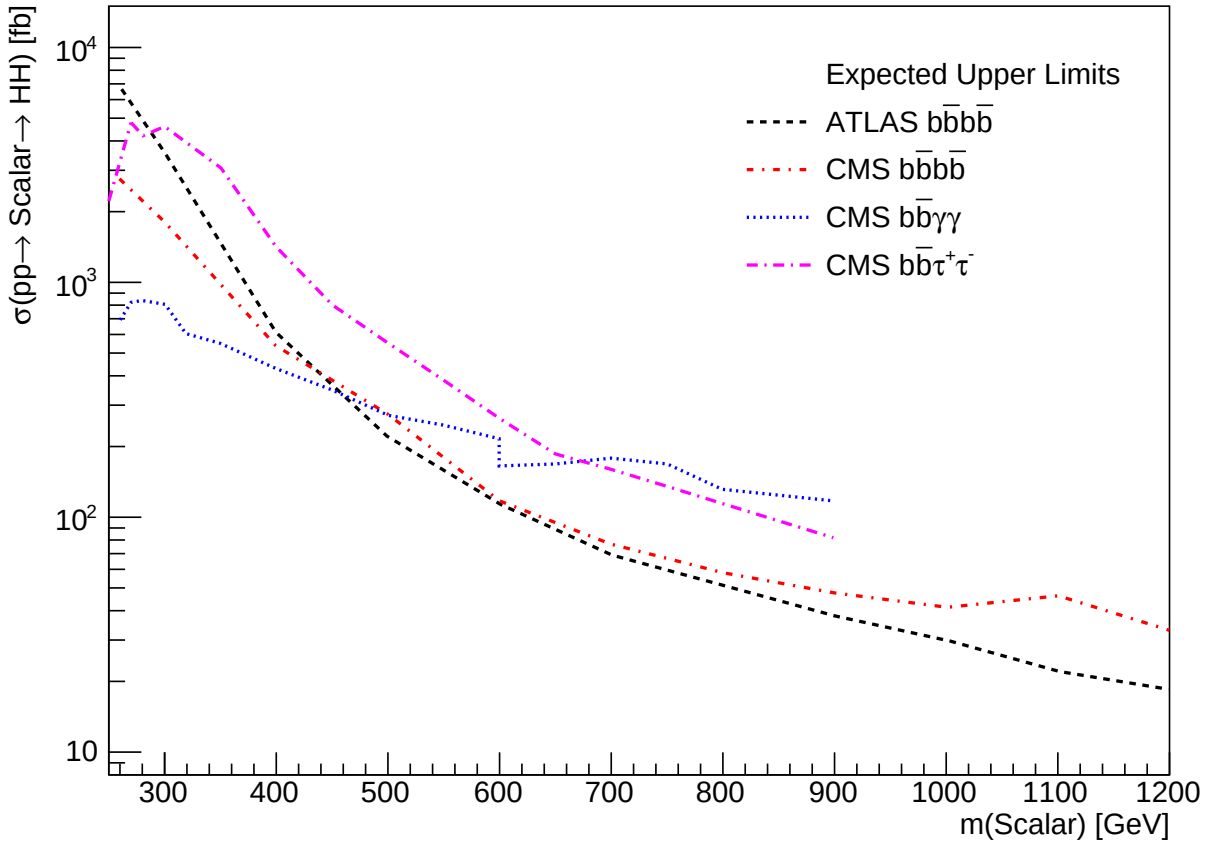

Figure 5.7: A comparison of expected limits on the cross section $\sigma(pp \to \text{Scalar} \to \text{HH})$ for narrow width scalar resonances as a function of the resonance mass assuming the SM Higgs branching ratios. The limits are taken from this thesis (see Chapter 14) and from [192] (CMS $b\bar{b}b\bar{b}$), [190] (CMS $b\bar{b}\gamma\gamma$) and [189] (CMS $b\bar{b}\tau^+\tau^-$). In combination with the ATLAS boosted HH selection (see Chapter 8.7 and [35]) the ATLAS limit shown here extends out to 3 TeV. At these masses no other final states offer competitive sensitivity.

Chapter 6

DATA AND SIMULATION SAMPLES

The results presented in this thesis use $3.2\,\text{fb}^{-1}$ and $24.3\,\text{fb}^{-1}$ datasets recorded in 2015 and 2016 collected at $\sqrt{s} = 13\,\text{TeV}$ by the ATLAS experiment [38]. The high level triggers used to select events differ significantly between the 2015 and 2016 datasets as the online b-tagging moved from using the IP3D+SV1 b-tagging algorithm in 2015 to using the MV2c20 b-tagging algorithm in 2016. These triggers are explained in detail in Chapter 9.

To account for the different triggers the background and signal trigger efficiencies are modeled separately in the two datasets and the results are combined statistically. A bug in the 2016 b-jet trigger menu resulted in the loss of $12\,\text{fb}^{-1}$ which is why this analysis does not have the full 36fb^{-1}used in the analysis of the boosted topology as described in [197]. This is discussed further in Section 9.

The majority of this thesis will be presented using the the 2016 dataset. Particular differences between 2015 and 2016 datasets will be highlighted in the main body of the text. The full suite of distributions for the 2015 dataset is provided in Appendices.

6.1 Simulated Signal and Background Samples

All the simulated samples used in this analysis are produced using the full detector simulation, with additional pile-up interactions in each simulated event modeled by adding multiple soft pp collisions generated by Pythia 8.165 [193] with the MSTW2008 LO PDF and AU2 tune [36]. After event generation and the addition of pile-up, the response of particles passing through the detector elements is simulated with the GEANT4 toolkit [12, 39] and events are reconstructed using the same software used to reconstruct events in data.

6.1.1 Signal Sample Production

A SM HH sample has been generated using aMC@NLO. These $gg \to HH \to b\bar{b}b\bar{b}$ events are generated at NLO, using the exact form factors for the top loop corrected to NLO, in the heavy top mass limit, taken from HPAIR [84, 171].

The gluon-fusion production cross-section used is evaluated at NNLO+NNLL in QCD [140]: $\sigma(pp \to HH \to b\bar{b}b\bar{b}) = 11.3 \pm 1.0\,\text{fb}$, where the uncertainty includes the effects of uncertainties in the renormalization and factorization scale, PDFs, α_S, effects of finite top-quark mass in loops and $Br\left(H \to b\bar{b}\right)$.

Two benchmark resonant signal models are considered: a spin-2 graviton within a Bulk Randall-Sundrum Kaluza-Klein model and a narrow spin-0 resonance. The Bulk RS KK graviton signal samples have been generated for 20 mass points from 300 to 3000 GeV using the MADGRAPH generator[126] with the NNPDF2.3 LO PDF [51] and the A14 tune [21], and hadronic showers are produced in PYTHIA 8. For all signal samples, the Higgs mass has been set to 125.0 GeV. Concerning the level of freedom in his model, Kaustubh Agashe [11] suggested that the graviton coupling $k/\overline{M}_{\text{Pl}}$ cannot be increased much beyond two.

The heavy scalar samples have been generated for the same 20 mass points from 300 to 3000 GeV using the MADGRAPH generator[126] with the CT10 PDF set. Hadronic showers are produced in HERWIG++ using CTEQ6L1 and the UEEE5 event tune. For all signal samples, the Higgs mass has been set to 125.0 GeV. The width of the heavy scalar, Γ_X, has been set to 1 GeV.

6.1.2 Background simulation

The dominant multijet background (∼90% of total) is estimated using data. A PYTHIA [193] dijet sample was used to understand the physical processes contributing to this background and characteristics of the event selection. The usefulness of this background sample is limited by the generated number of events, given the high background rejection factors of the analysis selection.

The second largest background, but with a much smaller contribution, arises from $t\bar{t}$. The $t\bar{t}$ background is modeled using large hadronic and semi-leptonic (including fully leptonic) decay mode samples that have both been generated with POWHEG [105] and showered with PYTHIA [193]. The top mass in both samples is set to 172.5 GeV. The $t\bar{t}$ samples are initially normalized to the NNLO+NLL predicted inclusive $t\bar{t}$ cross-section of 1821.87 pb multiplied by the all-hadronic branching ratio of 0.457 and semi-leptonic branching ratio of 0.543 as appropriate [2]. Scale factors are obtained from a combined fit to control regions in data as described in Chapter 10.2.

Chapter 7

OBJECT DEFINITIONS

This analysis uses the anti-k_t jet clustering algorithm [66] with distance parameter $R = 0.4$ to reconstruct Higgs boson candidates. These jets are formed from topological clusters of energy reconstructed in the calorimeter. The topological clusters are calibrated at the electromagnetic scale [24] and formed into jets. These jets are then calibrated as described in [25] with systematic uncertainties described in Chapter 11.2. Jets from pile-up interactions are rejected by the JVT algorithm [37] – which uses the fraction of tracks in a jet that point to the primary vertex as the primary discriminant – using the default recommended working point, resulting in a 92% efficiency for hard-scatter jets and 2.0% fake rate (measured in $Z \to \mu\mu + j$ events).

Jets containing b-hadrons are identified using the MV2c10 algorithm [23]. A 70% efficient b-tagging working point is used, which is a requirement that the MV2c10 value is greater than 0.8244. The number XX after c in MV2cXX specifies charm quark initiated jet ($c-$jet) percentage of the background training sample.

Muons are reconstructed by combining measurements from the inner tracking and muon spectrometer systems, and are required to satisfy medium muon identification quality criteria [26]. These are used to correct the jet four-momenta for the energy lost in semi-leptonic b-decay. If a muon with $p_{\mathrm{T}} > 4\,\mathrm{GeV}$ and $|\eta| < 2.5$ can be ΔR-matched to a b-tagged jet with the requirement that $\Delta R < 0.4$, then the four-momentum of the muon is added to that of the jet. The jet four-momenta is corrected for the expected energy deposited by the muon in the calorimeter. It should be noted that these muons are only used to correct the jet energy after b-tagging has been performed, and are not used for b-hadron identification.

Chapter 8

EVENT SELECTION

In this chapter we describe the proton collision event selection process. The fraction of HH signal events which pass all event selection criteria can be expressed as the product of two other fractions – "acceptance" and "efficiency". Acceptance refers to the fraction of events where the *true* particle trajectories and energies would pass the selection criteria. The efficiency is the fraction of accepted events whose *reconstructed* particle properties pass the selection criteria. Signal acceptance is generally limited by detector angular coverage and trigger thresholds while efficiency is limited by the dynamics of particle-detector interactions, measurement precision and reconstruction algorithms. For this search, the signal acceptance is limited by the angular coverage of the tracker which is needed for b-tagging and the trigger momentum thresholds. The efficiency is limited by our ability to tag b-jets and reconstruct their four-vectors precisely.

The combined acceptance times efficiency is summarized in Figure 8.1 for the graviton, narrow width scalar, and SM HH signal models.

8.1 Combinatoric Background

The selection begins with the requirement that the event contains at least four b-tagged anti-k_t $R = 0.4$ jets with $p_{\mathrm{T}} > 40\,\mathrm{GeV}$ and $|\eta| < 2.5$. The four jets with the highest b-tagging score are paired to construct two Higgs boson candidates.

There are three possible ways to pair these four jets into Higgs candidates. Signal events are expected to have at least one pairing which produces two dijets with invariant masses near the Higgs mass. Background events meanwhile have three opportunities to emulate

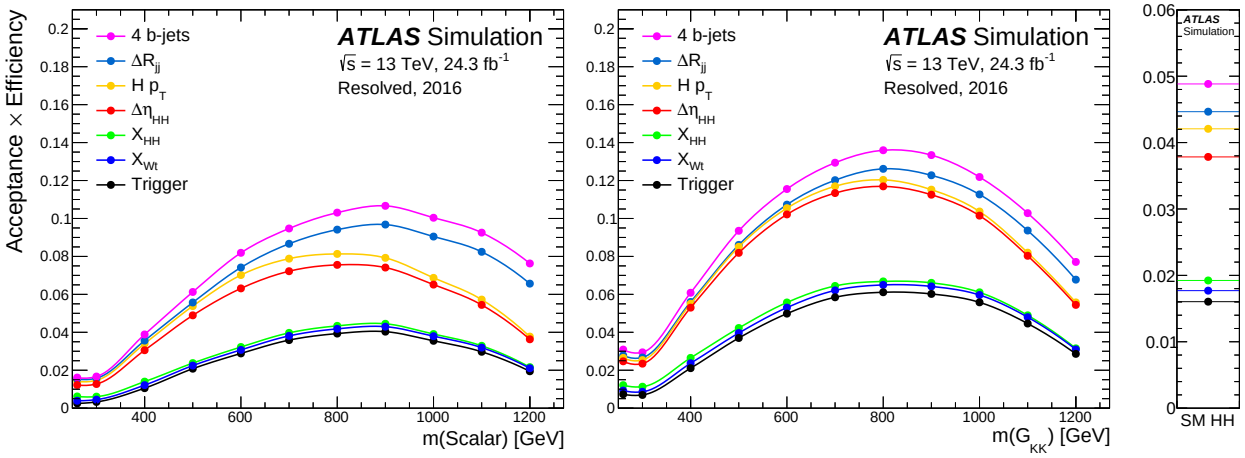

(a) Absolute Acceptance

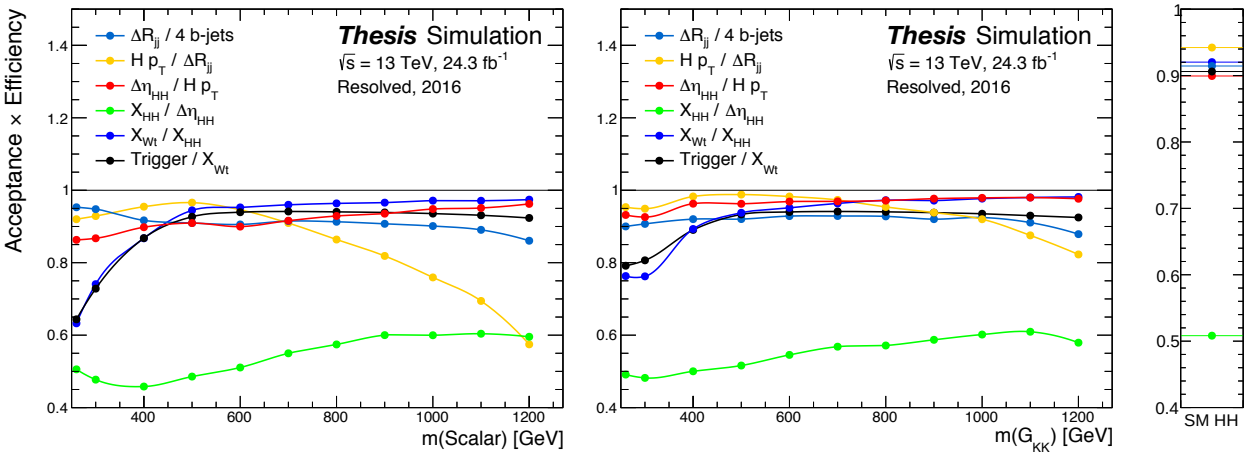

(b) Relative Acceptance

Figure 8.1: The signal acceptance at each stage of the event selection for narrow width scalar and graviton ($k/\overline{M}_{\mathrm{Pl}} = 1$) samples with a range of resonance masses and for the SM HH sample. The acceptance is higher for the graviton samples because spin-2 resonances decay more centrally than isotropic scalar resonances resulting in higher p_{T} jets for a given resonance mass.

the kinematics of a true Higgs pair decay. This ambiguity is referred to as "combinatoric background" because choosing the wrong pairing can reduce signal efficiency while amplifying the background.

One might hope to use the fact that Higgs bosons are neutral to reduce this combinatoric background. In principle the charge of the parton which initiates the jet may be estimated from the reconstructed charges of the tracks within the jet. Only pairings where the total charge of both dijets is zero need be considered. The charge identification of jets initiated by b-hadrons may be improved in semileptonic decays by using the charge of the muon track associated to the secondary vertex (or the tertiary vertex from semileptonic charm decays). We studied the feasibility of using the Jet Vertex Charge (JVC) [157] discriminant to reduce the combinatoric background but found poor discrimination power.

The combinatoric background can be substantially reduced by exploiting the angular correlations of jets in signal events. The angle between the decay products of the Higgs boson in the lab frame is dependent on the Lorentz boost of the Higgs boson and thus the invariant mass of the four-jet system, $m_{4\mathrm{j}}$. High mass resonances would generally produce Higgs bosons with sufficient boost to ensure their respective decay products are nearby in η and ϕ. Resonance masses close to $2 \times m_h$ produce Higgs bosons at rest in the lab frame and the Higgs decay products will be nearly back to back. Accordingly, only those jet pairings which

satisfy the following requirements are considered:

$$\left.\begin{array}{rl} \dfrac{360}{m_{4j}} - 0.5 < \Delta R_{jj}^{\text{lead}} < \dfrac{653}{m_{4j}} + 0.475 \\ \dfrac{235}{m_{4j}} < \Delta R_{jj}^{\text{subl}} < \dfrac{875}{m_{4j}} + 0.35 \end{array}\right\} \text{if } m_{4j} < 1250\,\text{GeV}$$
$$\left.\begin{array}{rl} 0 < \Delta R_{jj}^{\text{lead}} < 1 \\ 0 < \Delta R_{jj}^{\text{subl}} < 1 \end{array}\right\} \text{if } m_{4j} > 1250\,\text{GeV} \tag{8.1}$$

In these expressions, $\Delta R_{jj}^{\text{lead}}$ is the angular distance between jets in the leading Higgs boson candidate and $\Delta R_{jj}^{\text{subl}}$ for the sub-leading candidate. The leading Higgs boson candidate is defined to be the candidate with the highest scalar sum of jet p_{T}. Figure 8.1 shows the efficiency after requiring events to contain two Higgs boson candidates satisfying these criteria as the curve labeled "ΔR_{jj}". Most of the efficiency loss shown is the rejection of events where one of the b-tagged jets did not come from a Higgs boson decay. Figure 8.2 illustrates these ΔR_{jj} windows as a function of m_{4j} and shows that very few signal events passing the full selection are close to failing these criteria. Figure 8.3 plots the reduction in the combinatoric background resulting from the ΔR_{jj} requirements; very few signal events with $m_{4j} > 400\,\text{GeV}$ have more than one viable set of Higgs candidates.

In events with $m_{4j} < 400\,\text{GeV}$, there are likely to be multiple Higgs bosons candidates satisfying these requirements as shown in Figure 8.3, necessitating an algorithm to choose a jet pairing. The natural jet pairing for signal events is the one which gives two Higgs candidates closest to the Higgs mass. This choice maximizes both the signal and background efficiency by selecting the most likely to be in the Signal Region and is not found to give optimal sensitivity. The combinatoric background can be further reduced while keeping excellent signal efficiency by instead choosing the jet pairing which minimises the mass

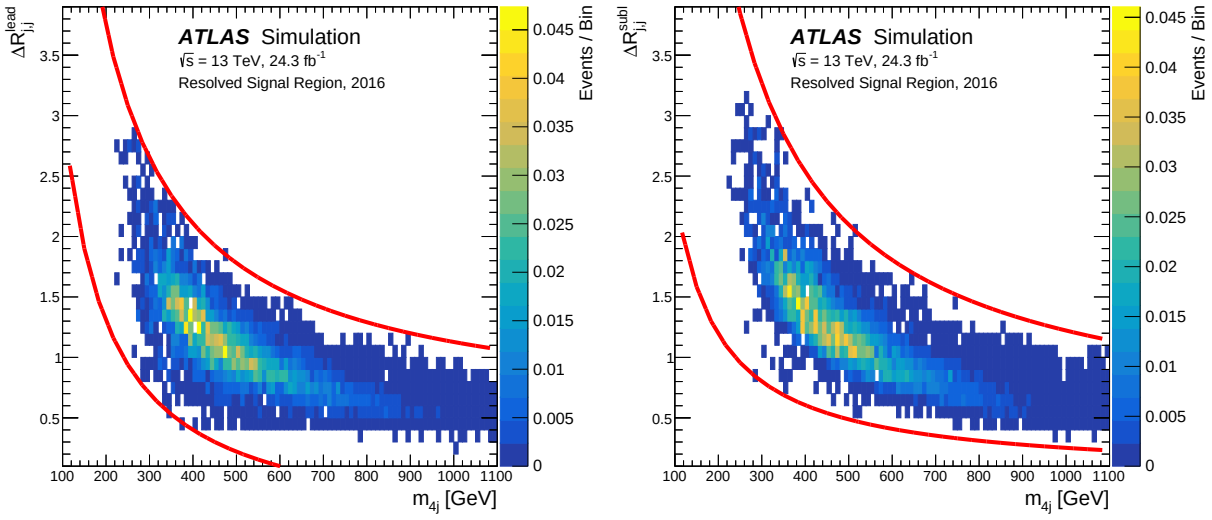

(a) SM HH

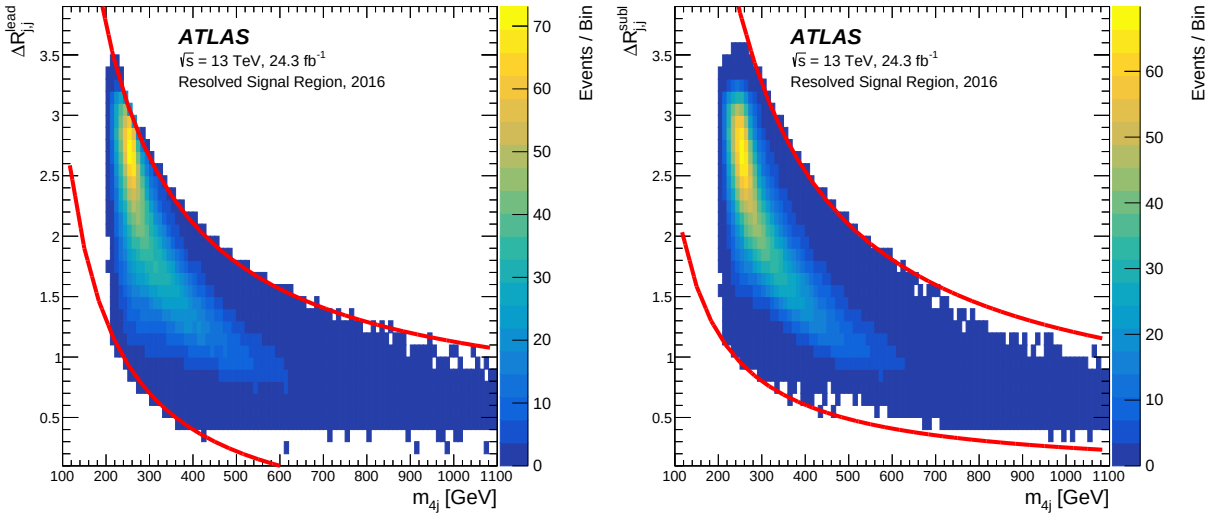

(b) Multijet Background

Figure 8.2: Plots illustrating the $m_{4\mathrm{j}}$ dependent Higgs candidate ΔR_{jj} requirements in the Signal Region after full selection. The plots show the $\Delta R_{\mathrm{jj}}^{\mathrm{lead}}$ and $\Delta R_{\mathrm{jj}}^{\mathrm{subl}}$ spectra of the selected Higgs candidates as a function of $m_{4\mathrm{j}}$. The spectra are constrained between the red lines which are the upper and lower bounds of the allowed ΔR_{jj} for Higgs candidate jet pairings. These requirements reduce the combinatoric background by reducing the number of considered jet pairings as shown in Figure 8.3.

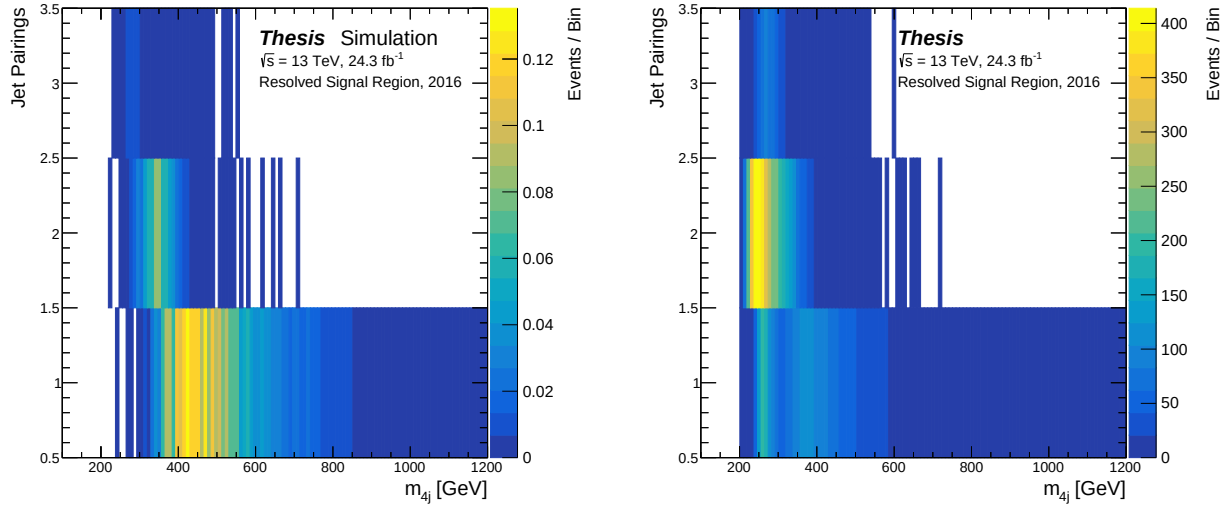

(a) SM HH

(b) Multijet Background

Figure 8.3: The number of Higgs candidate jet pairings per event which pass the $m_{4\mathrm{j}}$ dependent ΔR_{jj} requirements in the Signal Region after the full selection is applied. Without any ΔR_{jj} requirements there would be three different Higgs Candidate jet pairings for every event which would be the largest possible combinatoric background when using four jets for Higgs candidate construction. For signal events this combinatoric background can result in incorrectly constructing the true Higgs dijet system. For background events, a larger combinatoric background results in more background entering the Signal Region due to the D_{HH} minimization procedure 8.2.

difference between the two Higgs candidates. Due to semileptonic b-hadron decays where neutrinos carry away momentum and jet energy mismeasurements, we expect the subleading Higgs candidate to be biased to lower masses. To account for energy loss, the choice is modified to the pairing that minimizes the distance, D_{HH}, from a line connecting (0 GeV, 0 GeV) and (120 GeV, 110 GeV):

$$D_{HH} = \frac{\left| m_{2\mathrm{j}}^{\mathrm{lead}} - \frac{120}{110} m_{2\mathrm{j}}^{\mathrm{subl}} \right|}{\sqrt{1 + \left(\frac{120}{110}\right)^2}} \tag{8.2}$$

where $m_{2\mathrm{j}}^{\mathrm{lead}}$ is the mass of the leading Higgs boson candidate and $m_{2\mathrm{j}}^{\mathrm{subl}}$ the mass of the sub-leading candidate (see Figure 8.4). The values of 120 GeV and 110 GeV are the center of the Signal Region in $m_{2\mathrm{j}}^{\mathrm{lead}}$ and $m_{2\mathrm{j}}^{\mathrm{subl}}$ respectively. The dominant background process is two-to-two gluon scattering where each outgoing gluon propagator splits into $b\bar{b}$ pairs. Due to the large b quark mass, these outgoing gluon propagators are far off shell; this process is expected to produce low mass $b\bar{b}$ dijets. Minimizing D_{HH} for this process should then produce a peak in the two dimensional Higgs candidate mass plane as close to the origin as is kinematically possible given phase space requirements on p_{T} and ΔR_{jj}. This can be seen in Figure 8.7b at (70 GeV, 66 GeV). By picking the jet pairing which minimizes D_{HH}, we have the best of both worlds: Signal events should fall near the Signal Region while the dominant background process is pushed out of the Signal Region towards the origin of the mass plane.

8.2 Mass Dependent Selection

This search is sensitive to resonances with a wide range of masses, 260 GeV $< m <$ 1500 GeV, as well as non-resonant signals. Event selection criteria that vary as a function of the recon-

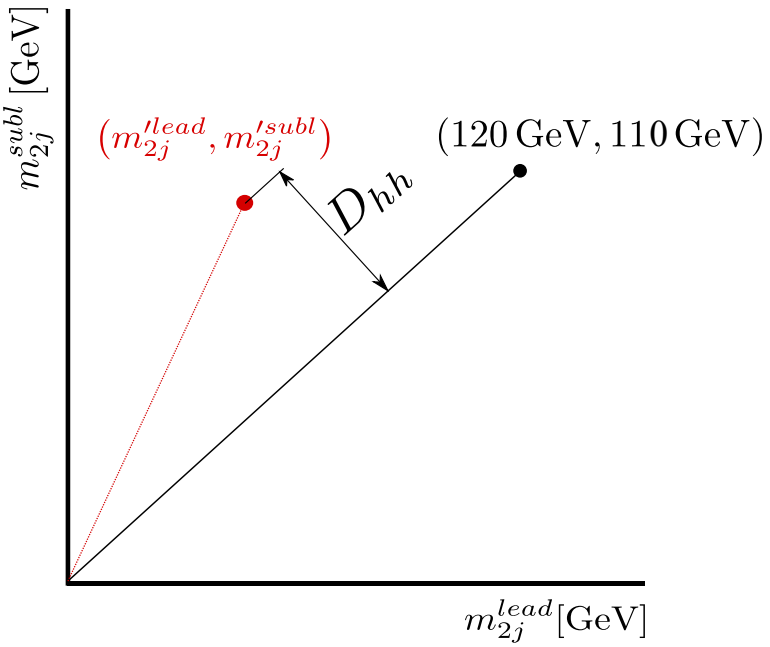

Figure 8.4: D_{HH} is used to choose the best pairing of jets into Higgs boson candidates in the resolved analysis. It is the distance of the pairing's $\left(m_{\mathrm{2j}}^{\mathrm{lead}}, m_{\mathrm{2j}}^{\mathrm{subl}}\right)$ from the line connecting $(0\,\mathrm{GeV}, 0\,\mathrm{GeV})$ and the center of the signal region, $(120\,\mathrm{GeV}, 110\,\mathrm{GeV})$.

structed resonance mass are used to enhance the analysis sensitivity across this range. For a fixed value of $m_{4\mathrm{j}}$, the dominant multijet background peaks in the forward regions of the detector because that minimizes the parton momentum exchange in the collision. This motivates Higgs candidate transverse momenta and pseudorapidity cuts. Mass dependent cuts are applied to the leading and subleading Higgs candidate p_{T}'s ($p_{\mathrm{T}}^{\mathrm{lead}}$ and $p_{\mathrm{T}}^{\mathrm{subl}}$ respectively):

$$\begin{aligned} p_{\mathrm{T}}^{\mathrm{lead}} &> m_{4\mathrm{j}} \times 0.51 - 103\,\mathrm{GeV} \\ p_{\mathrm{T}}^{\mathrm{subl}} &> m_{4\mathrm{j}} \times 0.33 - 73\,\mathrm{GeV} \end{aligned} \tag{8.3}$$

For these cuts the Higgs boson candidates are sorted by the vector sum of the jet p_{T}. These cuts are illustrated in Figure 8.5. The multijet background is further suppressed by a flat cut on the pseudorapidity difference between Higgs candidates, $|\Delta\eta_{HH}| < 1.5$. These cuts are chosen fairly loose in a compromise to balance model independence with signal sensitivity. The cuts give near optimal sensitivity for both the scalar and tensor signal models. Scalar resonances decay isotropically while tensor resonances decay more centrally. Cutting harder can increase the sensitivity to tensor signals by a few percent while loosening these cuts would similarly improve the sensitivity to scalar models. Future iterations of this search may consider defining non-orthogonal signal regions separately optimized for the discovery of resonances of differing spin.

8.3 $t\bar{t}$ Veto

The subdominant $t\bar{t}$ background is cut in half by rejecting events consistent with a hadronic top quark decay. Top quark candidates are built with three jets, at least one of which is selected from the four Higgs candidate jets. The Higgs candidate jet with the highest b-tagging score is used as the b-jet from the top decay while the other two jets are used to

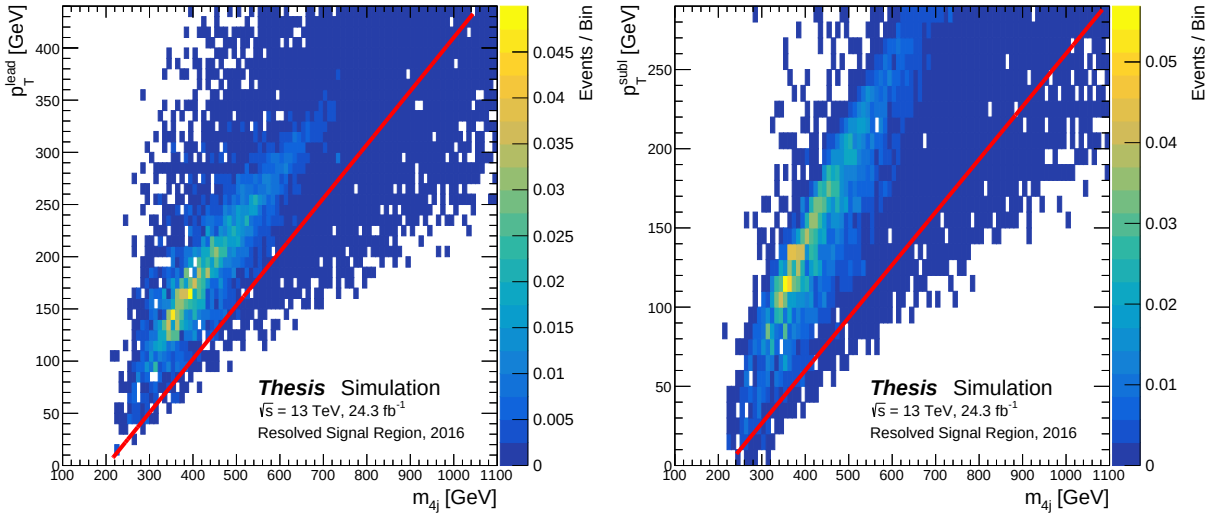

(a) SM HH

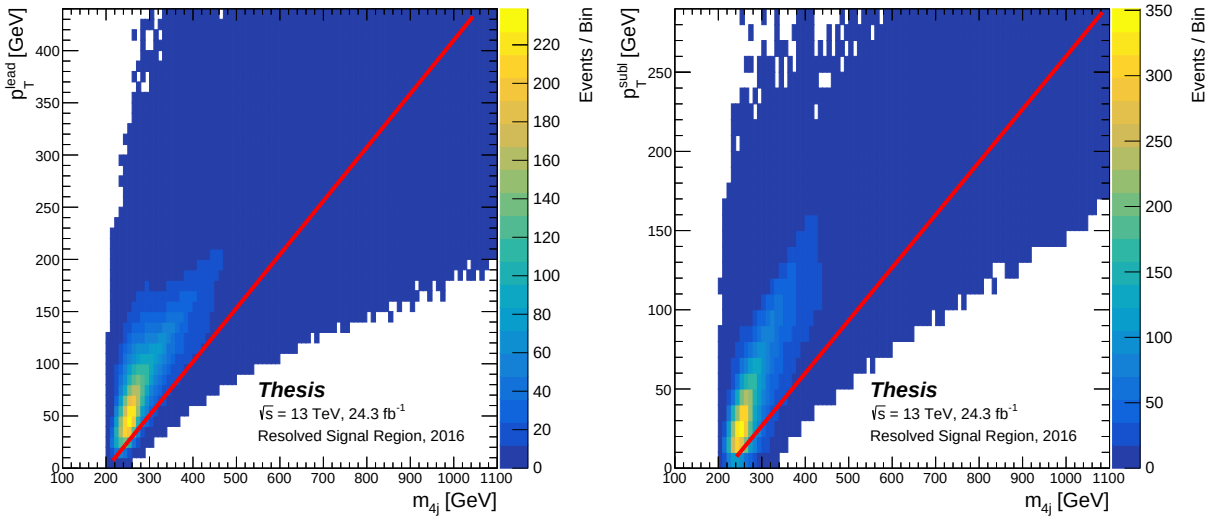

(b) Multijet Background

Figure 8.5: Plots illustrating the $m_{4\mathrm{j}}$ dependent cuts in the Signal Region. Events above the red lines are kept. The Higgs candidates are sorted by the p_{T} of the vector sum of their constituent jets for these cuts only.

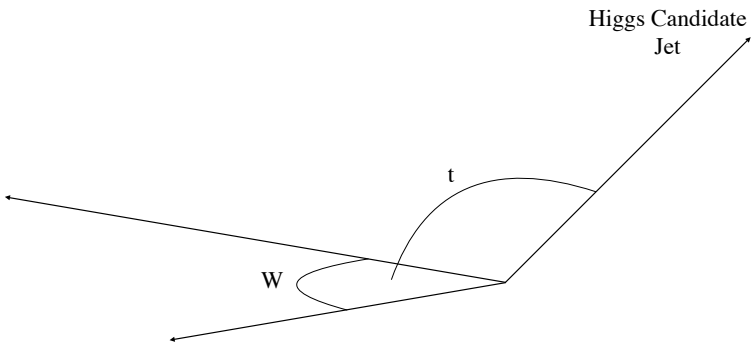

Figure 8.6: Illustration of top candidate building

build a W boson candidate as illustrated in 8.6.

$$X_{Wt} = \sqrt{\left(\frac{m_W - 80.4}{0.1 m_W}\right)^2 + \left(\frac{m_t - 172.5}{0.1 m_t}\right)^2} > 1.5 \tag{8.4}$$

The $0.1 m_W$ and $0.1 m_t$ terms in the denominators reflect the approximate 10% mass resolution of the reconstructed objects. A more sophisticated model incorporating the correlated measurements of the W boson and top quark masses was not found to offer a significant improvement. The top quark candidate with the smallest X_{Wt} defined in equation 8.4 is chosen for each event. Events with $X_{Wt} < 1.5$ are vetoed in the final selection while events with $X_{Wt} < 0.75$ are used to define a $t\bar{t}$ enriched data sample which constrains the $t\bar{t}$ normalization. The top veto has a small impact on the signal acceptance with the largest impact on the lowest signal masses (20% acceptance loss at 260 GeV falling to 10% at 400 GeV).

8.4 Higgs Candidate Mass Plane

A requirement on the Higgs candidate masses is used to define the Signal Region:

$$X_{HH} = \sqrt{\left(\frac{m_{2\mathrm{j}}^{\mathrm{lead}} - 120\,\mathrm{GeV}}{0.1 m_{2\mathrm{j}}^{\mathrm{lead}}}\right)^2 + \left(\frac{m_{2\mathrm{j}}^{\mathrm{subl}} - 110\,\mathrm{GeV}}{0.1 m_{2\mathrm{j}}^{\mathrm{subl}}}\right)^2} < 1.6 \tag{8.5}$$

where the $0.1m_{2j}$ terms represent the widths of the leading and subleading Higgs candidate mass distributions. The Signal Region is shown as the inner region of Figure 8.7. The acceptance of the full event selection, including this Signal Region requirement, is shown in Figure 8.1 as "X_{HH}".

The Sideband and Control regions are also shown in Figure 8.7 and are defined by the following circles:

$$\sqrt{(m_{2j}^{\text{lead}} - (120 \times 1.05)\,\text{GeV})^2 + (m_{2j}^{\text{subl}} - (110 \times 1.05)\,\text{GeV})^2} < 45\,\text{GeV} \tag{8.6}$$

$$\sqrt{(m_{2j}^{\text{lead}} - (120 \times 1.03)\,\text{GeV})^2 + (m_{2j}^{\text{subl}} - (110 \times 1.03)\,\text{GeV})^2} < 30\,\text{GeV} \tag{8.7}$$

Equation 8.6 is the yellow circle in Figure 8.7 and defines the outer limit of the Sideband Region. The center of the Sideband is shifted up by 5% relative to the center of the Signal Region. Equation 8.7 is the orange circle in Figure 8.7 and defines the inner limit of the Sideband Region and outer limit of the Control Region. The inner limit of the Control Region is defined by the Signal Region X_{HH} cut described above. The center of the Control Region is shifted up by 3% relative to the center of the Signal Region. These upward shifts were optimized to minimize the distances in the Higgs candidate mass plane between the arithmetic means of the three regions.

The total data yield and estimated backgrounds after the full selection for the Sideband, Control and Signal regions are shown separately for the 2015 and 2016 datasets in table 8.1.

2015, 3.2fb^{-1}	Sideband	Control	Signal
Semileptonic $t\bar{t}$	27.6 ± 1.4	19.7 ± 9.6	13.9 ± 6.8
Hadronic $t\bar{t}$	69.5 ± 0.35	56.1 ± 25	52.4 ± 24
Multijet	1208.7 ± 4.4	880.2 ± 5.1	866.0 ± 5.0
Total Background	1305.7 ± 36	956.0 ± 41	932.3 ± 40
SM HH	0.1 ± 0.0069	0.3 ± 0.0084	0.5 ± 0.012
Data	1303	969	928

2016, 24.3fb^{-1}	Sideband	Control	Signal
Semileptonic $t\bar{t}$	237.6 ± 12	167.8 ± 34	122.9 ± 25
Hadronic $t\bar{t}$	337.4 ± 1.6	275.7 ± 69	259.0 ± 65
Multijet	9844.6 ± 12	7109.4 ± 25	6751.9 ± 23
Total Background	10 419.5 ± 100	7552.9 ± 120	7133.8 ±110
SM HH	1.1 ± 0.049	1.8 ± 0.061	3.8 ± 0.091
Data	10 483	7656	7430

Table 8.1: Predicted and observed event yields in the Sideband, Control and Signal Regions. Uncertainties are purely statistical and result from the simulated $t\bar{t}$ sample size and the statistical uncertainty in the measurement of the $t\bar{t}$ and multijet scale factors. The uncertainty on the total background includes $\sqrt{N}$ added in quadrature to the uncertainties of the background components. ($\sqrt{N}$ is the statistical uncertainty in the Gaussian approximation of a sample of size N.)

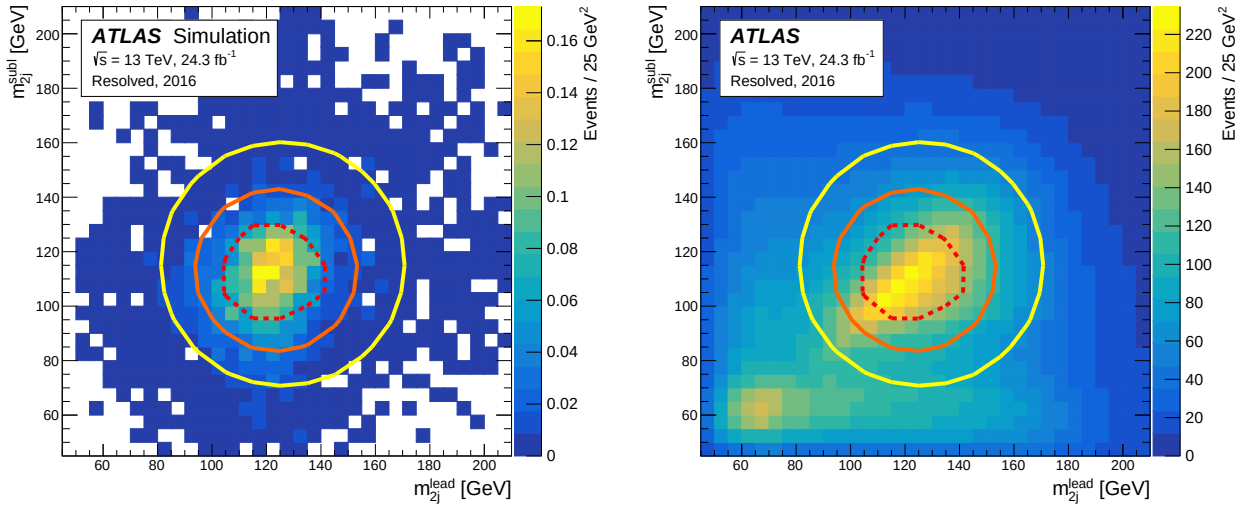

(a) SM HH (b) Multijet Background

Figure 8.7: Higgs candidate mass plane regions. The Signal Region is inside the red dashed curve defined by Eqn. 8.5. The Control Region is outside the Signal Region and within the orange circle defined by Eqn. 8.7. The Sideband is outside the Control Region and within the yellow circle defined by Eqn. 8.6.

8.5 Trigger

We utilize a combination of jet triggers requiring between 1 and 4 jets with various p_{T} thresholds, some of which are required to be b-tagged. If any one of these triggers is satisfied, the event is accepted. The effect of the trigger requirement is seen in the curve labeled "trigger" in Figure 8.1, which shows the total acceptance times efficiency of the event selection criteria and the trigger. The trigger is described in detail in Chapter 9.

8.6 Final Discriminant

The final analysis discriminant is the invariant mass of the selected four-jet system where the Higgs candidate four vector has been scaled by a single number to set the mass equal to

$125\,\text{GeV} \approx m_H$:

$$m_{HH} = \left\| \frac{125\,\text{GeV}}{\left\|p_\mu^{\text{lead}}\right\|} \times p_\mu^{\text{lead}} + \frac{125\,\text{GeV}}{\left\|p_\mu^{\text{subl}}\right\|} \times p_\mu^{\text{subl}} \right\| \tag{8.8}$$

where p_μ^{lead} and p_μ^{subl} are the four-vectors of the leading and subleading Higgs candidates and the four-vector norm $\left\|p_\mu\right\|$ denotes the usual Lorentz invariant mass $m = \sqrt{p_t^2 - p_x^2 - p_y^2 - p_z^2}$. This scaling sharpens the mass peak for resonant signals by accounting for jet mis-measurements and missing energy from neutrinos in semileptonic b decays. In the remainder of this thesis the corrected four-body invariant mass will be denoted m_{HH} while the uncorrected mass will be denoted $m_{4\text{j}}$.

8.7 "Boosted" Selection

The event selection described in this section and the analysis of the data described in the remainder of this thesis are referred to as the "Resolved" selection and analysis. The Higgs candidates are constructed from four individually resolved jets. Not all HH signal events are expected to have this topology. Signal jets may fail the η, p_{T} or b-tagging requirements used for the Resolved selection. No significant benefit has yet been found from attempting to recover these events, though low purity Signal Regions with looser b-tagging requirements may be useful in the future. HH signal events may also fail to be reconstructed in the Resolved search if the jets from individual Higgs boson decays overlap in the detector. This is expected to happen rarely for low mass resonances because the jet area is much smaller than the total detector area. Conversely, the Higgs bosons produced in the decay of high mass resonances are expected to produce overlapping b-jets. The average opening angle between the products of a two-body decay is proportional to the mass of the parent particle

and inversely proportional to the momentum of the parent particle:

$$\langle \Delta R \rangle \approx \frac{2m}{p} \tag{8.9}$$

Then in the limit $m_X \gg m_H \gg m_b$ this approximation is valid so we can expect the jets from Higgs decays to have $\Delta R_{\mathrm{jj}} < 0.4$ when $p_H > 600\,\mathrm{GeV}$. This is expected when $m_X > 2\sqrt{600^2 + 125^2} \approx 1200\,\mathrm{GeV}$. To recover these events, we also define a "Boosted" event selection and analysis which is described in detail in a combined paper [35] and in the sibling thesis [197] to this one. To ensure orthogonality with the Resolved selection, the Boosted selection vetoes events which fall in the Resolved Signal Region including the full event selection described here. For resonance masses above 700 GeV and below 1500 GeV a statistical combination of the Resolved and Boosted Signal Regions enhances the search sensitivity and mass reach. The final combined search covers resonance masses over a full order of magnitude from 260 GeV to 3000 GeV. The statistical analysis with an emphasis on the Resolved selection is described in Chapter 13.

Chapter 9

TRIGGER EFFICIENCY

This section describes the measurement of the trigger efficiency. A combination of multi-b-jet triggers is used in this analysis. The triggers are listed in Table 9.1. Combined, they provide high overall efficiency throughout the mass region searched.

The b-jet trigger menu differs in 2015 and 2016 and, as a result, the data periods are treated separately. In 2016, the online b-tagging was upgraded to use the offline vertexing algorithm and the offline-like multivariate MV2 taggers. The MV2 taggers have higher signal efficiency for fixed trigger rate and increase the overlap of jets tagged online and offline. The efficiency of the simulated triggers and their combination is shown as function of signal mass in Figure 9.1, for the scalar model. The efficiency is shown with respect to events passing the full selection in the Signal Region.

There are several differences between simulation and data that can lead to differences in trigger efficiency. The simulation assumes ideal online running conditions; the beam-spot is centered in the detector with no variation in position and there is no Inner Detector misalignment. In real data, the beam-spot is not exactly centered and drifts within and between runs. There are also relative movements of the Inner Detector sensors that can only be fully corrected offline, after the trigger decisions have been made. In addition, for the 2015 triggers, the simulation tuning was frozen before a full optimization of the b-tagging used for data had been completed. Therefore the simulation is expected to significantly underestimate the efficiency of the 2015 triggers in data. These differences between data and simulation make it critical that the simulation is corrected with the performance measured in data and that systematic uncertainties on the modeling of the trigger efficiency are assessed.

An inefficiency of the online primary vertex reconstruction was observed during the beginning

2015	**2016**	Level 1 Seed
2j35_btight_2j35	2j35_b60_2j35	4J15 $\|\eta\| < 2.5$
j100_2j55_bmedium	j100_2j55_b60	J75_3J20
j225_bloose	j225_b60	J100

Table 9.1: Triggers used in the 2016 and 2015 analyses. A number prior to "j" is a number of jets with a p_{T} threshold as specified by the number after "j". The qualifier after "b" is the online b-tag working point required for the jets immediately preceding "b". For example: j100_2j55_b60 requires two jets b-tagged online at the 60% working point, each with $p_{\mathrm{T}} > 55\,\mathrm{GeV}$ and an additional jet with $p_{\mathrm{T}} > 100\,\mathrm{GeV}$. The Level 1 (L1) hardware trigger selection must be passed before an event is considered for the High Level Trigger (HLT) software based trigger system. The L1 trigger thresholds are specified with a capital J to highlight the fact that they are uncalibrated and as such have slow turn on thresholds with respect to calibrated offline jets. The L1 multijet trigger items are inclusive, ie. J75_3J20 item requires 3 jets above 20 GeV, at least one of which must be greater than 75 GeV

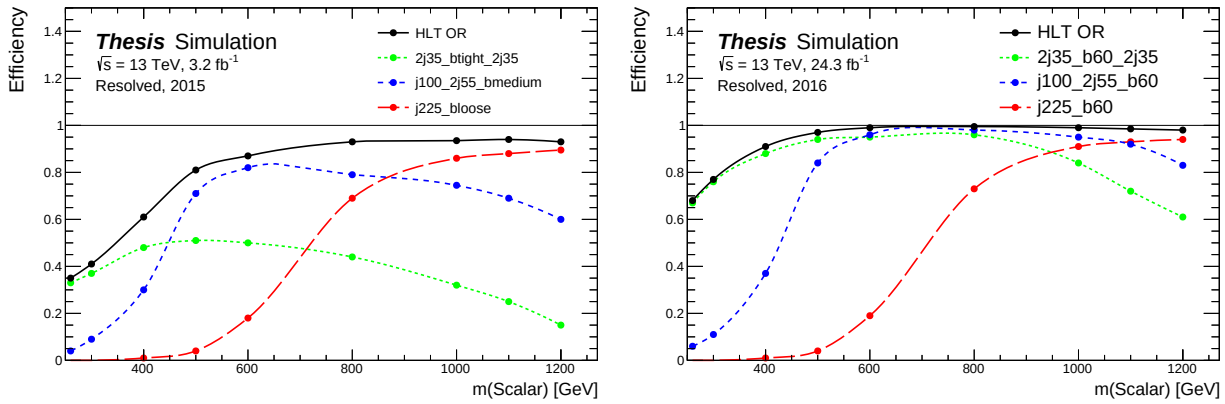

Figure 9.1: Simulated trigger efficiencies as a function of resonance mass for the scalar signal samples for the 2015 (left) and 2016 (right) trigger menu.

of the 2016 data taking. The problem was ultimately traced back to a bug in the offline vertexing algorithm, which was not properly correcting for the difference in coordinate frames used in the online and offline track reconstruction. The offline track reconstruction uses the center of the detector as the origin of the coordinate system. Online, the coordinate system is defined with respect to the center of the beam-spot. This bug, which effected the majority of the data collected in 2016, led to vertex inefficiencies when the beam-spot was significantly displaced from the center of the detector. To properly correct for this, a dedicated Good Run List (GRL) was created for analyses using b-jet triggers. This special GRL removes the 26% of the $33\,\text{fb}^{-1}$in the nominal GRL leaving $25\,\text{fb}^{-1}$of good data. Unfortunately these $11\,\text{fb}^{-1}$of lost data cannot be recovered because the bug impacted the final decision to keep a given event, unlike bugs in the offline reconstruction.

Measuring the efficiencies of these triggers in data is complicated by the fact that efficiencies can only be measured at the level of individual jets and not for entire events. Event-level efficiencies and uncertainties need to be derived from jet-level inputs, taking the proper correlation between the different jets and among the individual triggers items into account. The remainder of this section outlines the methodology behind the trigger efficiency measurement and presents the results.

9.1 Jet-level Trigger Efficiencies and Scale Factors

Leptonic top quark decays provide a clean, pure sample of b-jets from which the efficiency of the online b-tagging algorithm can be measured. Jet-level efficiencies and scale factors have been measured by the b-jet trigger group using fully leptonic $t\bar{t}$ events [29]. Leptons are used to trigger and calibration chains are run which calculate the online b-tagging discriminants but do not select events. The efficiency of the online b-tagging is then determined relative to jets that pass the offline b-tagging requirement. This sample is more than 95% pure in

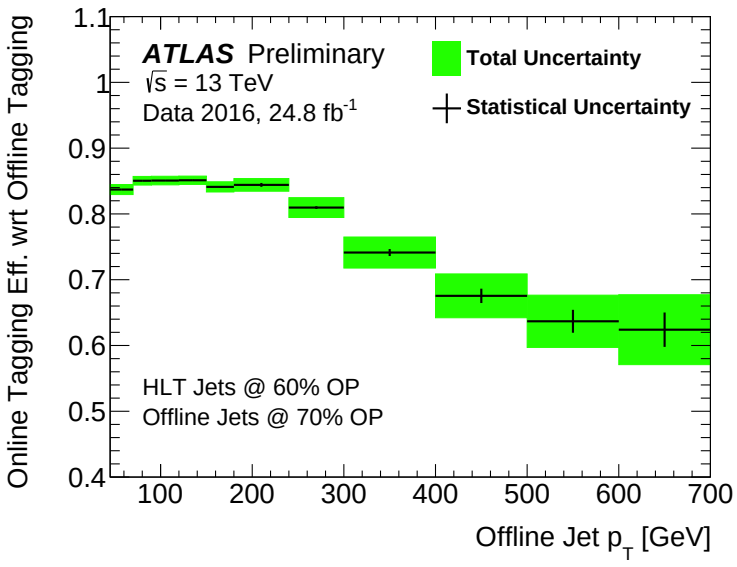

Figure 9.2: 2016 jet-level trigger efficiencies. The trigger efficiency is measured with respect to offline b-tagged jets.

b-jets. Impurities are corrected for and associated systematics are applied as described in [29].

The jet-level efficiency to tag a jet online at the 60% working point which was tagged offline for the working point used in this analysis (70%) is shown in Figure 9.2 as a function of jet p_{T}. Other kinematic distributions, jet η, number primary vertices, ΔR to the nearest jet, etc. were found to have little effect on the efficiency. Below 240 GeV, the uncertainty is dominated by the modeling of the light jet impurities both before and after the online b-tagging requirement. These sources of uncertainty are fully correlated between p_{T} bins. Above 240 GeV, the statistics in data begins to run out. Here the efficiencies are extrapolated using simulated events. The uncertainties associated with this extrapolation begins to dominate at higher p_{T}. These uncertainties are also fully correlated between p_{T} bins. In the following, the jet-level uncertainties are assumed to be 100% correlated.

9.2 Calculating the Event-level Efficiency: ϵ_{event}

This section describes the procedure for deriving event-level efficiencies from the jet-level inputs. The logic to emulate the trigger using jet-level inputs is as follows:

1. Assign each of the four Higgs candidates jets a random number from a uniform distribution between 0 and 1.
2. Interpret numbers less than (1-ϵ_{jet}) as failing the online b-tagging requirement where ϵ_{jet} is the pt-dependent trigger efficiency corrected to data.
3. Count jets considered as passing the online b-tagging requirement above the various p_{T} thresholds to derive event-level decisions.
4. Repeat steps 1-3 50 times.
5. Use the fraction of times the event passes the emulated trigger logic as the estimate of the trigger efficiency.

To be explicit, j225_b60 is considered satisfied if there is at least one jet with $p_{\text{T}} > 225$ GeV that is interpreted as passing the online b-tagging requirement. Similarly, j100_2j55_b60 is considered satisfied if there are at least three jets with $p_{\text{T}} > 55$ GeV, at least two of which are interpreted as passing the online b-tagging and at least one of which has $p_{\text{T}} > 100$ GeV. Finally, 2j35_b60_2j35 is considered satisfied if there are four jets with $p_{\text{T}} > 35$ GeV, at least two of which are interpreted as passing the online b-tagging. The combined event-level decision is made based on the OR of these input decisions.

One point to note is that this jet-level counting assumes efficiencies of the individual jets of the multi-jet items can be treated independently, i.e.:

$$\epsilon(\text{2j35\_b60\_2j35}) = \epsilon_{\text{jet}}^4 + 4(1-\epsilon_{\text{jet}})\epsilon_{\text{jet}}^3 + 6(1-\epsilon_{\text{jet}})^2\epsilon_{\text{jet}}^2 \tag{9.1}$$

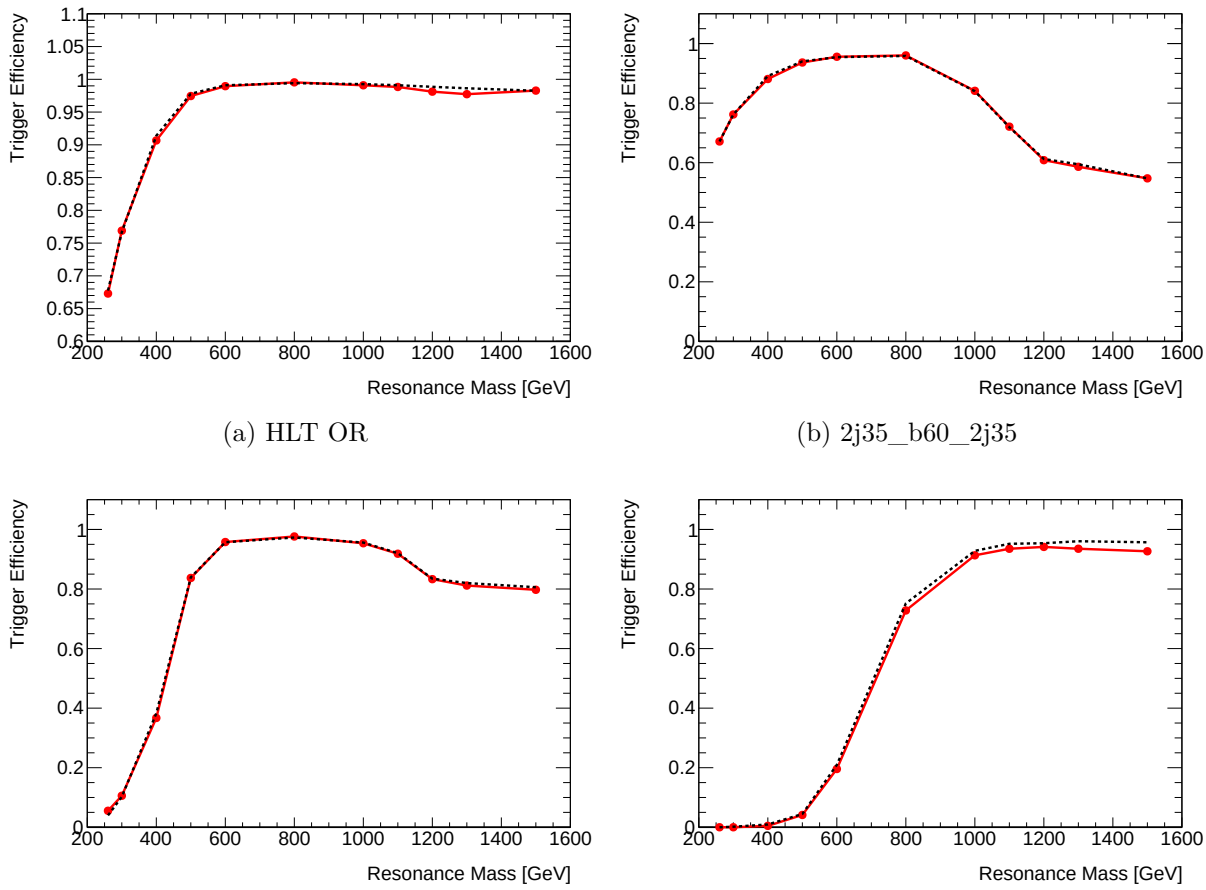

(a) HLT OR

(b) 2j35_b60_2j35

(c) j100_2j55_b60

(d) j255_b60

Figure 9.3: Comparison of the trigger efficiency in MC using the jet-level approximation, in black, to the simulated decisions including the full correlation, in red.

This assumption is tested explicitly in the simulation and a systematic uncertainty is assigned to cover any non-closure.

Figure 9.3 shows a validation of the method. The figures compare the event-level efficiencies of the full ATLAS simulation triggers to the results predicted by the trigger emulation algorithm using the ϵ_{jet} as measured in simulation. The agreement of the event-level efficiencies holds for the individual trigger items as well as their combination at the percent level.

9.3 Estimating the Efficiency Uncertainty: $\Delta\epsilon_{\text{event}}$

The uncertainty on the combined event-level trigger efficiency due to the uncertainty on the jet-level trigger efficiencies is derived as follows:

1. Generate a random number δ from a Gaussian distribution with unit variance.
2. Run the trigger emulation algorithm using a smeared jet-level efficiency curve:

$$\epsilon_{\text{jet}} + \delta \times \Delta\epsilon_{\text{jet}}$$

   where $\Delta\epsilon_{\text{jet}}$ is the uncertainty shown in green in Figure 9.2 (This curve for the online b-tagging was measured separately for the different online working points used in the 2015 triggers).
3. Repeat 1-2 40 times to get a distribution of ϵ_{event}.
4. Take the RMS of the ϵ_{event} distribution as the event-level systematic uncertainty resulting from the jet-level systematic uncertainty.

For a given iteration, the same δ is used for all jets and all p_{T} bins, explicitly building in the correlation in the jet-level efficiencies. This procedure propagates jet-level uncertainties to the event-level including the proper correlations among the jets and the different trigger items. This event-level uncertainty is added in quadrature with the uncertainty coming from the non-closure of the method assumptions discussed above.

The bug in the vertexing algorithm described above, has led to small residual event-level primary vertexing inefficiencies in the 2016 dataset. The vertex efficiency has been measured in data using $t\bar{t}$ events and is shown in Figure 9.4 as a function of the leading jet-η. The simulation is corrected for this inefficiency at the event-level. The systematic uncertainty

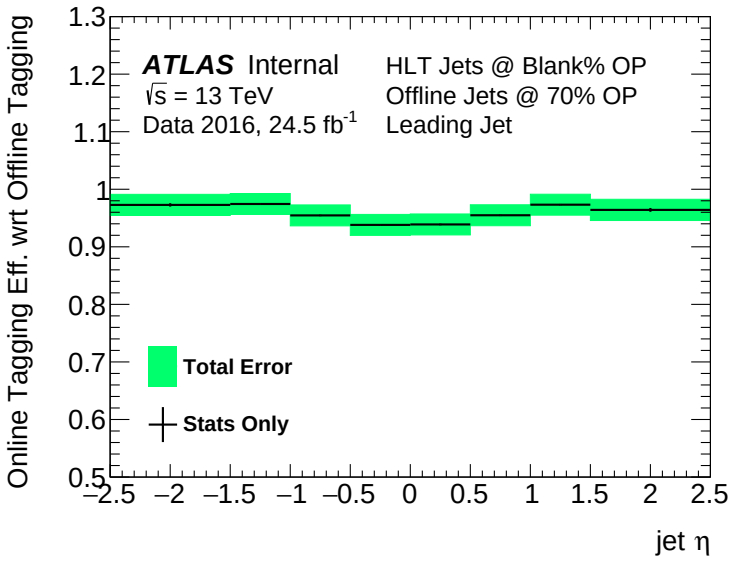

Figure 9.4: 2016 vertex-level trigger efficiency.

associated with the vertex efficiency is added in quadrature to the non-closure and jet-level uncertainties described above.

Figure 9.5 shows the final event-level trigger efficiencies for the various signal samples corrected for the jet-level efficiencies measured in data. The dashed lines indicate the systematic uncertainties on the trigger efficiency including all the components described here.

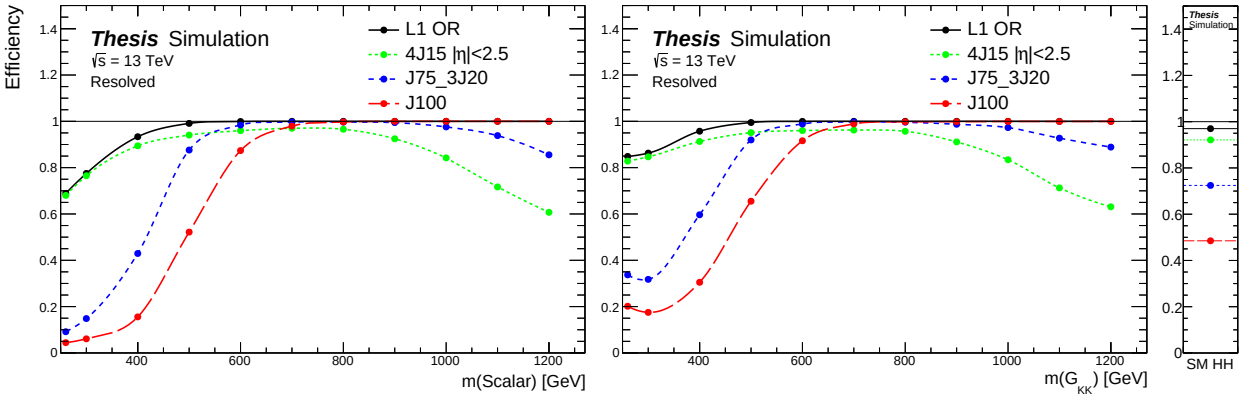

(a) L1

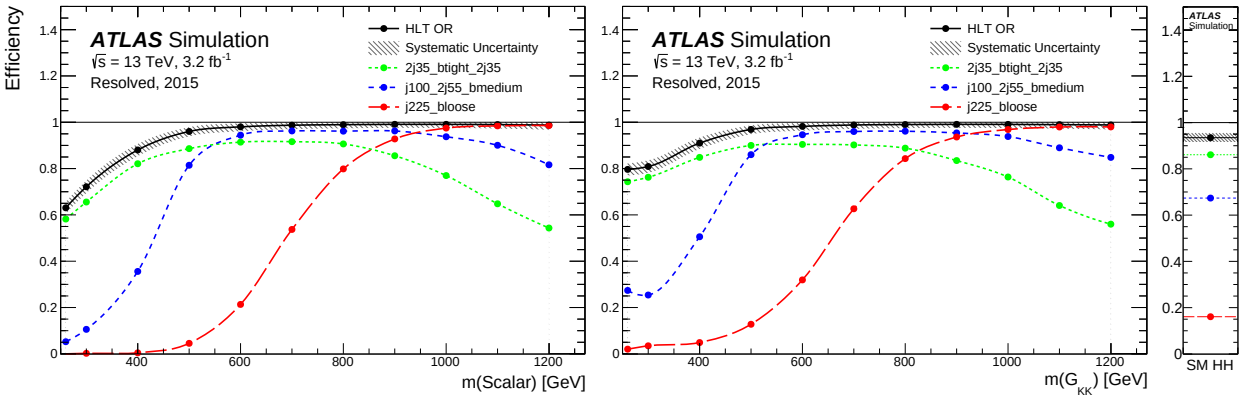

(b) 2015 L1 and HLT

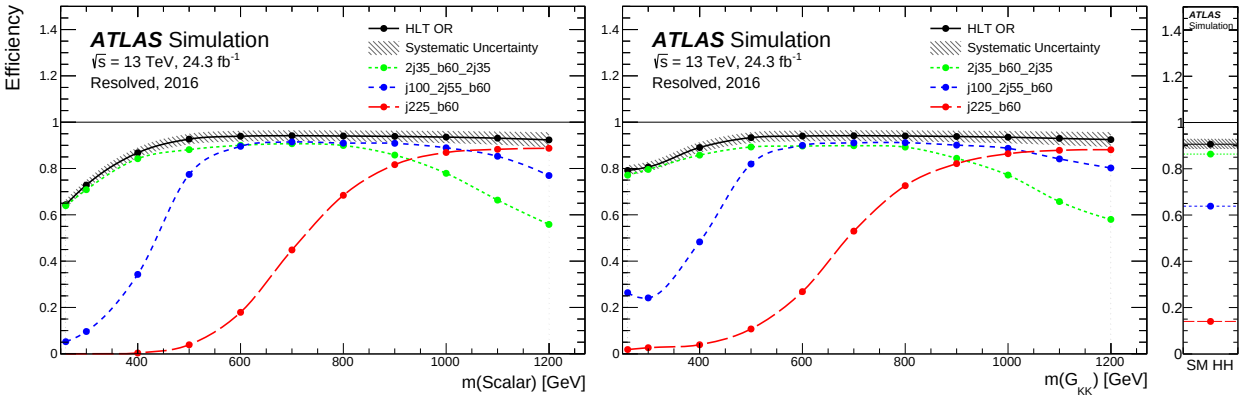

(c) 2016 L1 and HLT

Figure 9.5: The trigger efficiency for narrow width scalar and graviton ($k/\overline{M}_{\mathrm{Pl}} = 1$) samples with a range of resonance masses and for the SM HH sample. The efficiency is higher for the graviton samples because spin-2 resonances decay more centrally than isotropic scalar resonances resulting in higher p_{T} jets for a given resonance mass. Almost all of the efficiency from the trigger for low mass events is due to the L1 hardware trigger thresholds.

Chapter 10

BACKGROUND MODELING

After the event selection detailed in Chapter 8 there are two main backgrounds: events with four or more QCD produced jets (hereafter referred to as the "multijet" background) and top quark pair production ($t\bar{t}$). After the full selection $\sim 95\%$ of the background consists of multijet events. The multijet and $t\bar{t}$ background models are derived and constrained together in data with an iterative procedure as described in the following sections.

In Section 11 we demonstrate that the total background model is insensitive to $\mathcal{O}(1)$ variations of the $t\bar{t}$ backgrounds. The stability of the total background estimate is due to new $t\bar{t}$ normalization constraints in data and the ability of the multijet model to accommodate changes in other background components. This is a significant improvement over our previous result [33] which suffered from large systematic uncertainties in the $t\bar{t}$ background shape and normalization without dedicated $t\bar{t}$ control regions.

All background scale factors and reweighting functions are derived using the full event selection excluding the top quark veto ($X_{Wt} > 0.75$ where X_{Wt} is defined in equation 8.4). The X_{Wt} distribution is used to constrain the relative multijet and hadronic $t\bar{t}$ scale factors, μ_{multijet} and $\alpha_{t\bar{t}}^{\text{hadronic}}$. By deriving the background model prior to the X_{Wt} cut, we are able to use the modeling of the X_{Wt} distribution to constrain the relative multijet and $t\bar{t}$ yield. The semileptonic $t\bar{t}$ background scale factors, $\alpha_{t\bar{t},2b}^{\text{semileptonic}}$ and $\alpha_{t\bar{t},4b}^{\text{semileptonic}}$, are determined by looking at events with reconstructed prompt isolated muons.

A dedicated study described in H.1 was performed to estimate the background contribution from Z bosons produced in association with jets and found this background to be negligible.

We first use the Sideband to determine the nominal background model, and then the Control

Region to assess the systematic bias associated with extrapolating over the Higgs candidate mass plane into the Signal Region.

10.1 Multijet Background Modelling

The multijet background is modeled using an independent data sample. This data sample is selected from events where only two of the selected jets are b-tagged, giving two hundred times the nominal "four-tag" yield. Higgs candidates are built and the same event selection used to define the Signal Region is applied.

In past iterations of this analysis [33, 34], the jets used to form Higgs candidates in this "two-tag" region were also selected by their b-tagging score from the MV2 algorithm; the two non-tagged jets with the highest MV2 value were chosen in addition to the two b-tagged jets. In this iteration of the analysis we employ an improved algorithm to build Higgs candidates in the two-tag region that treats all selected non-tagged jets coherently. Section 10.1.1 gives an overview of the procedure for building Higgs candidates in the two-tag region; Section 10.1.4 presents the results of the method in the current analysis.

10.1.1 Two-Tag Higgs Candidates

As a reminder, events in the Signal Region are pre-selected to have at least four b-tagged jets. If there are more than four b-tagged jets, the jets are ordered by the MV2 discriminant and the top four are selected. These selected jets are then paired to form Higgs candidates following the procedure described in Section 8.

The multijet background passing the signal selection is modeled using events with fewer b-tagged jets. The working assumption is that the yield and kinematics of events selected

with a b-tagged jet ("t") can be modeled by scaling events selected using the same criteria but with the b-tagged jet replaced with a non-b-tagged jet ("n"). Schematically,

$$f \times n \xrightarrow{\text{models}} t \tag{10.1}$$

where f is a perjet scale factor that relates a non-tagged jet to a tagged jet. In other words, the background events selected with $X + (t)$ can be modeled using $X + (n)$ events with a weighting of f, where X represents the various other event selection criteria. The non-tagged jet n is said to be "pseudo-tagged"; after scaling the event weight by the perjet transfer factor f, the event selection proceeds as if n passed the b-tagging requirement. The perjet scale factor f is expected to have several kinematic dependencies which can be explicitly included in functional form. For example, a p_{T} dependence would be accounted for using,

$$f(p_{\mathrm{T}}) \times n(p_{\mathrm{T}}) \xrightarrow{\text{models}} t(p_{\mathrm{T}}). \tag{10.2}$$

As will be described in Section 10.1.3, this analysis implicitly corrects for kinematic dependencies by reweighting event-level distributions to account for effects that cannot be factorized on a per-jet basis (for example, the scattering matrix elements have differing jet-jet correlations). The notation in the remainder of the section suppresses any explicit kinematic dependence in f, but can be extended following the example of Equation 10.2.

The non-tagged jets used in the Higgs candidate building are selected by first deciding which of the non-tagged jets are to be considered as pseudo-tagged. Each potential assignment of pseudo-tagged jets is considered. The events are scaled by a weighting factor appropriate for there being at least two assigned pseudo-tagged jets. In the case where more that one assignment leads to there being at least two pseudo-tagged jets, one of the assignments is picked at random using the relative probabilities of each assignment. Higgs candidates are then built from the two b-tagged jets and the pseudo-tagged jets following the same logic as

in the four-tag selection. In particular, in the case where there are more than four b-tagged plus pseudo-tagged jets, the jets are order by MV2 discriminant and the top four jets are selected for Higgs candidate building. Note that this assures that the two b-tagged are always selected for Higgs candidate building. A few quick examples will help clarify this procedure.

First consider the case where there are only two non-tagged jets. This event will be represented using the notation:

$$t_1 + t_2 + n_1 + n_2 \tag{10.3}$$

where t_1 and t_2 represent the two-tagged jets and n_1 and n_2 represent the two non-tagged jets. This event can model four-tag events if both n_1 and n_2 are considered pseudo-tagged. As two pseudo-tagged jets are needed this event would have weight f^2. The extrapolation of this event to predict background in the four tag Signal Region can be written in our notation as:

$$t_1 + t_2 + (f \times n_1) + (f \times n_2). \tag{10.4}$$

In this example, only one assignment of which jets are considered as pseudo-tagged leads to there being at least two pseudo-tagged jets and thus four jets for Higgs candidate building, so no choice in among potential assignments in needed. All four jets are treated as if they were b-tagged and the Higgs candidate building and event selection proceeds as in the four-tag selection.

As a nontrivial example, consider the case of three non-tagged jets:

$$t_1 + t_2 + n_1 + n_2 + n_3 \tag{10.5}$$

Here, there are three assignments of pseudo-tagged jets which can model events with four

b-tagged jets and one non-tagged jet:

$$t_1 + t_2 + f^2(n_1 + n_2) + (1 - f)n_3 \tag{10.6a}$$

$$t_1 + t_2 + f^2(n_1 + n_3) + (1 - f)n_2 \tag{10.6b}$$

$$t_1 + t_2 + f^2(n_2 + n_3) + (1 - f)n_1 \tag{10.6c}$$

and one assignment that models events with five b-tagged jets:

$$t_1 + t_2 + f^3(n_1 + n_2 + n_3). \tag{10.7}$$

Each of the these four potential pseudo-tag assignments leads to at least four jets for Higgs candidate building. One of these four possible assignments is randomly chosen according to their relative weights. Assignments 10.6a–10.6c would each be chosen with probability $\frac{f^2(1-f)}{3f^2(1-f)+f^3}$ and assignment 10.7 would be selected with probability $\frac{f^3}{3f^2(1-f)+f^3}$. The event is scaled using the sum of weights of assignments that give at least two pseudo-tagged jets. Once the assignment is chosen, the pseudo-tagged jets are treated as b-tagged, the non-pseudo-tagged jets are treated as not b-tagged and the event in passed through the same Higgs candidate building and selection as in the four-tag sample. In particular if assignment 10.7 is chosen, the five selected jets are sorted by MV2 discriminant and Higgs candidates are built from the top four.

The general case can be extrapolated from these examples. Figure 10.1 sketches the logic. For each jet multiplicity n, the sum of weights of assignments giving at least two pseudo-tagged jets is calculated by considering all possible assignments. One of these assignments with at least two pseudo-tagged jets is chosen at random using the correct relative probabilities.

A significant difference between the method used for selecting pseudo-tagged jets described here and the method used in previous iterations of this analysis is the effective weights

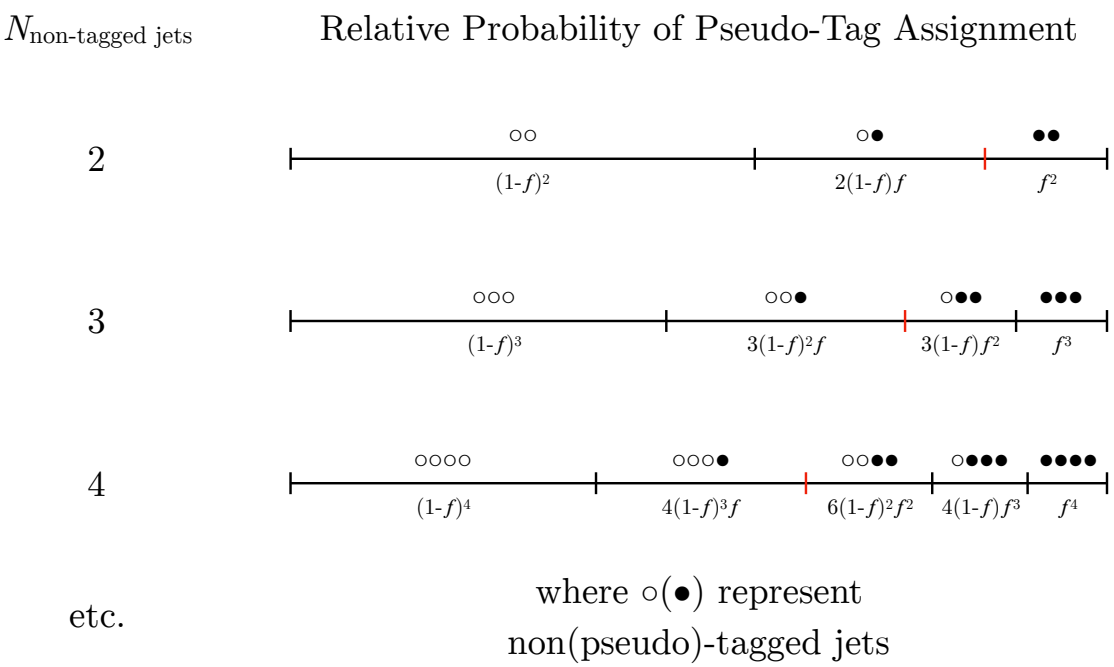

Figure 10.1: Sketch of generalization of pseudo-tag assignment to arbitrary numbers of non-tagged jets. The red bar represents the requirement of having at least two pseudo-tagged jets to allow the selection of four Higgs candidate jets. (Note that the relative size of the bars are not to scale).

applied to events with higher jet multiplicities. With the old method a common two-tag to four-tag scale factor was applied independent of jet multiplicity. In the new method described here, the event weight is given by the sum of weights of assignments that have at least two pseudo-tagged jets. The combinatorics of pseudo-tag jet assignments leads to event weights that increase with jet multiplicity. For example:

$(tt) + n + n$	events scale with weight:	f^2
$(tt) + n + n + n$	events scale with weight:	$(3 - 2f) \times f^2$
$(tt) + n + n + n + n$	events scale with weight:	$(6 - 8f + 3f^2) \times f^2$

In the general case, this combinatoric model generates a constant term ($N_{\text{non-taggedjets}}$ choose 2). For $f \ll 1$, this constant term determines the shape of the jet multiplicity model to first order. The parameter f can then be optimized to give the best possible modeling of the four-tag jet multiplicity with or without an overall scale factor: μ_{multijet}. By including an overall scale factor μ_{multijet}, the weak dependence of the jet multiplicity shape on f can be optimized independently of the normalization. The modeling of additional jet activity is thus a strong test of the assumptions and implementation of the improved method. Figure 10.2 compares the modeling of the additional jet activity between the old and new method in the Sideband region.

The parameter f can be determined from a fit to the four-tag jet multiplicity spectrum in two ways: A one parameter fit where μ_{multijet} is set to 1 or a two parameter fit where μ_{multijet} and f are fitted simultaneously.

In this analysis, f and μ_{multijet} are determined together so that f can be tuned to best match the jet multiplicity spectrum as described in section 10.1.2. The best fit value of f is sensitive to small statistical fluctuations while the overall modelling is not; f is small so the shape of the jet multiplicity model is dominated by the combinatoric prefactor ($N_{\text{non-tagged jets}}$ choose 2). Due to the weak dependence of the jet multiplicity shape on f, the best fit value is found to vary 70% between the 2015 and 2016 datasets as can be seen in Table 10.1. The

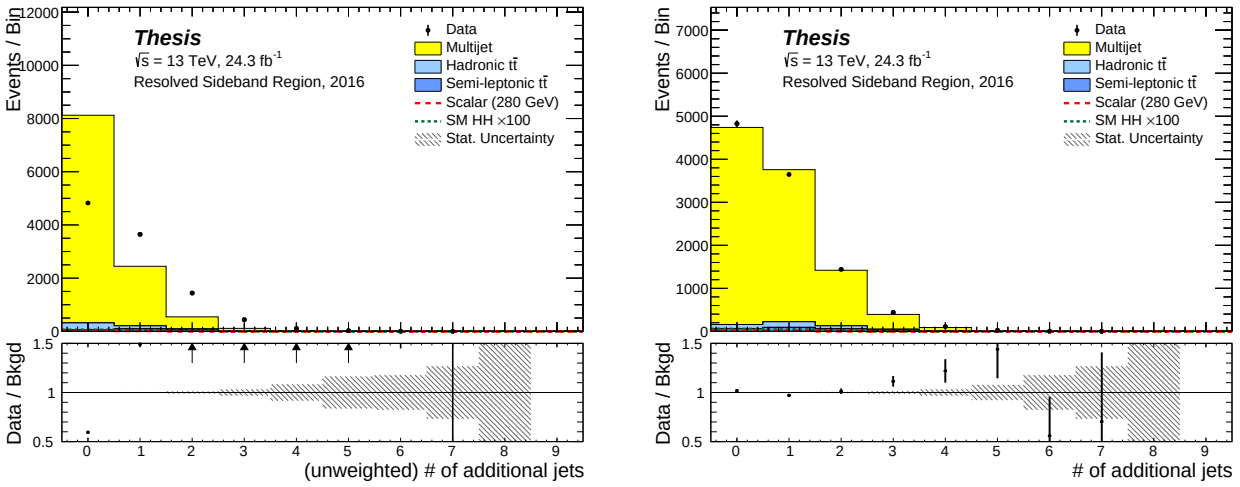

(a) Old Method

(b) New Method

Figure 10.2: Comparison of the modeling of jet multiplicity in the Sideband using the previous method versus the method used in this analysis. In this figure and others like it, "Data" refers to the four-tag selection and "Multijet" refers to the multijet background model constructed from the two-tag data.

multijet scale factor adjusts to compensate for this difference such that $\mu_{\text{multijet}} \times f^2$ only varies by 10% between years. The remaining discrepancy is due to changes in the triggers and pile-up conditions which can impact the relative event rate and jet multiplicity spectra between the two-tag and four-tag selections. With more online b-tagged jets an event has a higher probability of satisfying the online b-tagging requirement. Additionally, pile-up jets and light jets can sometimes satisfy the trigger requirements so changes in pile-up or trigger conditions are expected to have differing impacts on the trigger rate for two and four-tag events.

An alternative approach would be to use each two-tag event multiple times, once for each pseudo-tag assignment which has at least two pseudo-tagged jets. This would implicitly generate the combinatoric factors with each use of an event being weighted by a factor f for

each pseudo-tagged jet and $1 - f$ for each non-pseudo-tagged jet:

$$f^{N_{\text{pseudo-tagged}}} \times (1 - f)^{N_{\text{non-pseudo-tagged}}} \tag{10.8}$$

This approach is simple and gives nearly identical results, but complicates the statistical uncertainty of the background model as many events will be used multiple times giving correlated effects. As a result, this alternative procedure was not pursued further in this analysis.

10.1.2 Modeling Jet Multiplicity

In each reweighting iteration as described in the following section 10.1.3 the pseudo-tag rate is updated to fit the jet multiplicity distribution in the Sideband. This requires a guess for the pseudo-tag rate in the first iteration. This input is determined by running a few iterations and checking what the pseudo-tag rate converges towards, and then re-running the procedure with the first pass value. Once this value is set it fluctuates very little between iterations as can be seen in Table 10.1. The fitted jet multiplicity is shown in Figure 10.3.

10.1.3 Kinematic Reweighting

Kinematic quantities from object-level 4-vector distributions to event-level correlations in the two and four tag selections are expected to differ as a result of three primary effects:

1. In the previous section we addressed the sculpting of additional jet activity resulting from splitting the data set by the number of b-jets. In events with no additional jet activity and no missing energy the Higgs candidate transverse momenta must cancel out. With additional jets the phase space open to the four selected Higgs candidate

Iteration	2015	2016
0 (guess)	0.26	0.15
1	0.17 ± 0.04	0.13 ± 0.01
2	0.23 ± 0.04	0.15 ± 0.01
3	0.22 ± 0.04	0.15 ± 0.01
4	0.22 ± 0.04	0.15 ± 0.01
5	0.21 ± 0.04	0.15 ± 0.01
6	0.21 ± 0.04	0.15 ± 0.01
7	0.22 ± 0.04	0.15 ± 0.01

Table 10.1: Best fit pseudo-tag rate at each iteration of the reweighting. The values are not expected to be consistent between years due to the change in online b-tagging. Uncertainties are purely statistical.

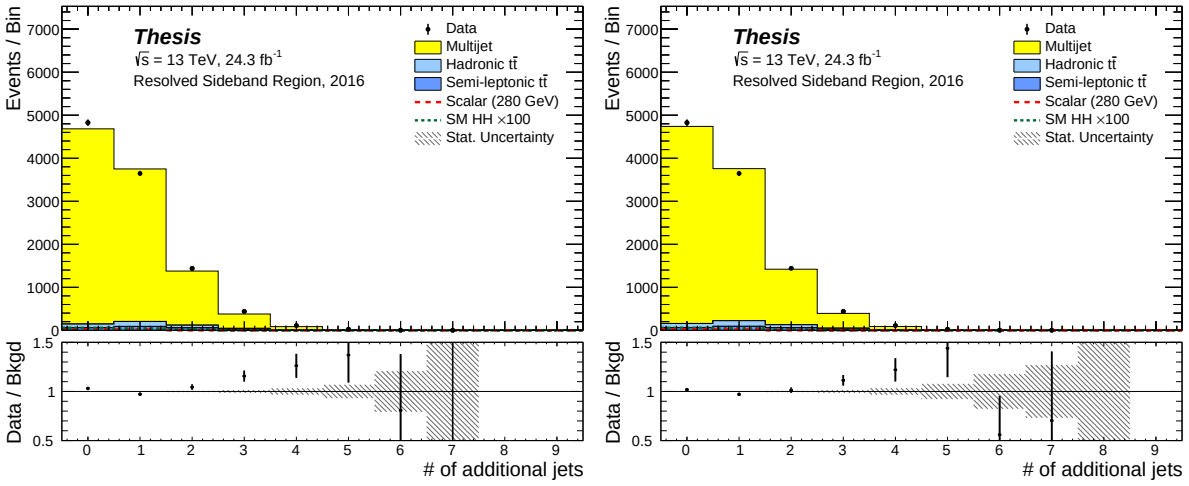

(a) Iteration 0

(b) Iteration 7

Figure 10.3: The result of the pseudo-tag rate fit in the first and last iterations.

jets is increased. By improving the modeling of additional jet activity, we more closely model the relative abundance of the regions of phase space where the Higgs candidates are able to recoil off of other jets in the event.

2. Jets are b-tagged in this analysis both online in the trigger and offline in the final reconstruction with a flat cut on the jet MV2 score. In both cases the b-tagging efficiency is a function of jet p_{T} and η.

3. The relative contribution of underlying physical scattering processes varies as a function of the b-tagging requirements placed on jet selection.

The first effect is effectively disentangled from the second and third as described in the previous section which can be seen in Figure 10.3. This improves our ability to correct for non-flat b-tagging efficiencies and differences in the underlying scattering processes with kinematic reweighting.

In principle and with infinite statistics the kinematic differences between our background model and the four tag data can be corrected to arbitrary precision. To do this one must measure the ratio of the event rate of the data over the background model as a multidimensional function of all observables. This ratio is then used to reweight the background model such that the new ratio is constant at 1. We assume the background model has support over the full phase space of the data. The ratio of event rates can be approximated by filling finely binned, multidimensional histograms for the background model and the data and taking their ratio.

In practice we trade statistical power for proximity to the Signal Region. Shrinking the Sideband and Control regions increases the statistical uncertainty of the reweighting histogram while decreasing the systematic bias due to the dependence of the reweighting histogram on the Higgs candidate masses. Additionally we can shift the centers of the Sideband and

Control regions to ensure balanced representation of high and low mass phase space in both regions. The centers are chosen to have the mean of the leading and subleading Higgs candidate masses of each region align as closely as possible with the predicted means of the Signal Region Higgs candidate mass distributions. The final definitions used are shown in Equations 8.6, 8.7.

We also reduce statistical uncertainty while increasing systematic bias by projecting the reweighting histogram into multiple lower dimensional distributions. Our model uses five one dimensional distributions to measure and correct kinematic differences between the multijet model and the four tag data. This dimensional reduction means that a single iteration of applying correction factors may not result in complete closure of the reweighted distributions. To account for correlations among the reweighted distributions we iteratively measure and reweight a smoothed ratio of the reweighting distributions. Schematically the procedure is as follows:

1. Fill histograms of the five reweighting distributions separately for two and four tag data and simulated $t\bar{t}$ events. Weight the two tag histogram entries with a product over the reweighting functions from previous iterations:

   Let r_i^a denote the reweighting functions where $a \in A$ specifies the reweighting distribution from the set of five variables A, and i specifies the iteration starting from 0. Let $w(f, N_{\text{untagged jets}})$ denote the combinatoric weight function described in the previous section 10.1.1. For a given event let x_a be the value of the kinematic variable denoted by a. Let I be the current iteration.

   The simplest method would be:

$$w = w(f, N_{\text{untagged jets}}) \times \prod_{i=0}^{i<\text{I}} \prod_{a \in A} r_i^a(x_a) \tag{10.9}$$

To improve the convergence rate we scale the difference of the weight from unity by a factor that approaches one in later iterations:

$$w = w(f, N_{\text{untagged jets}}) \times \prod_{i=0}^{i<\text{I}} \prod_{a \in A} \left[(r_i^a(x_a) - 1) \times (1 - \frac{1}{2^{i+1}}) + 1 \right] \tag{10.10}$$

2. Subtract the two and four tag $t\bar{t}$ histograms from the two and four tag data respectively.

3. Normalize the histograms to unit area.

4. Take the ratio of (four tag $t\bar{t}$ subtracted)/(two tag $t\bar{t}$ subtracted) reweighting histograms.

5. Smooth the ratio with ROOT.TGraphSmooth.SmoothKern() [62] to reduce impact of local statistical fluctuations.

6. Compute the ROOT.TGraph.Spline [62] of the smoothed ratio to define r_I^a.

7. Update the per-jet transfer factor f to minimize the χ^2 of the jet multiplicity modeling.

8. Repeat steps 1-7 until $r_I^a(x_a) \approx 1$ for all $a \in A$.

The five distributions that have been found to offer the most robust reweighting corrections are:

1. The turn on of $p_{\text{T},4}$ up to 80 GeV.

2. $p_{\text{T},2}$

3. $< |\eta_i| >= \frac{1}{4} \sum_{i=1}^{i=4} |\eta_i|$

4. $\Delta R_{\text{jj}}^{\text{close}}$, the ΔR_{jj} of the two closest jets out of the four selected for Higgs candidate construction

5. $\Delta R_{\mathrm{jj}}^{\mathrm{other}}$, the ΔR_{jj} of the other two Higgs candidate jets

Where $p_{\mathrm{T},i}$ and η_i denote the transverse momentum and pseudo rapidity of the four jets selected to build Higgs candidates sorted by p_{T} with 1 being the highest p_{T}. The reweighting of $p_{\mathrm{T},4}$, $p_{\mathrm{T},2}$ and $< |\eta_i| >$ are motivated primarily by the p_{T} and η dependence of b-tagging efficiency while $\Delta R_{\mathrm{jj}}^{\mathrm{close}}$ and $\Delta R_{\mathrm{jj}}^{\mathrm{other}}$ are reweighted to account for differences in dijet correlations from the underlying scattering processes.

10.1.4 Multijet Background Results

In Figure 10.4 we show the result of the ratio smoothing and splining procedure for the first and last iteration for the five reweighted distributions. This shows that the reweighting functions have converged to one to within 5%. Figures 10.5 show the full background model for the reweighted distributions in the Sideband where the weights were derived. Figures 10.6 show the same distributions in the Control region, illustrating that the correction is still applicable closer to the Signal Region.

The same plots for the 2015 data can be found in Appendix C.

To demonstrate that the reweighting procedure also improves the modeling of the kinematic distributions which were not directly reweighted, Figure 10.9 shows the Higgs candidate p_{T} distributions in the Sideband before and after the reweighting has been applied. Figure 10.10 shows the same distributions in the Control Region.

The modeling of key event level distributions are also improved by the reweighting procedure. Figures 10.7, 10.11 show the modeling of several event level quantities before and after the reweighting has been applied. The same distributions in the Control Region are shown in Figures 10.8, 10.12.

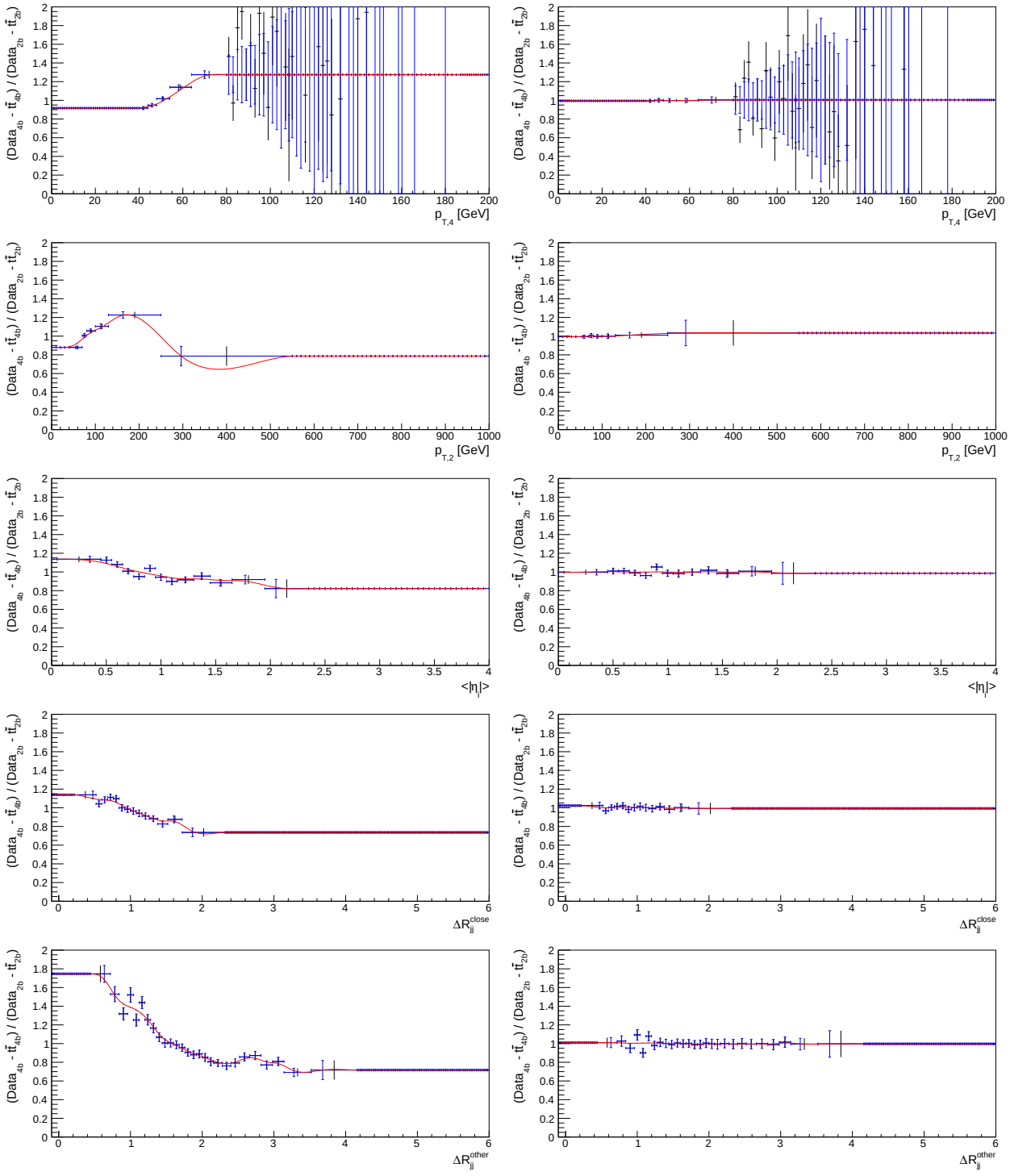

Figure 10.4: The five reweighted ratios before (left, iteration 0) and after (right, iteration 7) the reweighting procedure had been applied. In black is the raw ratio, in blue is the TGraph where the x values of the bins have been set to the mean of the background distribution in that bin and in red is the spline used for reweighting. For the $p_{\mathrm{T},4}$ ratio, the TGraph entries are kept constant above the statistically motivated cut-of of 80 GeV such that the spline becomes constant.

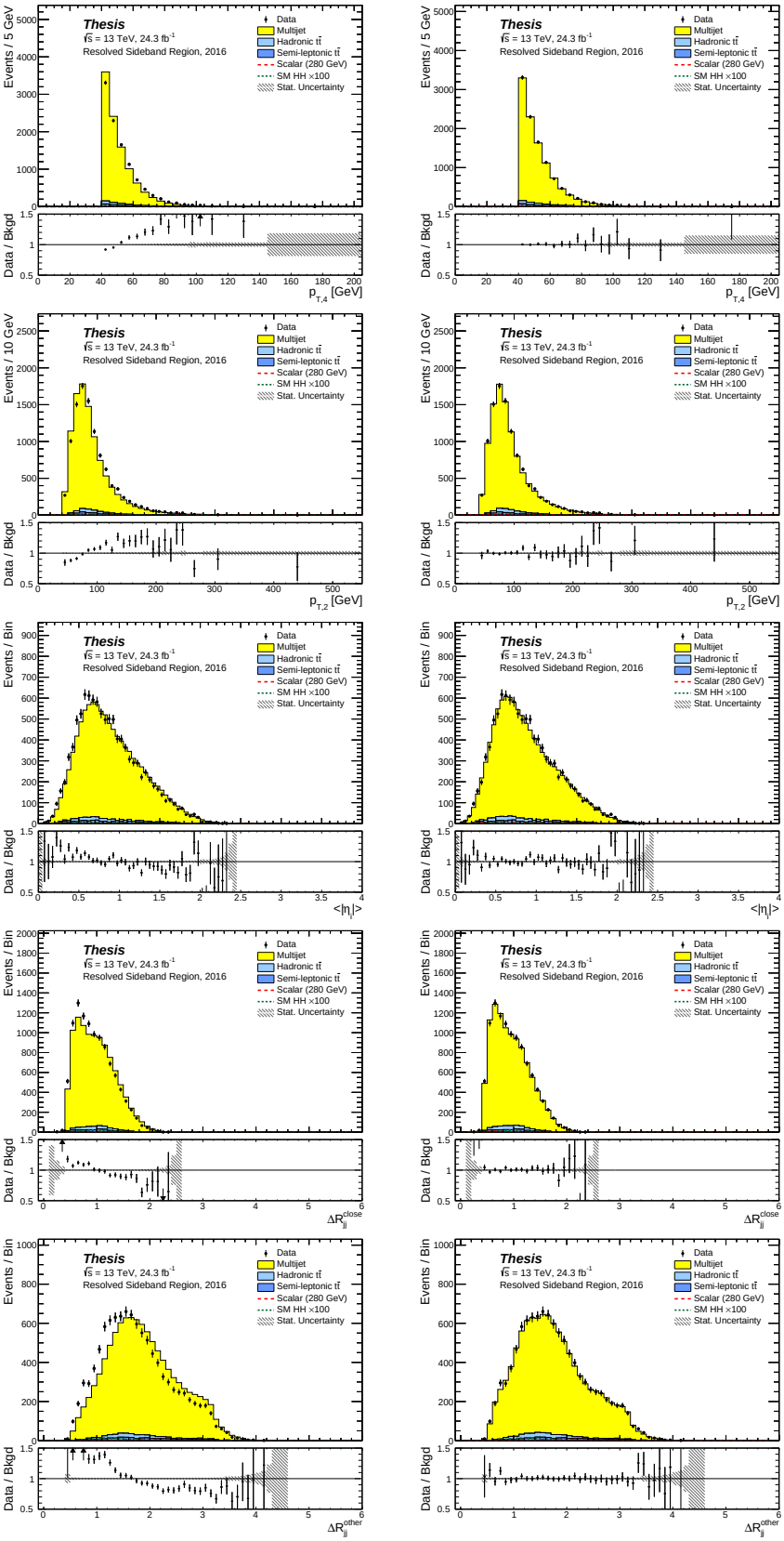

Figure 10.5: The reweighting distributions before (left) and after (right) the reweighting procedure had been applied.

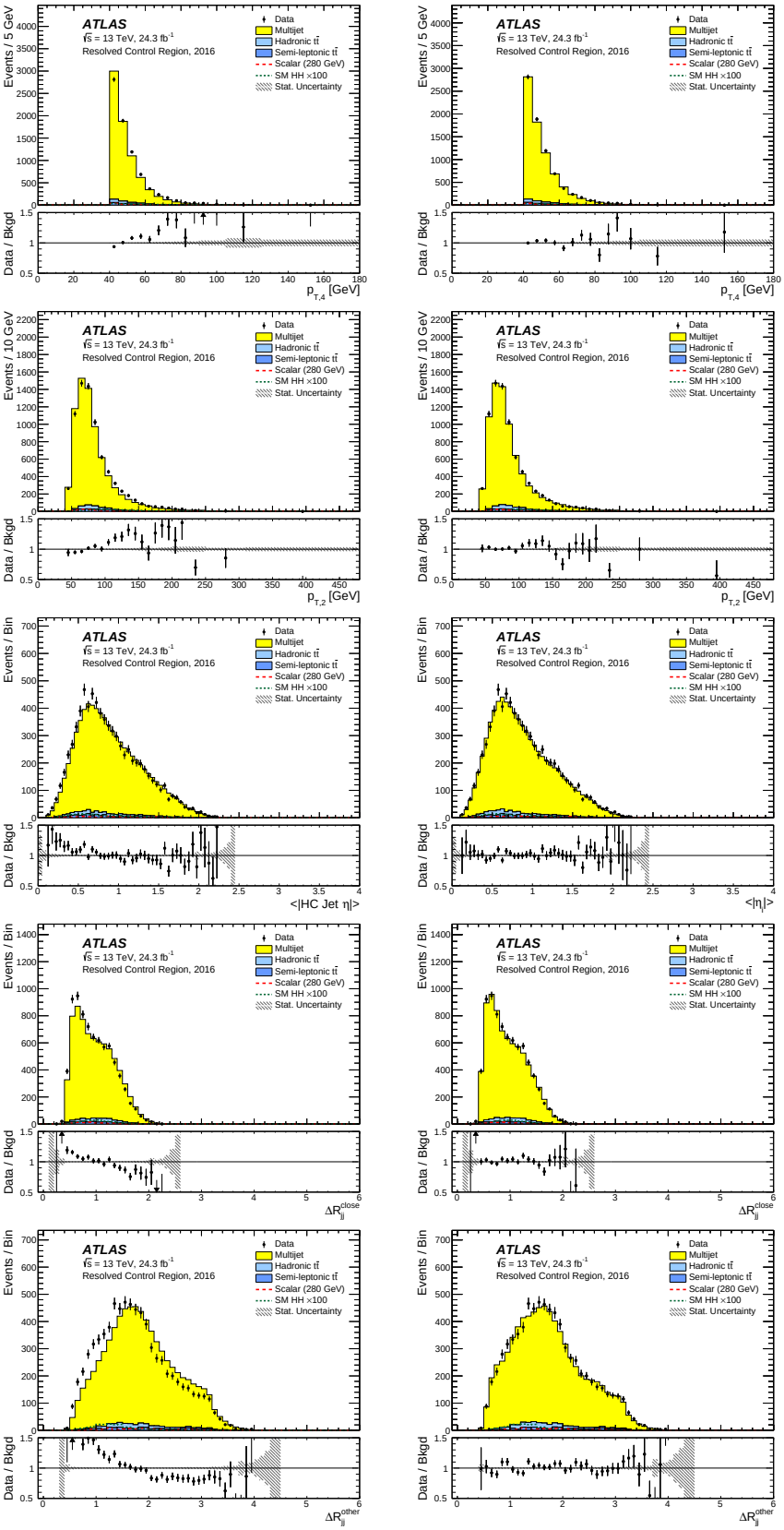

Figure 10.6: The Control Region reweighting distributions before (left) and after (right) the reweighting procedure had been applied.

	2015	2016
$\alpha^{\text{semileptonic}}_{t\bar{t},2b}$	0.91 ± 0.03	1.0 ± 0.01
$\alpha^{\text{semileptonic}}_{t\bar{t},4b}$	1.4 ± 0.5	1.7 ± 0.2

Table 10.2: Scale factors for the two and four tag semileptonic $t\bar{t}$ MC samples used for 2015 and 2016 data as measured in the Sideband. Uncertainties are purely statistical

To illustrate the robustness of the Sideband derived reweighting functions, Figure 10.13 shows the ratio of the data over the background model for the full two dimensional Higgs candidate mass plane. In particular this demonstrates that mismodeled features far outside the Sideband are corrected, giving confidence that the model may be extrapolated to the Signal Region. The most striking feature which is corrected is the low mass two to two gluon scattering peak which is expected to be more prevalent in the four-tag selection than the two-tag selection.

10.2 $t\bar{t}$ Background Modelling

Prior to the X_{Wt} top veto, $t\bar{t}$ makes up approximately 10% of the total expected background. The top veto removes about half of this remaining background. Absolute and relative acceptances for the $t\bar{t}$ cutflow are shown in Figure 10.14.

10.2.1 Semileptonic $t\bar{t}$

The semileptonic $t\bar{t}$ background shape is modelled using simulated events. The normalization is constrained in data using a semileptonic $t\bar{t}$ enriched region with at least one isolated muon with $p_{\text{T}} > 25\,\text{GeV}$. For the two tag selection the semileptonic $t\bar{t}$ is scaled directly to match the

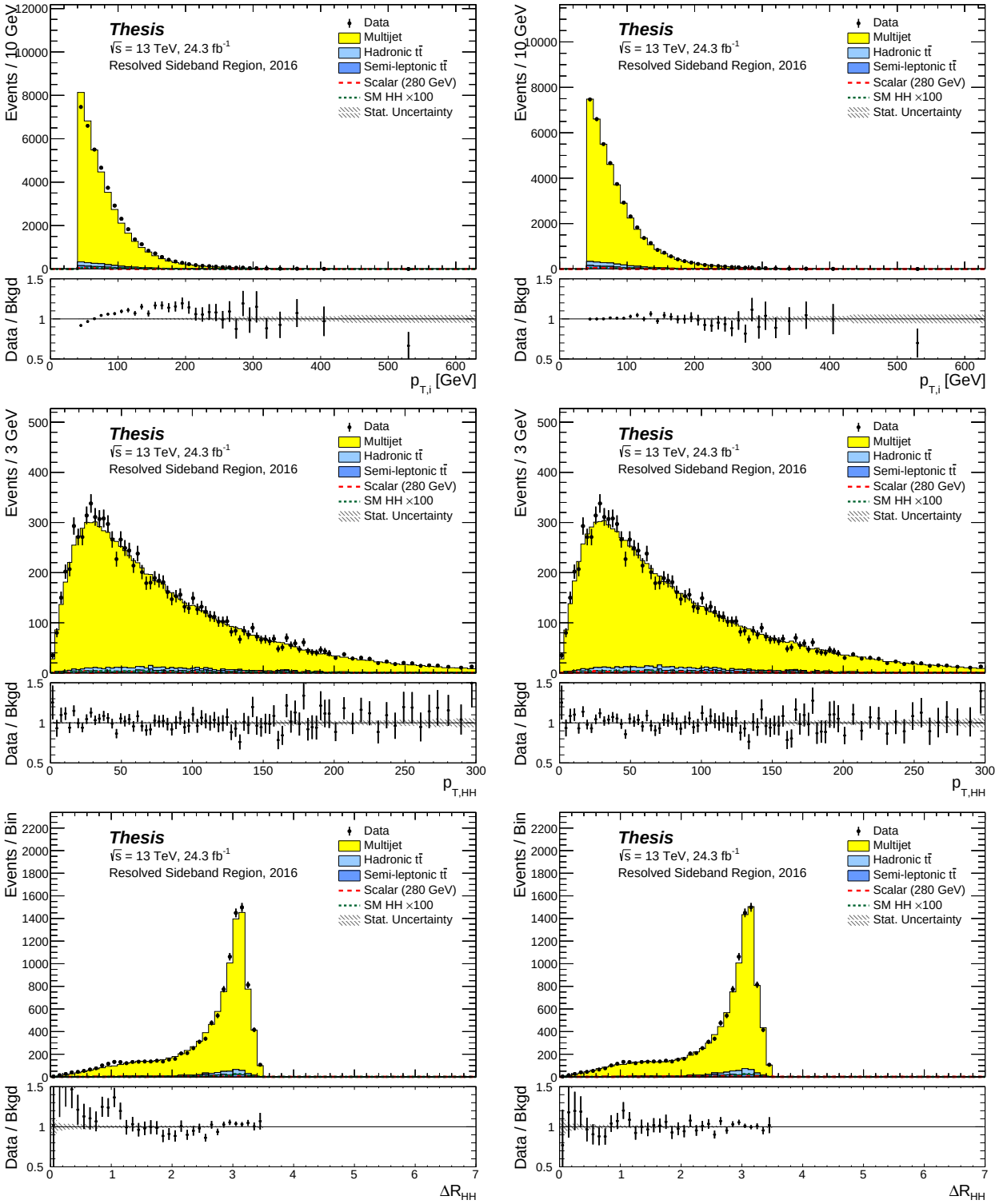

Figure 10.7: Sideband distributions before (left) and after (right) reweighting

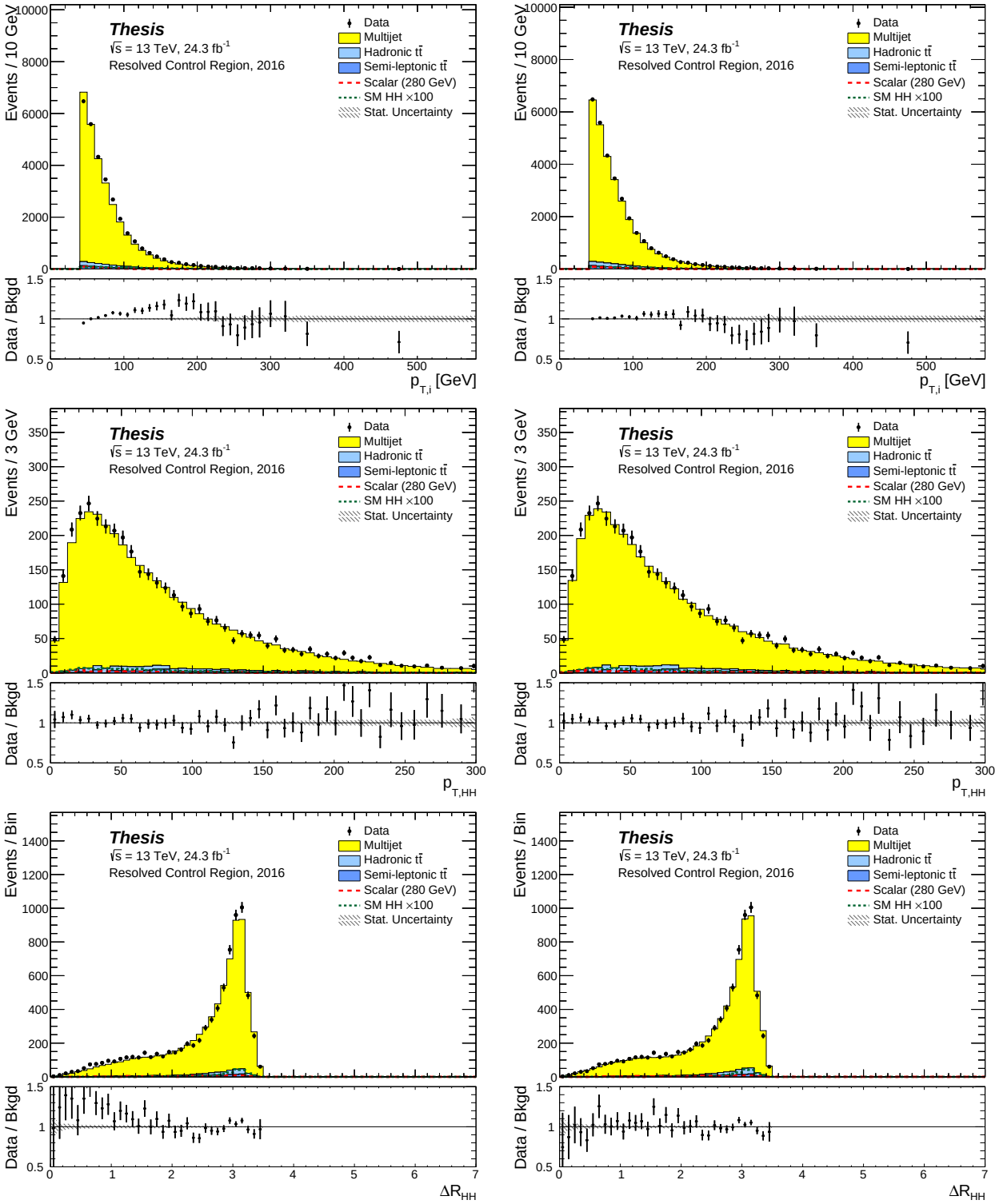

Figure 10.8: Control Region distributions before (left) and after (right) reweighting.

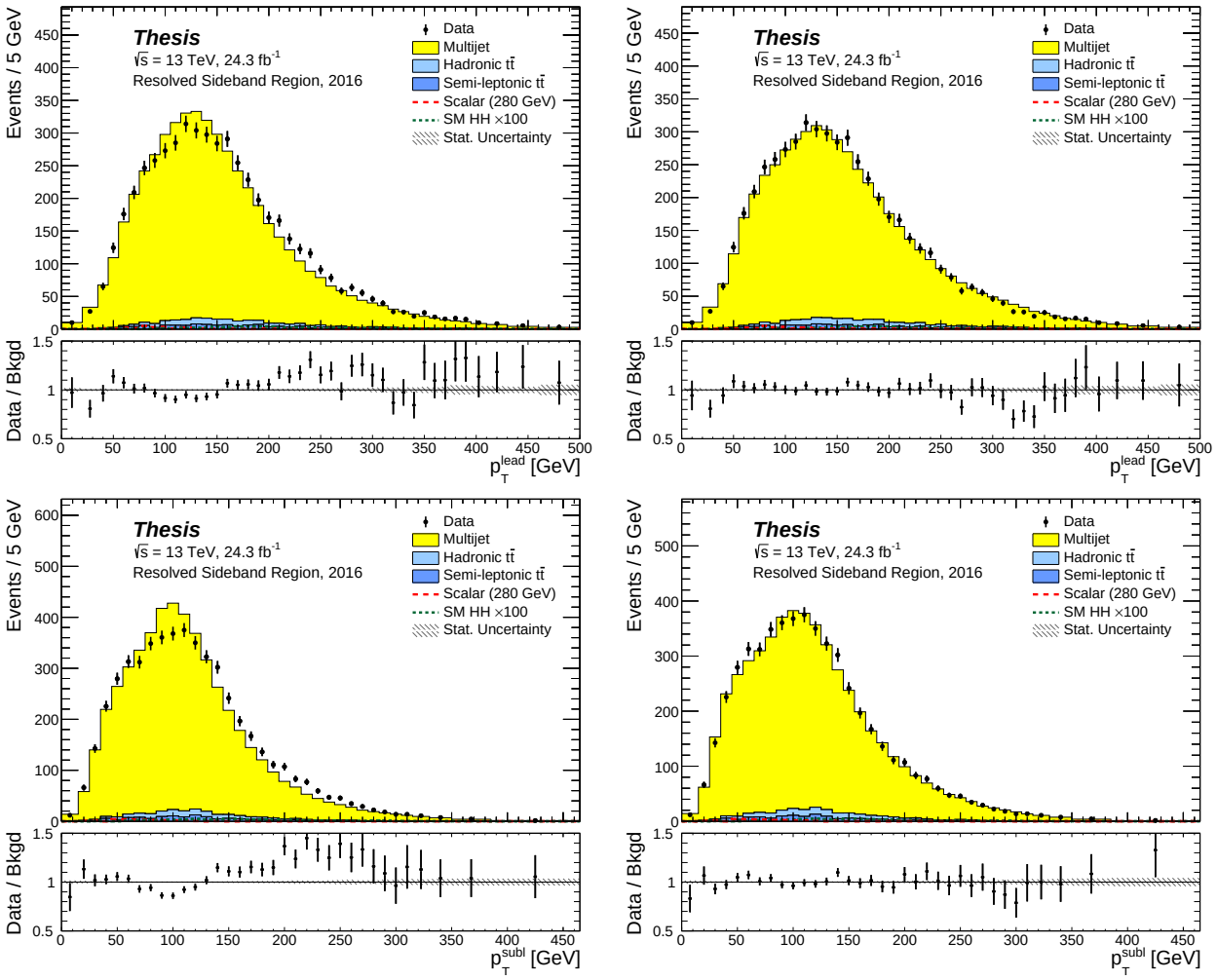

Figure 10.9: Sideband modeling of Higgs Candidate p_{T} in the Sideband and the full Higgs Candidate mass plane before (left) and after (right) reweighting.

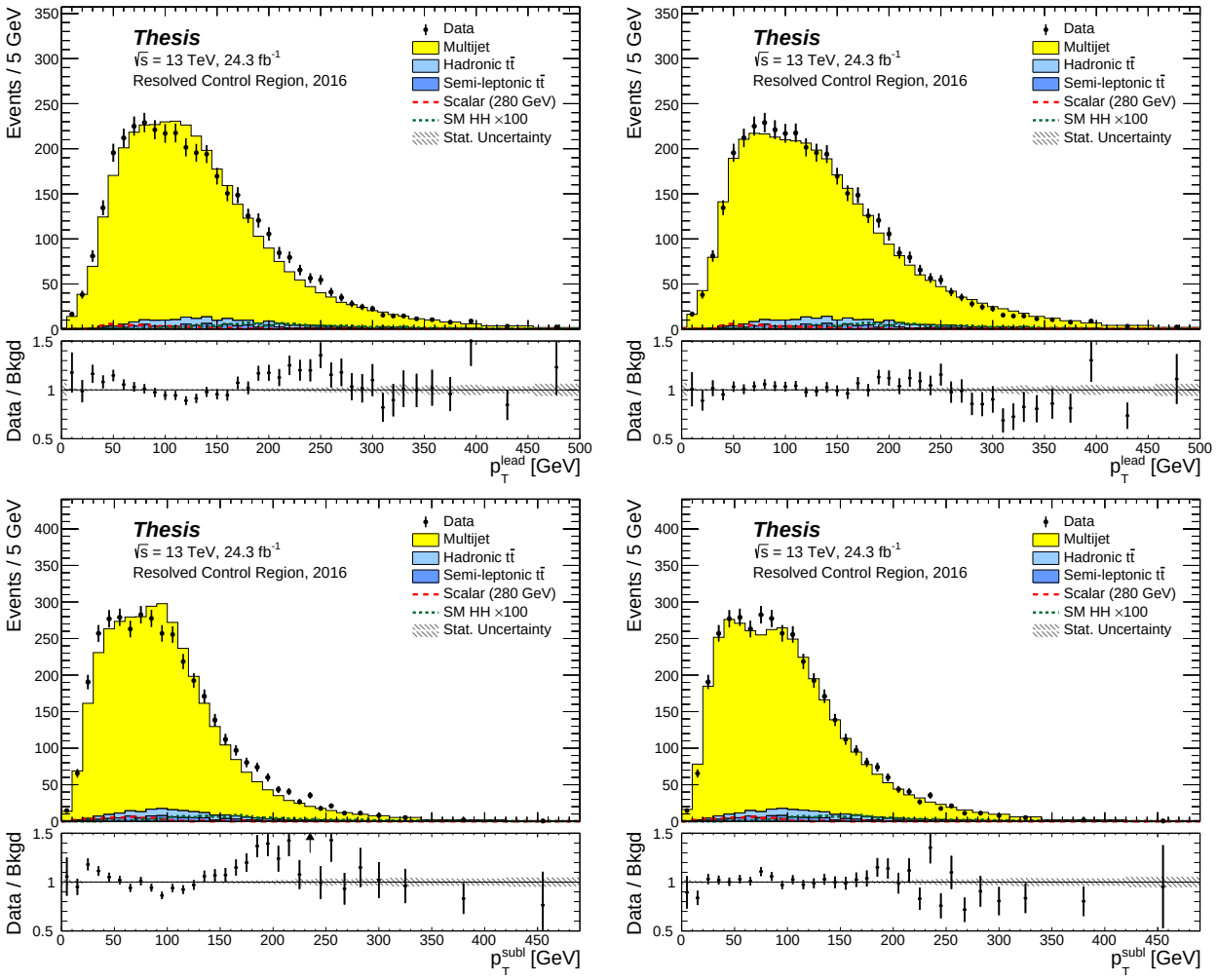

Figure 10.10: Control Region modeling of Higgs Candidate p_{T} in the Control Region before (left) and after (right) reweighting.

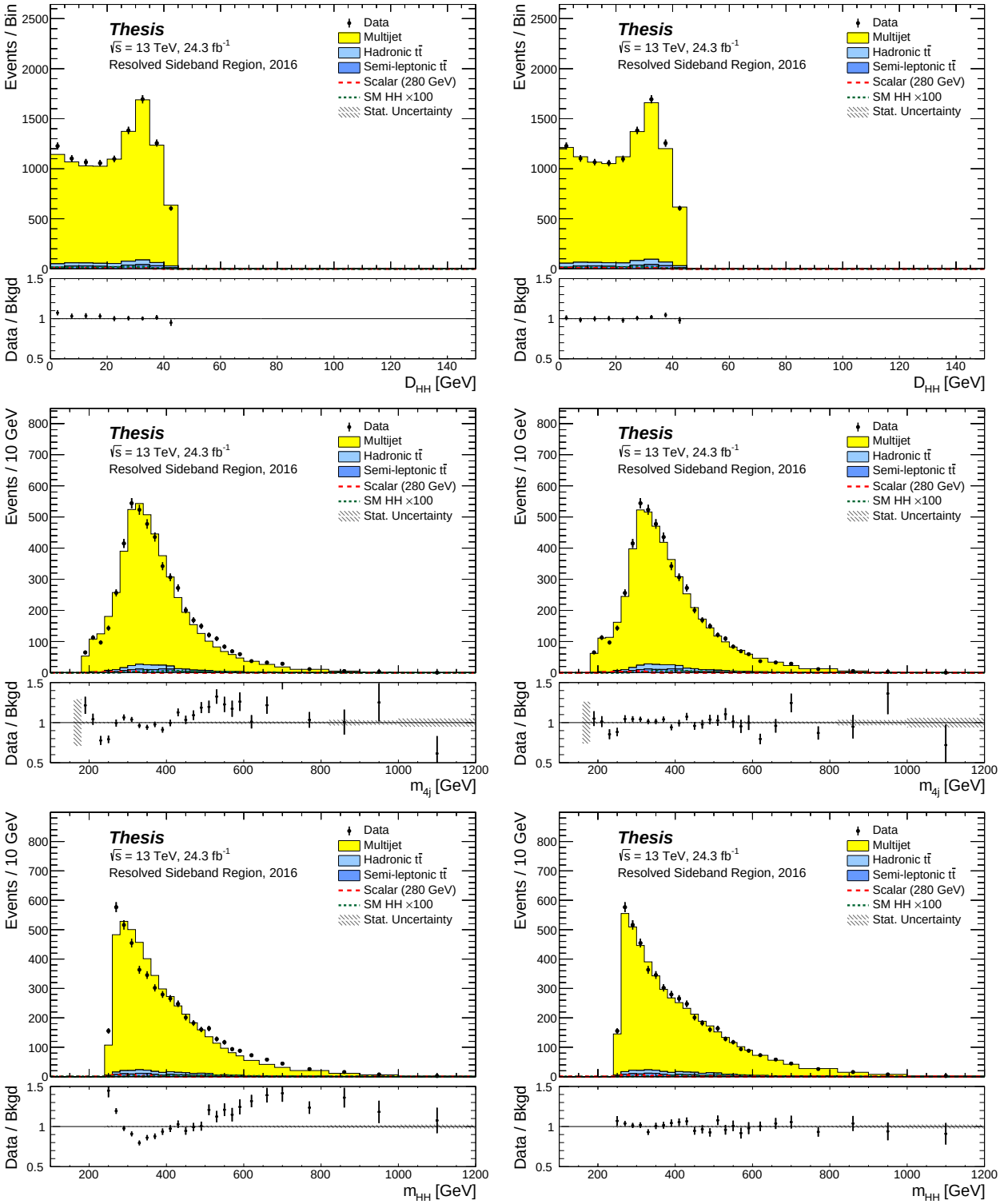

Figure 10.11: Sideband modeling of D_{HH}, and the corrected and uncorrected diHiggs spectra before (left) and after (right) reweighting.

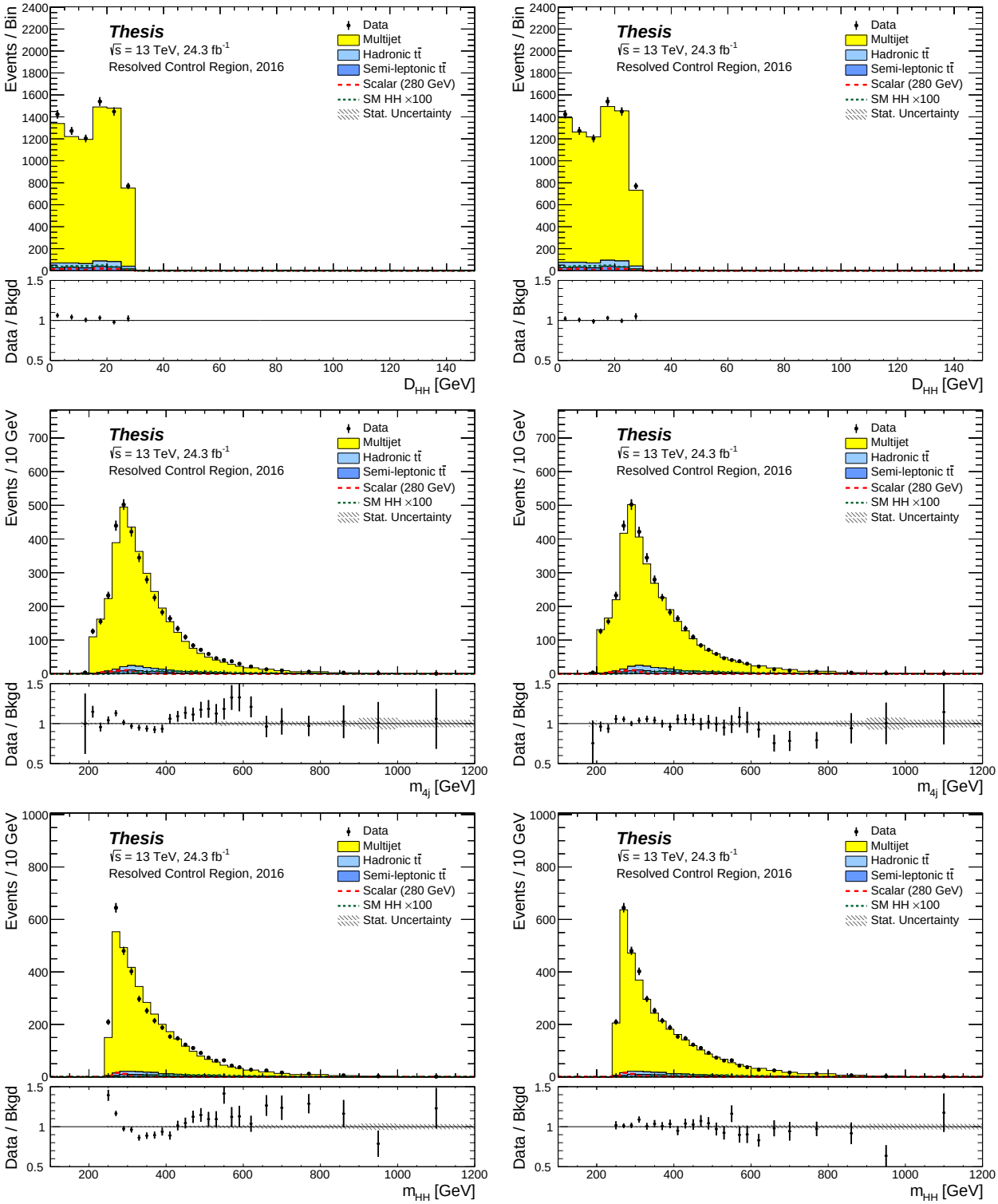

Figure 10.12: Control Region modeling of D_{HH}, and the corrected and uncorrected diHiggs spectra before (left) and after (right) reweighting.

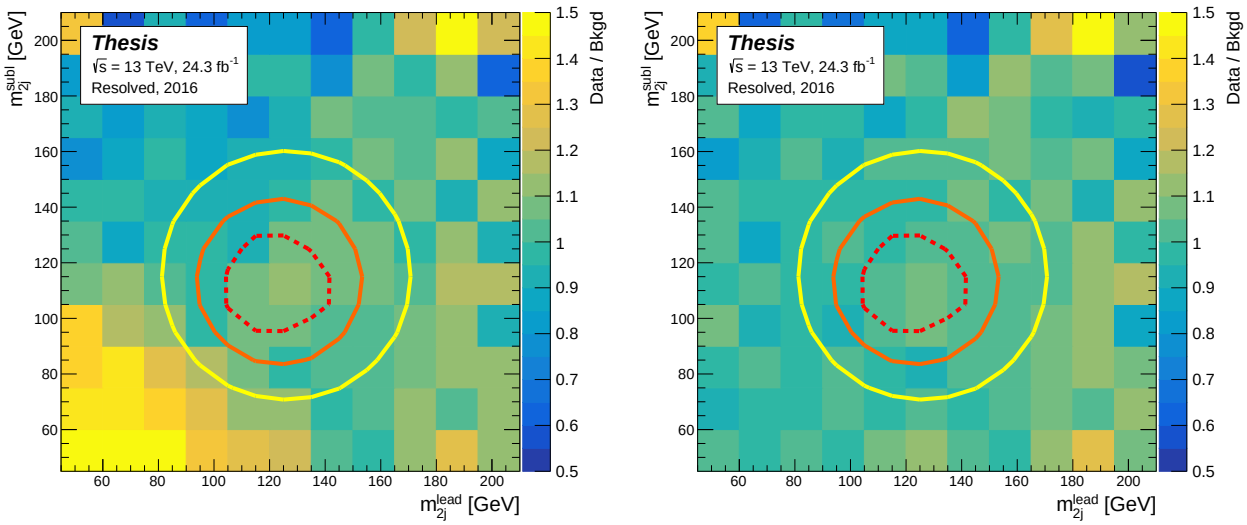

Figure 10.13: Modeling of the full Higgs Candidate mass plane before (left) and after (right) reweighting. The color axis of the plot represents the ratio of the data over the background model. The circles show the boundaries of the Sideband, Control and Signal Regions in yellow, orange and dashed red respectively.

data yield in the semileptonic $t\bar{t}$ enriched region. The ratio of the data over the background in Figure 10.15 is one by construction for the "two-tag" plots because the multijet background is defined as the data minus the $t\bar{t}$ components. These scale factors are shown in Table 10.2. For the four tag selection the semileptonic $t\bar{t}$ enriched region is used in a combined fit to extract the multijet and hadronic $t\bar{t}$ scale factors. The multijet and hadronic $t\bar{t}$ enriched regions are described in the following section and the results of the fit are summarized in Table 10.3. The scale factors $\alpha_{t\bar{t},4b}^{\text{semileptonic}}$ and $\alpha_{t\bar{t}}^{\text{hadronic}}$ are not necessarily expected to be consistent with 1 due to the difficulty of modeling the flavour fractions of additional jets in $t\bar{t}$ +jets processes. The impact of this uncertainty is estimated and found to be negligible as described in Section 11.1.

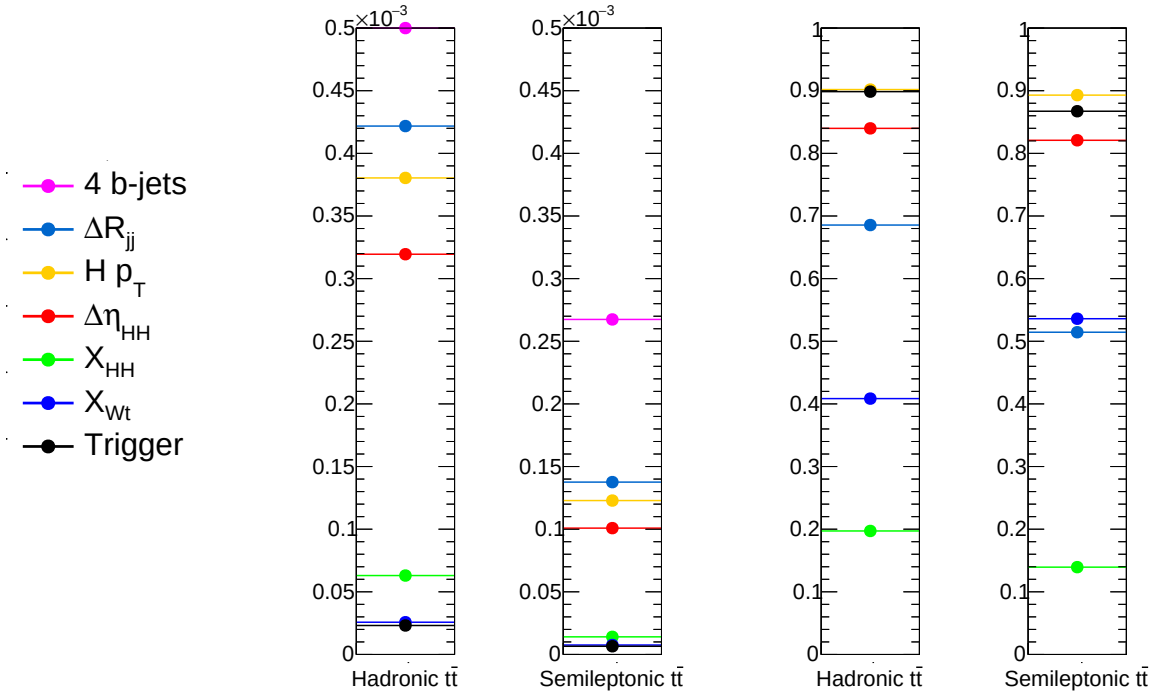

(a) Absolute Acceptance (b) Relative Acceptance

Figure 10.14: (a) $t\bar{t}$ acceptance at each stage of the cutflow. (b) Relative $t\bar{t}$ acceptance of each cut. The stages are shown in the order they were applied in the legend with the first cut at the top.

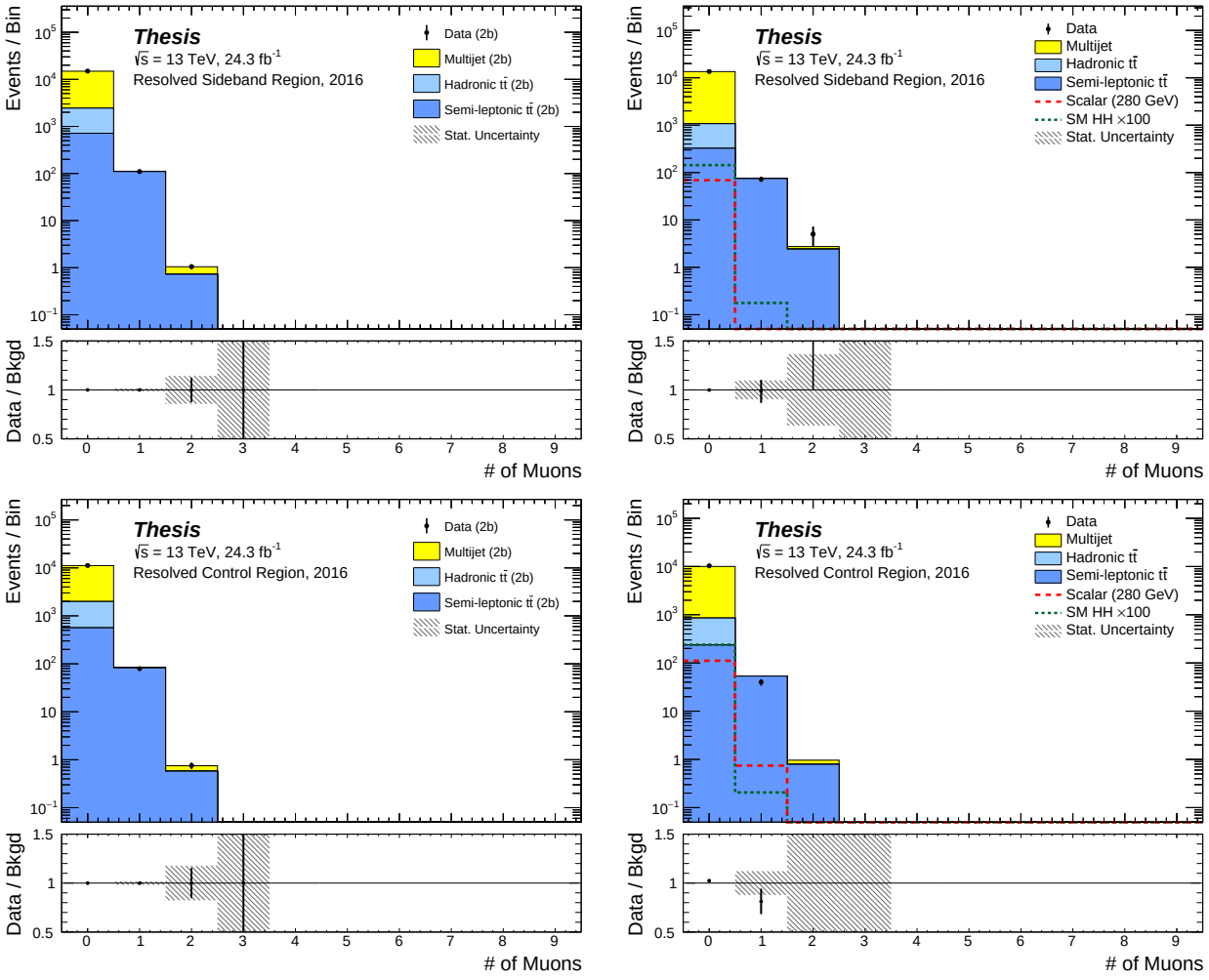

Figure 10.15: The two-tag (left) semileptonic $t\bar{t}$ is normalized with the > 1 prompt muon bins in the Sideband (top). The ratio is 1 by construction. The four-tag (right) semileptonic $t\bar{t}$ is constrained with a combined fit using the > 1 prompt muon bins as semileptonic $t\bar{t}$ enriched region. The yield in the Control Region (bottom) is consistent with the Sideband derived scale factor.

	2015			2016		
	μ_{multijet}	$\alpha_{t\bar{t}}^{\text{hadronic}}$	$\alpha_{t\bar{t},4b}^{\text{semileptonic}}$	μ_{multijet}	$\alpha_{t\bar{t}}^{\text{hadronic}}$	$\alpha_{t\bar{t},4b}^{\text{semileptonic}}$
Prefit	0.088	0.717	1.0	0.202	1.036	1.0
Postfit	0.084 ± 0.004	1.2 ± 0.5	1.4 ± 0.5	0.201 ± 0.003	1.2 ± 0.3	1.7 ± 0.2

Table 10.3: Scale factors before and after the combined fit to the multijet, allhadronic $t\bar{t}$ and semileptonic $t\bar{t}$ enriched regions in the Sideband

10.2.2 Hadronic $t\bar{t}$

The hadronic $t\bar{t}$ background shape is modelled with simulated events passing the two-tag selection, and is reweighted with the same reweighting functions as derived for the multijet background. The two-tag selection is used because the simulated four-tag hadronic $t\bar{t}$ statistics are low. All relevant kinematic distributions are modelled well as shown in Appendix B.

Prior to the top veto, the X_{Wt} (Equation 8.4) distribution is used to define multijet and hadronic $t\bar{t}$ enriched regions. Events with X_{Wt} below 0.75 are in the hadronic $t\bar{t}$ enriched region while events with X_{Wt} greater than 0.75 fall in the multijet enriched region. In order to properly account for statistical correlations, a combined fit is performed on the multijet, hadronic $t\bar{t}$ and semileptonic $t\bar{t}$ enriched regions. The prefit and postfit scale factors are summarized in Table 10.3 and the result of the fit in the final iteration of reweighting is shown in Figure 10.16

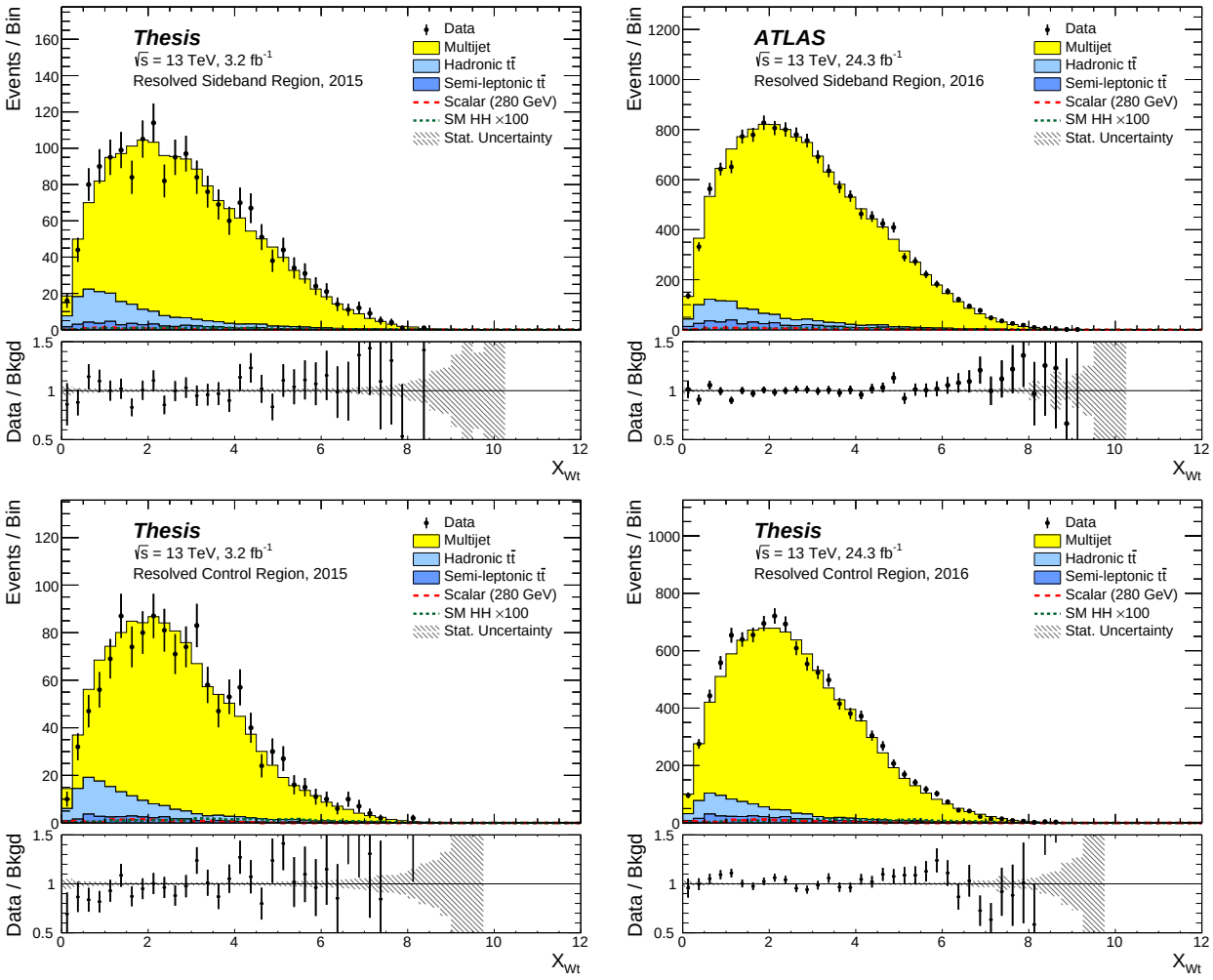

Figure 10.16: The post-fit X_{Wt} distributions in the Sideband (top) for 2015 (left) and 2016 (right) and the result in Control Region (bottom).

Chapter 11

SYSTEMATIC UNCERTAINTIES

In any physical measurement there are two primary categories of uncertainty: Statistical and systematic uncertainty. Statistical uncertainties are relatively straightforward to assess and are the consequence of a finite sample size of data and simulated events. Systematic uncertainties arise from underlying assumptions regarding the detector response, theoretical calculations and from potential biases due to the measurement procedure. This chapter summarizes the known sources of systematic uncertainty in both the signal and background modeling. In section 11.1 we show that the background modeling procedure is insensitive to large variations in the assumed $t\bar{t}$ model and then summarize our procedure for estimating the size of potential systematic biases in the total background model. Section 11.2 describes the impact of the detector modeling systematics on the signal simulation. Finally in 11.3 we describe our assessment of the theoretical uncertainty of the signal models.

11.1 Background Modeling Uncertainties

The background model is derived from data, and while there is uncertainty in the $t\bar{t}$ modeling, any variation in the $t\bar{t}$ model will result in a different derived multijet model due to the $t\bar{t}$ subtraction in the reweighting procedure (Section 10.1.3). In the ideal case of infinite statistics and a high dimensional reweighting function, the reweighted two tag data could model both the multijet and $t\bar{t}$ backgrounds without the need for simulated events. The $t\bar{t}$ modeling uncertainties are therefore absorbed by the uncertainties associated with the imperfect reweighting procedure.

To check this claim, we run the background derivation using two variations of the $t\bar{t}$ model,

artificially weighting simulated events:

1. Hard and Soft variations of the $m_{4\text{j}}$ $t\bar{t}$ shapes used for the four tag $t\bar{t}$ background models.

2. Up and Down variations of the X_{Wt} shape used for the hadronic $t\bar{t}$ constraint.

The resulting variations in the background components and the total background are shown in Figures 11.1 and 11.2 for the $m_{4\text{j}}$ and X_{Wt} variations. The change in the total background is covered by the statistical uncertainty of the background model despite the artificially large $t\bar{t}$ variations, demonstrating that the reweighting procedure can account for large $t\bar{t}$ mismodeling.

As an additional cross check, the background model is re-derived using a $t\bar{t}$ sample generated with AMC@NLO+Herwig instead of the nominal Powheg+Pythia sample. Again, the change in the total background model is found to be covered by the statistical uncertainty. The results are shown in Figure 11.3.

The nominal background model is derived by determining the multijet and $t\bar{t}$ normalizations, pseudo-tag rate for the jet multiplicity modeling and the kinematic reweighting functions in the Sideband Region of the Higgs candidate mass plane (Figure 8.7). We obtain an estimate for the bias resulting from deriving the background model away from the Signal Region by re-deriving the full background model using the Control Region. Figure 11.4 compares this new background model to the nominal background model in the Control Region. Both models are consistent with the data in the Control Region. The results of the background derivation in the Control Region are shown in more detail in Appendix D.

Non-closure between the Sideband and Control Region derived background models in the Signal Region are used to define systematic uncertainties in the final fit. In order to allow

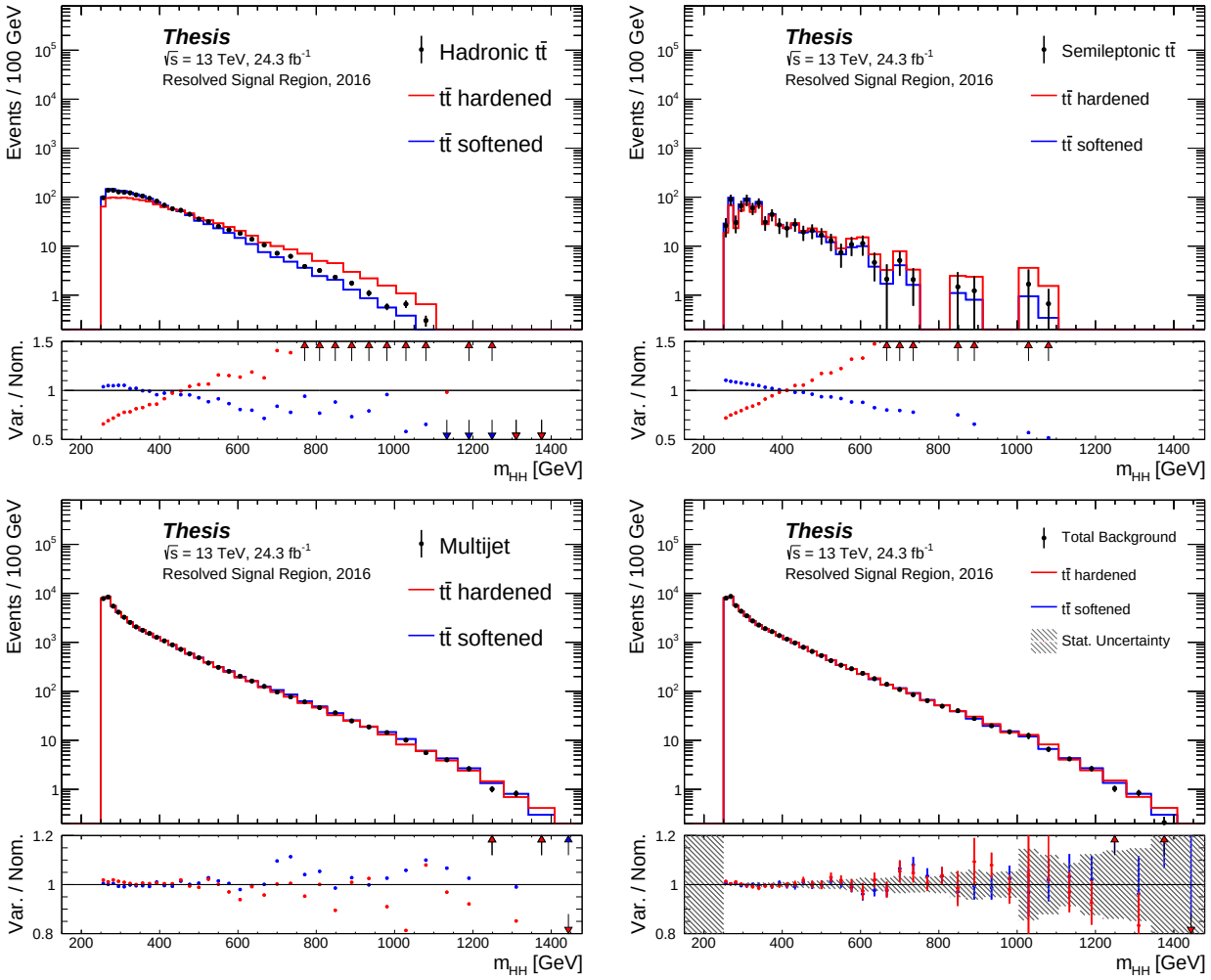

Figure 11.1: Artificial $t\bar{t}$ variations of $m_{4\mathrm{j}}$ and impact on the derived multijet and total background prediction in the Signal Region. Top Left: The hadronic $t\bar{t}$ background variations. Top Right: The semileptonic $t\bar{t}$ background variations. Bottom Left: The variation in the derived multijet background after the $t\bar{t}$ variations were applied. Bottom Right: The total derived background model after the $t\bar{t}$ variations were applied. No significant variation in the total background is observed.

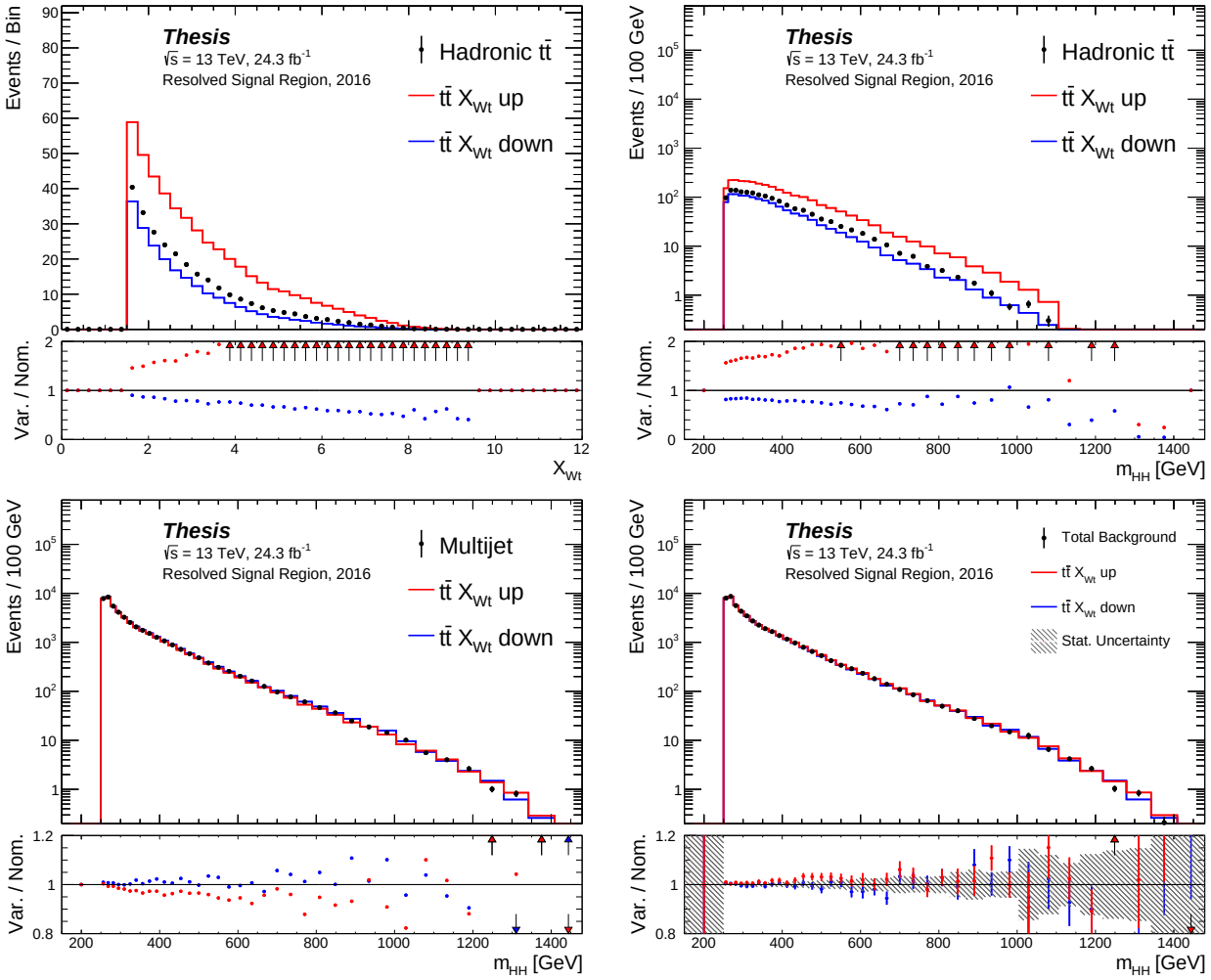

Figure 11.2: Artificial $t\bar{t}$ variations of X_{Wt} and impact on the derived multijet and total background prediction in the Signal Region. Top Left: The hadronic $t\bar{t}$ X_{Wt} distribution variations. Top Right: The hadronic $t\bar{t}$ m_{HH} spectra after applying the X_{Wt} variations. Bottom Left: The variation in the derived multijet background after the X_{Wt} variations were applied. Bottom Right: The total derived background model after the X_{Wt} variations were applied. No significant variation in the total background is observed.

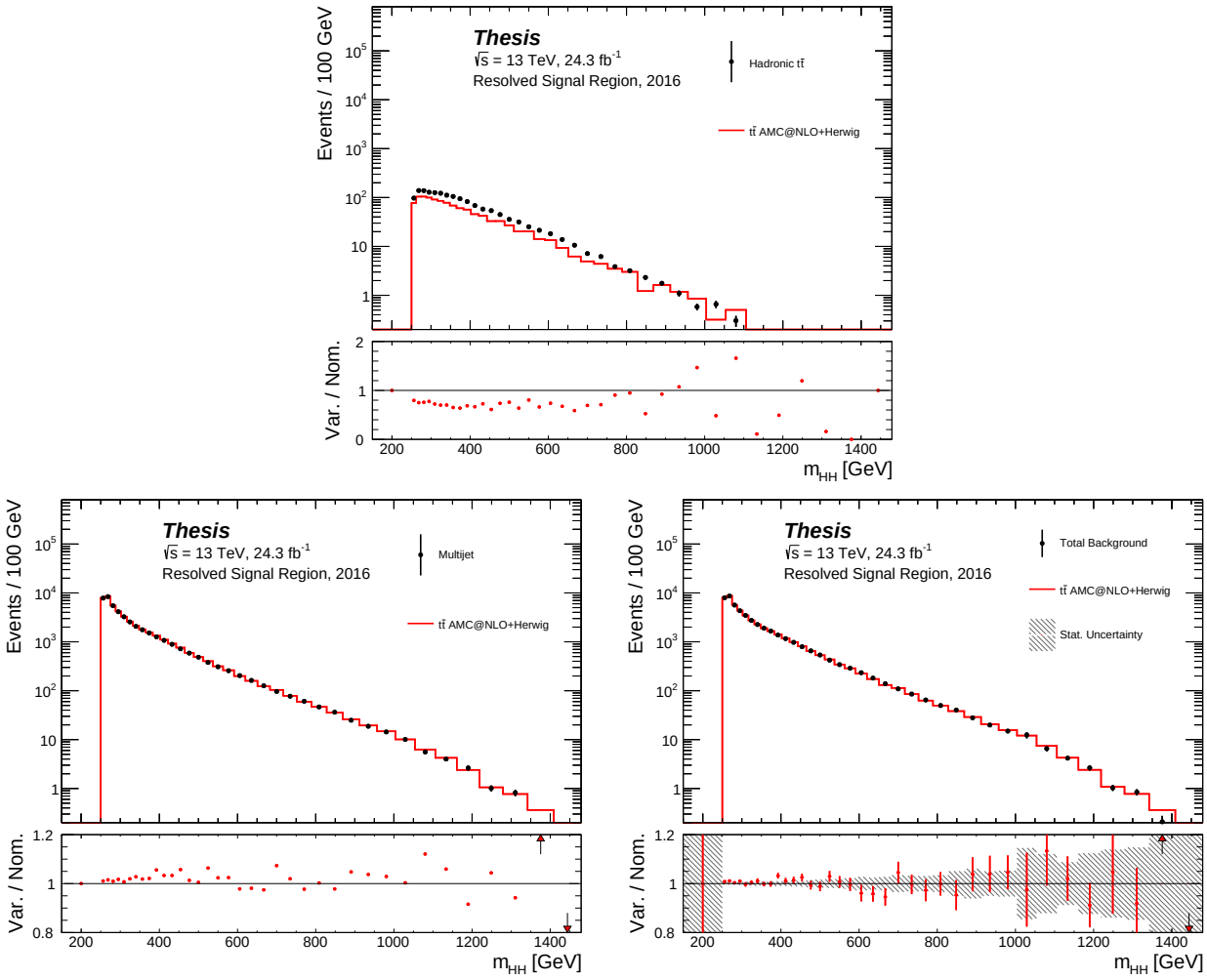

Figure 11.3: Comparison of the hadronic $t\bar{t}$ model when using AMC@NLO+Herwig versus the nominal model using Powheg+Pythia and the resulting multijet and total background models.

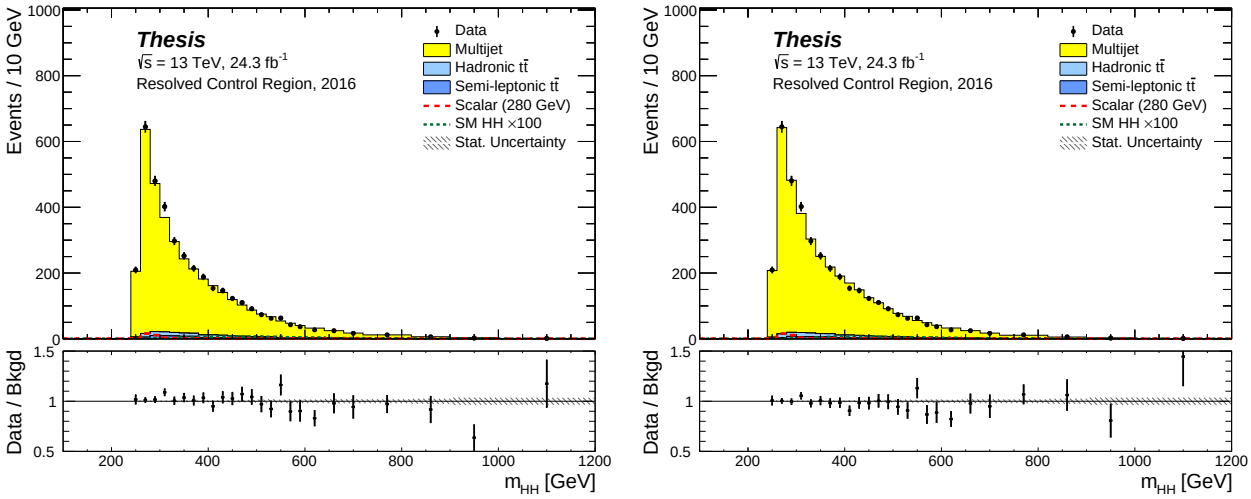

Figure 11.4: Background modeling in the Control Region using the nominal model as derived in the Sideband on the left and using the model as derived in the Control Region on the Right.

the final fit to vary the peak and tail of the m_{HH} distribution independently, we split the variations by the scalar sum of the Higgs candidate jet p_{T}'s which we call $\mathrm{H}_{\mathrm{T}}^{4\mathrm{j}}$. The low and high $\mathrm{H}_{\mathrm{T}}^{4\mathrm{j}}$ variations are split by considering events below and above $\mathrm{H}_{\mathrm{T}}^{4\mathrm{j}} = 300\,\mathrm{GeV}$ respectively. We assign $\pm 1\sigma$ variations by scaling the nominal background bin by bin in m_{HH} by the ratios of the variation over the nominal model and the nominal model over the variation. We refer to these variations as Control Region Weighted and Control Region Inverted respectively. Figure 11.5 shows the resulting model variations while Figure 11.6 shows the quadrature sum of the background systematic and statistical uncertainties in the Control Region.

11.2 Detector Modeling Uncertainties

In this section we describe the systematic uncertainties associated with the detector response using the SM HH sample to illustrate their impact across the full m_{HH} range. Figure 11.7 shows the impact of the trigger emulation uncertainty which is relatively flat at 2.5% across

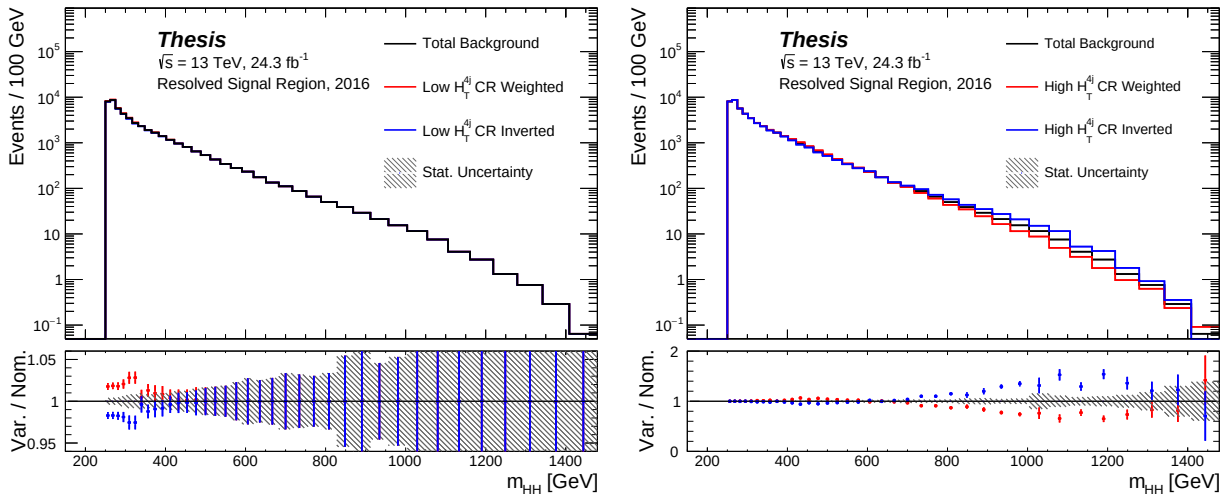

Figure 11.5: Background model variations. CR Weighted refers to the model derived in the Control Region while CR Inverted refers to the variation generated by inverting the ratio of the CR weighted model over the nominal model. The variations are split into high and low H_T^{4j} regions to allow more flexibility in the final fit.

the considered mass range. The derivation of this uncertainty is described in Chapter 9.3.

Jet Energy Scale - We provide a brief summary here of the derivation of the Jet Energy Scale (JES) and its associated uncertainties. For a complete description see reference [25]. The four-vectors of jets are extrapolated from the shape and total energy deposition of the shower generated in the sampling calorimeters and the location of the primary vertex. Additionally, tracking information is used like the number of tracks from the inner detector which point into the jet cone and the number of muon spectrometer segments associated to the jet in cases where the jet shower is not fully contained in the calorimeter. The algorithm which maps the detector response to a calibrated jet four-vector defines the JES and can be broken down into six stages:

1. **EM-Scale Jets:** Jets are constructed from clusters of calorimeter cells with signals above a noise threshold. Energies are computed assuming the interactions between the shower particles and the calorimeter were electromagnetic.

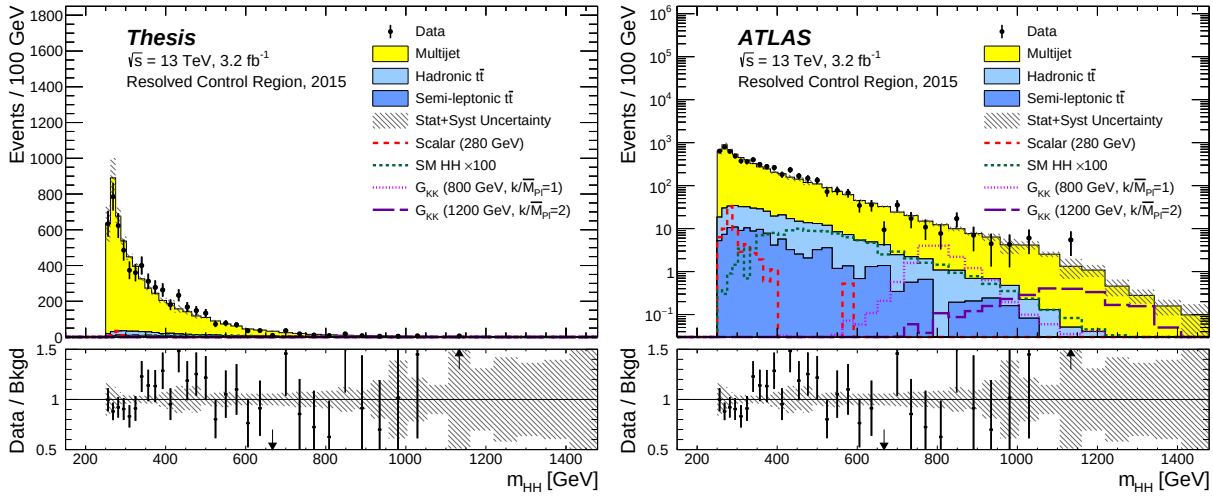

(a) 2015

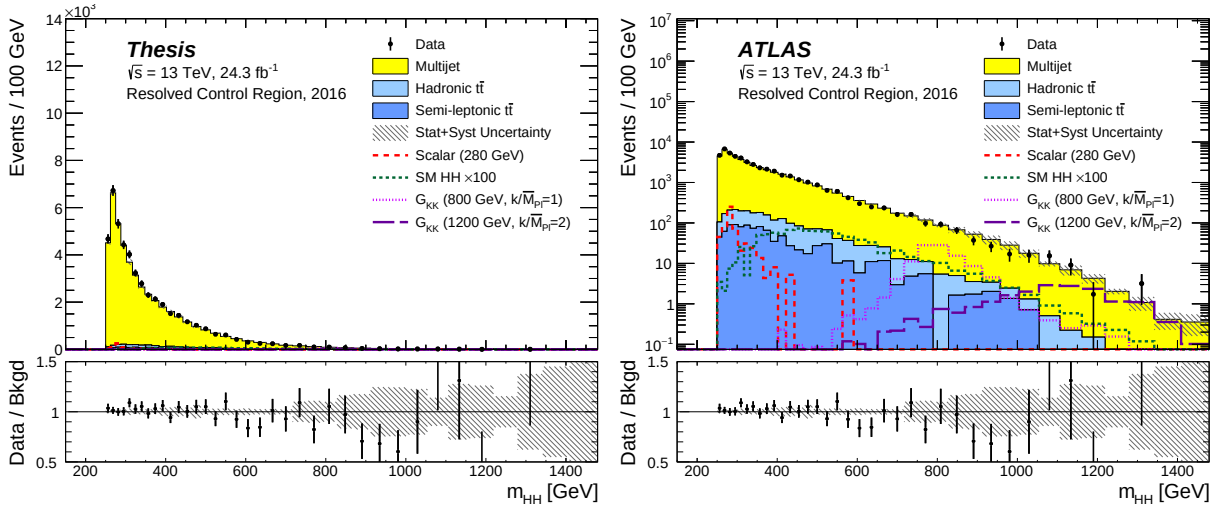

(b) 2016

Figure 11.6: Background model in the Control Region with systematic and statistical uncertainties added in quadrature (shown with linear (left) and log (right) scales on the y-axis).

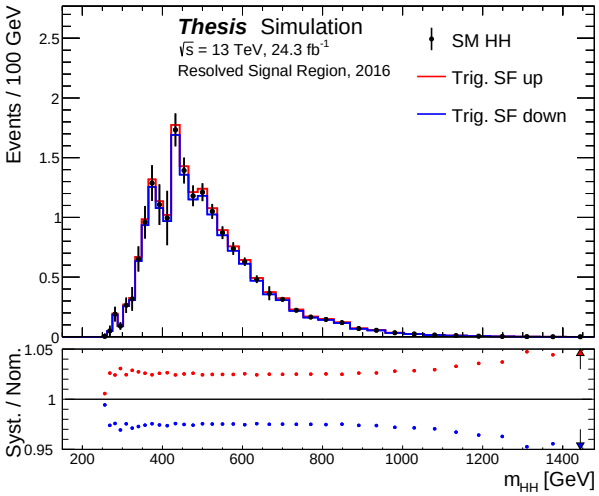

Figure 11.7: Trigger efficiency Scale Factor (SF) modeling uncertainties applied to the SM HH signal sample in the Signal Region.

2. **Origin Correction:** The jet four-vector is scaled to point at the primary vertex while keeping the total energy constant.

3. **Pile-up Correction:** The measured median energy density deposited by pile-up vertices as a function of η and ϕ is subtracted and an additional correction is applied as a function of the number of pile-up vertices and proton interactions.

4. **Particle Level Calibration:** Calorimeter response functions are determined by Gaussian fits to the ratio of the reconstructed energy over the sum of the energies of the truth level particles from simulation. The response functions are measured as a function of truth energy and detector η. Percent level residual biases in the reconstructed jet η due to jets with energy deposits in the barrel and endcap calorimeters are corrected by applying additional calibration factors to the jet η and p_{T}.

5. **Global Sequential Calibration:** GSC corrects for JES dependence on the flavor of the parton which initiated the jet as well as energy leakage either in uninstrumented regions or from jet showers not being fully contained in the calorimeter. Correction

factors are applied depending on the number and momentum of tracks associated to the jet and on the fraction of energy deposited in various layers of the calorimeter.

6. ***In Situ* Calibration:** This final stage corrects the calorimeter response as measured in data to that measured in simulation. It utilizes well calibrated objects to correct the p_{T} of less well calibrated objects by assuming the conservation of transverse momentum. Events with an isolated central jet with $|\eta| < 0.8$ and a forward jet with $0.8 < |\eta| < 4.5$ are used to balance the well calibrated central jet p_{T} against the p_{T} of the less well calibrated forward jet. This η-intercalibration stage flattens the ratio of the detector response in data to the response in simulation as a function of η and p_{T}. Next the absolute scale difference between data and simulation is determined by balancing jet p_{T} against the p_{T} of photons or Z bosons which decay to precisely measurable muons or electrons. This allows for the calibration of jets with p_{T} up to $\approx 1000\,\mathrm{GeV}$ at which point the statistics in data start to run out. Multijet events are then used by balancing jets with very high p_{T} against multiple jets which have already been calibrated. This Multijet Balance procedure can be bootstrapped up to momenta where the mulitjet statistics run out around $2000\,\mathrm{GeV}$. Jets above this scale cannot yet be calibrated in data and suffer from extrapolation uncertainties.

Each of these steps introduces sources of systematic uncertainty like the choice of simulation package, theoretical modeling of jet flavor composition, choices made in the event selection for the *in situ* calibration, and pile-up model. These are assessed by varying each choice and rerunning the JES derivation. Any non-closure as a function of reconstructed jet p_{T} and η for each variation is taken as a systematic uncertainty. This results in a huge list of uncertainties, many of which are highly correlated. To make the inclusion of these uncertainties computationally feasible for data analysis, an eigenvariation decomposition is performed. The three orthogonal directions in the space of variations with the largest uncertainties are

kept. This dimensional reduction only removes a small fraction of the total uncertainty correlation information and as such is considered sufficient for the majority of analyses, especially those that are already limited by statistics and analysis specific systematic uncertainty.

The impact of varying these three orthogonal JES nuisance parameters (NP 1-3) up and down are shown in Figure 11.8 in addition to single NP's derived for the η-intercalibration and Jet Energy Resolution (JER).

***b*-tagging Performance -** For the most recent complete public description of b-tagging in ATLAS see Reference [28]. This description is prior to the addition of the Insertable B-Layer (IBL) and uses the older multivariate tagging algorithm MV1 which is the same as the algorithm used in the 2016 trigger menu. Similar methods were used to calibrate the MV2c10 algorithm used for online b-tagging in this analysis [5]. For an early Run-2 performance study of the MV2 algorithms, see Reference [74]. The optimization of the MV2c10 algorithm used in this analysis is described in Reference [165].

Here we provide a brief summary of the measurement of the b-tagging efficiency and the derivation of b-jet scale factors and their associated uncertainties. A relatively pure ($\approx 90\%$) sample of leptonic $t\bar{t}$ events is selected in data by requiring two isolated opposite sign leptons (e, μ) with some additional kinematic selection: A tag and probe method requires the leptons be opposite flavor and exactly two jets be present with at least one b-tagged at the 85% working point. A complimentary approach based on a likelihood maximization allows same flavor leptons and two or three jets with no b-tagging requirement but places additional constraints on the missing transverse energy and the mass of the lepton pair to reduce the Z/γ+jets background. Both methods use an additional multivariate discriminant based on a boosted decision tree (BDT) utilizing kinematic inputs to enhance the $t\bar{t}$ purity. The two methods are found to give consistent results and similar uncertainties. In the following we focus on the conceptually simpler tag and probe method.

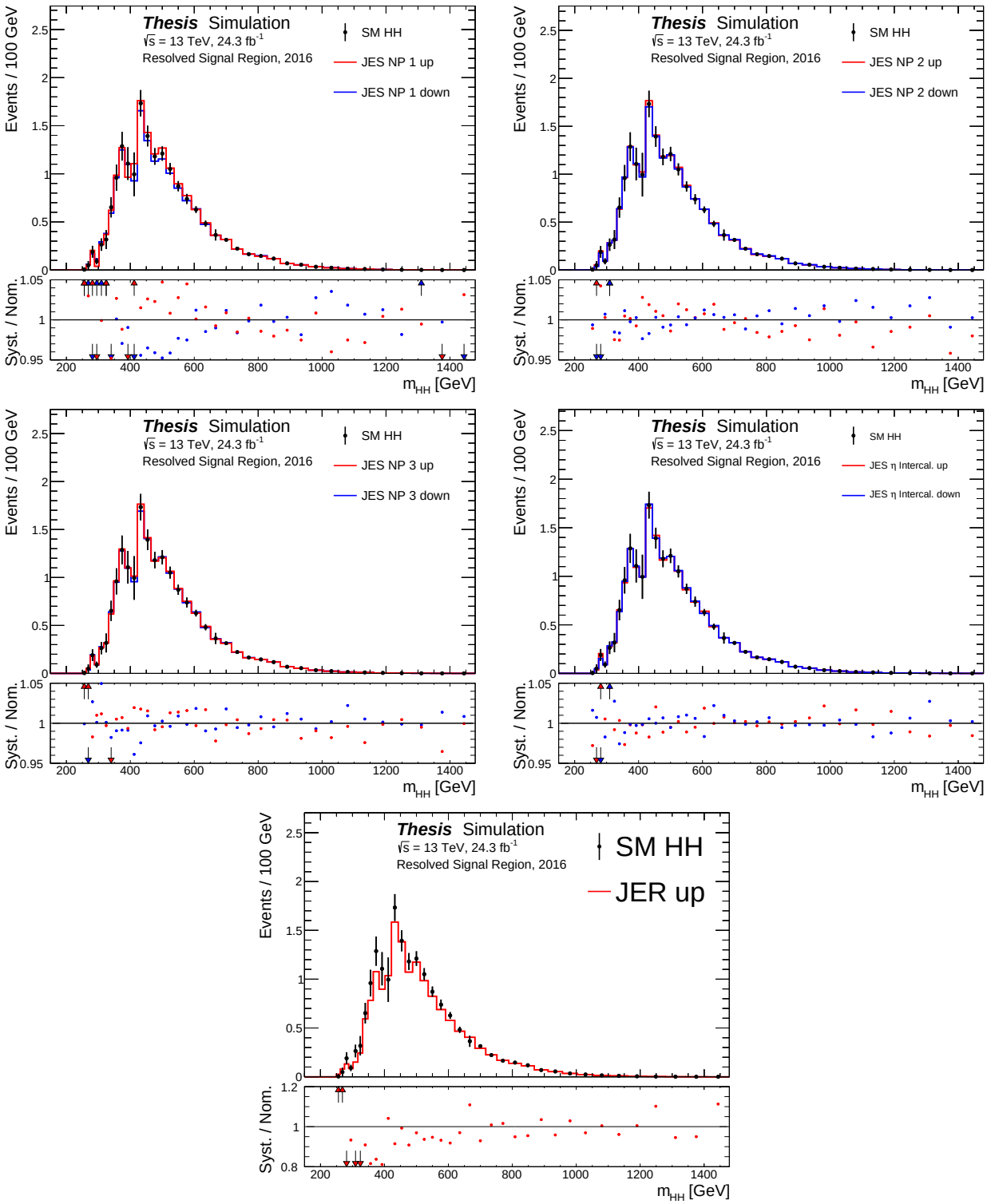

Figure 11.8: Calorimeter calibration and resolution modeling uncertainties applied to the SM HH signal sample in the Signal Region

The fraction of events in data where the second (probe) jet is also b-tagged (f_{tagged}) can be measured in bins of p_{T} and η. In these same bins, the fraction of events where the probe jet contains a true b-hadron (f_b) and the efficiency to tag a non-b-jet (ϵ_j) are taken from simulated $t\bar{t}$ samples. Then ϵ_b, the efficiency to tag a b-jet, is measured in each bin by solving the following equation:

$$f_{\text{tagged}} = f_b\epsilon_b + (1 - f_b)\epsilon_j \tag{11.1}$$

The dominant systematic uncertainty in this measurement of ϵ_b comes from the uncertainties in the simulated sample flavor composition and light jet rejection. Fortunately both $(1 - f_b)$ and ϵ_j are small due to the purity of the $t\bar{t}$ sample in data and the $\mathcal{O}(100)$ light jet rejection of the MV2c10 algorithm respectively.

Similarly to the procedure used for the JES uncertainties described above, an eigenvariation decomposition is performed over the full set of systematic variations. The six largest eigenvariations are kept and their impacts on the SM HH signal sample in the Signal Region after the full event selection are shown in Figure 11.9.

11.3 Theoretical Uncertainties

The theoretical uncertainties on the signal model acceptance times efficiency ($A \times \varepsilon$) are evaluated by analysis of specially-generated, particle-level signal samples. The generation of these samples follows the configuration of the baseline samples, but with modifications to probe the following theoretical uncertainties:

1. Uncertainties due to missing higher order terms in the scattering matrix elements.

2. Uncertainties in the modeling of the underlying event (including multi-parton interactions), of hadronic showers and of initial and final state radiation.

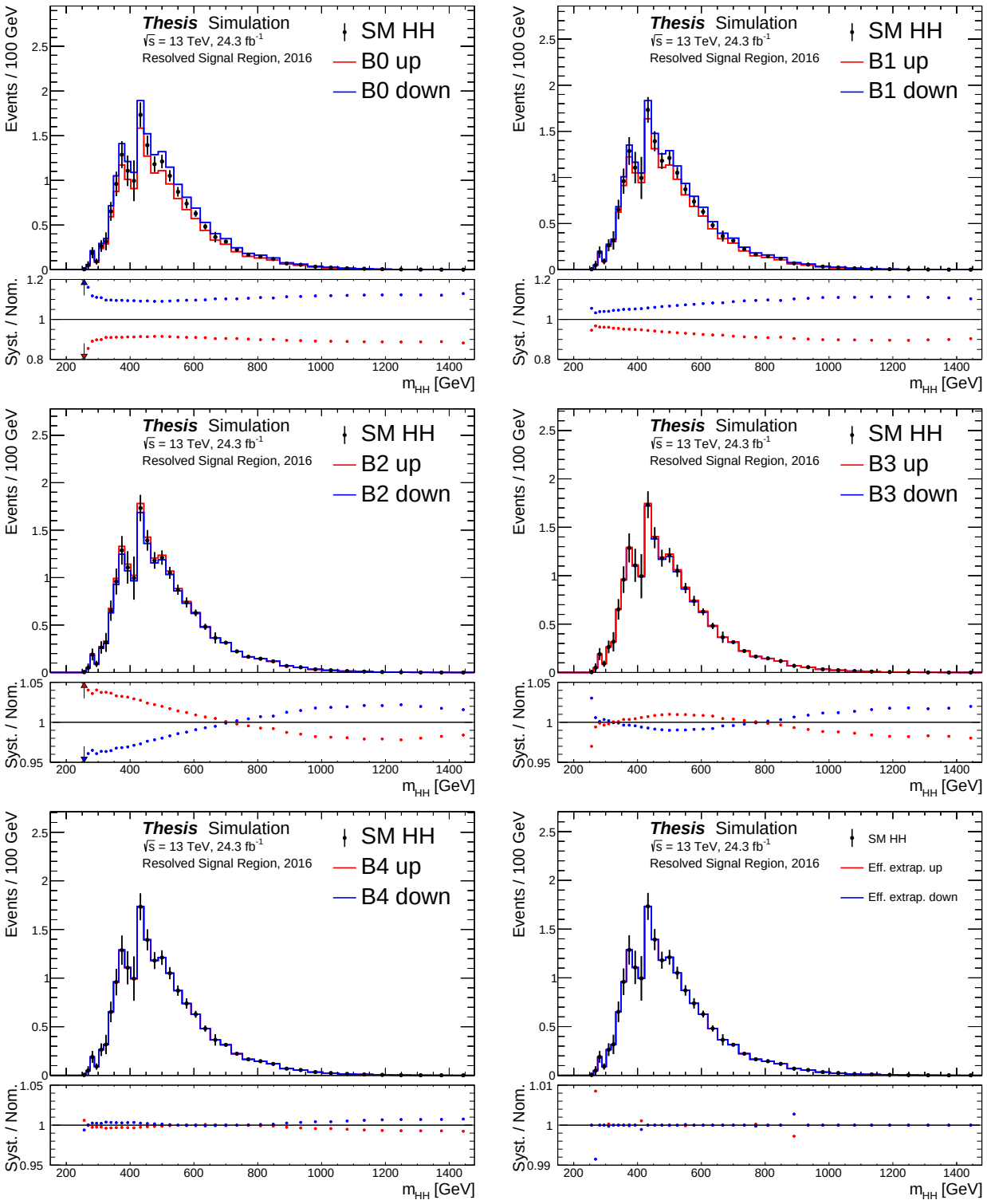

Figure 11.9: b-tagging modeling uncertainties applied to the SM HH signal sample in the Signal Region

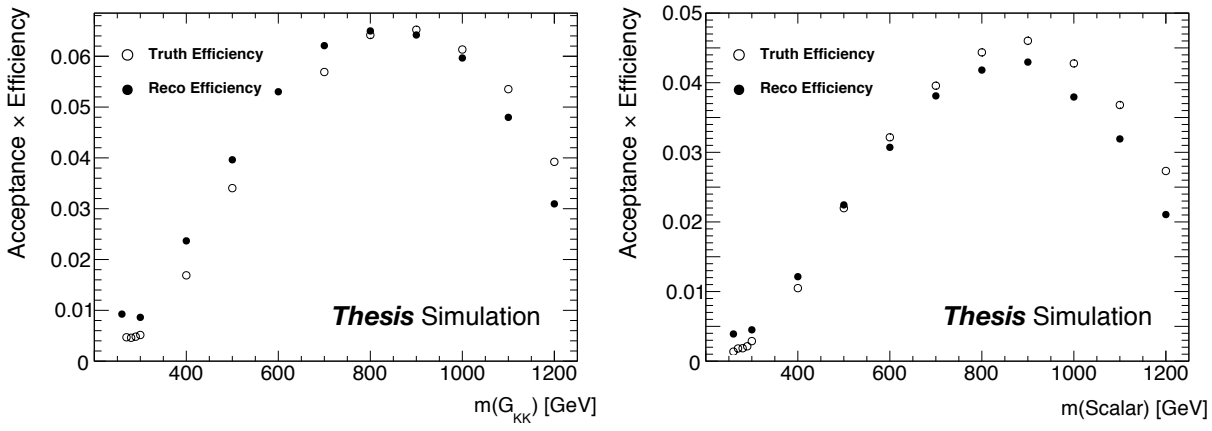

(a) (b)

Figure 11.10: $A \times \varepsilon$ measured in the particle-level analysis (open circles) and full, reconstruction-level analysis (filled circles) for (a) the graviton models with $k/\overline{M}_{\mathrm{Pl}} = 1$ and (b) the scalar models. Good agreement is observed across the mass range.

3. Uncertainties in the Parton Distribution Function (PDF).

The estimation of the theoretical uncertainties is performed using a Rivet-based analysis [13], which replicates the full analysis selection outlined in Section 8. The most important detector effects, b-tagging efficiency and jet energy resolution, are emulated. A finite jet energy resolution is emulated by smearing the particle-level jet energies, using the resolutions estimated in [22]. The b-tagging efficiency is treated using a truth-tagging approach, which weights events according to the combinatoric probabilities of which jets are b-tagged, using the measured b-tagging efficiencies described in the previous section.

Reasonably good agreement is observed between the $A \times \varepsilon$ of the particle-level analysis and of the full, reconstruction-level analysis when measured on independent samples generated using the same configuration (Figure 11.10). Perfect agreement is not necessary, since the theoretical uncertainties will be calculated using the relative change in $A \times \varepsilon$ between variations of the signal sample, as measured by the Rivet-based analysis.

Matrix Element Uncertainty - To evaluate the potential effect of missing higher order terms in the scattering matrix element, the renormalization and factorisation scales used in the signal generation were varied coherently by factors of 0.5× and 2× for the resonant signals. The effect is shown for the signal samples in Figure 11.11. For the graviton models with $k/\overline{M}_{\mathrm{Pl}} = 1$, the shift induced by varying the scales down is consistent with zero across the full mass range, however doubling the scales results in an increased acceptance for the lowest signal masses. The scale variations have $\leq 2\%$ impact on the graviton models with $k/\overline{M}_{\mathrm{Pl}} = 2$. There is a $\sim 6\%$ decrease for the low mass scalar models. The non-resonant sample is unaffected by scale variations.

Parton Shower Uncertainty - Uncertainties due to modelling of the parton shower and the underlying event (including multi-parton interactions) are evaluated by switching the simulation generator used. For the graviton models, this means switching from Pythia8 to Herwig++, while for the scalar and SM HH it is Herwig++ to Pythia 8. Figure 11.12 shows the impact of these variations on the signal acceptance. This variation has the largest impact on the acceptance for all signals principally due to the effect of initial state radiation.

PDF Uncertainty - PDF uncertainties are evaluated using PDF4LHC15 sets, which combine CT14, MMHT14 and NNPDF3.0 PDF sets [15]. For the resonant samples the set PDF4LHC15_nlo_mc is used, while for the SM HH sample the set PDF4LHC15_nlo_30 is used. The uncertainty is evaluated by calculating the acceptance for each PDF replica. The standard deviation of these acceptance values divided by the baseline acceptance is taken as the PDF uncertainty. For each mass point the distribution of these ratios is compatible with a Gaussian centred on one. The calculated PDF uncertainty is shown in Figure 11.13 as upward and downward shifts from unity. The uncertainty in acceptance due to PDF uncertainties is less than $\pm 1\%$ across the full mass range considered in this search. For this reason, it is neglected in the statistical analysis described in Section 13.

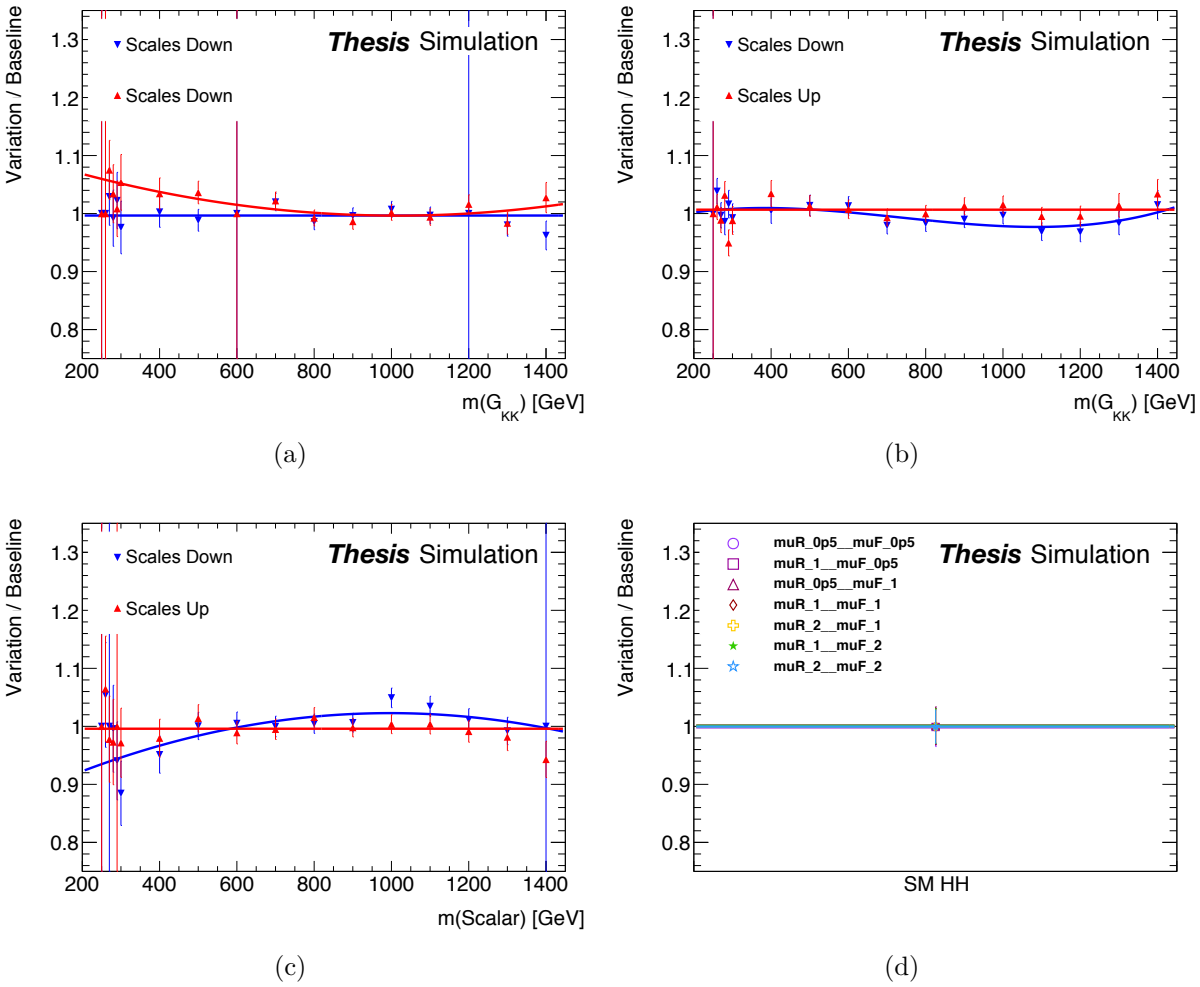

Figure 11.11: Ratio of acceptance times efficiency measured in the scale-varied samples over the baseline sample for: (a) the graviton models with $k/\overline{M}_{\mathrm{Pl}} = 1$, (b) $k/\overline{M}_{\mathrm{Pl}} = 2$, (c) the scalar models and (d) the SM HH model. The upward-pointing triangles in (a), (b) and (c) correspond to doubling both the renormalization and factorisation scales, while the downward-pointing triangles correspond to halving them. The polynomial fits shown as solid lines are used to assign the corresponding systematic variation in the final statistical analysis.

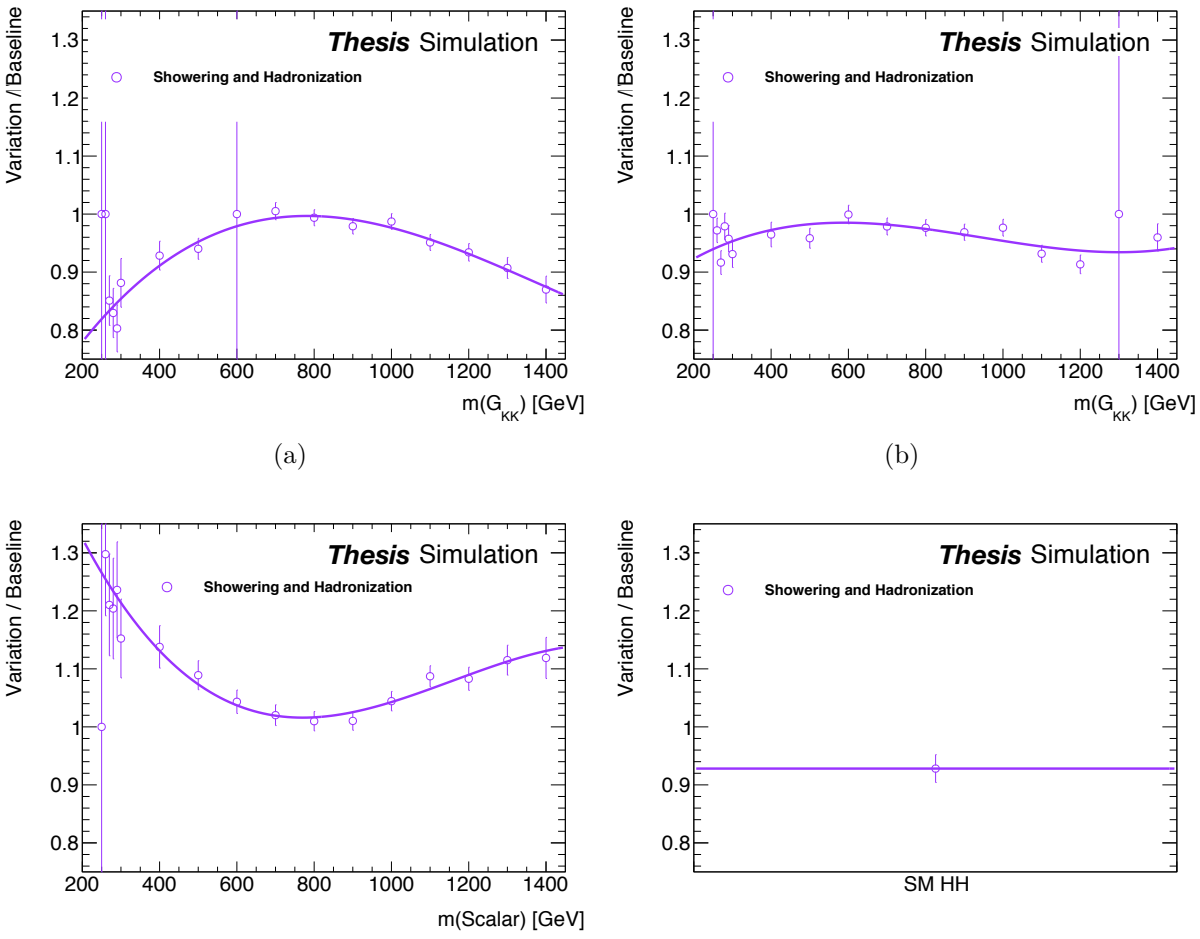

Figure 11.12: Ratio of $A \times \varepsilon$ measured in the shower-varied samples over the baseline sample shown as open circles: (a) the graviton models with $k/\overline{M}_{\mathrm{Pl}} = 1$, (b) $k/\overline{M}_{\mathrm{Pl}} = 2$, (c) the scalar models and (d) the SM HH model. The polynomial fits shown as solid lines are used to assign the corresponding systematic variation in the final statistical analysis.

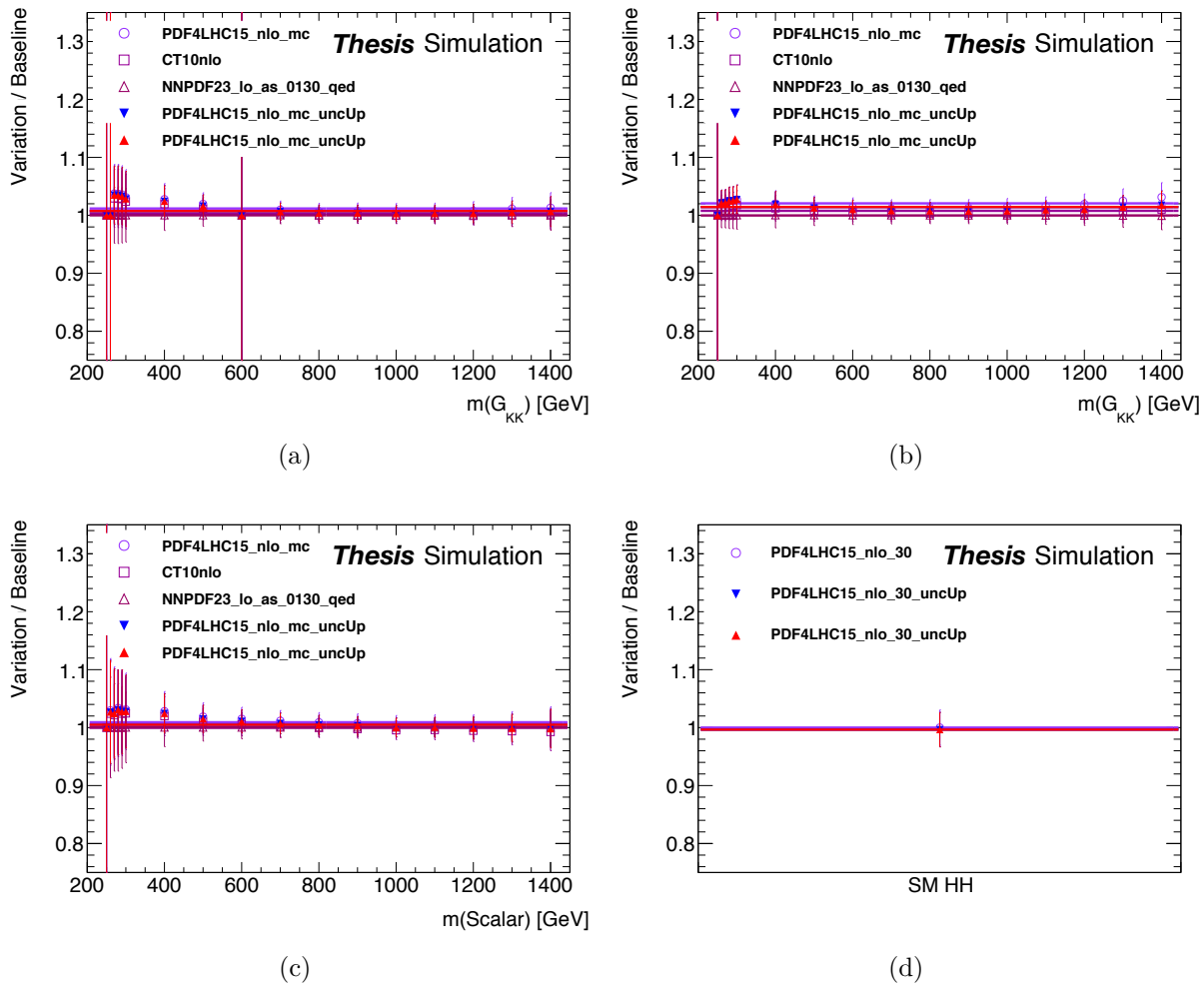

Figure 11.13: Ratio of $A \times \varepsilon$ measured in the PDF-varied samples over the baseline sample: (a) the graviton models with $k/\overline{M}_{\mathrm{Pl}} = 1$, (b) $k/\overline{M}_{\mathrm{Pl}} = 2$, (c) the scalar models and (d) the SM HH model. The upward-pointing triangles correspond to increases in the event weight resulting from the PDF uncertainties, while the downward-pointing triangles correspond to decreases. Results from alternative PDF sets are also shown. Given the small size of the variations, this is not included in the final statistical analysis.

Chapter 12

VALIDATION REGION RESULTS

A robust check of the background procedure can be made before unblinding by performing the full analysis targeting "pseudo-signal" regions in the Higgs candidate mass plane. The Sideband and Control Regions are designed to have balanced representation of Higgs candidate masses below and above the Signal Region to ensure the reweighting is not dominated by the low or high mass regions of phase space. We can then check that these distinct parts of phase space are independently modeled well by checking Low and High Mass Validation Regions (LMV and HMV Regions respectively). These regions are defined by cuts on shifted versions of X_{HH} (Equation 8.5) with centers on the D_{HH} line (Equation 8.2 and Figure 8.4) above and below the center of the Signal Region:

$$X_{\mathrm{LM}} = \sqrt{\left(\frac{m_{2\mathrm{j}}^{\mathrm{lead}} - 89.7\,\mathrm{GeV}}{0.1 m_{2\mathrm{j}}^{\mathrm{lead}}}\right)^2 + \left(\frac{m_{2\mathrm{j}}^{\mathrm{subl}} - 82.2\,\mathrm{GeV}}{0.1 m_{2\mathrm{j}}^{\mathrm{subl}}}\right)^2} < 1.6 \tag{12.1}$$

$$X_{\mathrm{HM}} = \sqrt{\left(\frac{m_{2\mathrm{j}}^{\mathrm{lead}} - 160\,\mathrm{GeV}}{0.1 m_{2\mathrm{j}}^{\mathrm{lead}}}\right)^2 + \left(\frac{m_{2\mathrm{j}}^{\mathrm{subl}} - 147\,\mathrm{GeV}}{0.1 m_{2\mathrm{j}}^{\mathrm{subl}}}\right)^2} < 1.6 \tag{12.2}$$

The cut on X_{LM} defines the LMV Region while X_{HM} defines the HMV Region. The regions are illustrated in Figure 12.1.

Both regions are modeled well as shown in Figures 12.2. The shape of the LMV Region spectrum is a result of two effects: The four body mass spectrum peaks lower for events with additional jets and the LMV Region overlaps with the W boson mass used in the definition 8.4 of X_{Wt} for the top veto. These effects are explained in detail in Appendix G.

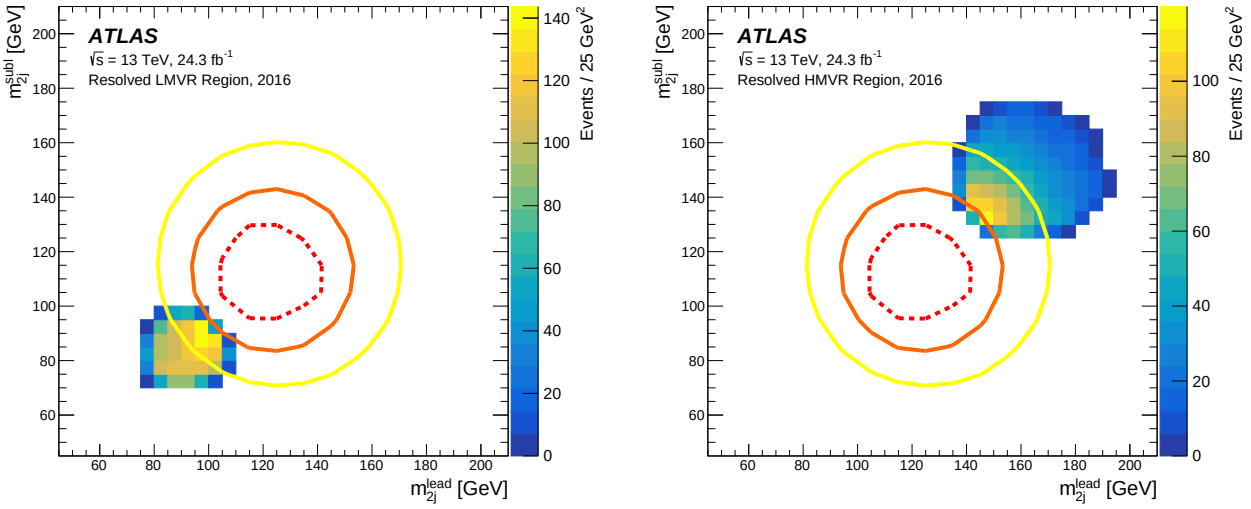

Figure 12.1: The background model in the LMV (left) and HMV (right) Regions. The regions are orthogonal to the Signal Region but not to the Sideband where the background model was derived.

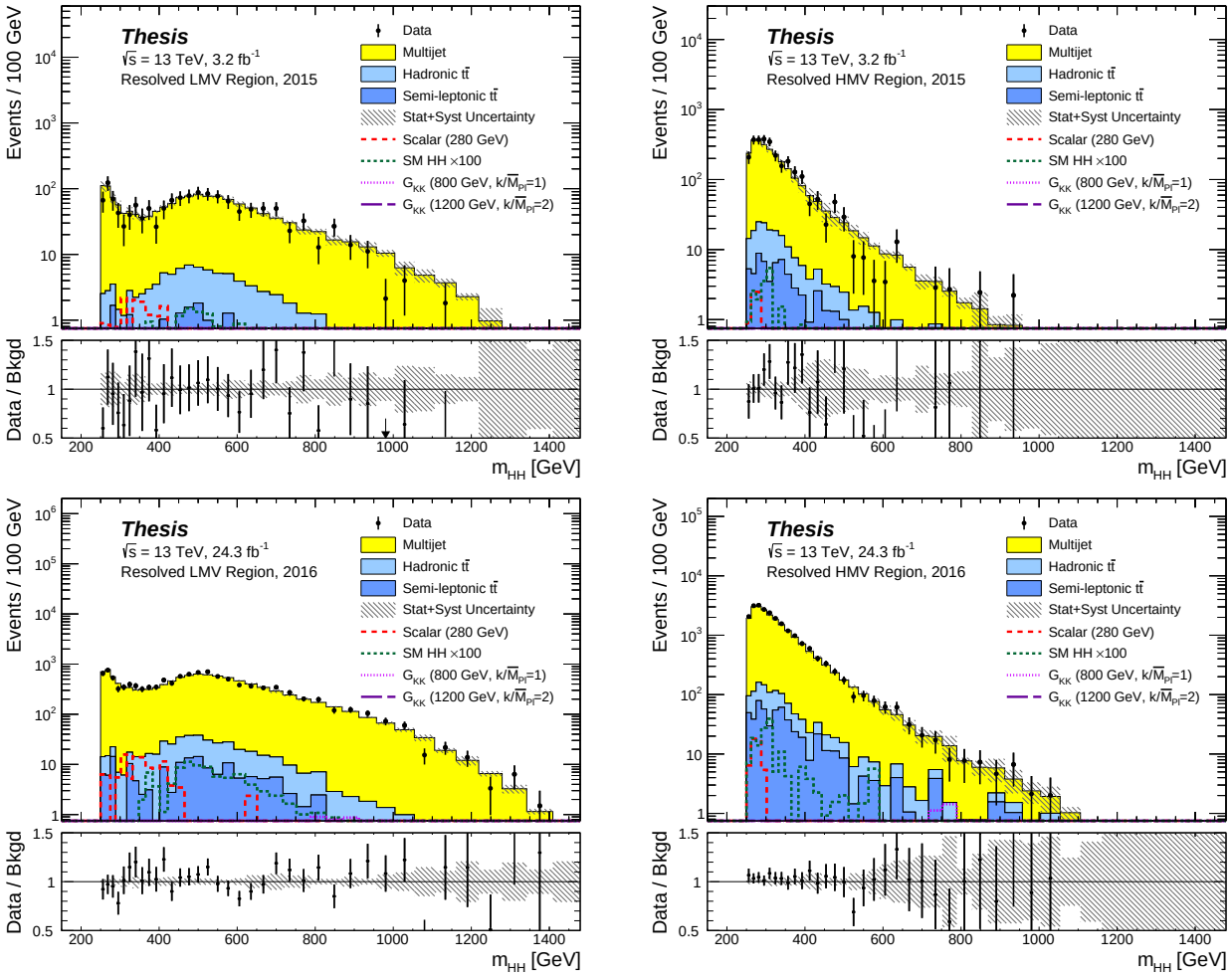

Figure 12.2: Background modeling in the low and high mass validation regions for the 2015 (top) and 2016 (bottom) data sets.

Chapter 13

STATISTICAL ANALYSIS

In this chapter we describe the statistical methods used to quantify the significance of our results and quantify the sensitivity of our search. We begin with a pedagogical introduction in section 13.1 before moving on to detail the analysis search procedure in section 13.2

13.1 Pedagogical Introduction

Background-only Hypothesis – Given a background model with associated uncertainties one can estimate the extent to which the observed data is described by the background model. First consider a binned background distribution with zero uncertainty. Each bin contains a non-negative real number as an estimate for the integer number of data entries one expects to see in the background-only scenario. The observed number of entries in each bin is an integer by construction, where each entry is statistically uncorrelated from each other entry. This is because we can treat collision events as separate experiments like individual flips of a coin; the collisions independently sample the underlying dynamics [1].

The background-only hypothesis is that the data samples Poisson distributions in each bin:

$$P_i(D_i) = \frac{B_i^{D_i}}{D_i!} e^{-B_i} \tag{13.1}$$

$P_i(D_i)$ gives the probability to observe D_i events given the background expectation B_i in

[1] In reality there are small correlations between consecutive proton collisions due to in and out of time pile-up. These effects are mitigated and estimated using techniques described in Section 11.2. Detector malfunctions could also cause data to become correlated over the duration of the malfunction. The time correlation between events entering our Signal Region has been checked explicitly in Appendix H.7 and no effect is observed.

bin i. The probability to observe a given binned distribution with m bins $D = \{D_1, ..., D_m\}$ is the product of the probabilities in each bin:

$$P(D) = \prod_{i=1}^{m} \frac{B_i^{D_i}}{D_i!} e^{-B_i} \tag{13.2}$$

In bins with $B_i \gg 1$, the computation of $P(D)$ can be simplified and accelerated by approximating the Poisson distribution with a unit normalized Gaussian (Normal) distribution with standard deviation $\sqrt{B_i}$. By choosing a binning such that all bins have $B_i \gg 1$ we can approximate equation 13.2 as

$$P(D) \approx \prod_{i=1}^{m} \left(\frac{1}{2\pi\sqrt{B_i}} \right)^{1/2} e^{-(D_i - B_i)^2/2B_i} \tag{13.3}$$

Equation 13.3 can be simplified by changing variables from B_i to the Pearson cumulative test statistic [99]:

$$\chi^2 \equiv \sum_{i=1}^{m} \chi_i^2 \equiv \sum_{i=1}^{m} \frac{(D_i - B_i)^2}{B_i} \tag{13.4}$$

In the Normal approximation, the standard deviation of χ_i is 1. Then equation 13.3 is simply

$$P(D) \approx (2\pi)^{-m/2} \, e^{-\chi^2/2} \tag{13.5}$$

where χ^2 is implicitly a function of the background model and observed data.[2]

With a large number of bins, the probability of even the most likely distribution D is extremely small and is not particularly meaningful on its own. Instead, we are interested in

[2]The prefactors $1/\sqrt{B_i}$ are eliminated in this change of variables because of the Jacobian in the normalization constraint of the probability distribution. We redefine the probability distribution $P(D)$ to keep unit normalization under integration over χ: Schematically $1 = \int_D P(D) dD = \int_{\chi(D)} P(D) \left| \frac{\partial D}{\partial \chi} \right| d\chi = \int_{\chi(D)} P(D) \prod_{i=1}^{m} \sqrt{B_i} d\chi \to \int_\chi P(D) d\chi$.

the sum probability of all test distributions T such that $P(T) \leq P(D)$:

$$\mathcal{C}(D) = \sum_{T,\, P(T) \leq P(D)} P(T) = 1 - \sum_{T,\, P(T) > P(D)} P(T)$$

In general, $\mathcal{C}(D)$ cannot be solved analytically. Instead, it can be numerically estimated by "throwing toys". Toys are randomly generated test distributions T where each entry T_i is a random non-negative integer taken with a probability given by the Poisson distribution in Equation 13.1 (or Normal distribution in Equation 13.3 if $B_i \gg 1$). Then the cumulative probability is approximated by the fraction of toys such that $P(T) \leq P(D)$:

$$\mathcal{C}(D) \approx \frac{N_{\text{toys,P(T)}\leq\text{P(D)}}}{N_{\text{toys}}}$$

Including a Signal Hypothesis – Now suppose we are not only interested in checking the consistency of the data with the background model, but we would also like to test for the presence of a hypothesized signal process. A simulated sample for the process can be generated giving a simulated binned distribution $S = \{S_1, ..., S_m\}$. The signal distribution S can be scaled by a "signal strength" factor which is the ratio of a test cross section over the theoretically predicted cross section: $\mu \equiv \sigma/\sigma_{\text{theory}}$ [3]. Assuming μS and B, the probability of observing the distribution D is the same as above, everywhere replacing B_i with $B_i + \mu S_i$:

$$P(D, \mu) = \prod_{i=1}^{m} \frac{(B_i + \mu S_i)^{D_i}}{D_i!} e^{-(B_i + \mu S_i)}$$

The extent to which the data favors the background plus signal hypothesis versus the

[3] For unfortunate historical reasons, the cross section of a process and the standard deviation of a Normal distribution are both represented by σ.

background-only hypothesis can be quantified with the following probability ratio:

$$q_0(D,\mu) = \frac{P(D,\mu)}{P(D,0)} \tag{13.6}$$

This ratio gives the probability to observe D given μS and B over the probability to observe D in the background-only scenario, $\mu = 0$. The "local p-value" denoted p_0^{local} is the probability to observe a value of q_0 greater than or equal to $q_0(D,\mu)$ in the background-only hypothesis. Again, this quantity is not particularly meaningful on its own, especially in our case where we are looking for many possible signal processes (resonances of different masses, spins and intrinsic widths as well as non-resonant HH production).

When searching for one of many signal processes, one must incorporate the "look elsewhere effect": A statistical fluctuation is more likely to look like evidence for a signal process if there are multiple signal processes from which to choose. The look elsewhere effect can be accounted for by modifying our definition of q_0 in equation 13.6 to take the signal model S and signal strength μ which maximizes $q_0(D,\mu)$:

$$q_0(D) = \max_{\mu,S}\left[\frac{P(D,\mu)}{P(D,0)}\right] \tag{13.7}$$

The "global p-value" denoted p_0^{global} is the probability of observing q_0 greater than or equal to $q_0(D)$ assuming the background-only hypothesis. The global p-value can again be estimated by throwing toys using the background model and taking the fraction of toys such that $q_0(T) \geq q_0(D)$.

Systematic Uncertainties – Thus far we have assumed the background and signal models have no systematic uncertainty and have only considered statistical fluctuations. The method of throwing toys can be easily generalized to include model uncertainties by randomly sampling the space of model variations and then throwing toys for each variation.

In this scenario the background and signal models are described by vectors of functions $B(\theta) = \{B_1(\theta), ..., B_m(\theta)\}$ and $S(\theta) = \{S_1(\theta), ..., S_m(\theta)\}$ respectively where $\theta = (\theta_1, ..., \theta_n)$ is a vector of n "nuisance parameters" (NPs)[4]. For example, the background model may depend on the statistical uncertainty of the simulated background process so each bin can be assigned a NP to allow that bin to vary within the statistical precision of the simulation. The probability distribution $P(D, \mu)$ can be extended to include factors given by the probability distributions of each NP. For our purposes we assume the probability distributions of the NPs to be Normal. Without loss of generality we can scale the NPs such that their standard deviation is 1 [5]. Putting this together, equation 13.5 can be extended to incorporate uncertain signal and background models:

$$P(D, \mu, \theta) \approx (2\pi)^{-(m+n)/2} e^{-(\chi^2+\theta^2)/2}$$

where we substitute $B_i \to B_i(\theta) + \mu S_i(\theta)$ in the definition 13.4 of χ^2 and we have used the vector notation $\theta^2 \equiv \sum_{j=1}^{n} \theta_j^2$. With this definition the probability distribution $P(D, \mu, \theta)$ falls off exponentially for large values of θ.

Let us define the "profile likelihood" $L(\mu)$:

$$L(\mu) \equiv \max_{\theta}[P(D, \mu, \theta)] \equiv P(D, \mu, \hat{\theta}_\mu) \tag{13.8}$$

where $\hat{\theta}_\mu$ is the value of θ which maximizes the likelihood.

When evaluating local and global p-values, we are interested in the fraction of toys with

[4] Each bin of both the signal and background models can in principle depend on each NP. There are often NPs which only impact the signal or the background or only a subset of the bins.

[5] In some cases the scale of an NP θ_j can be difficult to constrain. In such situations one can effectively set the variance of θ_j to infinity by removing it from the θ^2 term in the exponential and multiplying $P(D, \theta)$ by $\sqrt{2\pi}$. This is also a useful diagnostic tool to assess the impact of a given NP on the agreement of the data with the background model $\mathcal{C}(D)$

test statistic q_0 above and below the value observed in data. This means that any strictly increasing monotonic function can be used to redefine q_0 without changing the resulting p-value. With a large number of bins and NPs, the exponent in $P(D, \mu, \theta)$ will generally be a large negative number giving exponentially small values of $P(D, \mu, \theta)$.

It is numerically convenient to redefine q_0 as twice the natural log profile likelihood ratio rather than the ratio in Equations 13.6 and 13.7:

$$\begin{aligned} q_0 &= 2 \ln \left(\max_{\mu, S} \left[\frac{L(\mu)}{L(0)} \right] \right) \\ &\approx (\chi^2_{\mu=0} + \hat{\theta}_0^2) - (\chi^2_{\hat{\mu}, \hat{S}} + \hat{\theta}_{\hat{\mu}}^2) \end{aligned}$$

In the second line we show that in the Gaussian approximation our test statistic q_0 has the simple interpretation of the difference in goodness of fit of the background-only and signal plus background hypotheses for the best fit signal model $\hat{S}$ where we penalize the goodness of fit by the quadrature sum of the "pulls" on the NPs.

13.2 Search procedure

The statistical interpretation in this search uses the statistical procedure described in Reference [27]. A test statistic based on the profile likelihood ratio [77] is used to test hypothesized values of $\mu = \sigma/\sigma_{\text{theory}}$, the global signal strength factor, separately for each model tested. The statistical analysis described below is performed using the data observed in the Signal Region. As a reminder, the final discriminant is given by m_{HH} as defined in equation 8.8. The analysis is performed on the binned m_{HH} spectrum using variable bin widths where the width is set to 5% of the m_{HH} value at the lower edge of the bin rounded down to the nearest GeV. The 5% value was chosen to be approximately half of the m_{HH} detector resolution.

Systematic uncertainties are treated using Gaussian or log-normal constraint terms in the definition of the likelihood function. The 2015 and 2016 data sets are fitted simultaneously, treating the jet energy, b-tagging and theoretical systematic uncertainties as fully correlated between the two datasets. The luminosity, trigger efficiency and background modeling uncertainties are uncorrelated between the 2015 and 2016 data sets. These uncertainties are described in detail in Chapter 11.

The search for new resonances is performed using orthogonal selections referred to as "Resolved" and "Booosted" as described in Section 8.7. For the SM HH search, only the Resolved analysis is considered. For the resonant search, the Resolved 2015 and 2016 datasets are fitted simultaneously with the "Boosted" Signal Regions for resonance masses greater than 700 GeV and less than 1500 GeV. In this case the jet energy uncertainties are treated as uncorrelated between Resolved and Boosted Signal Regions because of the different techniques used in the calibration. In contrast, the b-tagging uncertainties are treated as fully correlated, due to the similarities in methods and datasets used in the calibration. This improves the limit at 1 TeV by less than 5% which is the point that is effected the most. Theoretical systematic uncertainties are also treated as correlated between the two analyses.

The statistical analysis of the data after unblinding consists first of a search for statistically significant deviation from the background model hypothesis consistent with any of the considered signal models. The test statistic used is a one sided profile likelihood ratio [76]:

$$q_0 = \begin{cases} -2\ln\frac{L(0)}{L(\hat{\mu})} & \hat{\mu} > 0 \\ 0 & \hat{\mu} < 0 \end{cases}$$

where $\hat{\mu}$ is the maximum likelihood (ML) value of μ, and the profile likelihood L is defined as in equation 13.8. The test statistic q_0 is set to zero (i.e. the value of q_0 when $\hat{\mu} = 0$) when the best fit signal strength is negative to reflect the fact that interference between the signal

and background processes are not considered in the current analysis and as such, a negative signal cross section is unphysical.

The local p-value, p_0^{local}, is defined as the probability for the background-only hypothesis to have a value of q_0 that is as high or higher than the value of q_0 in that data. In order to obtain p_0^{local}, toys are generated with the background-only model and the distribution of the test statistic, q_0, is built up from the values of the pseudo-experiments.

The graviton and scalar signal samples are tested with masses between $260 < m < 3000\,\text{GeV}$ at $10\,\text{GeV}$ intervals up to $300\,\text{GeV}$ followed by $100\,\text{GeV}$ intervals up to $1600\,\text{GeV}$, with $200\,\text{GeV}$ intervals up to $2000\,\text{GeV}$ and with $250\,\text{GeV}$ intervals between 2000 and $3000\,\text{GeV}$.

If a p_0^{local} value is obtained that corresponds to a significance of greater than 3σ, a correction for the look elsewhere effect will be computed in order to obtain the global p-value. This correction is obtained using the distribution of the test statistic, q_0, in background-only pseudo-experiments. The average number of upwards crossings, $< N_{1\sigma} >$, across the mass range tested of q_0 at the value of q_0 corresponding to 1σ significance, $q_0^{1\sigma}$, is estimated using the average number from the background-only pseudo-experiments and is used to obtain the correction to the local p-value using the equation:

$$p_0^{\text{global}} = \min[p_0^{\text{local}}] + < N_{1\sigma} > e^{-(\max[q_0] - q_0^{1\sigma})/2}$$

Where $\min[p_0^{\text{local}}]$ is the lowest p_0 value across the mass range tested, corresponding to the maximum test statistic value $\max[q_0]$.

13.3 Limit setting procedure

If the global p-value from the search corresponds to a significance of less than 3σ the following procedure will be used to set limits on the signal strengths of the considered signal models.

13.3.1 Choice of exclusion statistics

To evaluate an upper limit on the cross section for a given model - $\sigma(X \to HH \to b\bar{b}b\bar{b})$ - a frequentist method is used where a cross section is excluded on the basis of the statistic CL_s [179], which is defined as the ratio of CL_{s+b} to CL_b. CL_{s+b} is defined as $P_{s+b}(q \leq q_{obs})$, i.e. the probability of the signal plus background model to produce data with a value of q less than that observed. q is a test statistic which tests the compatibility with the signal plus background hypothesis, where low values indicate a high level of compatibility. $CL_b = P_b(q \leq q_{obs})$, i.e. the probability of the background model to produce data with the same or more compatibility with the background model as that observed. Cross sections are excluded if they have a value of $CL_s \leq 0.05$.

In order to calculate the p-values used to determine CL_{s+b} and CL_b the test statistic chosen is a one-sided profile likelihood ratio defined as:

$$\widetilde{q_\mu} = \begin{cases} 0 & \text{if } \hat{\mu} \geq 0 \text{ and } \mu < \hat{\mu} \\ -2\ln\frac{L(\mu)}{L(\hat{\mu})} & \text{if } \hat{\mu} \geq 0 \text{ and } \mu > \hat{\mu} \\ -2\ln\frac{L(\mu)}{L(0)} & \text{if } \hat{\mu} < 0 \end{cases}$$

where μ and $\hat{\mu}$ are again the signal strength and best fit signal strengths respectively. The first case ensures $\widetilde{q_\mu}$ is minimized by $\hat{\mu}$ if $\hat{\mu} \geq 0$. The second case makes q_μ continuous at $\mu = \hat{\mu}$ for $\hat{\mu} \geq 0$. The last case takes into account the fact that when searching for a signal

on top of a background the case where $\mu < 0$ is unphysical in the absence of interference.

13.3.2 Calculation of the test statistic

In order to obtain the distributions of the test statistic, $\widetilde{q_\mu}$, two approaches are usually considered: the asymptotic approximation and the toy method.

In the case of the asymptotic approximation the equations obtained in [76] are solved numerically. These equations can be derived using approximations of the distribution of $\hat{\mu}$ as Gaussian and the asymptotic approximation of the distribution of the profile likelihood ratio to a non-central chi-squared distribution.

The toy method works instead by generating datasets randomly sampling the background and signal plus background models, calculating the value of $\widetilde{q_\mu}$ for each individual dataset and then plotting these in a histogram to obtain the distributions and hence the p-values. The exclusion limits, for an individual signal mass point, are obtained by scanning over the values of μ, generating background and signal+background toys to find the p-values at that μ point and interpolating to find the value of μ at which $CL_s = 0.95$. This is done for the data to calculate the observed limit while the expected limit is calculated from the median value of the background-only distribution and for the points which contain 68%(95%) of the background-only distribution in the case of the $\pm 1\sigma(2\sigma)$ bands on the expected limits.

The statistical analysis is performed using the asymptotic approach. A study was performed to assess the differences between these results and those obtained using the toy method. No significant difference was found.

13.4 Results on Asimov dataset

Prior to unblinding, the statistical model is tested using Asimov datasets [76] constructed from the nominal model. The Asimov[6] dataset replaces the ensemble of all possible datasets and their corresponding likelihoods with a single representative dataset. The expected limits are discussed in Section 14. The pulls and correlations of the background model NPs are shown for the Asimov fit of the 280 GeV scalar model in Figure 13.1. In the correlation plots, only those NPs which have a correlation of magnitude greater than 10% with another model parameter are shown. The nuisance parameters are listed and defined in Table 13.1.

Only the Control Region derived shape uncertainties (High/Low H_T^{4j} CR) are expected to be constrained significantly in the fit. The statistics in the Signal Region are large enough to constrain the background shape systematic uncertainty. The shape uncertainties do not conserve the total background normalization, so there is a significant correlation between the CR and Norm. NPs. There is also a correlation between the Low H_T^{4j} CR shape uncertainty and the low mass resonant signals. This is the natural and unfortunate consequence of trying to resolve a signal peak on an uncertain background peak.

[6]The name Asimov comes from the short story *Franchise* by Isaac Asimov which depicts a society where elections are determined by a single voter chosen to represent the average of the electorate.

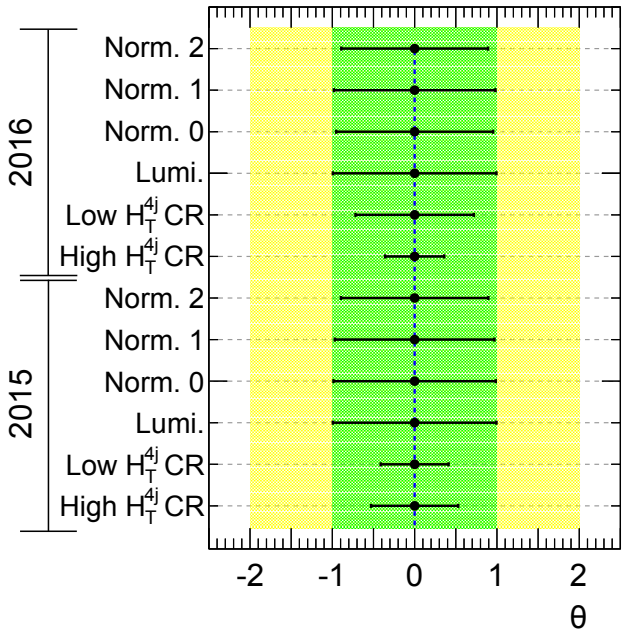

(a)

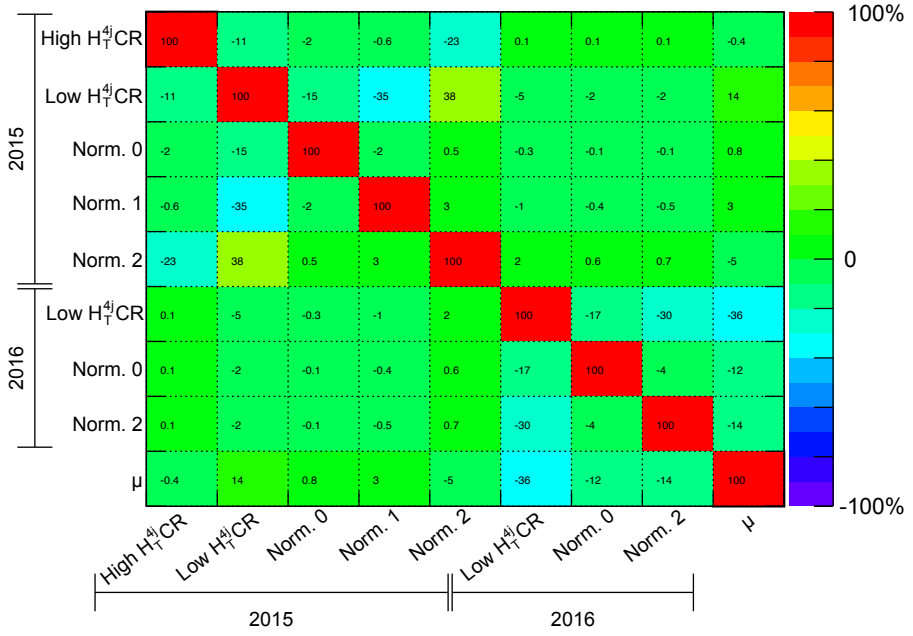

(b)

Figure 13.1: Pulls (a) and correlations (b) for the 280 GeV scalar model.

Nuisance Parameter	Definition
Norm {0,1,2}	Background fit uncertainty eigenvectors corresponding primarily to the uncertainty on the extracted multijet, hadronic $t\bar{t}$ and semileptonic $t\bar{t}$ normalizations respectively. The vectors are derived from the covariance matrix resulting from the fit described in Section 10.2.
High/Low H_T^{4j} CR	The background shape variations determined by the non-closure between Sideband and Control region derived models. Fully correlated between background components, uncorrelated between years. See Section 11.1.
Lumi.	The luminosity uncertainty is only applied to the signal model and corresponds to a normalization 2.1% (2.2%) uncertainty for the 2016 (2015) dataset and is uncorrelated between years.

Table 13.1: Definition and prune status of all nuisance parameters included in the Resolved channels. Items beginning with r15 (r16) are applied only to the 2015 (2016) dataset.

Chapter 14

RESULTS

The unblinded Signal Region m_{HH} distributions are shown in Figure 14.1. The 2015 and 2016 datasets are shown separately and both are shown with linear and log y-axis to better illustrate the peak and tails respectively. The most significant excess is at 280 GeV and is found to correspond to 2.3σ globally. In Section 14.1 we quantify this excess and because it is not found to be significant, limits on the signal models are set in Section 14.2.

14.1 Deviations from the background-only hypothesis

The asymptotic method described in Chapter 13.2 is used to calculate the local significance of any deviation from the background-only hypothesis using the q_0 test statistics. The largest deviation is found at 280 GeV, and the smallest p_0^{local} value is 0.000168 (3.6σ) for the narrow width scalar, and 0.00578 (2.5σ) for the c=1.0 Graviton model as shown in Figure 14.2. The $k/\overline{M}_{\text{Pl}}$ =2.0 Graviton model shows no local excess greater than 1σ.

The global significance is evaluated using toys generated from background-only fits profiled to the data, with randomized global observables. One toy is tossed for each analysis range, i.e. the resolved-only, the combined and the boosted-only range. Then, for each toy, all relevant mass points and the three signal models are used to fit for the largest local excess. The largest significance from each of the three toys is selected and a distribution of those local significances is sampled, repeating the procedure many times.

To improve the accuracy of the global significance, additional signal shapes have been interpolated from the available simulated samples to reflect the m_{HH} resolution. The tested mass points are: 260, 270, 280, 290, 300, *315*, *330*, *345*, *360*, *380*, 400, *420*, *440*, *460*, *480*,

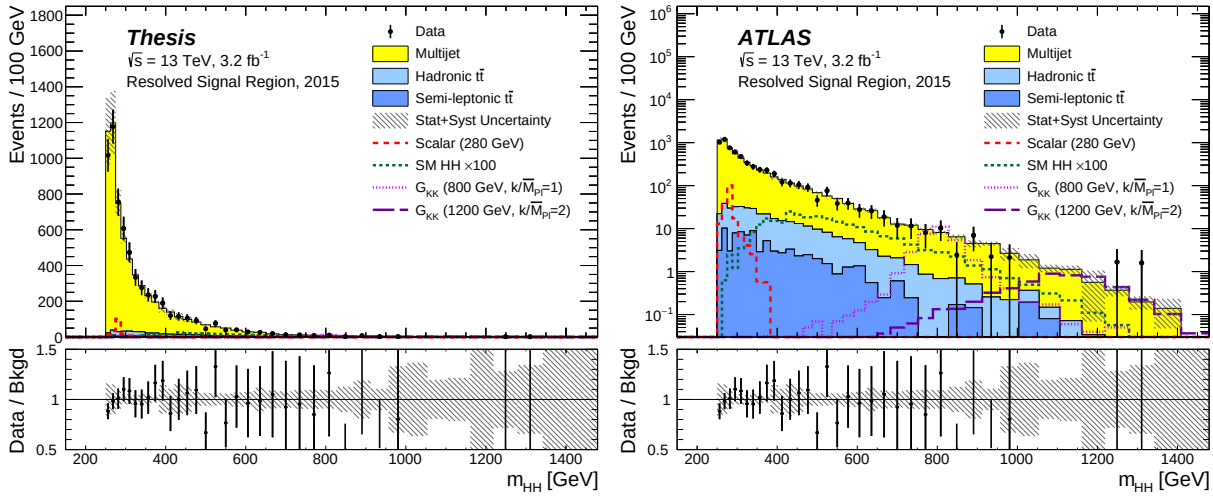

(a) 2015 Data Set

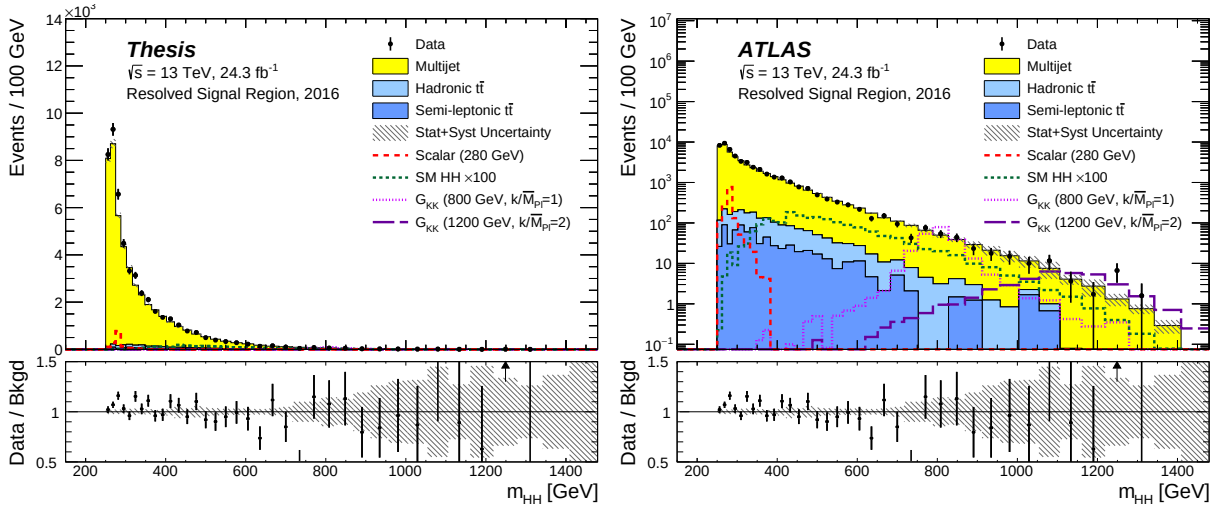

(b) 2016 Data Set

Figure 14.1: Unblinded Signal Region m_{HH} spectra with systematic and statistical uncertainties added in quadrature (shown with linear (left) and log (right) scales on the y-axis).

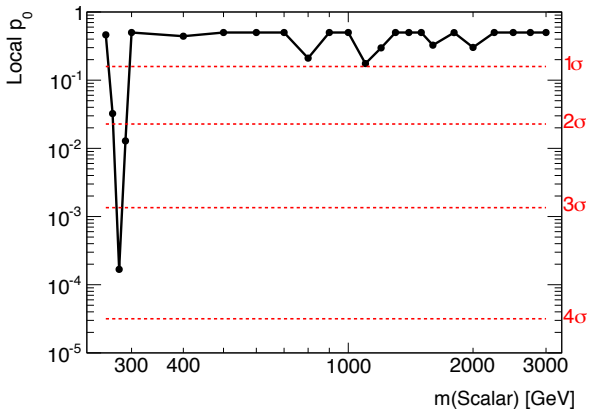

(a)

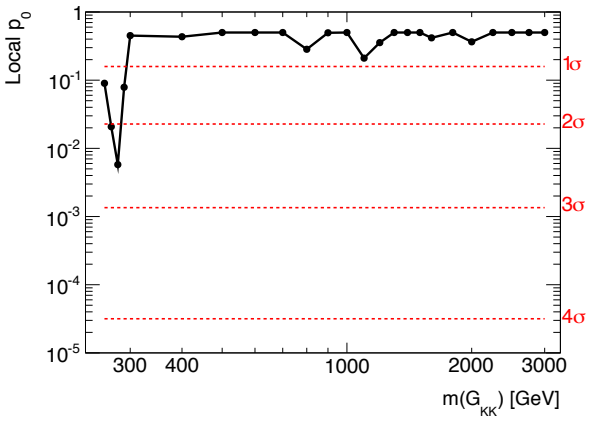

(b)

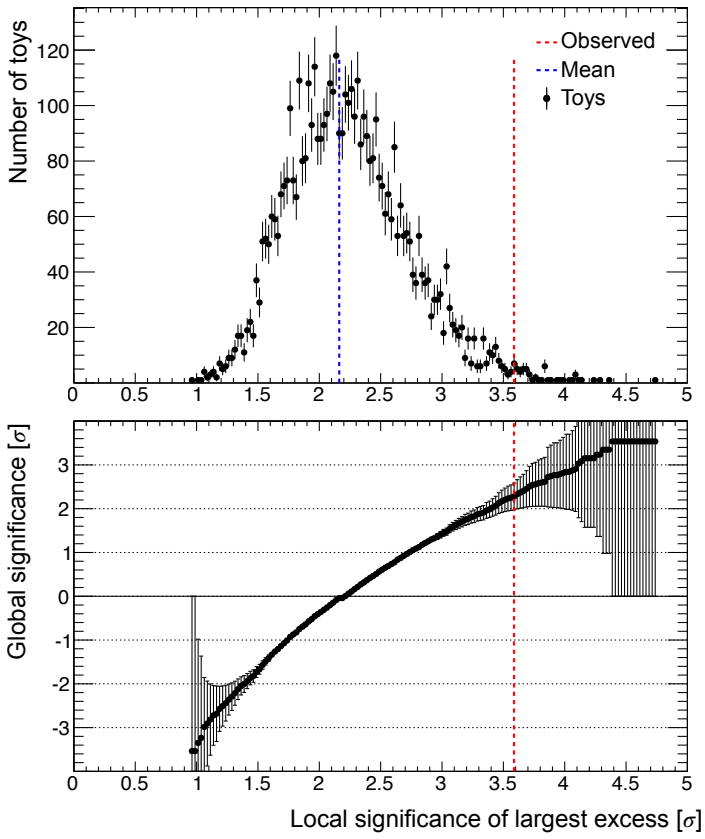

(c)

Figure 14.2: Local p_0 of the (a) scalar and (b) $k/\overline{M}_{\rm Pl}$ =1 graviton models. (c) Distribution of the largest local significances from toys in the upper panel and the global significance as a function of the observed largest local significance in the lower panel.

500, *525*, *550*, *575*, 600, *633*, *666*, 700, *733*, *766*, 800, 900, 1000, 1100, 1200, 1300, 1400, 1500, 1600, 1800, 2000, 2250, 2500, 2750, 3000. (The interpolated mass points are in italics.) The distribution of local significances and the global significance obtained from this distribution are shown in Figure 14.2c.

The global significance obtained from this method is 2.3σ. In 45% of the toys, the largest excess is found in the lowest mass range (260-315 GeV). In 80% of the toys the scalar model gave the largest excess. These effects are due to a combination of the sharpness of the low mass scalar signal peaks combined with the peaking background distribution and associated shape uncertainty.

Further studies of this excess can be found in Appendix H.

14.2 Exclusion limits

No globally significant excess is observed and upper limits on the cross sections for the different benchmark signal processes are set.

14.2.1 Limits on Resonances

Exclusion limits are based on the value of the statistic CL_s [179], with a value of μ regarded as excluded at the 95% confidence level (CL) when CL_s is less than 5% as described in Chapter 13.3.

Figure 14.3 shows the combined 95% CL upper limits for a spin-2 G_{KK} in the bulk RS model with $k/\overline{M}_{\mathrm{Pl}} = 1, 2$ and for generic narrow width scalar resonances.

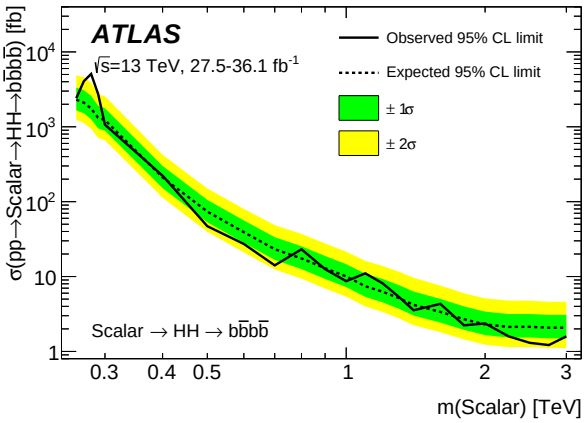

(a) Scalar

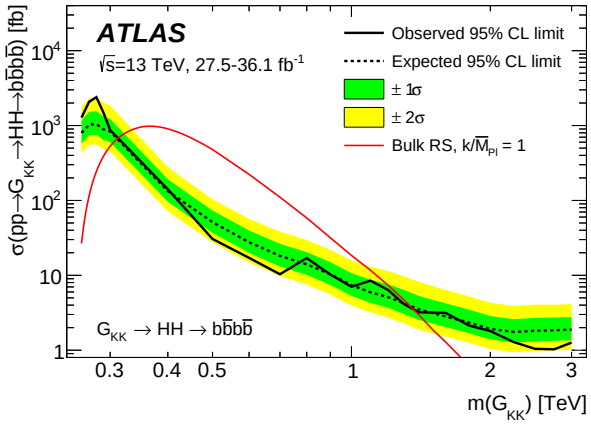

(b) $k/\overline{M}_{\mathrm{Pl}} = 1$ graviton

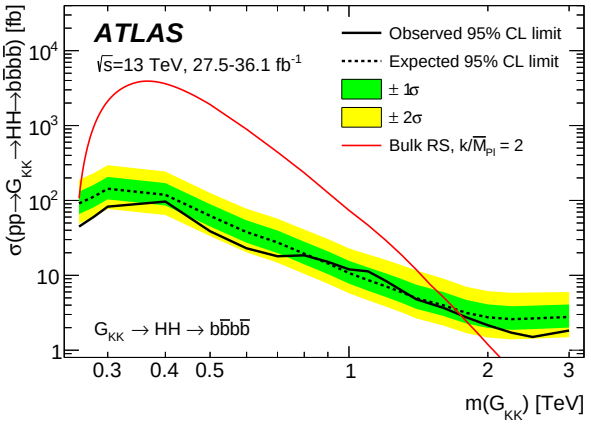

(c) $k/\overline{M}_{\mathrm{Pl}} = 2$ graviton

Figure 14.3: The observed and expected 95% CL upper limits on the production cross section times branching ratio for the (a) narrow-width scalar, (b) graviton with $k/\overline{M}_{\mathrm{Pl}} = 1$ and (c) graviton with $k/\overline{M}_{\mathrm{Pl}} = 2$ models. The additional red curves show the predicted cross sections as a function of graviton mass for each of the graviton models. The drop in the predicted cross sections for masses below $m_{\mathrm{KK}} = 350\,\mathrm{GeV}$ is due to a sharp decrease in the $G_{\mathrm{KK}} \to HH$ branching ratio. The limit for the low mass $k/\overline{M}_{\mathrm{Pl}} = 2$ graviton models is lower than expected due to the smeared signal shape (see Figure 14.4) and observed deficit around 700 GeV in the 2016 data.

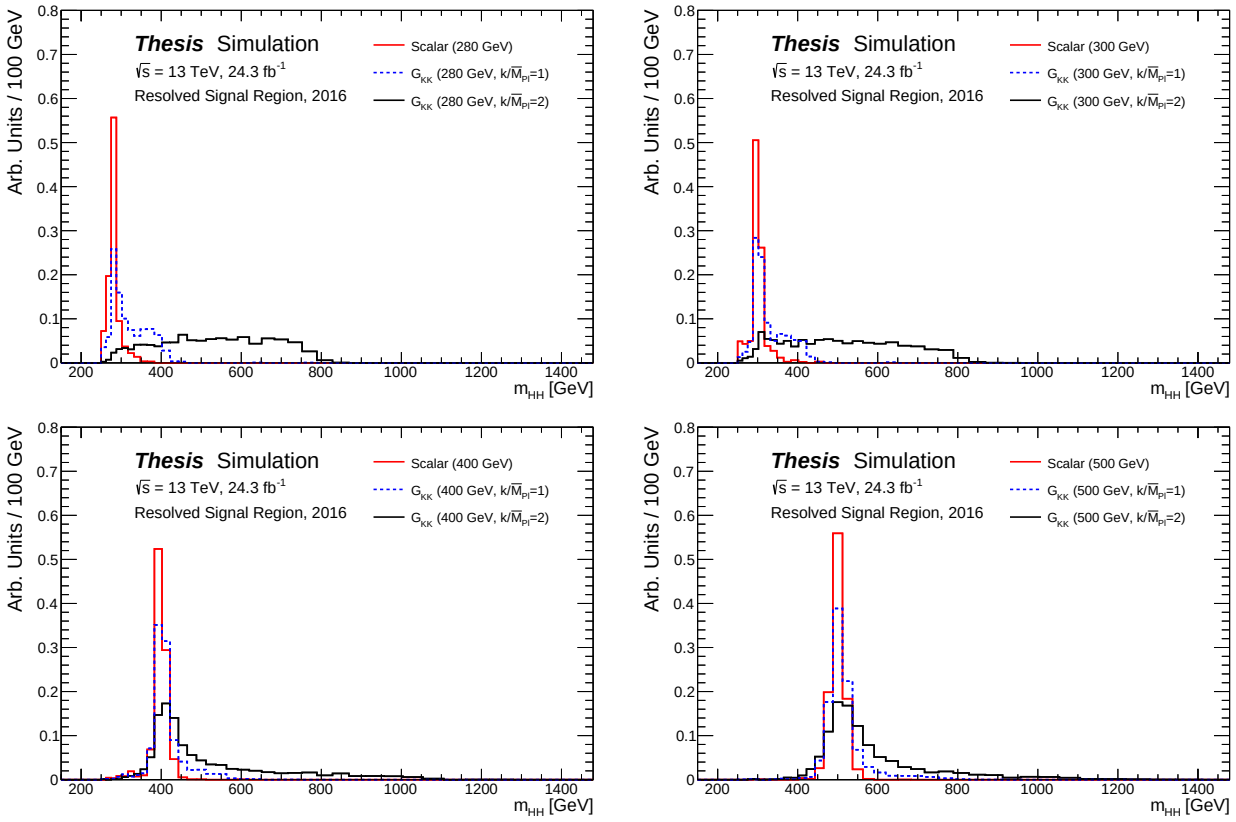

Figure 14.4: Signal Region m_{HH} spectrum shape comparisons for the 280, 300, 400 and 500 GeV signal models. Note that the $k/\overline{M}_{\mathrm{Pl}} = 2$ peaks are suppressed relative to their high mass tails by the small $G_{\mathrm{KK}} \to HH$ branching ratio below 400 GeV.

Observed	-2σ	-1σ	Expected	$+1\sigma$	$+2\sigma$
11.9	10.4	13.9	19.3	27.9	40.5

Table 14.1: 95% C.L exclusion limits for SM HH production without the finite top mass correction in units of the SM prediction for $\sigma(\mathrm{pp} \to \mathrm{HH} \to \mathrm{b\bar{b}b\bar{b}})$.

14.2.2 SM HH *Limit*

Exclusion limits are set on SM HH production using the same statistical procedures. SM HH production via gluon-fusion is used as the benchmark signal. The m_{HH} spectrum peaks at approximately 400 GeV and falls off rapidly so the Boosted results are not used.

The SM HH cross section times branching ratio to four bottom quarks is $33.45\,\mathrm{fb} \times 0.5824^2 = 11.34\,\mathrm{fb}$. After the SM HH simulated sample was generated assuming an infinite top quark mass, a differential NNLO correction including the effects of a finite top quark mass were calculated [60, 61]. We present the SM HH limits using the nominal signal sample (Table 14.1) as well as the limits after reweighting the m_{HH} spectrum of the SM HH sample to match the finite top mass calculation (Table 14.2). Figure 14.5 shows the impact of the finite top mass reweighting on the SM HH simulation. The spectrum is slightly softened by this correction and the limit is weaker as a result.

The observed limit is stronger than expected primarily due to the downward fluctuation in the bin at $m_{HH} \approx 730\,\mathrm{GeV}$ in the 2016 data. This bin is also driving the observed limit downward for the 700 GeV $k/\overline{M}_{\mathrm{Pl}} = 1$, 280, 300 (see Figure 14.4) and 600 GeV $k/\overline{M}_{\mathrm{Pl}} = 2$ graviton models.

Observed	-2σ	-1σ	Expected	$+1\sigma$	$+2\sigma$
12.9	11.1	14.9	20.7	30.0	43.6

Table 14.2: 95% CL exclusion limits for SM HH production with the finite top mass correction, in units of the SM prediction for $\sigma(pp \to HH \to b\bar{b}b\bar{b})$.

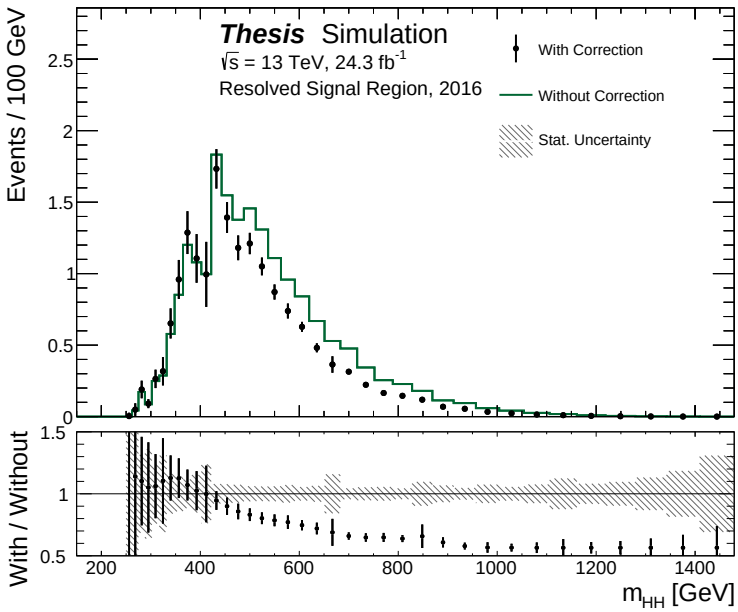

Figure 14.5: The m_{HH} spectrum is significantly softened by the correction, adversely impacting the limit.

Chapter 15

THE FUTURE OF HH PHYSICS

In the absence of new high mass resonances this phase space holds the most general promise for exciting physics. The ultimate benchmark for LHC HH physics is to be sensitive to SM HH production, and in particular to directly constrain the Higgs cubic coupling λ_{hhh}.

Sensitivity to SM HH production with the ability to constrain λ_{hhh} will have one of two consequences:

1. Confirm the SM mechanism of electroweak symmetry breaking (Chapter 2.6.4) and refute electroweak baryogenesis (Chapter 5.2.1) as the mechanism to provide an abundance of matter in the universe.

2. No observed HH production or an enhanced HH signal implying a modified Higgs potential or new fields coupled to the Higgs.

Our previous public result (released for the 2016 ICHEP conference in Chicago) in the $HH \rightarrow b\bar{b}b\bar{b}$ channel constituted the first attempt to select signal events across the full kinematically accessible phase space above $2m_H$. That result demonstrated the proof of concept that the four b-jet channel could compete with the $b\bar{b}\gamma\gamma$ and $b\bar{b}\tau\tau$ channels in the low mass phase space.

In that result we had not yet developed the $t\bar{t}$ background constraints in data or the corresponding $t\bar{t}$ veto. Our background model was substantially less sophisticated and prevented use of the corrected $m_{4\text{j}}$ spectrum m_{HH} as defined in equation 8.8 due to poor modeling. The resulting large background systematic uncertainties substantially limited our sensitivity while still allowing us to set what at the time was the world leading limit on SM HH production signal strength.

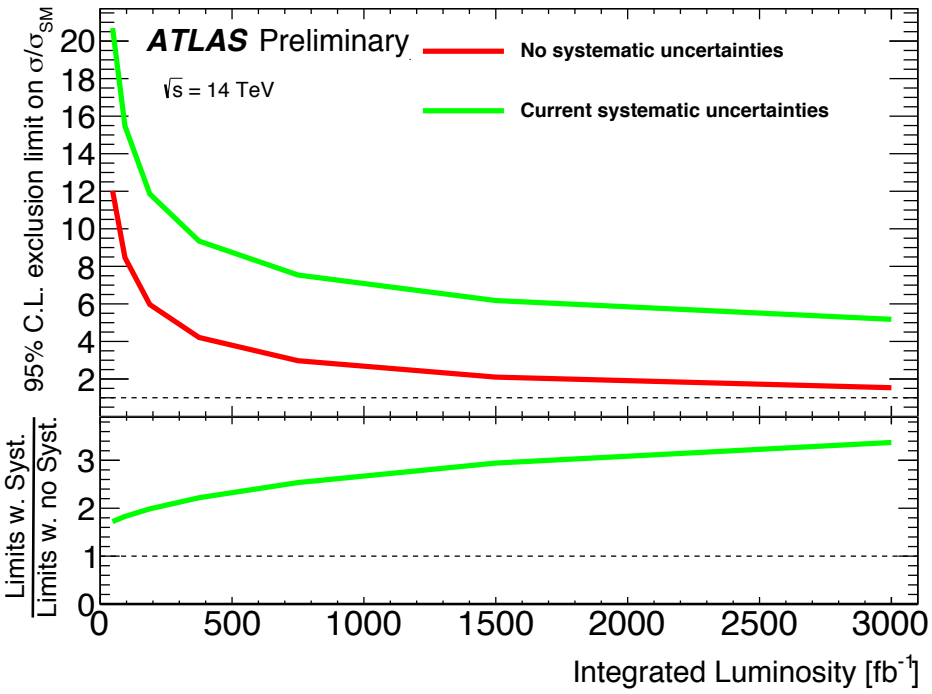

Figure 15.1: Expected 95% C.L. upper limit on the cross-section $\mu \equiv \sigma(HH \to b\bar{b}b\bar{b})/\sigma_{\mathrm{SM}}$, as a function of the integrated luminosity of the search. The red line shows the upper limit when evaluated without systematic uncertainties, while the green line assumes that the systematic uncertainties remain as they were in 2016. The lower panel shows the ratio between these two limits. The extrapolated sensitivity is shown using the jet p_{T} threshold of the 2016 search of 30 GeV with online trigger thresholds at the same 35 GeV as the primary trigger used in this analysis (see Chapter 9).

Despite the large background systematic uncertainties the 2016 ICHEP result provided the first useful benchmark for extrapolation of this channel to the end of the High Luminosity LHC (HL-LHC) run with 3000 fb^{-1} recorded at $\sqrt{s} = 14$ TeV [31]. Two benchmark extrapolations were compared assuming the same analysis procedures and event selection as applied in 2016, one with the same systematic uncertainties and one without systematic uncertainties. These provide a rough envelope for what kind of sensitivity may be reasonably achieved and are shown in Figure 15.1.

Whether we meet or hopefully exceed these extrapolations will depend sensitively on both analysis improvements and detector and trigger performance. In section 15.1 we address some

possible analysis improvements. Section 15.2 briefly introduces the Fast Tracker (FTK) – a system being developed by the ATLAS collaboration which will facilitate low threshold b-jet and τ triggers in high pileup data taking conditions.

15.1 Analysis Improvements

Figure 15.2 shows an event passing the Signal Region selection with the near threshold m_{HH} value of 272 GeV. Note that at this low mass the Higgs candidate jets are required to have $\Delta R_{\text{jj}} \gtrapprox 1$ so the Higgs candidates are built from nearly back to back jets. In the signal hypothesis one does not expect the jets from different Higgs decays to be highly correlated in η and ϕ while in the dominant background hypothesis we expect two to two gluon scattering to generate such a topology. It should be possible to further optimize the selection at low mass taking this into account to down-weight or remove events which are consistent with gluon scattering.

The extrapolation shown in Figure 15.1 uses the 2016 ICHEP analysis which had an expected 95% C.L. upper limit of $\mu < 38$ using $13.3\,\text{fb}^{-1}$ of data. If we scale up that background model to the $27.5\,\text{fb}^{-1}$ used in this thesis the expected limit would be approximately $\mu < 26$ while the actual expected limit achieved was $\mu < 21$. The improved background model, new $t\bar{t}$ veto and re-optimized kinematic cuts used in this thesis provided a 20% improvement in expected sensitivity over improvements from luminosity scaling!

To continue this trend we must improve our background modeling and validation techniques. With low statistics and high Higgs candidate p_{T} cuts, the Run-1 [32] and early Run-2 [34] searches could barely see a systematic shape difference between the two and four b-tag selections in data. A simple linear reweighting scheme with three variables was enough to ensure the background model in the Sideband and Control Regions was statistically consis-

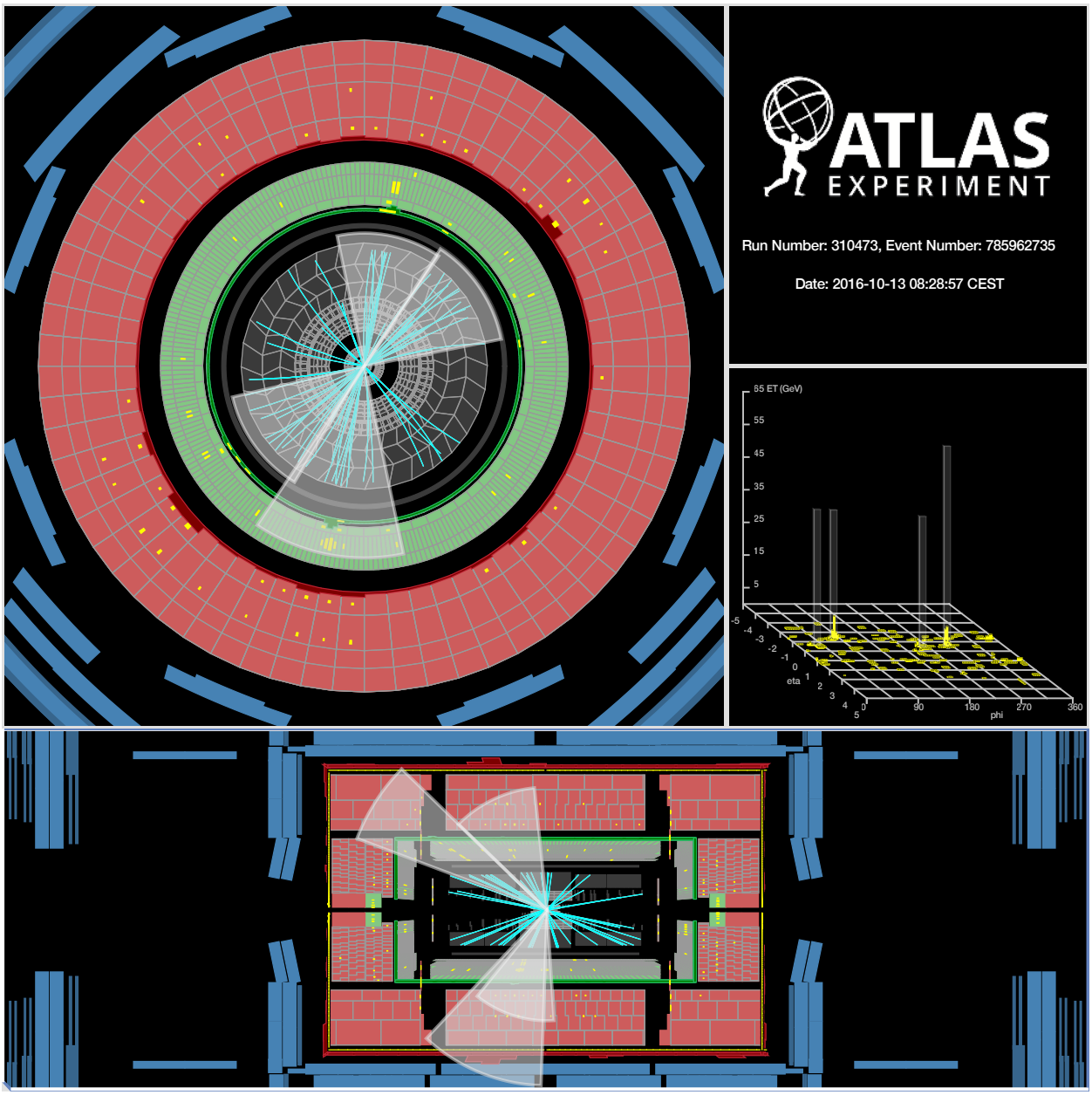

Figure 15.2: An event with four b-tagged jets passing the Signal Region selection, collected during 2016 in 13 TeV pp collision data. The value of m_{HH} is 272 GeV. The tracks shown have transverse momenta above 2 GeV, and the energy deposits in the calorimeters exceed 0.5 GeV.

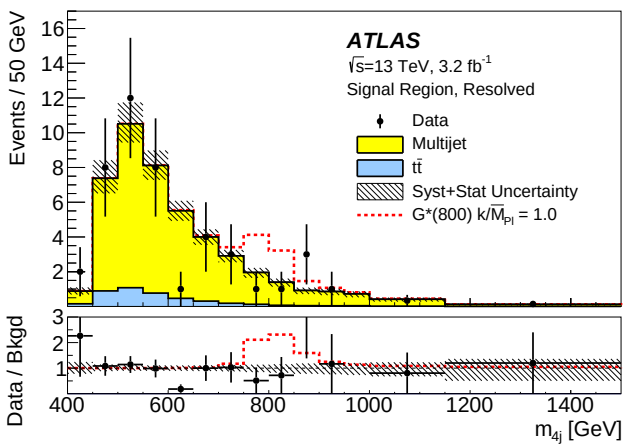

(a) 2015 Analysis [34]
≈ 15 events per fb^{-1}
≈ 30% statistical uncertainty at peak

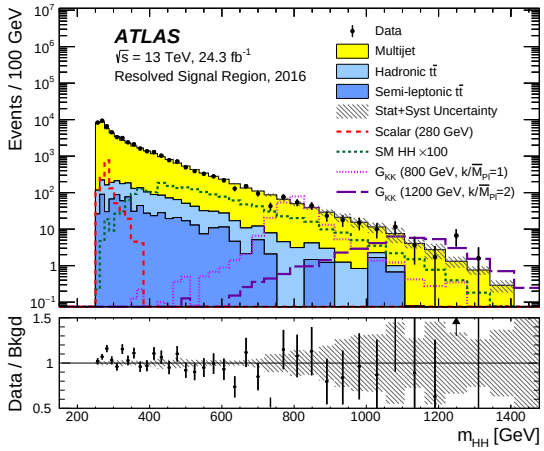

(b) This Thesis
≈ 300 events per fb^{-1}
≈ 3% statistical uncertainty at peak

Figure 15.3: The inclusive irreducible background cross section is twenty times larger than for the restricted phase space probed in the 2015 analysis. The statistical uncertainty in the peak of the background is already at the percent level. Note the change in y-axis range in the ratio plots.

tent with the data. Figure 15.3 shows the dramatic change in statistics and corresponding required statistical precision of the background model that comes from modeling the full m_{HH} spectrum.

This thesis places us firmly in the realm of percent level precision modeling of heavy flavor multijet processes. One could argue, given that other searches have not found a similar excess at $m_{HH} \approx 280\,\text{GeV}$ that there is statistical evidence for underestimated background systematics. Obviously it would be deeply unscientific to use modeling in the Signal Region to assess systematic uncertainties for a future analysis. We find ourselves in need of a way to validate the background model with the statistical precision of the SR. One possibility would be to bootstrap modeling uncertainties in stages by applying the nominal model procedure to a three b-tag selection. Such a selection should have negligible signal contamination, at least

in the low m_{HH} regime.[1] This would provide sufficient statistics to validate the modeling procedure but would not fully cover the extrapolation from two to four b-tags.

Another promising possibility is to test the full search procedure on the SM $pp \to ZZ \to b\bar{b}b\bar{b}$ process with a dedicated ZZ selection. The same technique was used with great success in the recent VH measurements [7, 161] as well as exotic searches for fat jet resonances such as [188] and [10].

While $BR(Z \to b\bar{b}) = 15\%$ is smaller than $BR(H \to b\bar{b}) = 58\%$, the total cross section $\sigma(pp \to ZZ) \approx 16\,\text{pb}$ is nearly five hundred times larger than the SM prediction $\sigma(pp \to HH) \approx 34\,\text{fb}$. The same principle applies to even greater effect for the $HH \to b\bar{b}\tau\tau$ searches. For $\sqrt{s} = 13\,\text{TeV}$ the SM cross section ratios are

$$\frac{\sigma(pp \to ZZ \to b\bar{b}b\bar{b})}{\sigma(pp \to HH \to b\bar{b}b\bar{b})} \approx 31$$

$$\frac{\sigma(pp \to ZZ \to b\bar{b}\tau\tau)}{\sigma(pp \to HH \to b\bar{b}\tau\tau)} \approx 71$$

Given that the current 95% C.L. upper limits on μ for the $b\bar{b}b\bar{b}$ and $b\bar{b}\tau\tau$ channels are both 13 (see Table 5.1) we should study the potential for measuring ZZ production prior to the next round of publications.

The results in this thesis are based on fits in a single signal region to the m_{HH} spectrum. With significant ZZ sensitivity a combined fit in ZZ, HH and multijet and $t\bar{t}$ background enhanced regions both the signal and background systematics could be constrained directly.

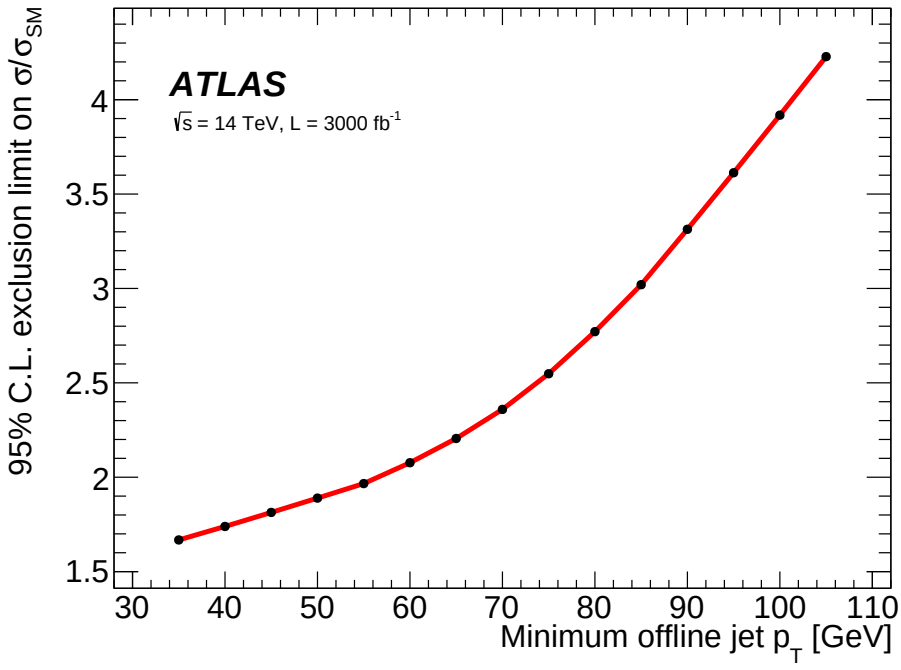

Figure 15.4: Expected 95% C.L. upper limit on the cross-section $\mu \equiv \sigma(HH \to b\bar{b}b\bar{b})/\sigma_{\mathrm{SM}}$, as a function of the online jet p_{T} threshold [70].

15.2 The Fast Tracker

Before analysis improvements can be implemented we must upgrade the ATLAS and CMS detectors such that they can efficiently trigger on HH signal events with all hadronic final states. Figure 15.4 shows the expected limit on μ from the $b\bar{b}b\bar{b}$ HL-LHC extrapolation [31] with zero systematic uncertainty as a function of the online jet p_{T} threshold. Keeping the threshold of a four jet trigger as used in this thesis (Chapter 9) below $\approx 60\,\mathrm{GeV}$ will be required to avoid significant losses in sensitivity.

The primary trigger used in this thesis requires four jets with transverse momentum above 35 GeV where at least two jets are b-tagged at the 60% working point. Online b-tagging is

[1] Around $1 < m_{HH} < 1.5\,\mathrm{TeV}$ a 3 b-tag Resolved selection may be competitive with the Boosted analysis but would significantly complicate orthogonality considerations. See Chapter 8.7 and [197] for more information about the Boosted analysis.

critical to keeping these p_{T} thresholds low but, requires high precision tracking for primary and secondary vertex identification. The CPU resources needed for precision tracking grows nonlinearly with the number of pileup interactions and a new approach will be needed in the High Luminosity era with pileup expected to exceed 200 interactions per bunch crossing.

The ATLAS collaboration is addressing this issue by developing hardware based track reconstruction systems starting with the Fast TracKer (FTK). The FTK is being integrated with the ATLAS trigger system now and is planned to be used for physics in Run-3 where we expect around 80 pileup interactions per bunch crossing. The FTK is designed to provide track reconstruction for the full inner detector (ID, see Chapter 4.1) at the 100 kHz L1 output rate. Software triggers in the HLT can then directly use tracks provided by FTK or use them to seed the full offline tracking algorithm. In either case, the track reconstruction burden placed on the HLT by b-jet triggers will be largely eliminated.

The FTK uses a staged, massively parallel architecture with seven types of custom printed circuit boards (PCBs) shown in Figure 15.5 and hundreds of high speed fiber optic links connecting them. The data flow and staged track fitting process is summarized below:

1. Raw hit data from the ID is clustered in the Input Mezzanine cards (IM).

2. Cluster coordinates and widths are grouped and distributed between Data Formatter boards before being routed to the appropriate track fitting boards. Clusters from 5 SCT layers and three pixel layers are sent to the first stage tracking boards (AUX) while the data from the other three SCT layers and IBL are sent to the Second Stage Boards (SSB).

3. The clusters from the eight layers sent to the AUX are converted to coarse resolution hits called Super Strips (SSID). The full resolution clusters are stored in a linked memory structure by their SSID while the SSIDs are sent to the Associative Memory

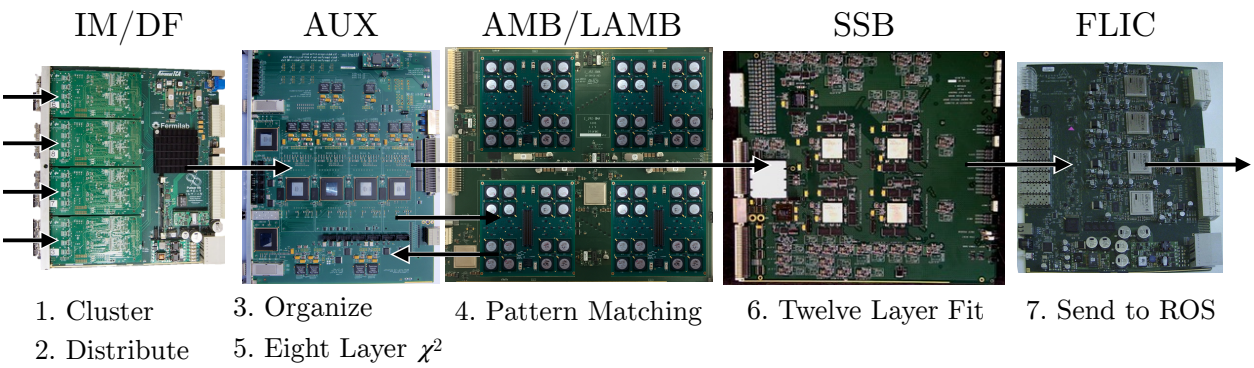

Figure 15.5: The seven custom PCB types of FTK. The full system will consist of 128 Input Mezzanines (IM), 32 Data Formatters (DF), 128 Auxiliary cards (AUX), 128 Associative Memory Boards (AMB), 512 Local AMBs (LAMB), 32 Second Stage Boards (SSB) and 2 FTK Level-2 Interface Cards (FLIC).

Board (AMB).

4. The AMB routes the SSID streams through custom ASICs which each store rough track patterns called Roads. The ID number for Roads matched to at least seven out of eight layers are then sent back to the AUX.

5. The AUX looks up the SSIDs contained in each returned Road and retrieves the corresponding full resolution cluster data. A linearized track candidate χ^2 (goodness of fit) is computed for all possible combinations of clusters in a Road. Track candidates passing a maximum χ^2 threshold are passed on for overlap removal. The candidate with the lowest χ^2 in a given Road is forwarded to an SSB.

6. The SSB extrapolates the first stage tracks to the other four detector layers and computes a new twelve layer χ^2 and helix parameters. Overlap removal is then applied to tracks which pass the twelve layer χ^2 threshold.

7. Second stage tracks are formatted by the FTK Level-2 Interface Cards (FLIC) and sent to the Readout System (ROS) for use in the software based triggers.

Glossary

acceptance Fraction of events where the *true* particle trajectories and energies would pass the selection criteria.. 121

baryon Baryons are bound states of three quarks as in the case of protons (two up quarks and one down quark) and neutrons (two down quarks and one up quark). Conversely, antibaryons are bound states of three antiquarks.. 108, 109

efficiency The fraction of accepted events whose *reconstructed* particle properties pass the selection criteria.. 121

JES Jet Energy Scale. Refers to the algorithm 11.2 which maps the detector response of a jet to a calibrated four-vector. For a detailed description see Reference [25]. 181

jet Strongly coupled particles like quarks and gluons form bound states called hadrons in $\mathcal{O}(10^{-23}\,\mathrm{s})$ and as such are never directly observed in the detector. Instead, high energy quarks and gluons hadronize in collimated sprays of particles which can be algorithmically clustered to form observables called "jets". The jet definition used in this thesis is described in Chapter 7.. 85, 89, 96

parton The general name for any fundamental constituent of a hadron. The proton is made up of quark and gluons which can collectively be called partons.. 75

PDF Parton Distribution Function. Describes probability for a parton to carry a given fraction of the total proton momentum.. 75, 189, 190

radiation length X_0: A material property describing the amount high energy charged particles interact as they pass through. A high energy electron's energy is reduced by a factor of $\frac{1}{e} \approx 37\%$ via bremsstrahlung (photon radiation) on average when passing

through 1 radiation length of material. For high energy photons, the mean free path for pair production ($\gamma \to e^+e^-$) is $\frac{9}{7}X_0$. xxii, 84

VEV Vacuum Expectation Value. Scalar fields are able to have a nonzero VEV without violating the Lorentz symmetry of the vacuum. The Higgs mechanism exploits this fact to allow chiral fermions to obtain a mass term via a yukawa coupling with a VEV that maintains gauge invariance of terms coupling the left and right handed components of Dirac fermions. The spontaneously broken SU(2) symmetry of the scalar results in massive vector bosons and instead of generating a massless Nambu-Goldstone boson, the unbroken generator provides transverse polarization modes for the massive vector bosons in appropriately physical field redefinitions. See Chapter 2.6.4. ix, xi, 53, 54, 58, 104–107

Bibliography

[1] URL: https://flexiblesusy.hepforge.org/images.html (visited on 08/16/2018).

[2] In: (). URL: http://twiki.cern.ch/twiki/bin/viewauth/AtlasProtected/TopCommonParametersMC12.

[3] M. Tanabashi et al. (Particle Data Group). In: *Phys. Rev. D 98, 030001* (2018). URL: http://pdg.lbl.gov/2018/listings/rpp2018-list-p.pdf.

[4] Morad Aaboud et al. "A search for resonant and non-resonant Higgs boson pair production in the $b\bar{b}\tau^+\tau^-$ decay channel in pp collisions at $\sqrt{s} = 13$ TeV with the ATLAS detector". In: *Submitted to: Phys. Rev. Lett.* (2018). arXiv: 1808.00336 [hep-ex].

[5] Morad Aaboud et al. "Measurements of b-jet tagging efficiency with the ATLAS detector using $t\bar{t}$ events at $\sqrt{s} = 13$ TeV". In: (2018). arXiv: 1805.01845 [hep-ex].

[6] Morad Aaboud et al. "Measurements of Higgs boson properties in the diphoton decay channel with 36 fb^{-1} of pp collision data at $\sqrt{s} = 13$ TeV with the ATLAS detector". In: (2018). arXiv: 1802.04146 [hep-ex]. URL: https://atlas.web.cern.ch/Atlas/GROUPS/PHYSICS/PAPERS/HIGG-2016-21/.

[7] Morad Aaboud et al. "Observation of $H \to b\bar{b}$ decays and VH production with the ATLAS detector". In: (2018). arXiv: 1808.08238 [hep-ex].

[8] Morad Aaboud et al. "Observation of Higgs boson production in association with a top quark pair at the LHC with the ATLAS detector". In: (2018). arXiv: 1806.00425 [hep-ex]. URL: https://atlas.web.cern.ch/Atlas/GROUPS/PHYSICS/PAPERS/HIGG-2018-13/.

[9] Morad Aaboud et al. "Search for Higgs boson pair production in the $\gamma\gamma b\bar{b}$ final state with 13 TeV pp collision data collected by the ATLAS experiment". In: (2018). arXiv: 1807.04873 [hep-ex].

[10] Morad Aaboud et al. "Search for light resonances decaying to boosted quark pairs and produced in association with a photon or a jet in proton-proton collisions at $\sqrt{s} = 13$ TeV with the ATLAS detector". In: (2018). arXiv: 1801.08769 [hep-ex].

[11] Kaustubh Agashe. (private communication). *I* think it is difficult to imagine more than a factor of 2 or so enhancement in BR to Higgs, the reason being that the top quark HAS to be localized close to the TeV/Higgs brane in order to reproduce it's large Yukawa coupling to Higgs/mass... so that decay width to top cannot really be reduced, beyond O(1) factor, i.e, the residual freedom in top quark localization... (Just for completeness, let me mention that other SM fermions can be localized away from TeV brane, since their masses are much smaller...) What about simply increasing the $k/\overline{M}_{\rm Pl}$ parameter - again, one can't make it larger than 2 or so - such that overall cross-section is larger?

[12] S. Agostinelli et al. "GEANT4: A simulation toolkit". In: *Nucl. Instrum. Meth. A* 506 (2003), p. 250.

[13] A. Buckley et al. "Rivet user manual". In: (2013). arXiv: 1003.0694v8 [hep-ph]. URL: https://arxiv.org/abs/1003.0694v8.

[14] J Buchanan et al. "Design and implementation of the Front End Board for the readout of the ATLAS liquid argon calorimeters". In: 3 (Mar. 2008), P03004.

[15] J. Butterworth et al. "PDF4LHC recommendations for LHC Run II". In: *Journal of Physics G: Nuclear and Particle Physics* 43.2 (2016), p. 023001. URL: http://stacks.iop.org/0954-3899/43/i=2/a=023001.

[16] Ahmed Almheiri et al. "Black holes: complementarity or firewalls?" In: *Journal of High Energy Physics* 2013.2 (Feb. 2013), p. 62. ISSN: 1029-8479. DOI: 10.1007/JHEP02(2013)062. URL: https://doi.org/10.1007/JHEP02(2013)062.

[17] Carl D. Anderson and Seth H. Neddermeyer. "Cloud Chamber Observations of Cosmic Rays at 4300 Meters Elevation and Near Sea-Level". In: *Phys. Rev.* 50 (4 Aug. 1936), pp. 263–271. DOI: 10.1103/PhysRev.50.263. URL: https://link.aps.org/doi/10.1103/PhysRev.50.263.

[18] P. W. Anderson. "Plasmons, Gauge Invariance, and Mass". In: *Phys. Rev.* 130 (1 Apr. 1963), pp. 439–442. DOI: 10.1103/PhysRev.130.439. URL: https://link.aps.org/doi/10.1103/PhysRev.130.439.

[19] G. Arnison et al. "Experimental Observation of Lepton Pairs of Invariant Mass Around 95-GeV/c**2 at the CERN SPS Collider". In: *Phys. Lett.* B126 (1983). [,7.55(1983)], pp. 398–410. DOI: 10.1016/0370-2693(83)90188-0.

[20] Peter Athron et al. "FlexibleSUSY – A spectrum generator generator for supersymmetric models". In: *Comput. Phys. Commun.* 190 (2015), pp. 139–172. DOI: 10.1016/j.cpc.2014.12.020. arXiv: 1406.2319 [hep-ph].

[21] ATLAS Collaboration. *ATLAS Pythia 8 tunes to 7 TeV data*. ATL-PHYS-PUB-2014-021. 2014. URL: https://cds.cern.ch/record/1966419.

[22] ATLAS Collaboration. *Data-driven determination of the energy scale and resolution of jets reconstructed in the ATLAS calorimeters using dijet and multijet events at* $\sqrt{s} = 8$ *TeV*. ATLAS-CONF-2015-017. 2015. URL: https://cds.cern.ch/record/2008678.

[23] ATLAS Collaboration. "Expected performance of the ATLAS b-tagging algorithms in Run-2". In: ATL-PHYS-PUB-2015-022 (2015). URL: https://cds.cern.ch/record/2037697.

[24] ATLAS Collaboration. "Jet energy measurement with the ATLAS detector in proton-proton collisions at $\sqrt{s} = 7\,\text{TeV}$". In: *Eur. Phys. J. C* 73 (2013), p. 2304. DOI: 10.1140/epjc/s10052-013-2304-2. arXiv: 1112.6426 [hep-ex].

[25] ATLAS Collaboration. "Jet energy scale measurements and their systematic uncertainties in proton-proton collisions at $\sqrt{s} = 13$ TeV with the ATLAS detector. Jet energy scale measurements and their systematic uncertainties in proton-proton collisions at $\sqrt{s} = 13$ TeV with the ATLAS detector". In: *Phys. Rev. D* 96.CERN-EP-2017-038. 7 (Mar. 2017). 51 pages in total, author list starting page 35, 15 figures, 1 table, submitted to Phys. Rev. D., all figures including auxilary figures are available at https://atlas.web.cern.ch/Atlas/GROUPS/PHYSICS/PAPERS/PERF-2016-04/, 072002. 36 p. URL: https://cds.cern.ch/record/2257300.

[26] ATLAS Collaboration. "Measurement of the muon reconstruction performance of the ATLAS detector using 2011 and 2012 LHC proton–proton collision data". In: *Eur. Phys. J. C* 74 (2014), p. 3130. DOI: 10.1140/epjc/s10052-014-3130-x. arXiv: 1407.3935 [hep-ex].

[27] ATLAS Collaboration. "Observation of a new particle in the search for the Standard Model Higgs boson with the ATLAS detector at the LHC". In: *Phys. Lett. B* 716 (2012), p. 1. DOI: 10.1016/j.physletb.2012.08.020. arXiv: 1207.7214 [hep-ex].

[28] ATLAS Collaboration. "Performance of b-Jet Identification in the ATLAS Experiment. Performance of b-Jet Identification in the ATLAS Experiment". In: *JINST* 11.CERN-PH-EP-2015-216 (Dec. 2015). 111 pages plus author list + cover page (128 pages total), 55 figures, 17 tables, submitted to JINST, All figures including auxiliary figures are available at http://atlas.web.cern.ch/Atlas/GROUPS/PHYSICS/PAPERS/PERF-2012-04/, P04008. 127 p. URL: https://cds.cern.ch/record/2110203.

[29] ATLAS Collaboration. "Performance of the ATLAS Trigger System in 2015". In: *Eur. Phys. J. C* 77.CERN-EP-2016-241. 5 (Nov. 2016). 77 pages in total, author list starting page 61, 50 figures, 1 table. Published in Eur. Phys. J. C. All figures including auxiliary figures are available at http://atlas.web.cern.ch/Atlas/GROUPS/PHYSICS/PAPERS/TRIG-2016-01/, 317. 76 p. URL: https://cds.cern.ch/record/2235584.

[30] ATLAS Collaboration. "Performance of the ATLAS Trigger System in 2015". In: *Eur. Phys. J. C* 77 (2017), p. 317. DOI: 10.1140/epjc/s10052-017-4852-3. arXiv: 1611.09661 [hep-ex].

[31] ATLAS Collaboration. *Projected sensitivity to Higgs boson pair production in the $b\bar{b}b\bar{b}$ final state using proton–proton collisions at HL-LHC with the ATLAS detector*. ATL-PHYS-PUB-2016-024. 2016. URL: https://cds.cern.ch/record/2221658.

[32] ATLAS Collaboration. "Search for Higgs boson pair production in the $b\bar{b}b\bar{b}$ final state from pp collisions at $\sqrt{s} = 8$ TeV with the ATLAS detector". In: *Eur. Phys. J. C* 75 (2015), p. 412. DOI: 10.1140/epjc/s10052-015-3628-x. arXiv: 1506.00285 [hep-ex].

[33] ATLAS Collaboration. *Search for pair production of Higgs bosons in the $b\bar{b}b\bar{b}$ final state using proton–proton collisions at $\sqrt{s} = 13$ TeV with the ATLAS detector*. ATLAS-CONF-2016-049. 2016. URL: https://cds.cern.ch/record/2206131.

[34] ATLAS Collaboration. "Search for pair production of Higgs bosons in the $b\bar{b}b\bar{b}$ final state using proton–proton collisions at $\sqrt{s} = 13$ TeV with the ATLAS detector". In: *Phys. Rev. D* 94 (2016), p. 052002. DOI: 10.1103/PhysRevD.94.052002. arXiv: 1606.04782 [hep-ex].

[35] ATLAS Collaboration. "Search for pair production of Higgs bosons in the $b\bar{b}b\bar{b}$ final state using proton-proton collisions at $\sqrt{s} = 13$ TeV with the ATLAS detector". In: (2018). arXiv: 1804.06174 [hep-ex].

[36] ATLAS Collaboration. "Summary of ATLAS Pythia 8 tunes". In: (2012). URL: http://cdsweb.cern.ch/record/1474107.

[37] ATLAS Collaboration. *Tagging and suppression of pileup jets with the ATLAS detector*. ATLAS-CONF-2014-018. 2014. URL: https://cds.cern.ch/record/1700870.

[38] ATLAS Collaboration. "The ATLAS Experiment at the CERN Large Hadron Collider". In: *JINST* 3 (2008), S08003.

[39] ATLAS Collaboration. "The ATLAS simulation infrastructure". In: *Eur. Phys. J. C* 70 (2010), p. 823. arXiv: 1005.4568 [physics.ins-det].

[40] ATLAS Collaboration. *The Run-2 ATLAS Trigger System*. Tech. rep. ATL-DAQ-PROC-2016-003. Geneva: CERN, Feb. 2016. URL: https://cds.cern.ch/record/2133909.

[41] *ATLAS inner detector: Technical Design Report, 1*. Technical Design Report ATLAS. Geneva: CERN, 1997. URL: https://cds.cern.ch/record/331063.

[42] "ATLAS inner detector: Technical design report. Vol. 2". In: (1997).

[43] *ATLAS Insertable B-Layer Technical Design Report*. Tech. rep. CERN-LHCC-2010-013. ATLAS-TDR-19. Sept. 2010. URL: http://cds.cern.ch/record/1291633.

[44] *ATLAS liquid-argon calorimeter: Technical Design Report*. Technical Design Report ATLAS. Geneva: CERN, 1996. URL: https://cds.cern.ch/record/331061.

[45] "ATLAS muon spectrometer: Technical design report". In: (1997).

[46] *ATLAS tile calorimeter: Technical Design Report*. Technical Design Report ATLAS. Geneva: CERN, 1996. URL: https://cds.cern.ch/record/331062.

[47] J. J. Aubert et al. "Experimental Observation of a Heavy Particle J". In: *Phys. Rev. Lett.* 33 (23 Dec. 1974), pp. 1404–1406. DOI: 10.1103/PhysRevLett.33.1404. URL: https://link.aps.org/doi/10.1103/PhysRevLett.33.1404.

[48] J. -E. et al. Augustin. "Discovery of a Narrow Resonance in e^+e^- Annihilation". In: *Phys. Rev. Lett.* 33 (23 Dec. 1974), pp. 1406–1408. DOI: 10.1103/PhysRevLett.33.1406. URL: https://link.aps.org/doi/10.1103/PhysRevLett.33.1406.

[49] John C. Baez. "Struggles with the Continuum". In: (2016). arXiv: 1609.01421 [math-ph].

[50] P. Bagnaia et al. "Evidence for Z0 —> e+ e- at the CERN anti-p p Collider". In: *Phys. Lett.* B129 (1983). [,7.69(1983)], pp. 130–140. DOI: 10.1016/0370-2693(83)90744-X.

[51] Richard D. Ball et al. "Parton distributions with LHC data". In: *Nucl. Phys. B* 867 (2013), p. 244. DOI: 10.1016/j.nuclphysb.2012.10.003. arXiv: 1207.1303.

[52] J. Bardeen, L. N. Cooper, and J. R. Schrieffer. "Theory of Superconductivity". In: *Phys. Rev.* 108 (5 Dec. 1957), pp. 1175–1204. DOI: 10.1103/PhysRev.108.1175. URL: https://link.aps.org/doi/10.1103/PhysRev.108.1175.

[53] J. S. Bell. "Time reversal in field theory". In: (1955). [Proc. Roy. Soc. Lond.A231,479(1955)]. DOI: 10.1098/rspa.1955.0189.

[54] Brando Bellazzini et al. "Beyond Positivity Bounds and the Fate of Massive Gravity". In: *Phys. Rev. Lett.* 120 (16 Apr. 2018), p. 161101. DOI: 10.1103/PhysRevLett.120.161101. URL: https://link.aps.org/doi/10.1103/PhysRevLett.120.161101.

[55] Bastian Bergerhoff and Christof Wetterich. "Electroweak Phase Transition in the Early Universe?" In: *Current Topics in Astrofundamental Physics: Primordial Cosmology*. Ed. by N. Sánchez and A. Zichichi. Dordrecht: Springer Netherlands, 1998, pp. 211–240. ISBN: 978-94-011-5046-0. DOI: 10.1007/978-94-011-5046-0_6. URL: https://doi.org/10.1007/978-94-011-5046-0_6.

[56] H. A. Bethe. "The Electromagnetic Shift of Energy Levels". In: *Phys. Rev.* 72 (4 Aug. 1947), pp. 339–341. DOI: 10.1103/PhysRev.72.339. URL: https://link.aps.org/doi/10.1103/PhysRev.72.339.

[57] Wolfgang Bietenholz and Lilian Prado. "Revolutionary physics in reactionary Argentina". In: *Physics Today* 67.2 (2014), pp. 38–43. DOI: 10.1063/PT.3.2277. eprint: https://doi.org/10.1063/PT.3.2277. URL: https://doi.org/10.1063/PT.3.2277.

[58] T. Blum et al. "Working Group Report: Lattice Field Theory". In: *Proceedings, 2013 Community Summer Study on the Future of U.S. Particle Physics: Snowmass on the Mississippi (CSS2013): Minneapolis, MN, USA, July 29-August 6, 2013*. 2013. arXiv: 1310.6087 [hep-lat]. URL: https://inspirehep.net/record/1261893/files/arXiv:1310.6087.pdf.

[59] C. G. Bollini and J. J. Giambiagi. "Dimensional Renormalization: The Number of Dimensions as a Regularizing Parameter". In: *Nuovo Cim.* B12 (1972), pp. 20–26. DOI: 10.1007/BF02895558.

[60] S. Borowka et al. "Full top quark mass dependence in Higgs boson pair production at NLO". In: *JHEP* 10 (2016), p. 107. DOI: 10.1007/JHEP10(2016)107. arXiv: 1608.04798 [hep-ph].

[61] S. Borowka et al. "Higgs boson pair production in gluon fusion at NLO with full top-quark mass dependence". In: *Phys. Rev. Lett.* 117.1 (2016), p. 012001. DOI: 10.1103/PhysRevLett.117.012001. arXiv: 1604.06447 [hep-ph].

[62] Rene Brun and Fons Rademakers. "ROOT - An Object Oriented Data Analysis Framework". In: *Proceedings, AIHENP'96 Workshop, Lausanne, Nucl. Inst. and Meth. in Phys. Res. A 389*. 1997, pp. 81–86. URL: http://root.cern.ch/.

[63] Oliver Sim Bruning et al. *LHC Design Report*. CERN Yellow Reports: Monographs. Geneva: CERN, 2004. URL: https://cds.cern.ch/record/782076.

[64] Francis Bursa. "The Undulator Radiation Collider: An Energy Efficient Design For A $\sqrt{s} = 10^{15}$ GeV Collider". In: (2017). arXiv: 1704.04469 [physics.acc-ph].

[65] Nicola Cabibbo. "Unitary Symmetry and Leptonic Decays". In: *Phys. Rev. Lett.* 10 (12 June 1963), pp. 531–533. DOI: 10.1103/PhysRevLett.10.531. URL: https://link.aps.org/doi/10.1103/PhysRevLett.10.531.

[66] Matteo Cacciari, Gavin P. Salam, and Gregory Soyez. "The anti-k$_t$ jet clustering algorithm". In: *JHEP* 04 (2008), p. 063. DOI: 10.1088/1126-6708/2008/04/063. arXiv: 0802.1189.

[67] Marcela Carena, Zhen Liu, and Marc Riembau. "Probing the electroweak phase transition via enhanced di-Higgs boson production". In: *Phys. Rev. D* 97 (9 May 2018), p. 095032. DOI: 10.1103/PhysRevD.97.095032. URL: https://link.aps.org/doi/10.1103/PhysRevD.97.095032.

[68] Sarah Charley. "The LHC does a dry run". In: *Symmetry Magazine* (2015). URL: https://www.symmetrymagazine.org/article/march-2015/the-lhc-does-a-dry-run.

[69] J. H. Christenson et al. "Evidence for the 2π Decay of the K_2^0 Meson". In: *Phys. Rev. Lett.* 13 (4 July 1964), pp. 138–140. DOI: 10.1103/PhysRevLett.13.138. URL: https://link.aps.org/doi/10.1103/PhysRevLett.13.138.

[70] ATLAS Collaboration. *Technical Design Report for the Phase-II Upgrade of the ATLAS TDAQ System*. Tech. rep. CERN-LHCC-2017-020. ATLAS-TDR-029. Geneva: CERN, Sept. 2017. URL: https://cds.cern.ch/record/2285584.

[71] The ATLAS collaboration. "Search for Higgs boson pair production in the final state of $\gamma\gamma WW^*(\rightarrow l\nu jj)$ using 13.3 fb^{-1} of pp collision data recorded at $\sqrt{s} = 13$ TeV with the ATLAS detector". In: (2016).

[72] "Combined Analysis of Neutrino and Antineutrino Oscillations at T2K". In: *Phys. Rev. Lett.* 118 (15 Apr. 2017), p. 151801. DOI: 10.1103/PhysRevLett.118.151801. URL: https://link.aps.org/doi/10.1103/PhysRevLett.118.151801.

[73] *Combined measurements of Higgs boson production and decay using up to 80 fb^{-1} of proton–proton collision data at $\sqrt{s}$ = 13 TeV collected with the ATLAS experiment*. Tech. rep. ATLAS-CONF-2018-031. Geneva: CERN, July 2018. URL: https://cds.cern.ch/record/2629412.

[74] *Commissioning of the ATLAS b-tagging algorithms using $t\bar{t}$ events in early Run-2 data*. Tech. rep. ATL-PHYS-PUB-2015-039. Geneva: CERN, Aug. 2015. URL: http://cds.cern.ch/record/2047871.

[75] C. L. Cowan et al. "Detection of the Free Neutrino: a Confirmation". In: *Science* 124.3212 (1956), pp. 103–104. ISSN: 0036-8075. DOI: 10.1126/science.124.3212.103. eprint: http://science.sciencemag.org/content/124/3212/103.full.pdf. URL: http://science.sciencemag.org/content/124/3212/103.

[76] G. Cowan et al. "Asymptotic formulae for likelihood-based tests of new physics". In: *Eur. Phys. J. C* 71 (2011), p. 1554. arXiv: 1007.1727 [hep-ex].

[77] Glen Cowan et al. "Asymptotic formulae for likelihood-based tests of new physics". In: *Eur. Phys. J. C* 71 (2011), p. 1554. DOI: 10.1140/epjc/s10052-011-1554-0. arXiv: 1007.1727 [hep-ex].

[78] *Cross-section measurements of the Higgs boson decaying to a pair of tau leptons in proton–proton collisions at $\sqrt{s}$ = 13 TeV with the ATLAS detector*. Tech. rep. ATLAS-CONF-2018-021. Geneva: CERN, June 2018. URL: http://cds.cern.ch/record/2621794.

[79] "CURRENT ALGEBRA AT SMALL DISTANCES". In: *Proceedings of the International School of Physics* SLAC-PUB-338 (Aug. 1967). URL: http://www.slac.stanford.edu/cgi-wrap/getdoc/slac-pub-0338.pdf.

[80] Sakharov A. D. "Violation of CP Invariance, C Asymmetry, and Baryon Asymmetry of the Universe". In: *JETP Letters* 5 (1967), pp. 24–26. URL: http://www.jetpletters.ac.ru/ps/1643/article_25089.pdf.

[81] Guido D'Amico et al. "Flavour anomalies after the RK∗ measurement". In: *Journal of High Energy Physics* 2017.9 (Sept. 2017), p. 10. ISSN: 1029-8479. DOI: 10.1007/JHEP09(2017)010. URL: https://doi.org/10.1007/JHEP09(2017)010.

[82] G. Danby et al. "Observation of High-Energy Neutrino Reactions and the Existence of Two Kinds of Neutrinos". In: *Phys. Rev. Lett.* 9 (1 July 1962), pp. 36–44. DOI: 10.1103/PhysRevLett.9.36. URL: https://link.aps.org/doi/10.1103/PhysRevLett.9.36.

[83] Raymond Davis, Don S. Harmer, and Kenneth C. Hoffman. "Search for Neutrinos from the Sun". In: *Phys. Rev. Lett.* 20 (21 May 1968), pp. 1205–1209. DOI: 10.1103/PhysRevLett.20.1205. URL: https://link.aps.org/doi/10.1103/PhysRevLett.20.1205.

[84] S. Dawson, S. Dittmaier, and M. Spira. "Neutral Higgs boson pair production at hadron colliders: QCD corrections". In: *Phys. Rev. D* 58 (1998), p. 115012. DOI: 10.1103/PhysRevD.58.115012. arXiv: hep-ph/9805244.

[85] Bryce S. DeWitt. "Quantum Theory of Gravity. III. Applications of the Covariant Theory". In: *Phys. Rev.* 162 (5 Oct. 1967), pp. 1239–1256. DOI: 10.1103/PhysRev.162.1239. URL: https://link.aps.org/doi/10.1103/PhysRev.162.1239.

[86] E. Diehl. "Calibration and Performance of the ATLAS Muon Spectrometer". In: *Particles and fields. Proceedings, Meeting of the Division of the American Physical Society, DPF 2011, Providence, USA, August 9-13, 2011*. 2011. arXiv: 1109.6933 [physics.ins-det]. URL: http://inspirehep.net/record/930228/files/arXiv:1109.6933.pdf.

[87] P. A. M. Dirac. "The Quantum Theory of the Electron". In: *Proceedings of the Royal Society of London. Series A, Containing Papers of a Mathematical and Physical Character* 117.778 (1928), pp. 610–624. ISSN: 09501207. URL: http://www.jstor.org/stable/94981.

[88] Michel Dubois-Violette. "Exceptional quantum geometry and particle physics". In: *Nuclear Physics B* 912 (2016). Mathematical Foundations of Quantum Field Theory: A volume dedicated to the Memory of Raymond Stora, pp. 426–449. ISSN: 0550-3213. DOI: https://doi.org/10.1016/j.nuclphysb.2016.04.018. URL: http://www.sciencedirect.com/science/article/pii/S0550321316300566.

[89] Michel Dubois-Violette and Ivan Todorov. "Exceptional quantum geometry and particle physics II". In: (2018). arXiv: 1808.08110 [hep-th].

[90] F. J. Dyson. "The Radiation Theories of Tomonaga, Schwinger, and Feynman". In: *Phys. Rev.* 75 (3 Feb. 1949), pp. 486–502. DOI: 10.1103/PhysRev.75.486. URL: https://link.aps.org/doi/10.1103/PhysRev.75.486.

[91] Astrid Eichhorn and Aaron Held. "Top mass from asymptotic safety". In: *Physics Letters B* 777 (2018), pp. 217–221. ISSN: 0370-2693. DOI: https://doi.org/10.1016/j.physletb.2017.12.040. URL: http://www.sciencedirect.com/science/article/pii/S0370269317310171.

[92] A. Einstein. "Über einen die Erzeugung und Verwandlung des Lichtes betreffenden heuristischen Gesichtspunkt". In: *Annalen der Physik* 322.6 (), pp. 132–148. DOI: 10.1002/andp.19053220607. eprint: https://onlinelibrary.wiley.com/doi/pdf/10.1002/andp.19053220607. URL: https://onlinelibrary.wiley.com/doi/abs/10.1002/andp.19053220607.

[93] A. Einstein. "Zur Elektrodynamik bewegter Körper". In: *Annalen der Physik* 322.10 (), pp. 891–921. DOI: 10.1002/andp.19053221004. eprint: https://onlinelibrary.

wiley.com/doi/pdf/10.1002/andp.19053221004. URL: https://onlinelibrary.wiley.com/doi/abs/10.1002/andp.19053221004.

[94] Albert Einstein. "Physics and reality". In: *Journal of the Franklin Institute* 221.3 (1936), pp. 349–382. ISSN: 0016-0032. DOI: https://doi.org/10.1016/S0016-0032(36)91047-5. URL: http://www.sciencedirect.com/science/article/pii/S0016003236910475.

[95] Joshua Ellis. "TikZ-Feynman: Feynman diagrams with TikZ". In: (2016). arXiv: 1601.05437 [hep-ph]. URL: http://arxiv.org/abs/1601.05437.

[96] Henriette Elvang and Yu-tin Huang. *Scattering Amplitudes in Gauge Theory and Gravity*. Cambridge University Press, 2015. ISBN: 978-1-107-06925-1.

[97] F. Englert and R. Brout. "Broken Symmetry and the Mass of Gauge Vector Mesons". In: *Phys. Rev. Lett.* 13 (9 Aug. 1964), pp. 321–323. DOI: 10.1103/PhysRevLett.13.321. URL: https://link.aps.org/doi/10.1103/PhysRevLett.13.321.

[98] "Experimental observation of isolated large transverse energy electrons with associated missing energy at s=540 GeV". In: *Physics Letters B* 122.1 (1983), pp. 103–116. ISSN: 0370-2693. DOI: https://doi.org/10.1016/0370-2693(83)91177-2. URL: http://www.sciencedirect.com/science/article/pii/0370269383911772.

[99] Karl Pearson F.R.S. "X. On the criterion that a given system of deviations from the probable in the case of a correlated system of variables is such that it can be reasonably supposed to have arisen from random sampling". In: *The London, Edinburgh, and Dublin Philosophical Magazine and Journal of Science* 50.302 (1900), pp. 157–175. DOI: 10.1080/14786440009463897. eprint: https://doi.org/10.1080/14786440009463897. URL: https://doi.org/10.1080/14786440009463897.

[100] R. P. Feynman. "Space-Time Approach to Non-Relativistic Quantum Mechanics". In: *Rev. Mod. Phys.* 20 (2 Apr. 1948), pp. 367–387. DOI: 10.1103/RevModPhys.20.367. URL: https://link.aps.org/doi/10.1103/RevModPhys.20.367.

[101] R. P. Feynman. "Space-Time Approach to Quantum Electrodynamics". In: *Phys. Rev.* 76 (6 Sept. 1949), pp. 769–789. DOI: 10.1103/PhysRev.76.769. URL: https://link.aps.org/doi/10.1103/PhysRev.76.769.

[102] Liam Fitzpatrick et al. "Searching for the Kaluza-Klein graviton in bulk RS models". In: *JHEP* 09 (2007), p. 013. DOI: 10.1088/1126-6708/2007/09/013. arXiv: hep-ph/0701150.

[103] Mario Flory, Robert C. Helling, and Constantin Sluka. "How I Learned to Stop Worrying and Love QFT". In: (2012). arXiv: 1201.2714 [math-ph].

[104] H. Fritzsch, M. Gell-Mann, and H. Leutwyler. "Advantages of the color octet gluon picture". In: *Physics Letters B* 47.4 (1973), pp. 365–368. ISSN: 0370-2693. DOI: https://doi.org/10.1016/0370-2693(73)90625-4. URL: http://www.sciencedirect.com/science/article/pii/0370269373906254.

[105] Stefano Frixione, Paolo Nason, and Carlo Oleari. "Matching NLO QCD computations with Parton Shower simulations: the POWHEG method". In: *JHEP* 11 (2007), p. 070. arXiv: 0709.2092.

[106] C. Furey. "$SU(3)_C \times SU(2)_L \times U(1)_Y$ ($\times U(1)_X$) as a symmetry of division algebraic ladder operators". In: *Eur. Phys. J.* C78.5 (2018), p. 375. DOI: 10.1140/epjc/s10052-018-5844-7. arXiv: 1806.00612 [hep-th].

[107] C. Furey. "Standard model physics from an algebra?" PhD thesis. Waterloo U., 2015. arXiv: 1611.09182 [hep-th].

[108] M. Gell-Mann. "A schematic model of baryons and mesons". In: *Physics Letters* 8.3 (1964), pp. 214–215. ISSN: 0031-9163. DOI: https://doi.org/10.1016/S0031-9163(64)92001-3. URL: http://www.sciencedirect.com/science/article/pii/S0031916364920013.

[109] Walther Gerlach and Otto Stern. "Der experimentelle Nachweis der Richtungsquantelung im Magnetfeld". In: *Zeitschrift für Physik* 9.1 (Dec. 1922), pp. 349–352. ISSN: 0044-3328. DOI: 10.1007/BF01326983. URL: https://doi.org/10.1007/BF01326983.

[110] G. F. Giudice, P. Paradisi, and M. Passera. "Testing new physics with the electron g-2". In: *JHEP* 11 (2012), p. 113. DOI: 10.1007/JHEP11(2012)113. arXiv: 1208.6583 [hep-ph].

[111] S. L. Glashow, J. Iliopoulos, and L. Maiani. "Weak Interactions with Lepton-Hadron Symmetry". In: *Phys. Rev. D* 2 (7 Oct. 1970), pp. 1285–1292. DOI: 10.1103/PhysRevD.2.1285. URL: https://link.aps.org/doi/10.1103/PhysRevD.2.1285.

[112] Sheldon L. Glashow. "Partial-symmetries of weak interactions". In: *Nuclear Physics* 22.4 (1961), pp. 579–588. ISSN: 0029-5582. DOI: https://doi.org/10.1016/0029-5582(61)90469-2. URL: http://www.sciencedirect.com/science/article/pii/0029558261904692.

[113] Sheldon L. Glashow. "The renormalizability of vector meson interactions". In: *Nuclear Physics* 10 (1959), pp. 107–117. ISSN: 0029-5582. DOI: https://doi.org/10.1016/0029-5582(59)90196-8. URL: http://www.sciencedirect.com/science/article/pii/0029558259901968.

[114] E W Nigel Glover and Jochum J Van der Bij. "Higgs boson pair production via gluon fusion". In: *Nucl. Phys. B* 309.CERN-TH-4934-87 (Dec. 1987), 282–294. 20 p. URL: https://cds.cern.ch/record/183945.

[115] Wesley Gohn. "The Muon g-2 Experiment at Fermilab". In: 2017. arXiv: 1801.00084 [hep-ex]. URL: http://lss.fnal.gov/archive/2017/conf/fermilab-conf-17-602-ppd.pdf.

[116] Jeffrey Goldstone, Abdus Salam, and Steven Weinberg. "Broken Symmetries". In: *Phys. Rev.* 127 (3 Aug. 1962), pp. 965–970. DOI: 10.1103/PhysRev.127.965. URL: https://link.aps.org/doi/10.1103/PhysRev.127.965.

[117] André de Gouvêa. "Neutrino Mass Models". In: *Annual Review of Nuclear and Particle Science* 66.1 (2016), pp. 197–217. DOI: 10.1146/annurev-nucl-102115-044600. eprint: https://doi.org/10.1146/annurev-nucl-102115-044600. URL: https://doi.org/10.1146/annurev-nucl-102115-044600.

[118] M. Grazzini et al. "Higgs boson pair production at NNLO with top quark mass effects". In: *Journal of High Energy Physics* 2018.5 (May 2018), p. 59. ISSN: 1029-8479. DOI: 10.1007/JHEP05(2018)059. URL: https://doi.org/10.1007/JHEP05(2018)059.

[119] V. Gribov and B. Pontecorvo. "Neutrino astronomy and lepton charge". In: *Physics Letters B* 28.7 (1969), pp. 493–496. ISSN: 0370-2693. DOI: https://doi.org/10.1016/0370-2693(69)90525-5. URL: http://www.sciencedirect.com/science/article/pii/0370269369905255.

[120] David J. Gross and Frank Wilczek. "Ultraviolet Behavior of Non-Abelian Gauge Theories". In: *Phys. Rev. Lett.* 30 (26 June 1973), pp. 1343–1346. DOI: 10.1103/PhysRevLett.30.1343. URL: https://link.aps.org/doi/10.1103/PhysRevLett.30.1343.

[121] G. S. Guralnik, C. R. Hagen, and T. W. B. Kibble. "Global Conservation Laws and Massless Particles". In: *Phys. Rev. Lett.* 13 (20 Nov. 1964), pp. 585–587. DOI: 10.1103/PhysRevLett.13.585. URL: https://link.aps.org/doi/10.1103/PhysRevLett.13.585.

[122] D. Hanneke, S. Fogwell, and G. Gabrielse. "New Measurement of the Electron Magnetic Moment and the Fine Structure Constant". In: *Phys. Rev. Lett.* 100 (12 Mar. 2008), p. 120801. DOI: 10.1103/PhysRevLett.100.120801. URL: https://link.aps.org/doi/10.1103/PhysRevLett.100.120801.

[123] W. Heisenberg. "Über den Bau der Atomkerne. I". In: *Zeitschrift für Physik* 77.1 (Jan. 1932), pp. 1–11. ISSN: 0044-3328. DOI: 10.1007/BF01342433. URL: https://doi.org/10.1007/BF01342433.

[124] S. W. Herb et al. "Observation of a Dimuon Resonance at 9.5 GeV in 400-GeV Proton-Nucleus Collisions". In: *Phys. Rev. Lett.* 39 (5 Aug. 1977), pp. 252–255. DOI: 10.1103/PhysRevLett.39.252. URL: https://link.aps.org/doi/10.1103/PhysRevLett.39.252.

[125] Benoît Hespel, David López-Val, and Eleni Vryonidou. "Higgs pair production via gluon fusion in the Two-Higgs-Doublet Model". In: *Journal of High Energy Physics* 2014.9 (Sept. 2014), p. 124. ISSN: 1029-8479. DOI: 10.1007/JHEP09(2014)124. URL: https://doi.org/10.1007/JHEP09(2014)124.

[126] Benoit Hespel and Eleni Vryonidou. *Higgs Pair Production*. 2015. URL: https://cp3.irmp.ucl.ac.be/projects/madgraph/wiki/HiggsPairProduction (visited on 04/24/2015).

[127] Peter W. Higgs. "Broken Symmetries and the Masses of Gauge Bosons". In: *Phys. Rev. Lett.* 13 (16 Oct. 1964), pp. 508–509. DOI: 10.1103/PhysRevLett.13.508. URL: https://link.aps.org/doi/10.1103/PhysRevLett.13.508.

[128] G. 't Hooft and M. Veltman. "Regularization and renormalization of gauge fields". In: *Nuclear Physics B* 44.1 (1972), pp. 189–213. ISSN: 0550-3213. DOI: https://doi.org/10.1016/0550-3213(72)90279-9. URL: http://www.sciencedirect.com/science/article/pii/0550321372902799.

[129] Fa Peng Huang et al. "Testing the electroweak phase transition and electroweak baryogenesis at the LHC and a circular electron-positron collider". In: *Phys. Rev. D* 93 (10 May 2016), p. 103515. DOI: 10.1103/PhysRevD.93.103515. URL: https://link.aps.org/doi/10.1103/PhysRevD.93.103515.

[130] Peisi Huang, Andrew J. Long, and Lian-Tao Wang. "Probing the electroweak phase transition with Higgs factories and gravitational waves". In: *Phys. Rev. D* 94 (7 Oct. 2016), p. 075008. DOI: 10.1103/PhysRevD.94.075008. URL: https://link.aps.org/doi/10.1103/PhysRevD.94.075008.

[131] Stephen P. Jordan, Keith S. M. Lee, and John Preskill. "Quantum Computation of Scattering in Scalar Quantum Field Theories". In: (2011). [Quant. Inf. Comput.14,1014(2014)]. arXiv: 1112.4833 [hep-th].

[132] Alexander Keshavarzi, Daisuke Nomura, and Thomas Teubner. "Muon $g-2$ and $\alpha(M_Z^2)$: A new data-based analysis". In: *Phys. Rev. D* 97 (11 June 2018), p. 114025. DOI: 10.1103/PhysRevD.97.114025. URL: https://link.aps.org/doi/10.1103/PhysRevD.97.114025.

[133] Felix Kling, Jose Miguel No, and Shufang Su. "Anatomy of exotic Higgs decays in 2HDM". In: *Journal of High Energy Physics* 2016.9 (Sept. 2016), p. 93. ISSN: 1029-8479. DOI: 10.1007/JHEP09(2016)093. URL: https://doi.org/10.1007/JHEP09(2016)093.

[134] Zirô Koba, Takao Tati, and Sin-ichirô Tomonaga. "On a Relativistically Invariant Formulation of the Quantum Theory of Wave Fields. III Case of Interacting Electromagnetic and Electron Fields". In: *Progress of Theoretical Physics* 2.4 (1947), pp. 198–208. DOI: 10.1143/ptp/2.4.198. eprint: /oup/backfile/content_public/journal/ptp/2/4/10.1143/ptp/2.4.198/2/2-4-198.pdf. URL: http://dx.doi.org/10.1143/ptp/2.4.198.

[135] Makoto Kobayashi and Toshihide Maskawa. "CP-Violation in the Renormalizable Theory of Weak Interaction". In: *Progress of Theoretical Physics* 49.2 (1973), pp. 652–657. DOI: 10.1143/PTP.49.652. eprint: /oup/backfile/content_public/journal/ptp/49/2/10.1143/ptp.49.652/2/49-2-652.pdf. URL: http://dx.doi.org/10.1143/PTP.49.652.

[136] K. Kodama et al. "Observation of tau neutrino interactions". In: *Phys. Lett.* B504 (2001), pp. 218–224. DOI: 10.1016/S0370-2693(01)00307-0. arXiv: hep-ex/0012035 [hep-ex].

[137] Arthur Kosowsky, Michael S. Turner, and Richard Watkins. "Gravitational waves from first-order cosmological phase transitions". In: *Phys. Rev. Lett.* 69 (14 Oct. 1992), pp. 2026–2029. DOI: 10.1103/PhysRevLett.69.2026. URL: https://link.aps.org/doi/10.1103/PhysRevLett.69.2026.

[138] "Latest update in the search for the Higgs boson. Latest update in the search for the Higgs boson". In: (July 2012). URL: http://cds.cern.ch/record/1459565.

[139] T. D. Lee and C. N. Yang. "Question of Parity Conservation in Weak Interactions". In: *Phys. Rev.* 104 (1 Oct. 1956), pp. 254–258. DOI: 10.1103/PhysRev.104.254. URL: https://link.aps.org/doi/10.1103/PhysRev.104.254.

[140] LHC Higgs Cross Section Working Group. Geneva, 2016. URL: https://twiki.cern.ch/twiki/bin/view/LHCPhysics/LHCHXSWG.

[141] Daniel F. Litim and Francesco Sannino. "Asymptotic safety guaranteed". In: *Journal of High Energy Physics* 2014.12 (Dec. 2014), p. 178. ISSN: 1029-8479. DOI: 10.1007/JHEP12(2014)178. URL: https://doi.org/10.1007/JHEP12(2014)178.

[142] Ziro Maki, Masami Nakagawa, and Shoichi Sakata. "Remarks on the Unified Model of Elementary Particles". In: *Progress of Theoretical Physics* 28.5 (1962), pp. 870–880. DOI: 10.1143/PTP.28.870. eprint: /oup/backfile/content_public/journal/ptp/

28/5/10.1143/ptp.28.870/2/28-5-870.pdf. URL: http://dx.doi.org/10.1143/PTP.28.870.

[143] Konstantin T. Matchev and Scott Thomas. "Higgs and Z-boson signatures of supersymmetry". In: *Phys. Rev. D* 62 (7 Sept. 2000), p. 077702. DOI: 10.1103/PhysRevD.62.077702. URL: https://link.aps.org/doi/10.1103/PhysRevD.62.077702.

[144] J. Clerk Maxwell. "A Dynamical Theory of the Electromagnetic Field". In: *Philosophical Transactions of the Royal Society of London* 155 (1865), pp. 459–512. ISSN: 02610523. URL: http://www.jstor.org/stable/108892.

[145] *Measurement of gluon fusion and vector boson fusion Higgs boson production cross-sections in the $H \to WW^* \to e\nu\mu\nu$ decay channel in pp collisions at $\sqrt{s} = 13$ TeV with the ATLAS detector*. Tech. rep. ATLAS-CONF-2018-004. Geneva: CERN, Mar. 2018. URL: http://cds.cern.ch/record/2308392.

[146] "Measurement of the Inelastic Proton-Proton Cross Section at $\sqrt{s} = 13$ TeV with the ATLAS Detector at the LHC". In: *Phys. Rev. Lett.* 117 (18 Oct. 2016), p. 182002. DOI: 10.1103/PhysRevLett.117.182002. URL: https://link.aps.org/doi/10.1103/PhysRevLett.117.182002.

[147] *Measurements of Higgs boson properties in the diphoton decay channel in proton-proton collisions at $\sqrt{s} = 13$ TeV*. Tech. rep. CMS-HIG-16-040. CMS-HIG-16-040-003. * Temporary entry *. Geneva: CERN, Apr. 2018. URL: https://cds.cern.ch/record/2312121.

[148] *Measurements of properties of the Higgs boson decaying to a W boson pair in pp collisions at $\sqrt{s} = 13$ TeV*. Tech. rep. CMS-HIG-16-042. CMS-HIG-16-042-003. * Temporary entry *. Geneva: CERN, June 2018. URL: https://cds.cern.ch/record/2624194.

[149] *Measurements of properties of the Higgs boson in the four-lepton final state at* $\sqrt{s} =$ 13 TeV. Tech. rep. CMS-PAS-HIG-18-001. Geneva: CERN, 2018. URL: https://cds.cern.ch/record/2621419.

[150] *Measurements of the Higgs boson production, fiducial and differential cross sections in the* 4ℓ *decay channel at* $\sqrt{s} = 13$ *TeV with the ATLAS detector*. Tech. rep. ATLAS-CONF-2018-018. Geneva: CERN, June 2018. URL: http://cds.cern.ch/record/2621479.

[151] Bruce Mellado Garcia et al. "CERN Report 4: Part I Standard Model Predictions". In: (May 2016). URL: https://cds.cern.ch/record/2150771.

[152] Guy D. Moore. "The Sphaleron rate: Where we stand". In: *Strong and electroweak matter '98. Proceedings, Conference, SEWM'98, Copenhagen, Denmark, December 2-5, 1998*. 1998, pp. 23–33. arXiv: hep-ph/9902464 [hep-ph].

[153] Paul Musset and Jean-Pierre Vialle. "Neutrino physics with gargamelle". In: *Physics Reports* 39.1 (1978), pp. 1–130. ISSN: 0370-1573. DOI: https://doi.org/10.1016/0370-1573(78)90051-0. URL: http://www.sciencedirect.com/science/article/pii/0370157378900510.

[154] Y. Nambu and G. Jona-Lasinio. "Dynamical Model of Elementary Particles Based on an Analogy with Superconductivity. I". In: *Phys. Rev.* 122 (1 Apr. 1961), pp. 345–358. DOI: 10.1103/PhysRev.122.345. URL: https://link.aps.org/doi/10.1103/PhysRev.122.345.

[155] Y. Nambu and G. Jona-Lasinio. "Dynamical Model of Elementary Particles Based on an Analogy with Superconductivity. II". In: *Phys. Rev.* 124 (1 Oct. 1961), pp. 246–254. DOI: 10.1103/PhysRev.124.246. URL: https://link.aps.org/doi/10.1103/PhysRev.124.246.

[156] Yoichiro Nambu. "Quasi-Particles and Gauge Invariance in the Theory of Superconductivity". In: *Phys. Rev.* 117 (3 Feb. 1960), pp. 648–663. DOI: 10.1103/PhysRev.117.648. URL: https://link.aps.org/doi/10.1103/PhysRev.117.648.

[157] Snezana Nektarijevic. *Jet Vertex Charge Reconstruction*. Tech. rep. ATL-PHYS-PROC-2015-200. Geneva: CERN, Dec. 2015. URL: https://cds.cern.ch/record/2117630.

[158] E. Noether. "Invariant variation problems". In: *Transport Theory and Statistical Physics* 1 (Jan. 1971), pp. 186–207. DOI: 10.1080/00411457108231446. arXiv: 0503066. URL: https://arxiv.org/abs/physics/0503066.

[159] *Observation of $H \to b\bar{b}$ decays and VH production with the ATLAS detector*. Tech. rep. ATLAS-CONF-2018-036. Geneva: CERN, July 2018. URL: https://cds.cern.ch/record/2630338.

[160] "Observation of $t\bar{t}H$ production". In: *Phys. Rev. Lett.* 120.CMS-HIG-17-035. CMS-HIG-17-035-003 (Apr. 2018). Replaced with the published version. Added the journal reference and the DOI. All the figures and tables, including additional supplementary figures and tables, can be found at http://cms-results.web.cern.ch/cms-results/public-results/publications/HIG-17-035 (CMS Public Pages), 231801. 17 p. URL: https://cds.cern.ch/record/2312113.

[161] *Observation of Higgs boson decay to bottom quarks*. Tech. rep. arXiv:1808.08242. CMS-HIG-18-016-003. * Temporary entry *. Geneva: CERN, Aug. 2018. URL: https://cds.cern.ch/record/2636067.

[162] "Observation of single isolated electrons of high transverse momentum in events with missing transverse energy at the CERN pp collider". In: *Physics Letters B* 122.5 (1983), pp. 476–485. ISSN: 0370-2693. DOI: https://doi.org/10.1016/0370-2693(83)91605-2. URL: http://www.sciencedirect.com/science/article/pii/0370269383916052.

[163] "Observation of the Higgs boson decay to a pair of τ leptons with the CMS detector". In: *Phys. Lett. B* 779.CMS-HIG-16-043. CMS-HIG-16-043-003 (Aug. 2017). Replaced with the published version. Added the journal reference. All the figures and tables can be found at http://cms-results.web.cern.ch/cms-results/public-results/publications/HIG-16-043 (CMS Public Pages), 283–316. 34 p. URL: https://cds.cern.ch/record/2276465.

[164] "Observation of Top Quark Production in $\overline{p}p$ Collisions with the Collider Detector at Fermilab". In: *Phys. Rev. Lett.* 74 (14 Apr. 1995), pp. 2626–2631. DOI: 10.1103/PhysRevLett.74.2626. URL: https://link.aps.org/doi/10.1103/PhysRevLett.74.2626.

[165] *Optimisation of the ATLAS b-tagging performance for the 2016 LHC Run*. Tech. rep. ATL-PHYS-PUB-2016-012. Geneva: CERN, June 2016. URL: http://cds.cern.ch/record/2160731.

[166] W. Pauli. "Zur Quantenmechanik des magnetischen Elektrons". In: *Zeitschrift für Physik* 43.9 (Sept. 1927), pp. 601–623. ISSN: 0044-3328. DOI: 10.1007/BF01397326. URL: https://doi.org/10.1007/BF01397326.

[167] MissMJ PBS NOVA Fermilab US DoE PDG. *Standard Model of Elementary Particles*. [Online; accessed August 27, 2018]. 2018. URL: https://en.wikipedia.org/wiki/Standard_Model#/media/File:Standard_Model_of_Elementary_Particles.svg.

[168] D. Perepelitsa. "Sakharov Conditions for Baryogenesis". In: (2008). URL: http://phys.columbia.edu/~dvp/dvp-sakharov.pdf.

[169] M. L. et al. Perl. "Evidence for Anomalous Lepton Production in $e^+ - e^-$ Annihilation". In: *Phys. Rev. Lett.* 35 (22 Dec. 1975), pp. 1489–1492. DOI: 10.1103/PhysRevLett.35.1489. URL: https://link.aps.org/doi/10.1103/PhysRevLett.35.1489.

[170] Martin L. Perl. "Evidence for, and Properties of, the New Charged Heavy Lepton". In: *Proceedings: 12th Rencontres de Moriond, Leptons and Multi-Leptons. Flaine-Haute Savoie, France Mar 6-Mar 18 1977. 1.* 1977, pp. 75–97. URL: http://www-public.slac.stanford.edu/sciDoc/docMeta.aspx?slacPubNumber=SLAC-PUB-1923.

[171] T. Plehn, M. Spira, and P.M. Zerwas. "Pair production of neutral Higgs particles in gluon-gluon collisions". In: *Nucl. Phys. B* 479 (1996). [Erratum: Nucl. Phys. B **531** (1998) 655], p. 46. DOI: 10.1016/0550-3213(96)00418-X. arXiv: hep-ph/9603205.

[172] H. David Politzer. "Reliable Perturbative Results for Strong Interactions?" In: *Phys. Rev. Lett.* 30 (26 June 1973), pp. 1346–1349. DOI: 10.1103/PhysRevLett.30.1346. URL: https://link.aps.org/doi/10.1103/PhysRevLett.30.1346.

[173] B. Pontecorvo. "Inverse beta processes and nonconservation of lepton charge". In: *Sov. Phys. JETP* 7 (1958). [Zh. Eksp. Teor. Fiz.34,247(1957)], pp. 172–173. URL: http://www.jetp.ac.ru/cgi-bin/dn/e_007_01_0172.pdf.

[174] J. Preskill. "Quantum Computing in the NISQ era and beyond". In: *ArXiv e-prints* (Jan. 2018). arXiv: 1801.00862 [quant-ph].

[175] J. Milnor R. Bott. In: *University of Michigan, Oxford University Presses* (1958).

[176] Lisa Randall and Raman Sundrum. "An Alternative to Compactification". In: *Phys. Rev. Lett.* 83 (23 Dec. 1999), pp. 4690–4693. DOI: 10.1103/PhysRevLett.83.4690. URL: https://link.aps.org/doi/10.1103/PhysRevLett.83.4690.

[177] Lisa Randall and Raman Sundrum. "Large Mass Hierarchy from a Small Extra Dimension". In: *Phys. Rev. Lett.* 83 (17 Oct. 1999), pp. 3370–3373. DOI: 10.1103/PhysRevLett.83.3370. URL: https://link.aps.org/doi/10.1103/PhysRevLett.83.3370.

[178] Franco Rasetti. "Disintegration of Slow Mesotrons". In: *Phys. Rev.* 60 (3 Aug. 1941), pp. 198–204. DOI: 10.1103/PhysRev.60.198. URL: https://link.aps.org/doi/10.1103/PhysRev.60.198.

[179] Alexander L. Read. "Presentation of search results: The CL(s) technique". In: *J. Phys. G* 28 (2002), p. 2693. DOI: 10.1088/0954-3899/28/10/313.

[180] Lucio Rossi. "Superconductivity: its role, its success and its setbacks in the Large Hadron Collider of CERN". In: *Superconductor Science and Technology* 23.3 (2010), p. 034001. URL: http://stacks.iop.org/0953-2048/23/i=3/a=034001.

[181] Abdus Salam and J. C. Ward. "Weak and electromagnetic interactions". In: *Il Nuovo Cimento (1955-1965)* 11.4 (Feb. 1959), pp. 568–577. ISSN: 1827-6121. DOI: 10.1007/BF02726525. URL: https://doi.org/10.1007/BF02726525.

[182] V. H. Satheesh Kumar and P. K. Suresh. "Gravitons in Kaluza-Klein theory". In: (2006). arXiv: gr-qc/0605016 [gr-qc].

[183] Julian Schwinger. "Quantum Electrodynamics. III. The Electromagnetic Properties of the Electron—Radiative Corrections to Scattering". In: *Phys. Rev.* 76 (6 Sept. 1949), pp. 790–817. DOI: 10.1103/PhysRev.76.790. URL: https://link.aps.org/doi/10.1103/PhysRev.76.790.

[184] "Search for High Mass Top Quark Production in $p\overline{p}$ Collisions at $\sqrt{s} =$ 1.8 TeV". In: *Phys. Rev. Lett.* 74 (13 Mar. 1995), pp. 2422–2426. DOI: 10.1103/PhysRevLett.74.2422. URL: https://link.aps.org/doi/10.1103/PhysRevLett.74.2422.

[185] *Search for Non-Resonant Higgs Pair-Production in the* $\mathrm{b\overline{b}b\overline{b}}$ *Final State with the CMS detector*. Tech. rep. CMS-PAS-HIG-17-017. Geneva: CERN, 2018. URL: https://cds.cern.ch/record/2628554.

[186] *Search for pair production of higgsinos in final states with at least 3 b-tagged jets using the ATLAS detector in* $\sqrt{s} = 13$ *TeV pp collisions*. Tech. rep. ATLAS-CONF-2017-081. Geneva: CERN, Dec. 2017. URL: http://cds.cern.ch/record/2297400.

[187] Marco Serone, Gabriele Spada, and Giovanni Villadoro. "$\lambda\phi^4$ Theory I: The Symmetric Phase Beyond NNNNNNNNLO". In: (2018). arXiv: 1805.05882 [hep-th].

[188] Albert M Sirunyan et al. "Inclusive search for a highly boosted Higgs boson decaying to a bottom quark-antiquark pair". In: *Phys. Rev. Lett.* 120.7 (2018), p. 071802. DOI: 10.1103/PhysRevLett.120.071802. arXiv: 1709.05543 [hep-ex]. URL: https://arxiv.org/abs/1709.05543.

[189] Albert M Sirunyan et al. "Search for Higgs boson pair production in events with two bottom quarks and two tau leptons in proton–proton collisions at $\sqrt{s}$ =13TeV". In: *Phys. Lett.* B778 (2018), pp. 101–127. DOI: 10.1016/j.physletb.2018.01.001. arXiv: 1707.02909 [hep-ex].

[190] Albert M Sirunyan et al. "Search for Higgs boson pair production in the $\gamma\gamma\mathrm{b\bar{b}}$ final state in pp collisions at $\sqrt{s} = 13$ TeV". In: (2018). DOI: 10.3204/PUBDB-2018-02192. arXiv: 1806.00408 [hep-ex].

[191] Albert M Sirunyan et al. "Search for resonant and nonresonant Higgs boson pair production in the $b\bar{b}\ell\nu\ell\nu$ final state in proton-proton collisions at $\sqrt{s} = 13$ TeV". In: *JHEP* 01 (2018), p. 054. DOI: 10.1007/JHEP01(2018)054. arXiv: 1708.04188 [hep-ex].

[192] Albert M Sirunyan et al. "Search for resonant pair production of Higgs bosons decaying to bottom quark-antiquark pairs in proton-proton collisions at 13 TeV". In: *Submitted to: JHEP* (2018). arXiv: 1806.03548 [hep-ex].

[193] Torbjorn Sjostrand, Stephen Mrenna, and Peter Z. Skands. "A Brief Introduction to PYTHIA 8.1". In: *Comput. Phys. Commun.* 178 (2008), p. 852. DOI: 10.1016/j.cpc.2008.01.036. arXiv: 0710.3820.

[194] Mark Srednicki. "Quantum Field Theory. Part 1. Spin Zero". In: (2004). arXiv: hep-th/0409035 [hep-th].

[195] J. C. Street and E. C. Stevenson. "New Evidence for the Existence of a Particle of Mass Intermediate Between the Proton and Electron". In: *Phys. Rev.* 52 (9 Nov. 1937), pp. 1003–1004. DOI: 10.1103/PhysRev.52.1003. URL: https://link.aps.org/doi/10.1103/PhysRev.52.1003.

[196] "Tests of General Relativity with GW150914". In: *Phys. Rev. Lett.* 116 (22 May 2016), p. 221101. DOI: 10.1103/PhysRevLett.116.221101. URL: https://link.aps.org/doi/10.1103/PhysRevLett.116.221101.

[197] Tony Tong and Melissa Franklin. "Search for pair production of Higgs bosons in the four b quark final state with the ATLAS detector". Presented 27 Apr 2018. May 2018. URL: https://cds.cern.ch/record/2634867.

[198] S. Weinberg. *Understanding the Fundamental Constituents of Matter*. Ed. by A. Zichichi. New York: Plenum Press, 1977.

[199] Steven Weinberg. "A Model of Leptons". In: *Phys. Rev. Lett.* 19 (21 Nov. 1967), pp. 1264–1266. DOI: 10.1103/PhysRevLett.19.1264. URL: https://link.aps.org/doi/10.1103/PhysRevLett.19.1264.

[200] David J. Weir. "Gravitational waves from a first-order electroweak phase transition: a brief review". In: *Philosophical Transactions of the Royal Society of London A: Mathematical, Physical and Engineering Sciences* 376.2114 (2018). ISSN: 1364-503X. DOI: 10.1098/rsta.2017.0126. eprint: http://rsta.royalsocietypublishing.org/

content/376/2114/20170126.full.pdf. URL: http://rsta.royalsocietypublishing.org/content/376/2114/20170126.

[201] Fred L. Wilson. "Fermi's Theory of Beta Decay". In: *American Journal of Physics* 36.12 (1968), pp. 1150–1160. DOI: 10.1119/1.1974382. URL: https://doi.org/10.1119/1.1974382.

[202] Kenneth G. Wilson. "Confinement of quarks". In: *Phys. Rev. D* 10 (8 Oct. 1974), pp. 2445–2459. DOI: 10.1103/PhysRevD.10.2445. URL: https://link.aps.org/doi/10.1103/PhysRevD.10.2445.

[203] Edward Witten. *Phil Anderson and Gauge Symmetry Breaking*. Feb. 2016, pp. 73–89. ISBN: 978-981-4733-61-8. URL: https://pdfs.semanticscholar.org/e6fa/83f186f9555a4864c3e50d3e488f6f09c5cd.pdf.

[204] Edward Witten. "Symmetry and Emergence". In: *Nature Phys.* 14 (2018), pp. 116–119. DOI: 10.1038/nphys4348. arXiv: 1710.01791 [hep-th].

[205] P. Woit. *Quantum Theory, Groups and Representations*. Gewerbestrasse 11, 6330 Cham, Switzerland: Springer International Publishing AG, 2017. DOI: 10.1007/978-3-319-64612-1.

[206] C. S. Wu et al. "Experimental Test of Parity Conservation in Beta Decay". In: *Phys. Rev.* 105 (4 Feb. 1957), pp. 1413–1415. DOI: 10.1103/PhysRev.105.1413. URL: https://link.aps.org/doi/10.1103/PhysRev.105.1413.

[207] C. N. Yang and R. L. Mills. "Conservation of Isotopic Spin and Isotopic Gauge Invariance". In: *Phys. Rev.* 96 (1 Oct. 1954), pp. 191–195. DOI: 10.1103/PhysRev.96.191. URL: https://link.aps.org/doi/10.1103/PhysRev.96.191.

[208] Hideki Yukawa. "On the Interaction of Elementary Particles I". In: *Proc. Phys. Math. Soc. Jap.* 17 (1935). [Prog. Theor. Phys. Suppl.1,1(1935)], pp. 48–57. DOI: 10.1143/PTPS.1.1.

[209] G Zweig. *An SU_3 model for strong interaction symmetry and its breaking; Version 1.* Tech. rep. CERN-TH-401. Geneva: CERN, Jan. 1964. URL: http://cds.cern.ch/record/352337.

Appendices

Appendix A

INTRODUCTION TO VARIATIONAL CALCULUS AND LAGRANGIAN MECHANICS

We will now outline how to mathematically "pick" paths through phase space given some function over the same space. The function outputs a number for points in phase space, but we want to study paths through phase space. By integrating the function along a general path one can define a functional[1] over the space of all paths. Special paths called "critical paths" are those for which small changes in the path to first order do not change the output of the functional. Critical paths are determined by the zeros of the "functional derivative" which is the rate of change of the functional output as the path is changed keeping two end points fixed.

It is now worth considering an example to make this concept explicit. The simplest phase space is the two dimensional space resulting from a system with one degree of freedom x and its rate of change $\dot{x} \equiv \frac{\mathrm{d}x}{\mathrm{d}t}$. For a concrete mental image, x could be the position of a mass bouncing on a spring. Then both x and $\dot{x}$ are functions of time t which parametrizes a path from a starting position and velocity $(x(t_1),\, \dot{x}(t_1))$ to a phase space point at some later time $(x(t_2),\, \dot{x}(t_2))$.

Let us define a function over phase space called the "Lagrangian" and denote it by $L(x, \dot{x})$ where our functional is defined as the integral of the Lagrangian over time

$$S = \int_{t_1}^{t_2} L(x,\, \dot{x})\, \mathrm{d}t$$

[1] A functional is a mathematical object which outputs a number given a function, for example $\int_0^1 f(x)\, \mathrm{d}x$ gives a number for every integrable function $f(x)$ defined on the real numbers between 0 and 1. Functionals allow for the definition of generalized functions called "distributions" like the $\delta(x)$ which is defined such that $\int \delta(x-y) f(y)\, \mathrm{d}y = f(x)$.

which we call the "action". To construct the functional derivative, consider changing the path by adding a multiple ϵ of some function of time $f(t)$ to $x(t)$ with $f(t_1) = f(t_2) = 0$. Then the path is transformed as follows:

$$x(t) \to x(t) + \epsilon f(t)$$
$$\dot{x}(t) \to \dot{x}(t) + \epsilon \dot{f}(t)$$

The action is thus demoted to a regular old function of ϵ so we can compute its derivative and evaluate at $\epsilon = 0$:

$$\begin{aligned} 0 &= \frac{\mathrm{d}S}{\mathrm{d}\epsilon}\Big|_{\epsilon=0} \\ &= \int_{t_1}^{t_2} \left[\frac{\mathrm{d}}{\mathrm{d}\epsilon} L(x + \epsilon f,\, \dot{x} + \epsilon \dot{f})\right]_{\epsilon=0} \mathrm{d}t \\ &= \int_{t_1}^{t_2} f\frac{\partial L}{\partial x} + \dot{f}\frac{\partial L}{\partial \dot{x}}\,\mathrm{d}t \end{aligned}$$

We can integrate the second term in the last line by parts to give

$$0 = \int_{t_1}^{t_2} f\frac{\partial L}{\partial x} - f\frac{\mathrm{d}}{\mathrm{d}t}\frac{\partial L}{\partial \dot{x}}\,\mathrm{d}t + f\frac{\partial L}{\partial \dot{x}}\Big|_{t_2} - f\frac{\partial L}{\partial \dot{x}}\Big|_{t_1}$$

If we assume $\frac{\partial L}{\partial \dot{x}}$ is finite and use the boundary conditions $f(t_1) = f(t_2) = 0$ we have

$$0 = \int_{t_1}^{t_2} f\left(\frac{\partial L}{\partial x} - \frac{\mathrm{d}}{\mathrm{d}t}\frac{\partial L}{\partial \dot{x}}\right)\mathrm{d}t$$

This is true for general $f(t)$ if and only if the term in parentheses is zero:

$$0 = \frac{\partial L}{\partial x} - \frac{\mathrm{d}}{\mathrm{d}t}\frac{\partial L}{\partial \dot{x}}$$

This is the "Euler-Lagrange" equation for a system with one degree of freedom. It gives a

differential equation relating the Lagrangian to the critical paths of the action $(x(t), \dot{x}(t))$. We arrived at this equation by making use of a generalization of the typical derivative of calculus. In particular we avoided any subleties associated to the inifinte dimensional space in which the functional derivative lives by only considering points where the functional derivative was zero.

Now we need a mechanism to pick out these critical paths from all possible paths. We have defined the action functional as the integral of the Lagrangian over any given path. To pick out the critical paths we want to define some kind of global object which depends on all possible paths which can then generate the critical paths as its output. Then we will have defined a mathematical machine which generates the same paths through phase space as nature.

Integrals compute quantities that depend on the value of a function over a region of the function's input space. "Functional integrals" compute quantities that depend on the value of a functional over a region of the space of functions.[2] In our case we can imagine integrating the action or a function of the action over the space of paths defined by functions $x(t)$ connecting the endpoints $x(t_1) \rightarrow x(t_2)$. Let us denote this space of functions $\mathcal{F}$ and the measure of the functional integral as $\mathcal{D}X$ where $X \equiv x(t) \in \mathcal{F}$. Then we can denote the functional integral of a function of the action $f(S[L(X, \dot{X})])$ as follows:

$$\int_{\mathcal{F}} \mathcal{D}X f(S[L(X, \dot{X})])$$

Critical paths by definition are those for which the action is independent of the path to first order. If we map the action onto the space of unit vectors in the plane we could consider

[2] The space of functions is infinite dimensional and depends on the class of functions under consideration. Subtle issues of how to define the measure of the functional integral over the chosen space of functions generically arise but we will not delve into those issues here. We will restrict our attention to functions with a countably infinite fourier basis.

adding up all of these vectors multiplied by a functional measure $\mathcal{D}X$. A convenient way to do this is to use capitalize on the geometry of the complex plane using Euler's formula 2.4.

Let us suggestively define $\theta = S/\hbar$. Then $\hbar$ is the period of the mapping from the action in real numbers to the unit circle. In the limit $\hbar \to 0$ the functional $e^{iS/\hbar}$ oscillates wildly as the path X changes except at critical paths where the action is stationary to first order. This suggests there should be some way of defining the functional measure $\mathcal{D}X$ such that a distribution with support only on the critical paths arises from the limit $\hbar \to 0$:

$$\lim_{\hbar \to 0} \int_{\mathcal{F}} \mathcal{D}X e^{iS[L(X, \dot{X})]/\hbar} = \delta(x(t))$$

where $\delta(x)$ is the typical delta distribution defined such that $\int \delta(x)$

Thus we have constructed a rather unwieldy mathematical machine which outputs critical paths. It turns out that Lagrangians can be straight forwardly constructed to model classical systems where the resulting critical path nicely coincides with the true path taken by nature. What's remarkable is that we now understand that nature does *not* take this limit of $\hbar \to 0$, rather $\hbar$ is tiny in human scale units.

Appendix B

COMPARISON OF TWO AND FOUR b-tag HADRONIC $t\bar{t}$

Here we show that there is reasonable agreement in shape of several key distributions between the four tag hadronic $t\bar{t}$ and the reweighted two tag simulated samples. The pseudo tag rate was chosen seperately for the MC using the 2015 and 2016 emulated trigger menus such that the sum of event weights was roughly equal between 2b and 4b. The values used are 0.040 (0.042) for 2016 (2015). Figure B.1 shows that there is no evidence of mismodeling of four key distributions after the full event selection has been applied for all events within the Sideband, Control and Signal Regions.

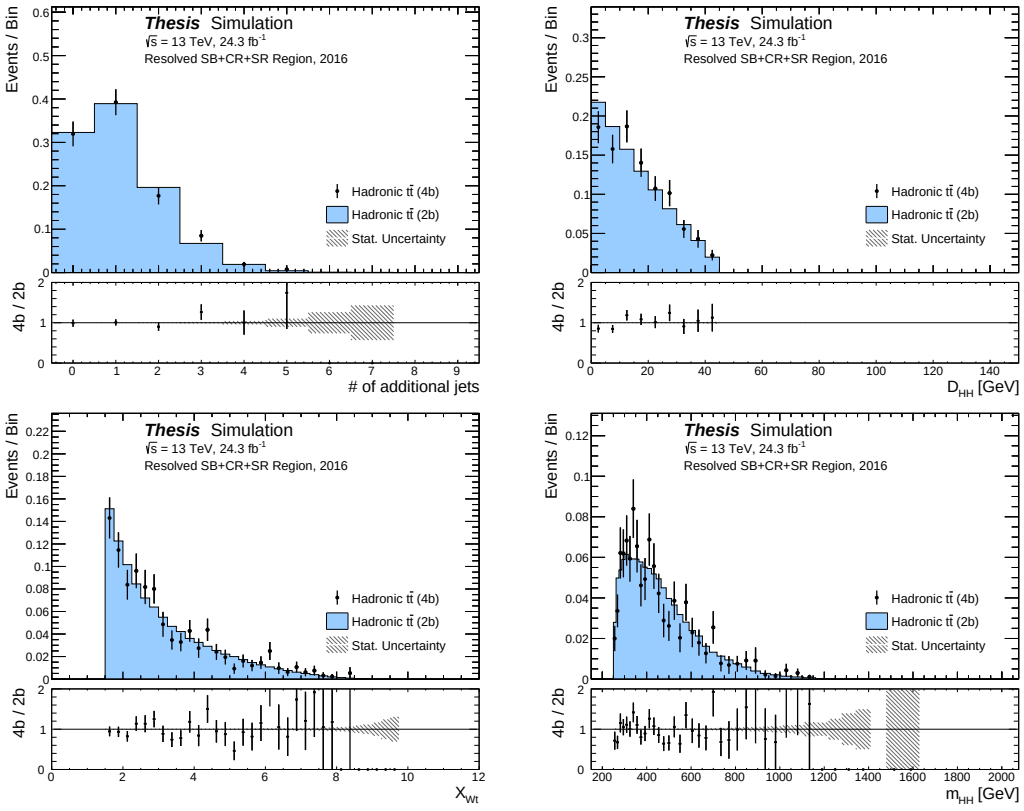

Figure B.1: Shape comparisons between four tag MC and the model using two tag MC of key distributions. All histograms are normalized to unit area.

Appendix C

KINEMATIC REWEIGHTING APPLIED TO 2015 DATA

In Figure C.1 we show the result of the ratio smoothing and splining procedure for the first and last iteration for the five reweighted distributions. This shows that the reweighting functions have converged to one to within 5%. Figures C.2, C.3 show the full background model for the reweighted distributions in the Sideband where the weights were derived. Figures C.4, C.5 show the same distributions in the Control region, illustrating that the correction is still applicable closer to the Signal Region.

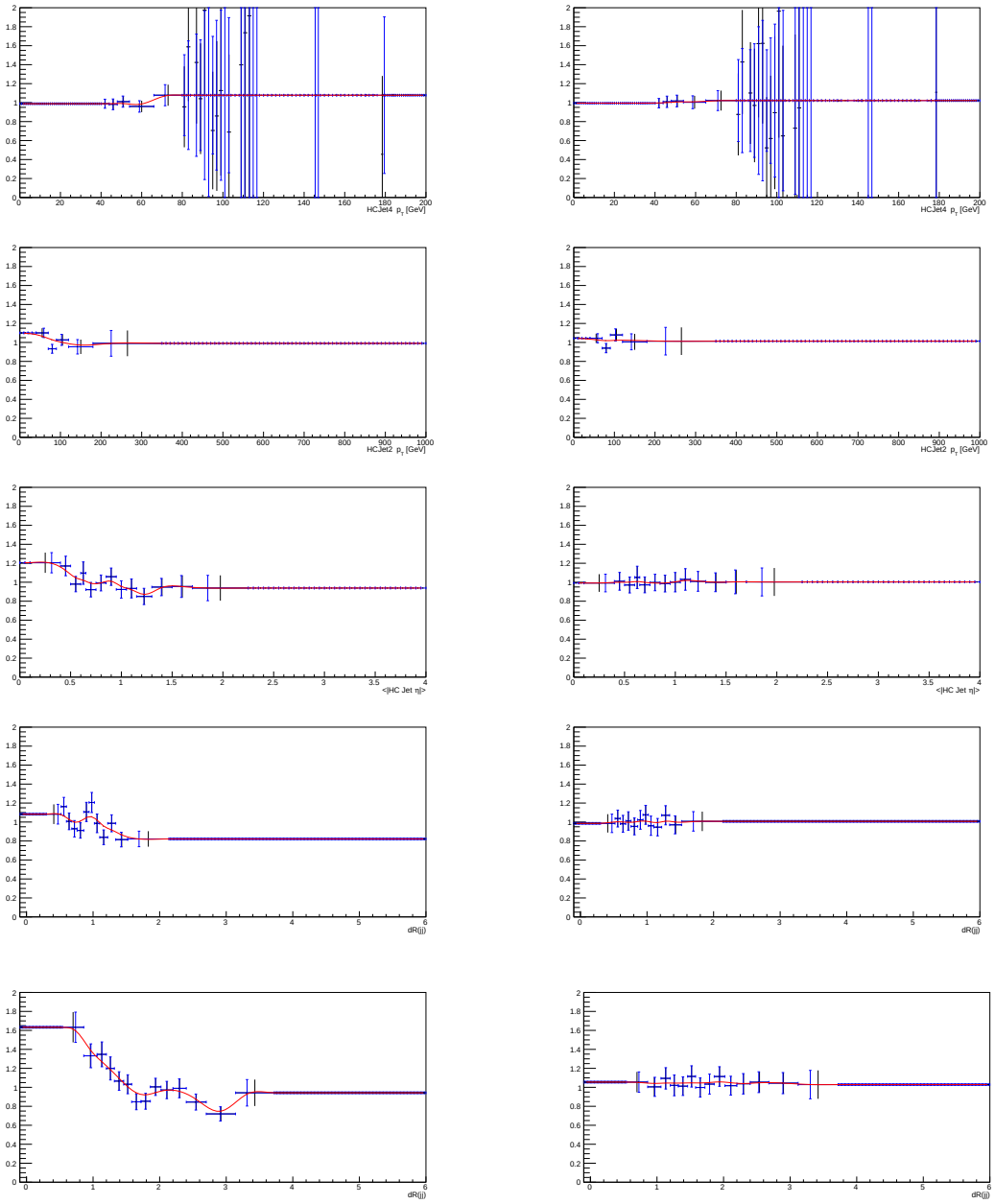

(a) Iteration 0 (b) Iteration 7

Figure C.1: The five reweighted ratios before and after the reweighting procedure had been applied. In black is the raw ratio, in blue is TGraph where the x values of the bins have been set to the mean of the background distribution in that bin and in red is the spline used for reweighting.

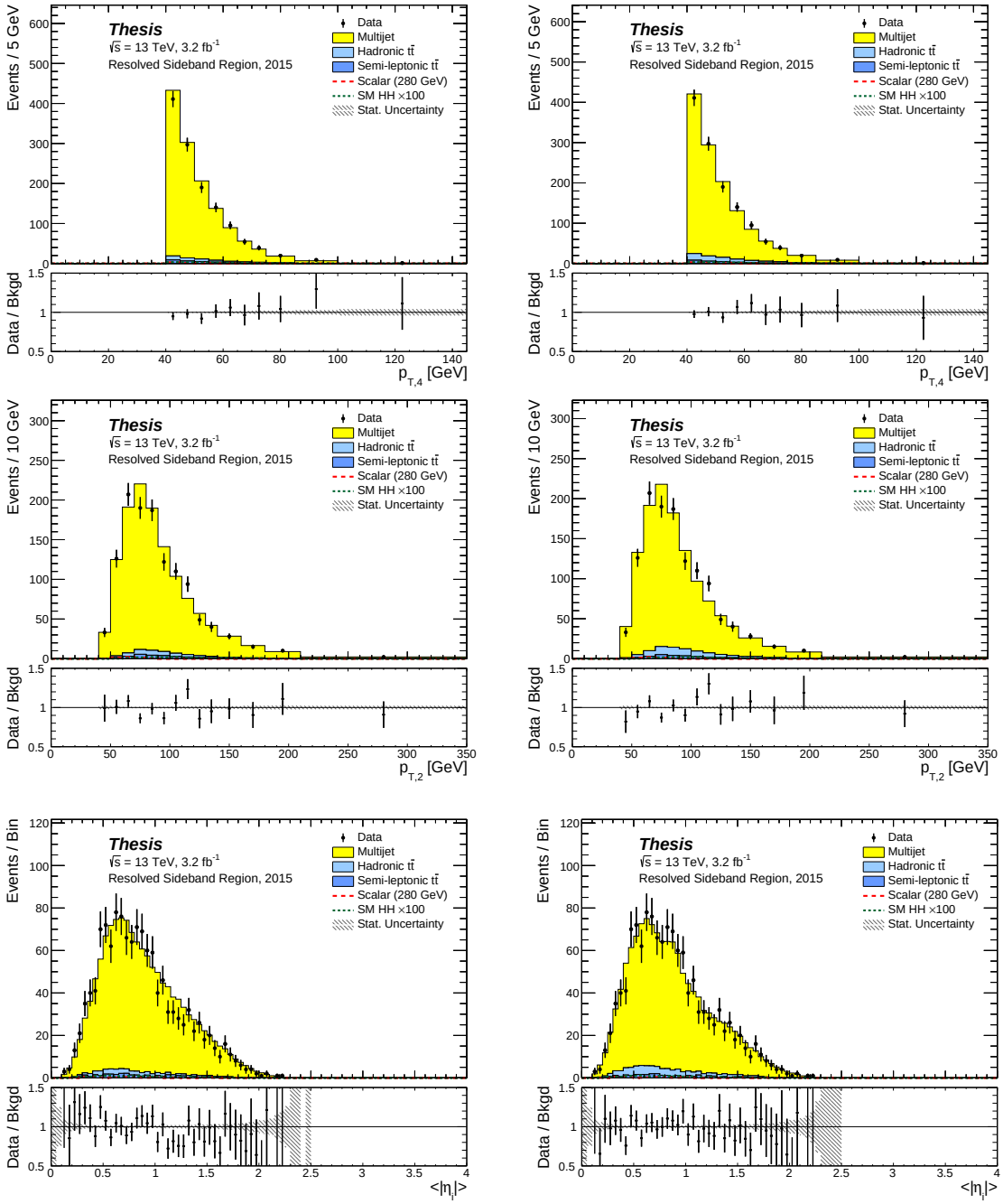

Figure C.2: The reweighted $p_{\mathrm{T}\ i}$ and $< |\eta_i| >$ distributions before and after the reweighting procedure had been applied.

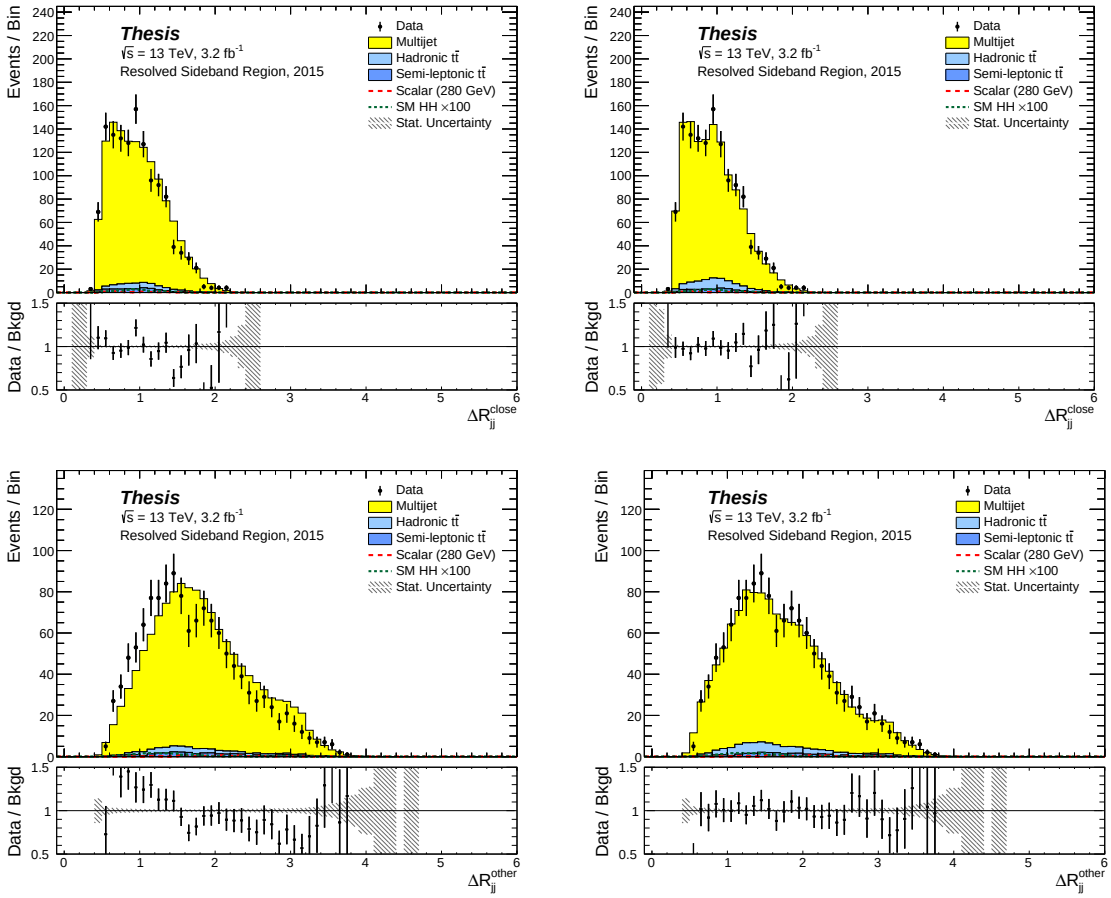

(a) Iteration 0

(b) Iteration 7

Figure C.3: The reweighted ΔR_{jj} distributions before and after the reweighting procedure had been applied.

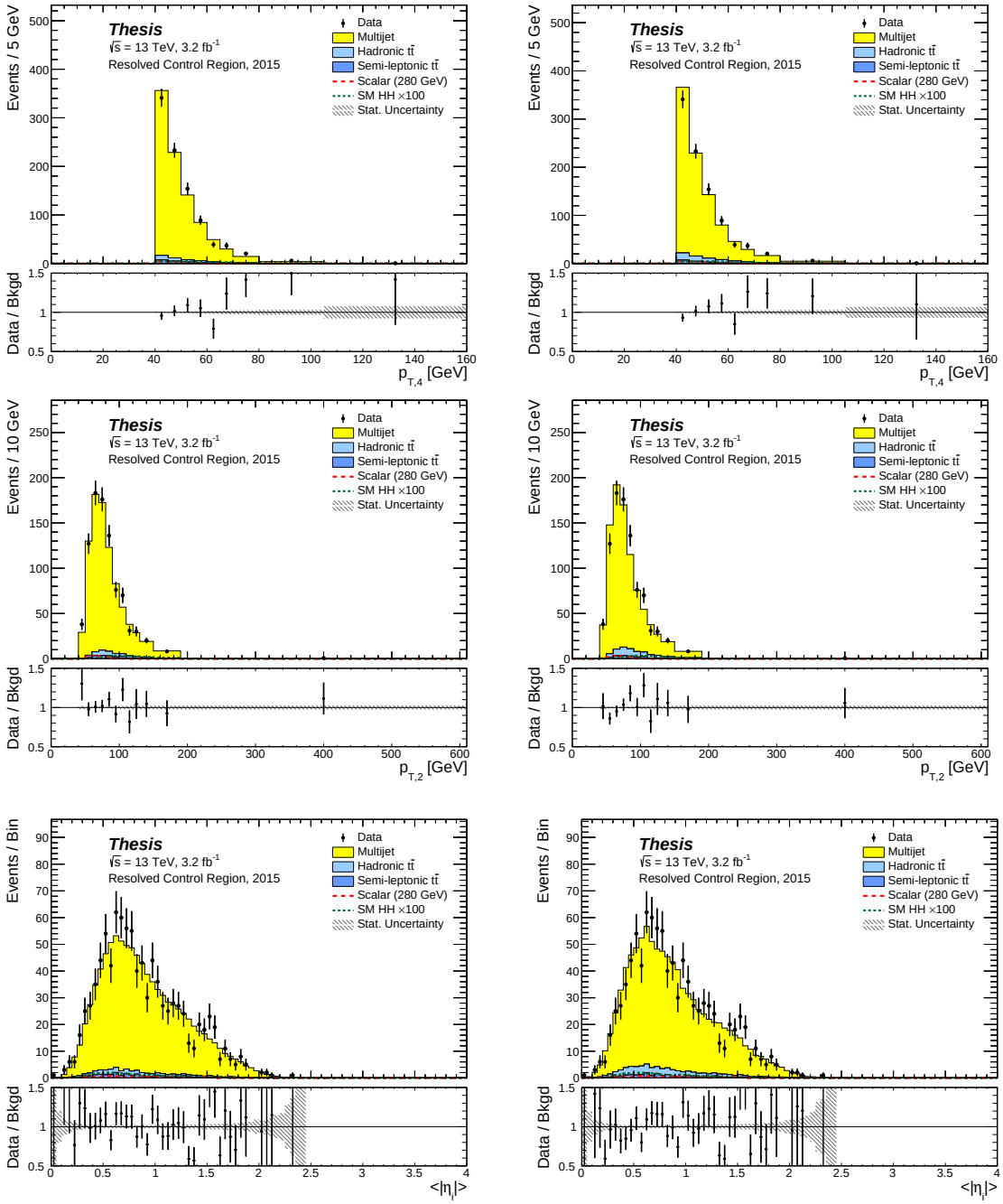

Figure C.4: The reweighted $p_{\mathrm{T}\ i}$ and $< |\eta_i| >$ distributions before and after the reweighting procedure had been applied.

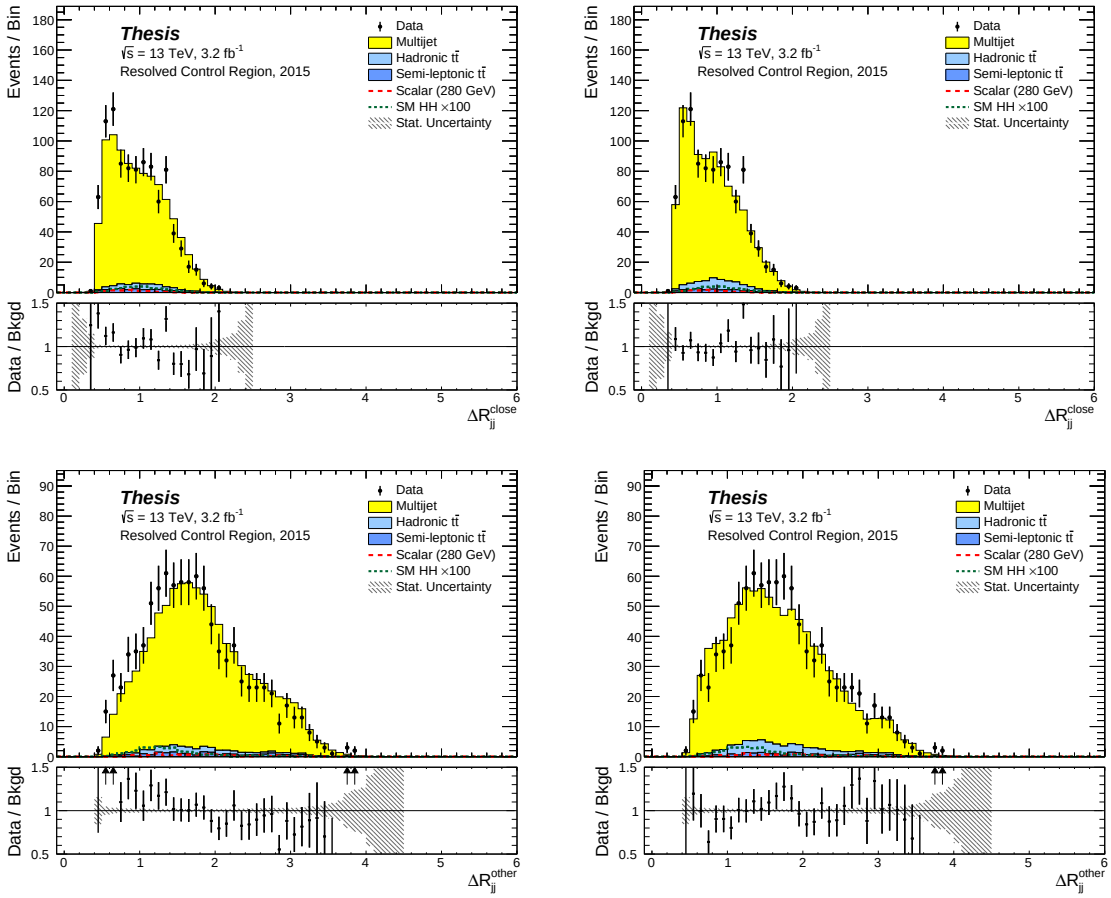

(a) Iteration 0

(b) Iteration 7

Figure C.5: The reweighted ΔR_{jj} distributions before and after the reweighting procedure had been applied.

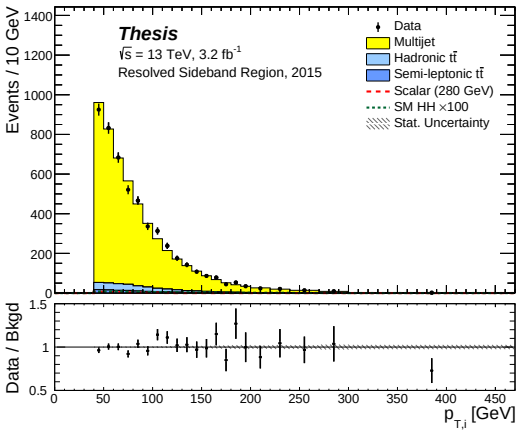

(a) p_{T} of all HC jets

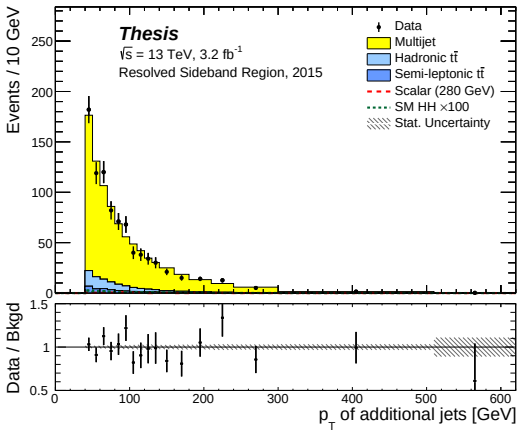

(b) p_{T} of all other jets in the event

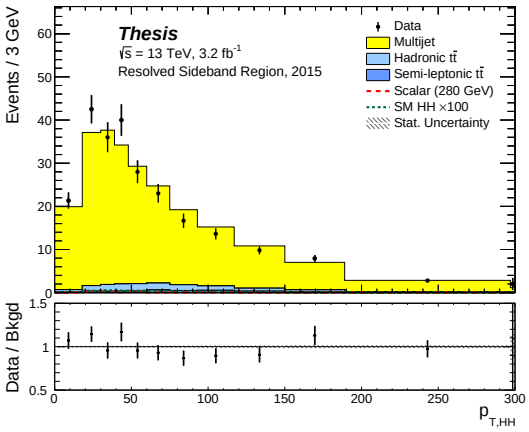

(c) p_{T} of the di-higgs candidate system

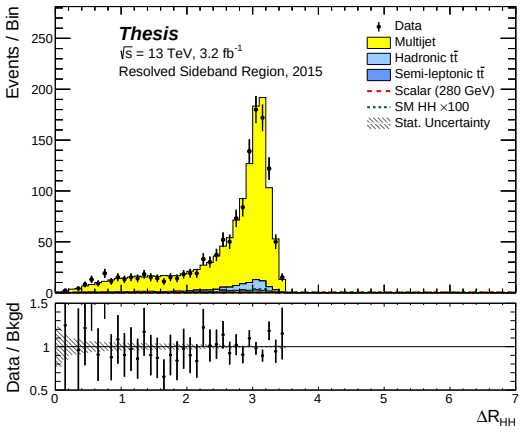

(d) ΔR between the two higgs candidates

Figure C.6: Figures a and b show that the p_{T} of both the higgs candidate jets and the other jets in the event are well modelled in the Sideband. Figures c and d show that higher level quantities like the p_{T} and openning angle of the di-higgs candidate system are also well modelled as a result.

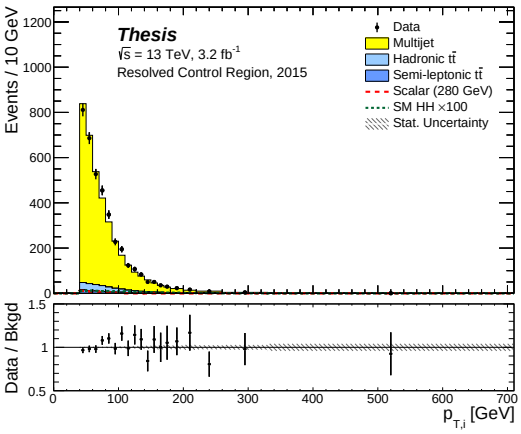

(a) p_{T} of all HC jets

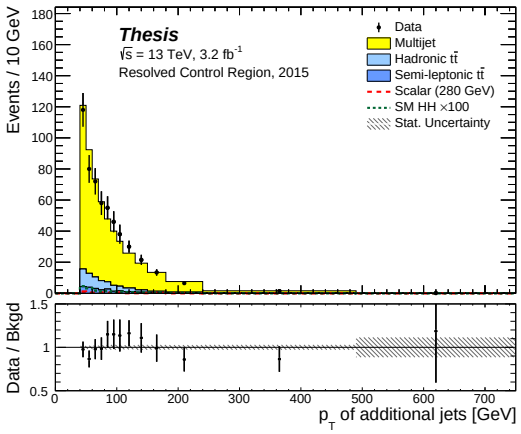

(b) p_{T} of all other jets in the event

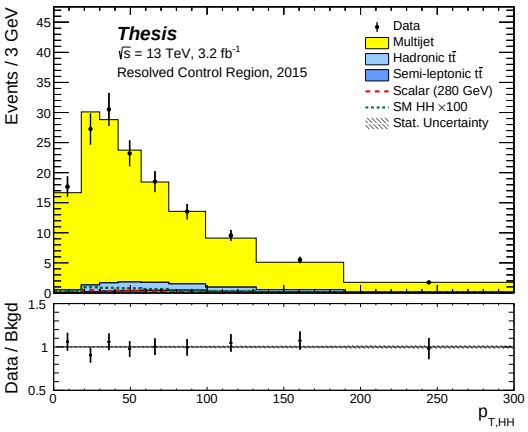

(c) p_{T} of the di-higgs candidate system

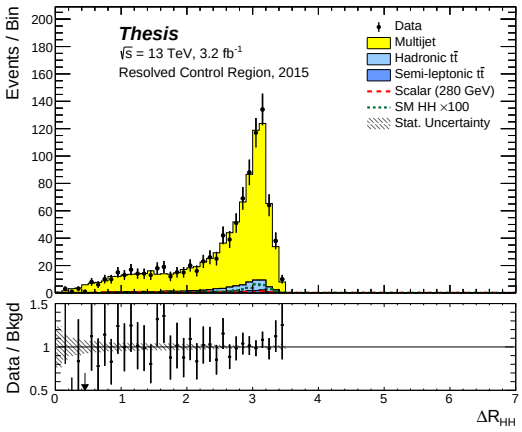

(d) ΔR between the two higgs candidates

Figure C.7: The same distributions as Figure C.6, but this time in the Control region to demonstrate that event level quantities remain well modelled as we move towards the Signal Region.

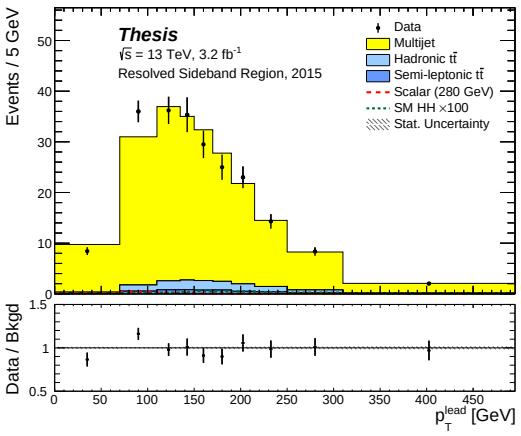

(a) Leading Higgs Candidate p_{T}

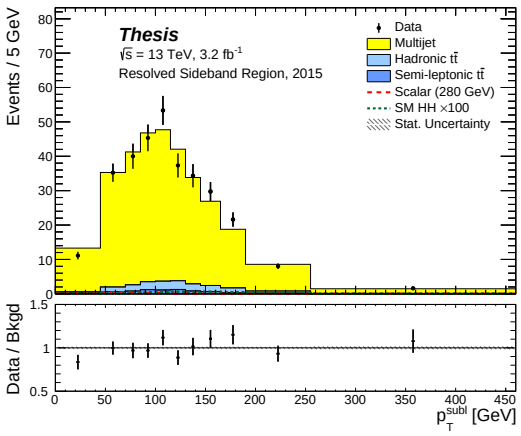

(b) Subleading Higgs Candidate p_{T}

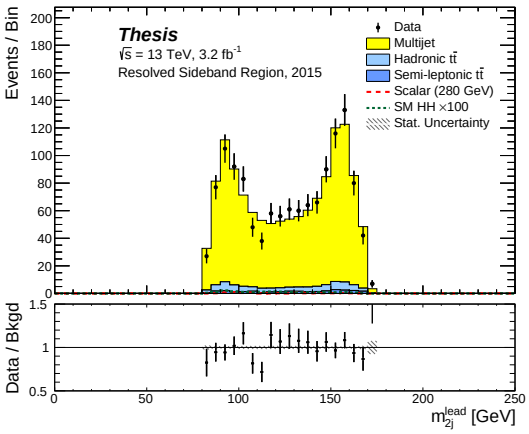

(c) Leading Higgs Candidate Mass

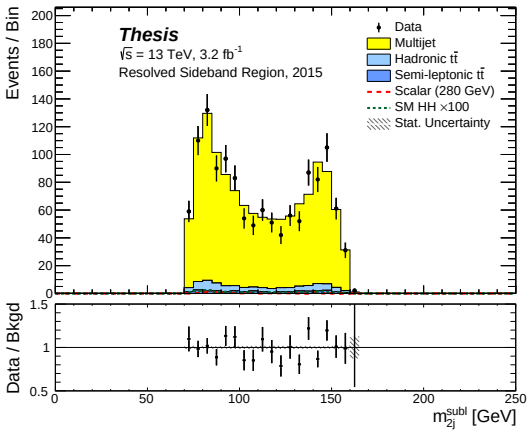

(d) Subleading Higgs Candidate Mass

Figure C.8: Modelling of Higgs Candidate kinematics in the Sideband.

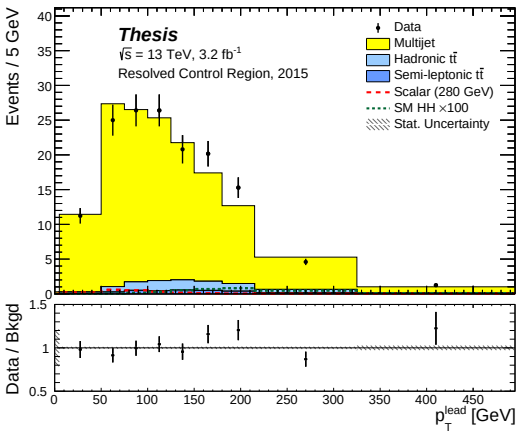

(a) Leading Higgs Candidate p_{T}

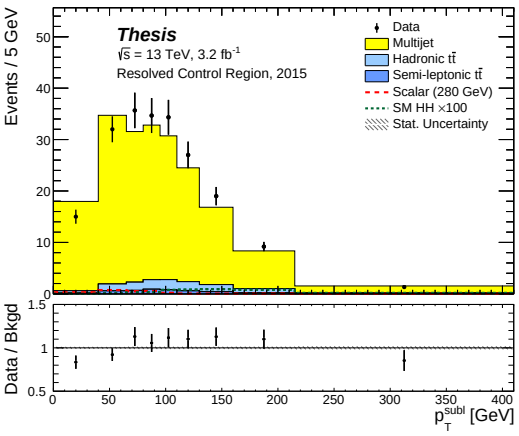

(b) Subleading Higgs Candidate p_{T}

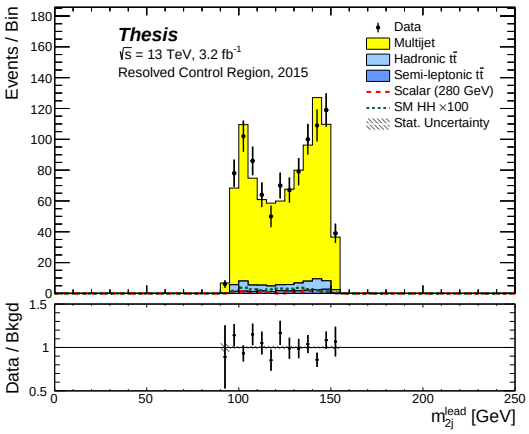

(c) Leading Higgs Candidate Mass

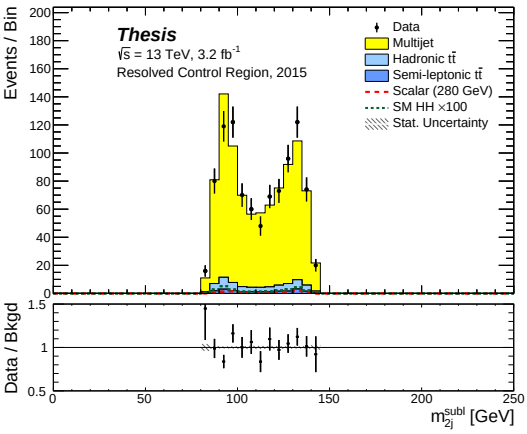

(d) Subleading Higgs Candidate Mass

Figure C.9: Modelling of Higgs Candidate kinematics in the Control Region.

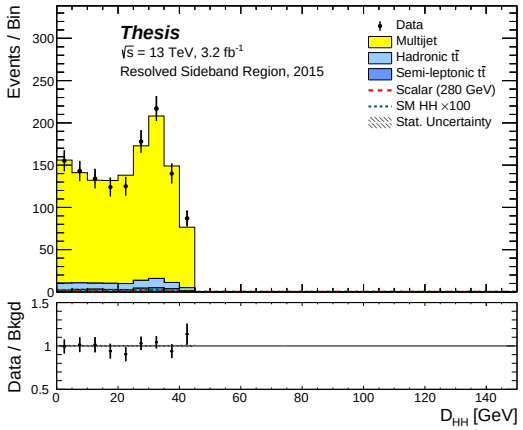

(a) The minimized jet pairing quantity D_{HH}

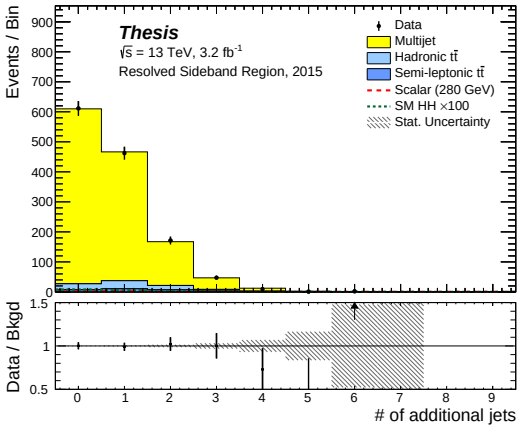

(b) The number of additional jets

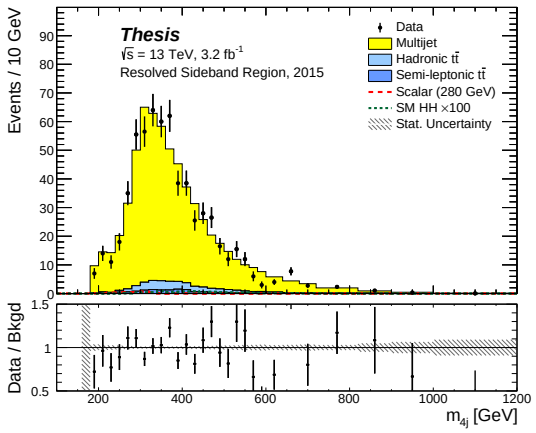

(c) The di-higgs candidate Mass

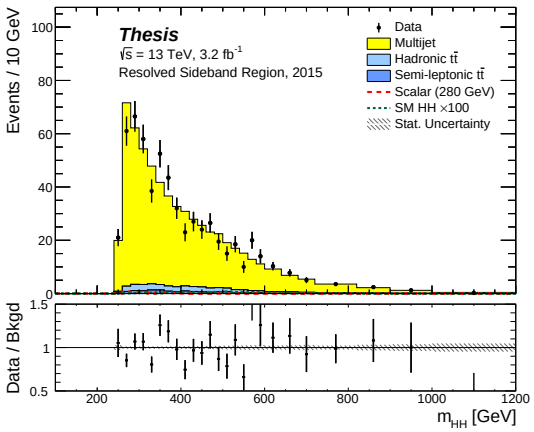

(d) The corrected di-higgs candidate Mass

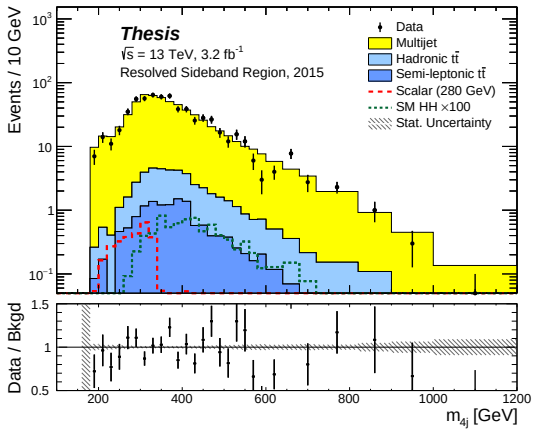

(e) Log scale of (c)

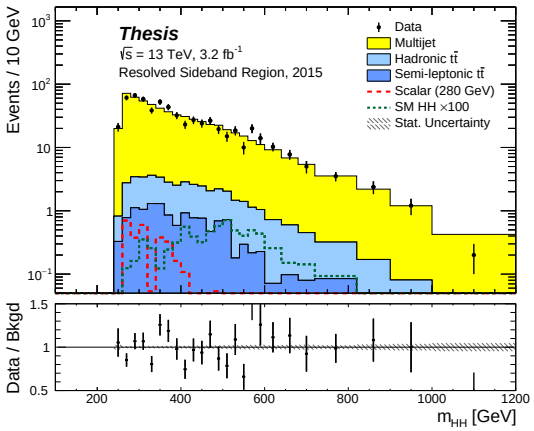

(f) Log scale of (d)

Figure C.10: Modelling of D_{HH}, the number of additional jets and the corrected and uncorrected di-higgs spectra. The corrected di-higgs mass is constructed by scaling the higgs candidate four vectors to have mass = 125 GeV and then computing the four body invariant mass.

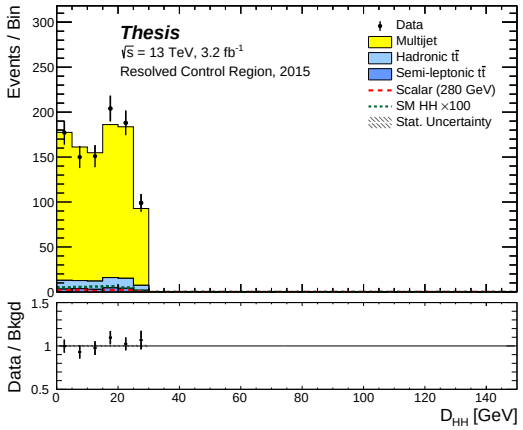

(a) The minimized jet pairing quantity D_{HH}

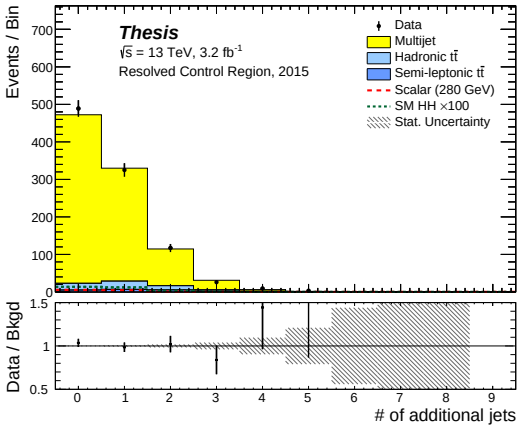

(b) The number of additional jets

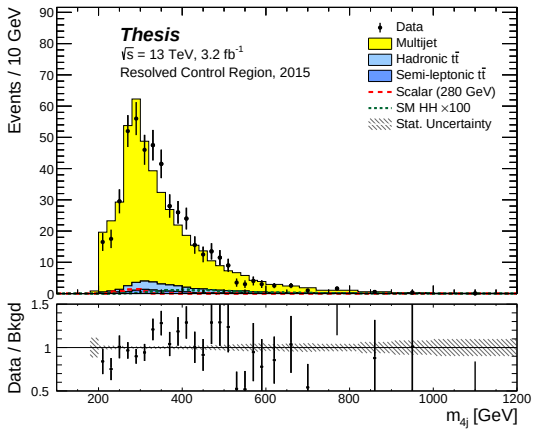

(c) The di-higgs candidate Mass

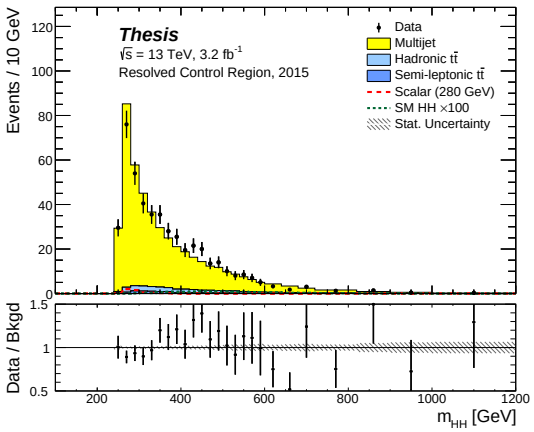

(d) The corrected di-higgs candidate Mass

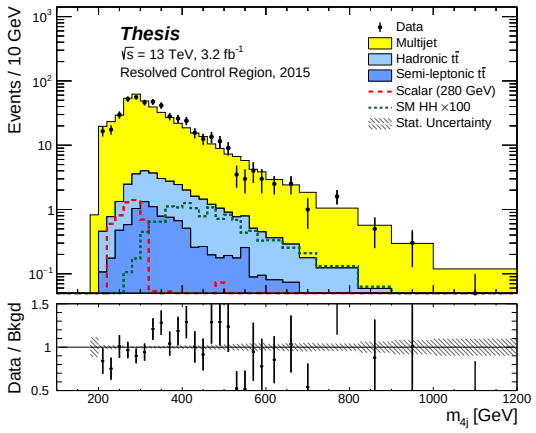

(e) Log scale of (c)

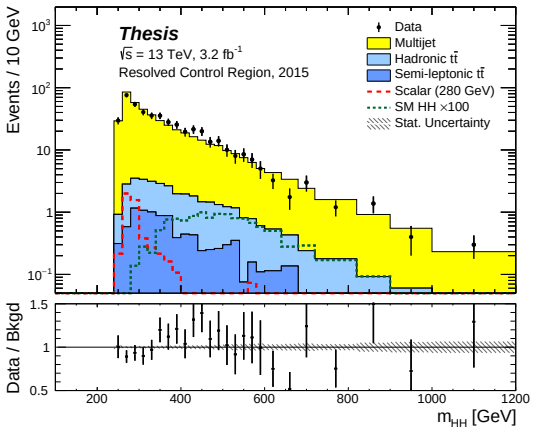

(f) Log scale of (d)

Figure C.11: Modelling of D_{HH}, the number of additional jets and the corrected and uncorrected di-higgs spectra. The corrected di-higgs mass is constructed by scaling the higgs candidate four vectors to have mass = 125 GeV and then computing the four body invariant mass.

Appendix D

KINEMATIC REWEIGHTING APPLIED TO 2016 CONTROL REGION

In Figure D.1 we show the result of the ratio smoothing and splining procedure for the first and last iteration for the five reweighted distributions. This shows that the reweighting functions have converged to one to within 5%. Figures D.2, D.3 show the full background model for the reweighted distributions in the Sideband. Figures D.4, D.5 show the same distributions in the Control region where the weights were derived.

	2015	2016
Two Tag	0.86 ± 0.04	1.0 ± 0.02
Four Tag	0.92 ± 0.5	1.3 ± 0.2

Table D.1: Scale factors for the two and four tag nonallhadronic $t\bar{t}$ MC samples used for 2015 and 2016 data as measured in the Control Region. Uncertainties are purely statistical

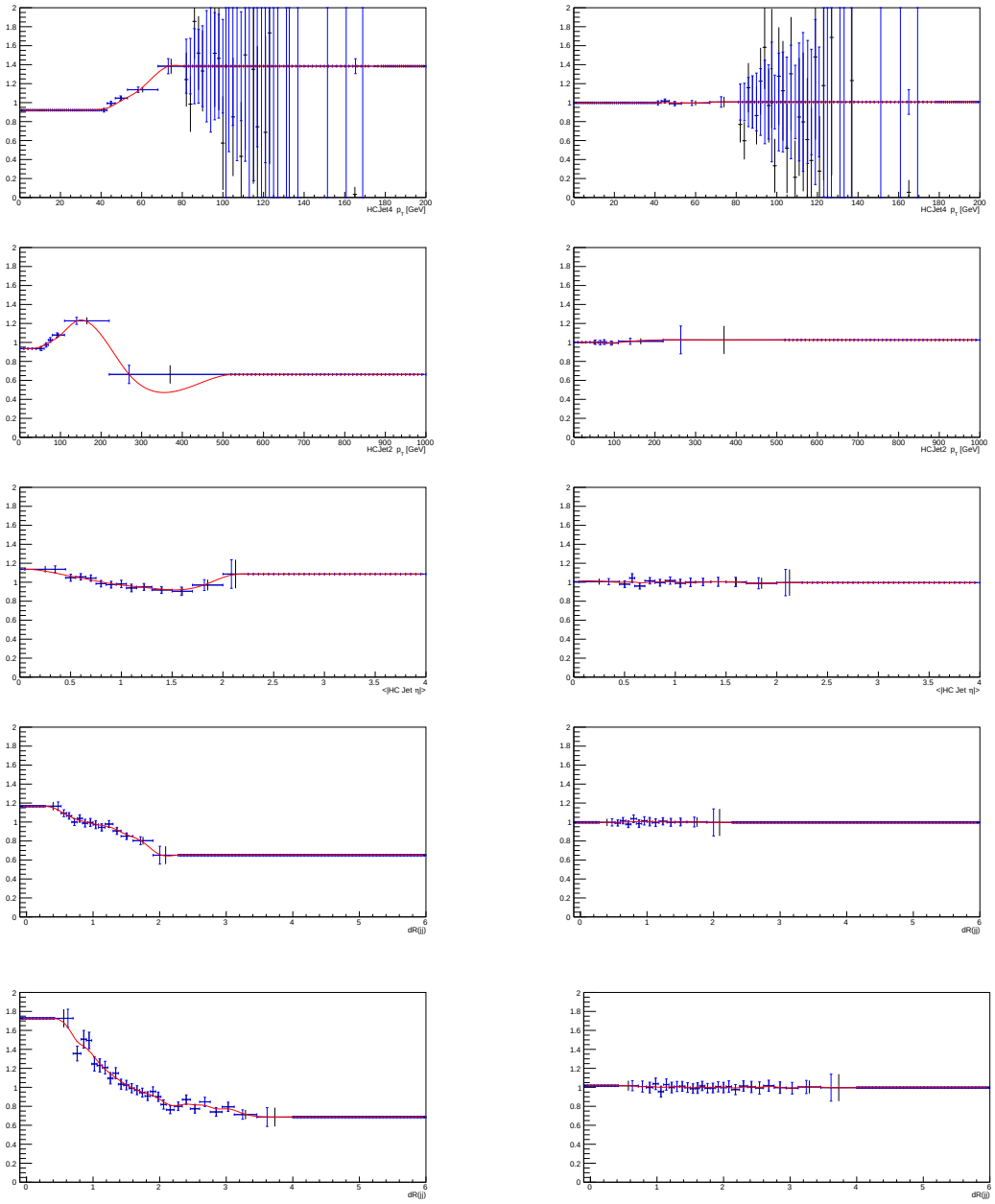

(a) Iteration 0 (b) Iteration 7

Figure D.1: The five reweighted ratios before and after the reweighting procedure had been applied. In black is the raw ratio, in blue is TGraph where the x values of the bins have been set to the mean of the background distribution in that bin and in red is the spline used for reweighting.

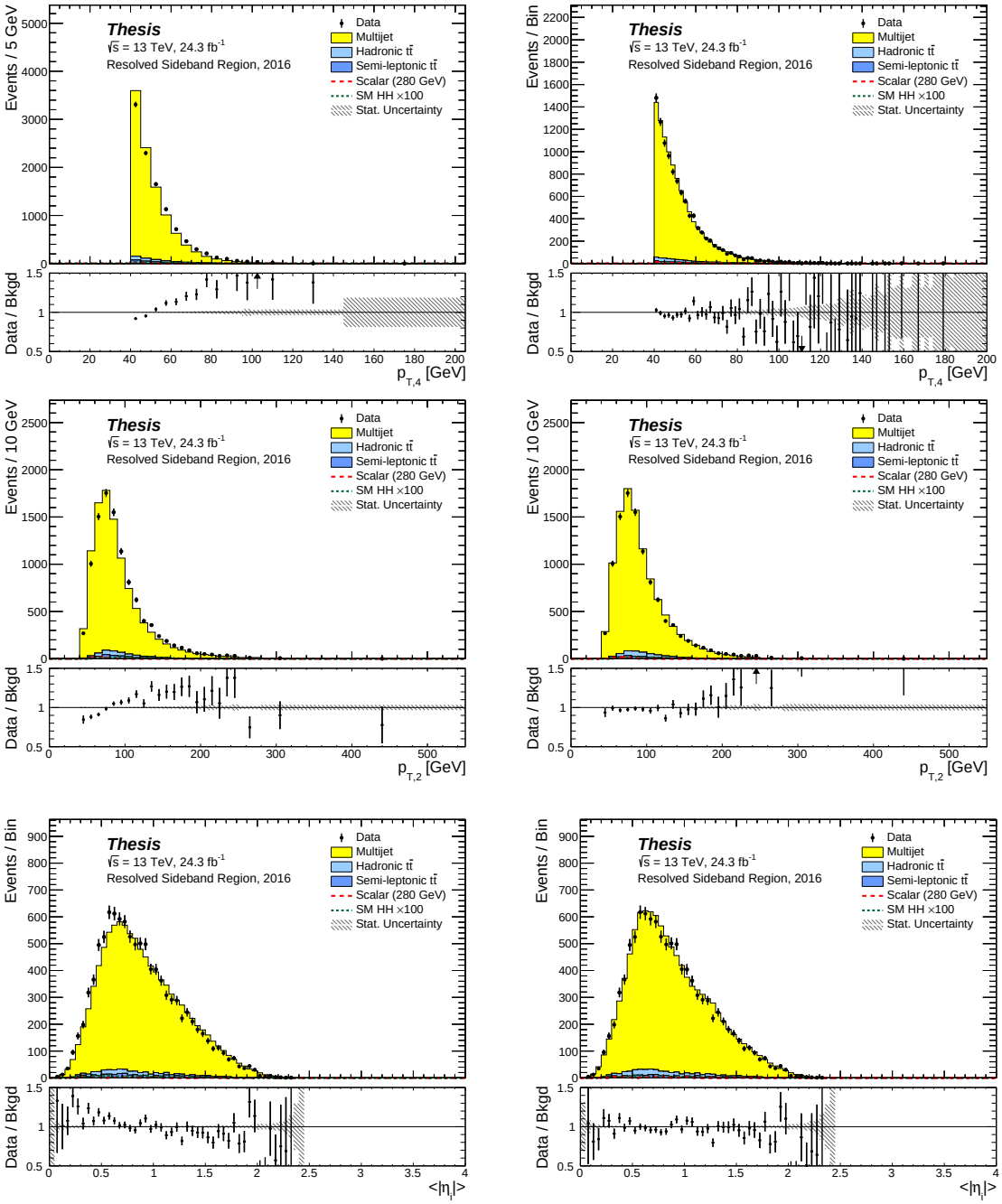

Figure D.2: The reweighted $p_{\mathrm{T}\ i}$ and $< |\eta_i| >$ distributions before and after the reweighting procedure had been applied.

	2015		2016	
	μ_{multijet}	$\alpha_{t\bar{t}}^{\text{hadronic}}$	μ_{multijet}	$\alpha_{t\bar{t}}^{\text{hadronic}}$
Prefit	0.151	0.934	0.289	0.991
Postfit	0.15 ± 0.007	0.74 ± 0.6	0.287 ± 0.005	1.1 ± 0.3

Table D.2: Scale factors before and after the combined fit to the multijet, allhadronic $t\bar{t}$ and non-allhadronic $t\bar{t}$ enriched regions in the Control Region

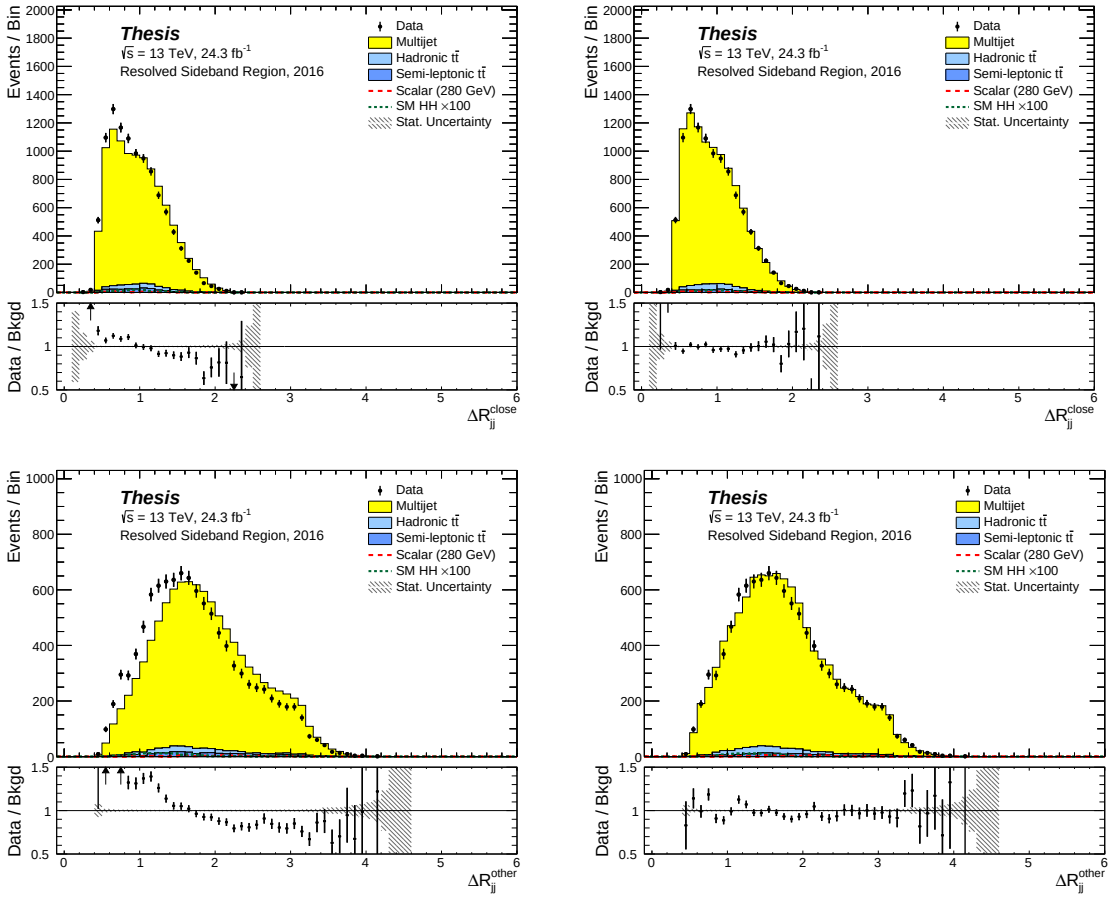

(a) Iteration 0

(b) Iteration 7

Figure D.3: The reweighted ΔR_{jj} distributions before and after the reweighting procedure had been applied.

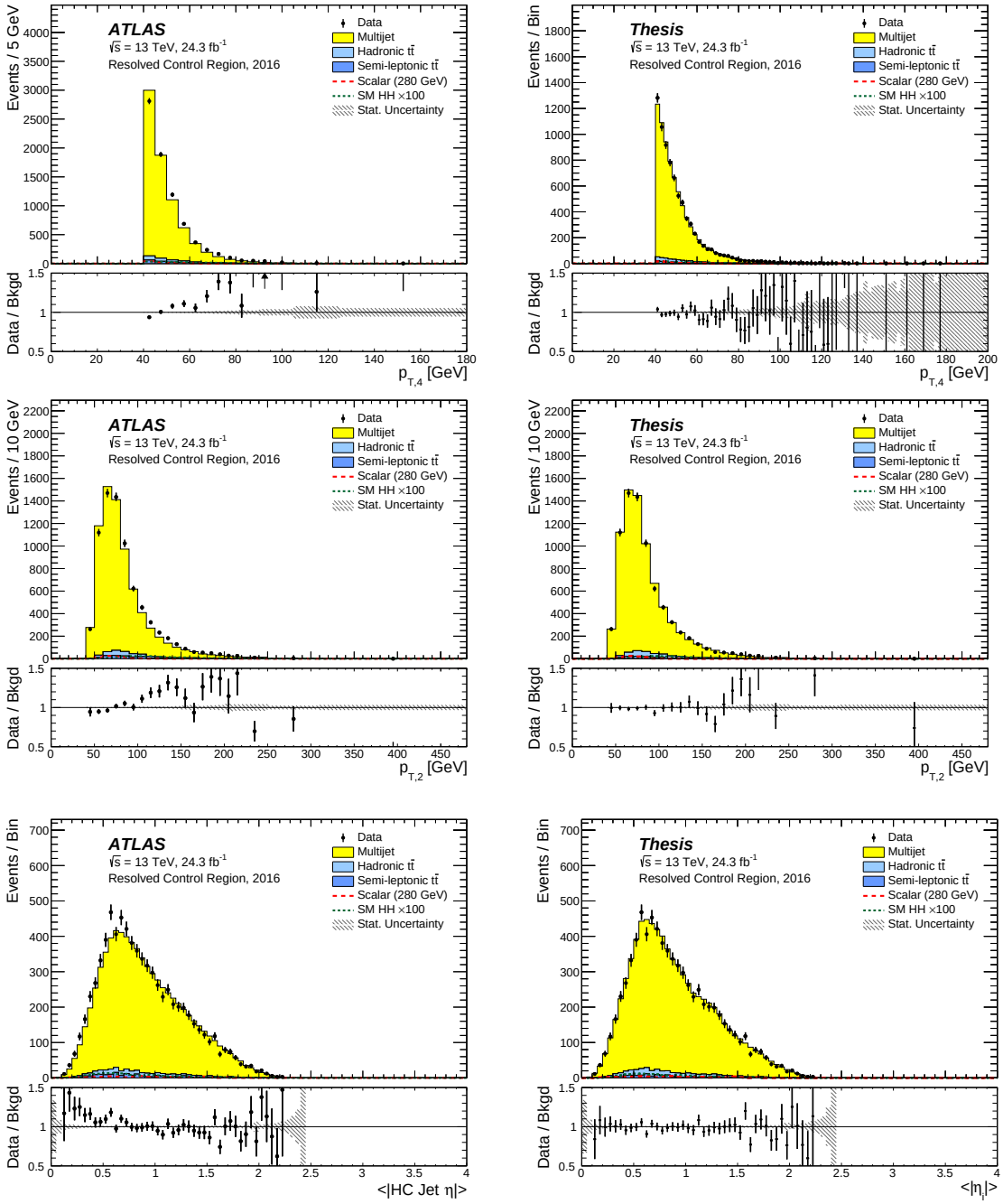

(a) Iteration 0

(b) Iteration 7

Figure D.4: The reweighted $p_{\mathrm{T}\ i}$ and $< |\eta_i| >$ distributions before and after the reweighting procedure had been applied.

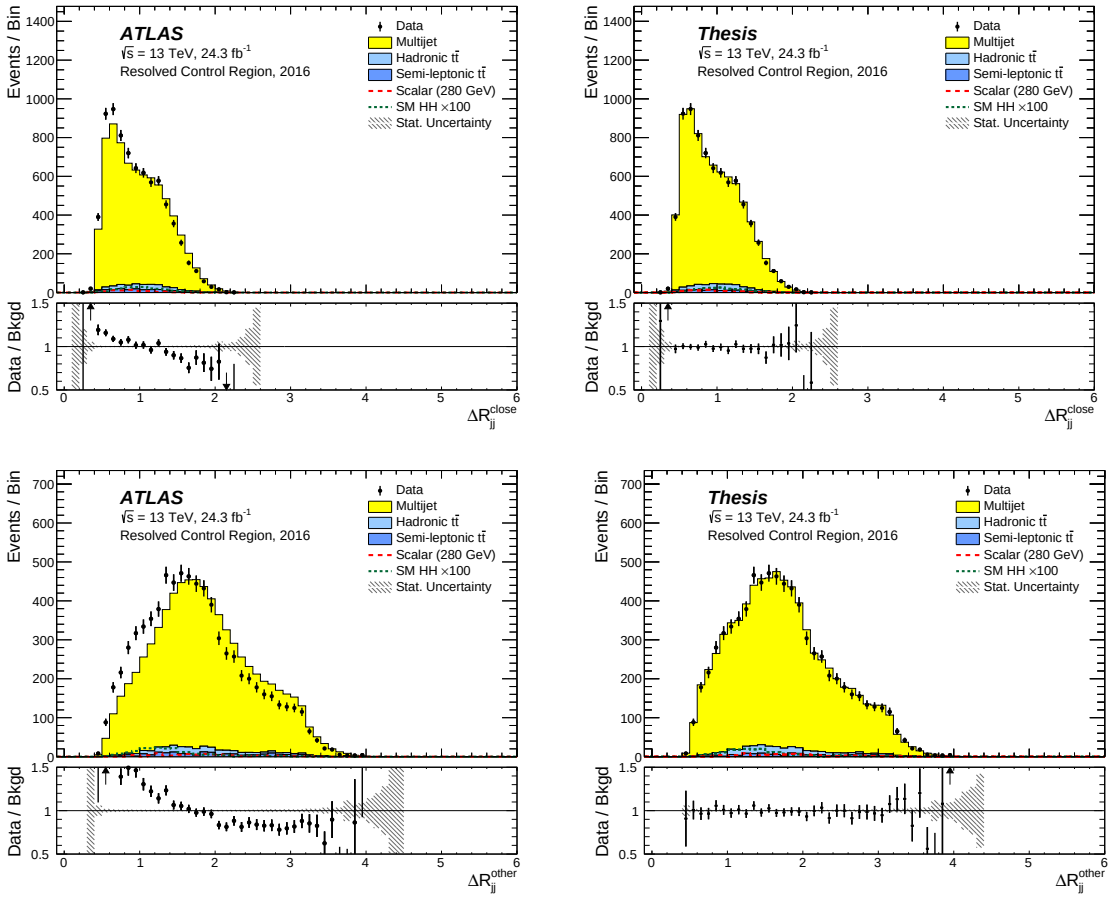

(a) Iteration 0

(b) Iteration 7

Figure D.5: The reweighted ΔR_{jj} distributions before and after the reweighting procedure had been applied.

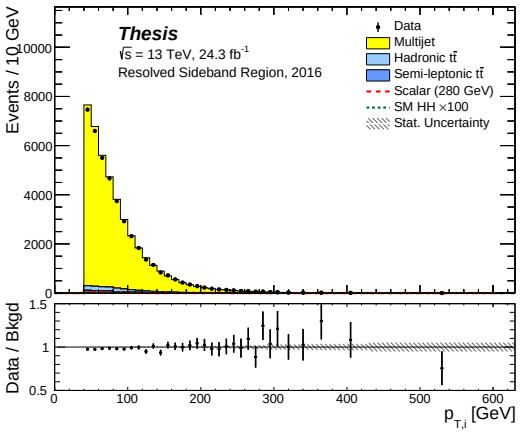

(a) p_{T} of all HC jets

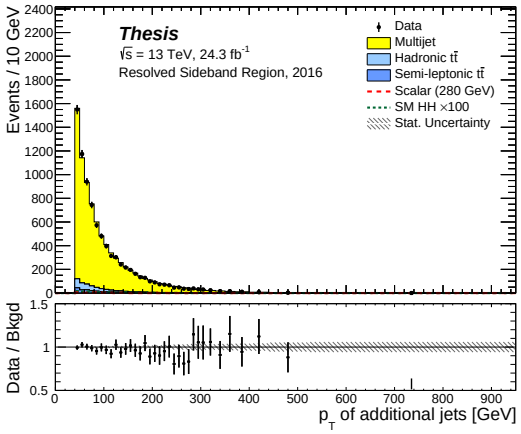

(b) p_{T} of all other jets in the event

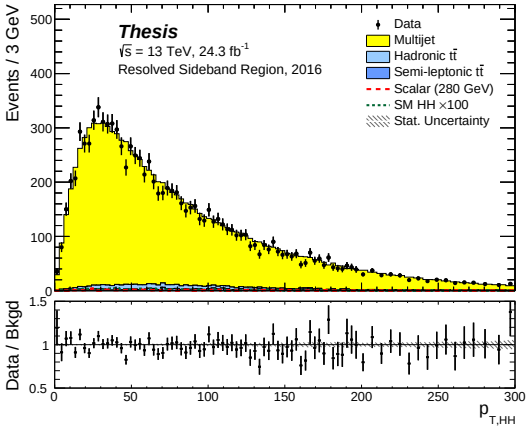

(c) p_{T} of the di-higgs candidate system

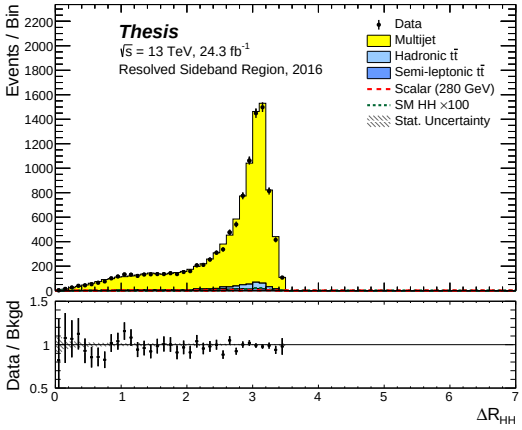

(d) ΔR between the two higgs candidates

Figure D.6: Figures a and b show that the p_{T} of both the higgs candidate jets and the other jets in the event are well modelled in the Sideband. Figures c and d show that higher level quantities like the p_{T} and openning angle of the di-higgs candidate system are also well modelled as a result.

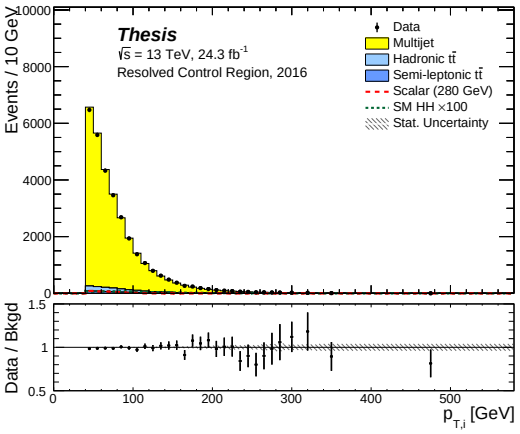

(a) p_{T} of all HC jets

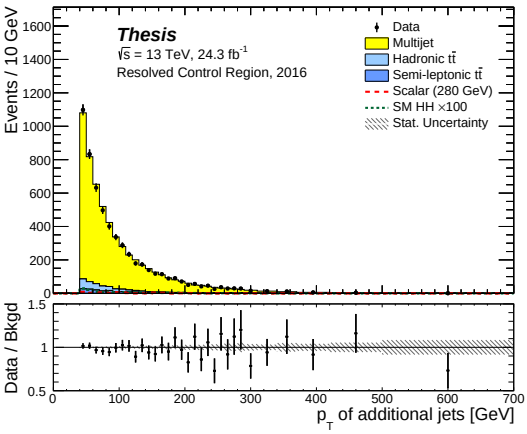

(b) p_{T} of all other jets in the event

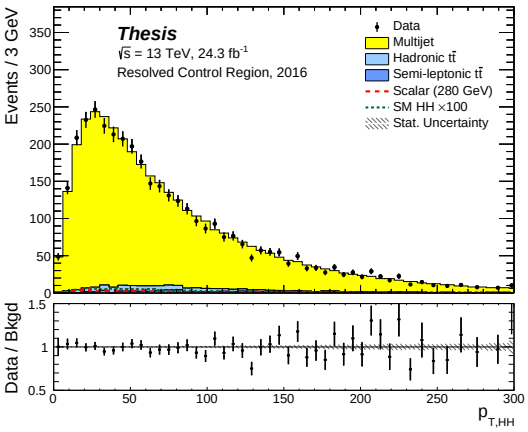

(c) p_{T} of the di-higgs candidate system

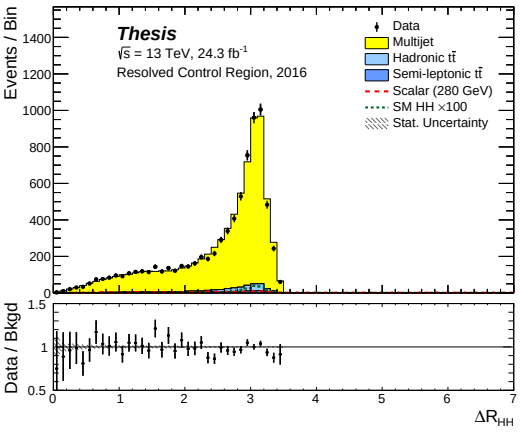

(d) ΔR between the two higgs candidates

Figure D.7: The same distributions as Figure D.6, but this time in the Control region to demonstrate that event level quantities remain well modelled as we move towards the Signal Region.

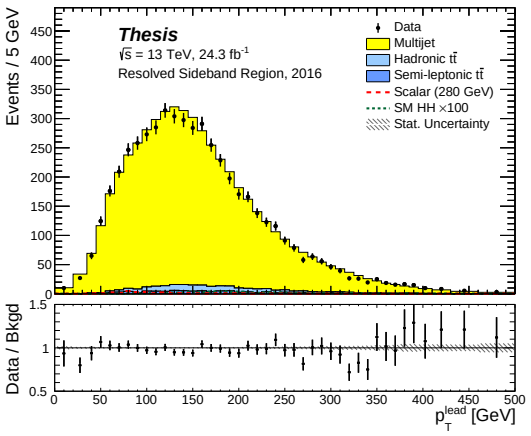

(a) Leading Higgs Candidate p_{T}

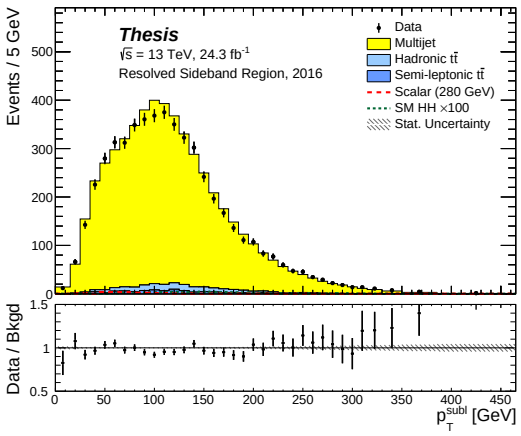

(b) Subleading Higgs Candidate p_{T}

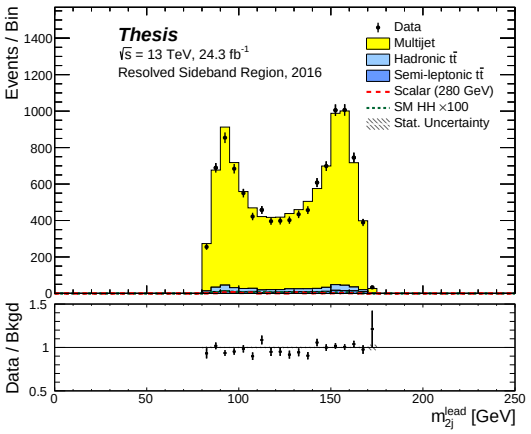

(c) Leading Higgs Candidate Mass

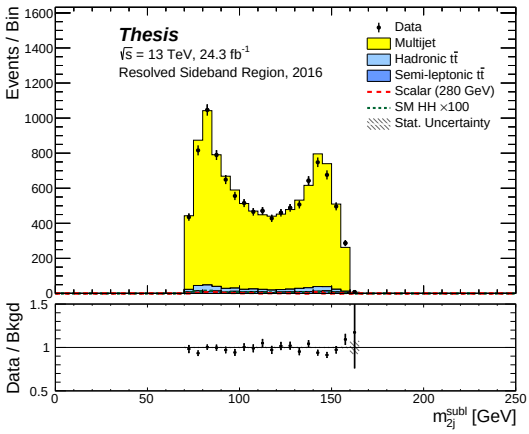

(d) Subleading Higgs Candidate Mass

Figure D.8: Modelling of Higgs Candidate kinematics in the Sideband.

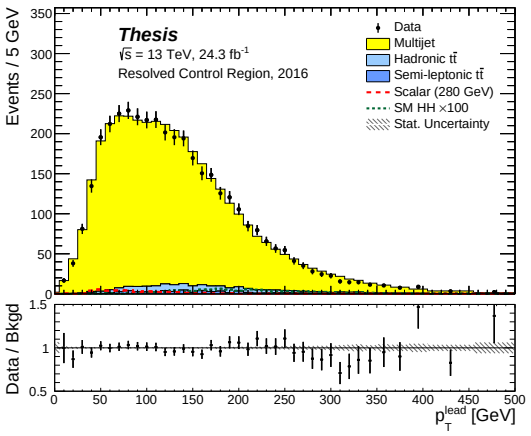

(a) Leading Higgs Candidate p_{T}

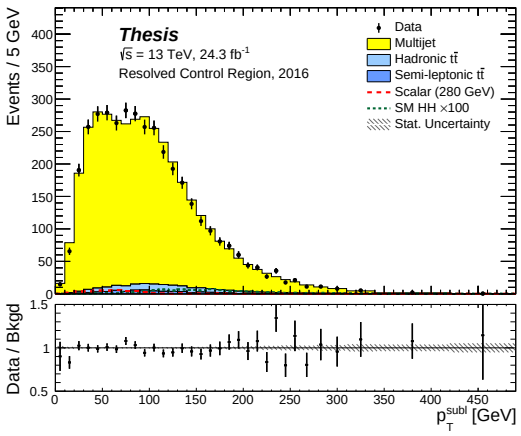

(b) Subleading Higgs Candidate p_{T}

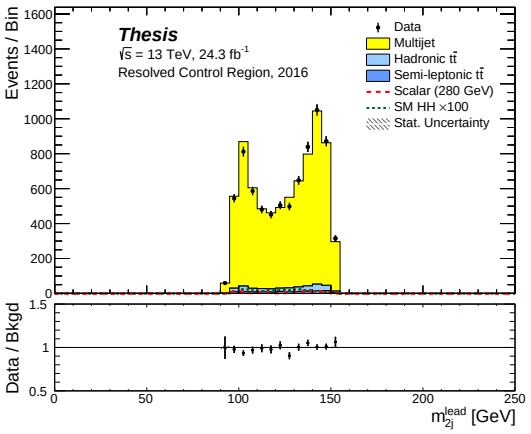

(c) Leading Higgs Candidate Mass

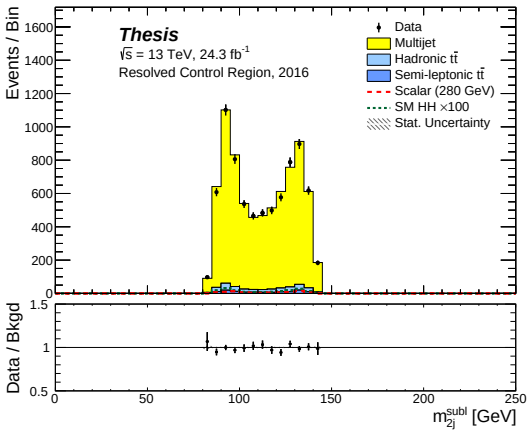

(d) Subleading Higgs Candidate Mass

Figure D.9: Modelling of Higgs Candidate kinematics in the Control Region.

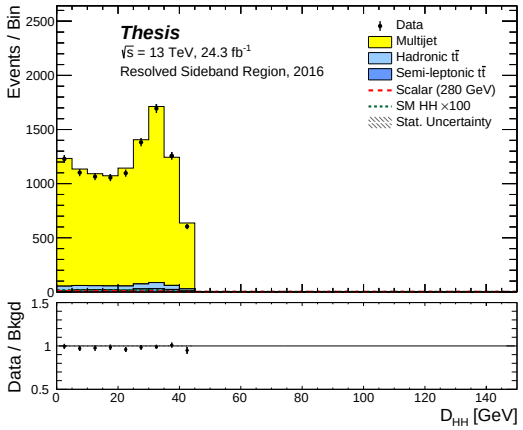

(a) The minimized jet pairing quantity D_{HH}

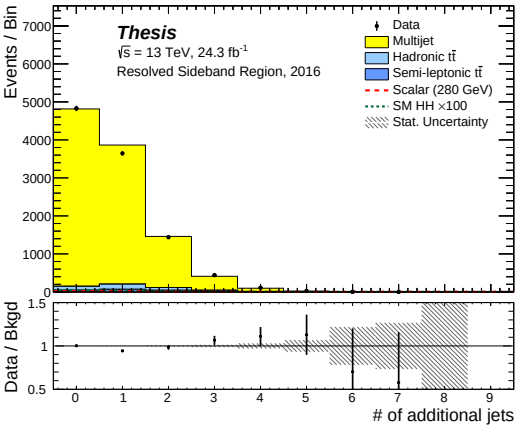

(b) The number of additional jets

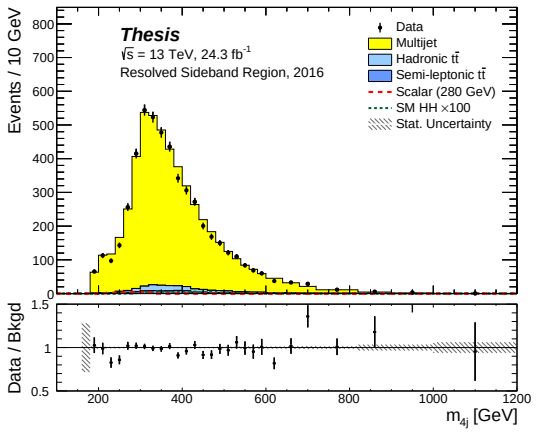

(c) The di-higgs candidate Mass

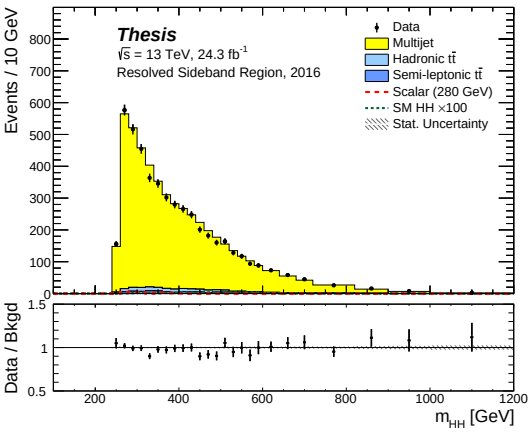

(d) The corrected di-higgs candidate Mass

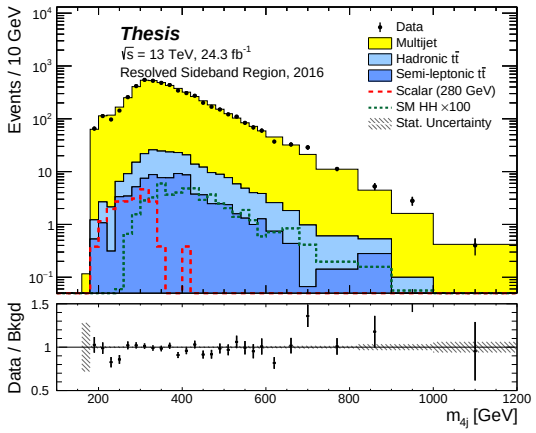

(e) Log scale of (c)

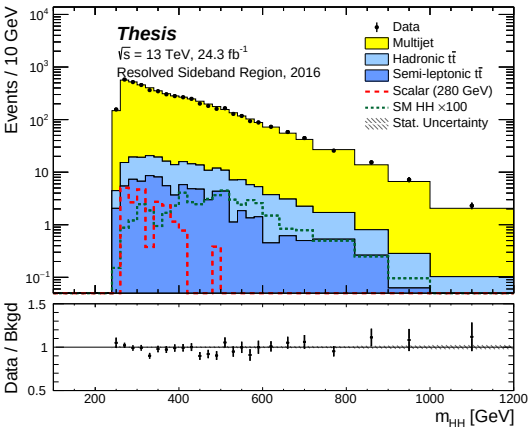

(f) Log scale of (d)

Figure D.10: Modelling of D_{HH}, the number of additional jets and the corrected and uncorrected di-higgs spectra. The corrected di-higgs mass is constructed by scaling the higgs candidate four vectors to have mass = 125 GeV and then computing the four body invariant mass.

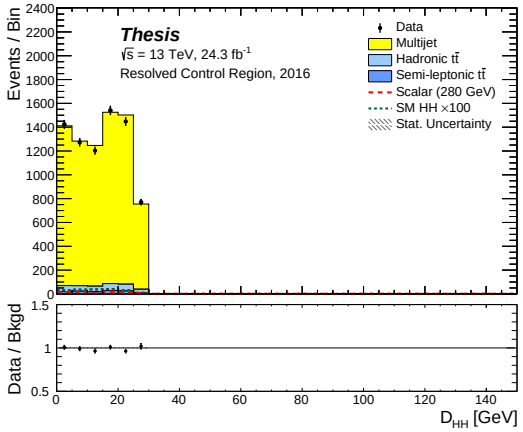

(a) The minimized jet pairing quantity D_{HH}

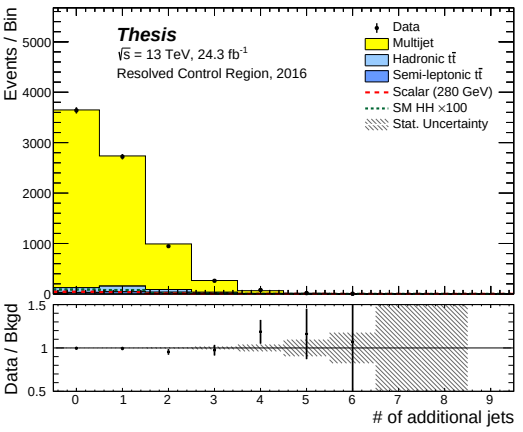

(b) The number of additional jets

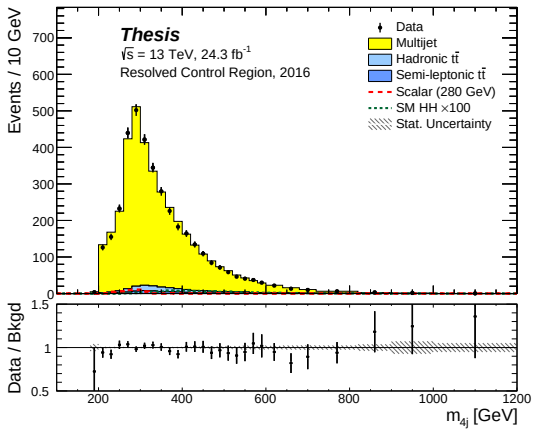

(c) The di-higgs candidate Mass

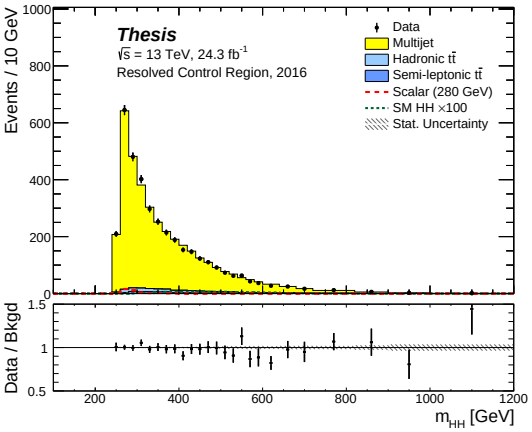

(d) The corrected di-higgs candidate Mass

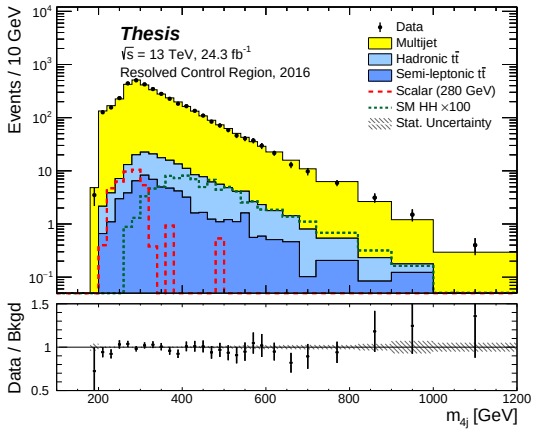

(e) Log scale of (c)

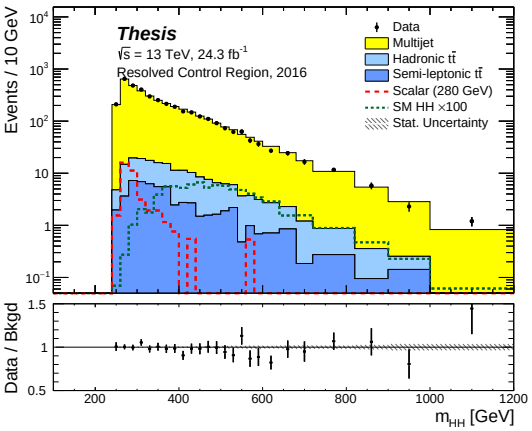

(f) Log scale of (d)

Figure D.11: Modelling of D_{HH}, the number of additional jets and the corrected and uncorrected di-higgs spectra. The corrected di-higgs mass is constructed by scaling the higgs candidate four vectors to have mass = 125 GeV and then computing the four body invariant mass.

Appendix E

KINEMATIC REWEIGHTING APPLIED TO 2015 CONTROL REGION

In Figure E.1 we show the result of the ratio smoothing and splining procedure for the first and last iteration for the five reweighted distributions. This shows that the reweighting functions have converged to one to within 5%. Figures E.2, E.3 show the full background model for the reweighted distributions in the Sideband. Figures E.4, E.5 show the same distributions in the Control region where the weights were derived.

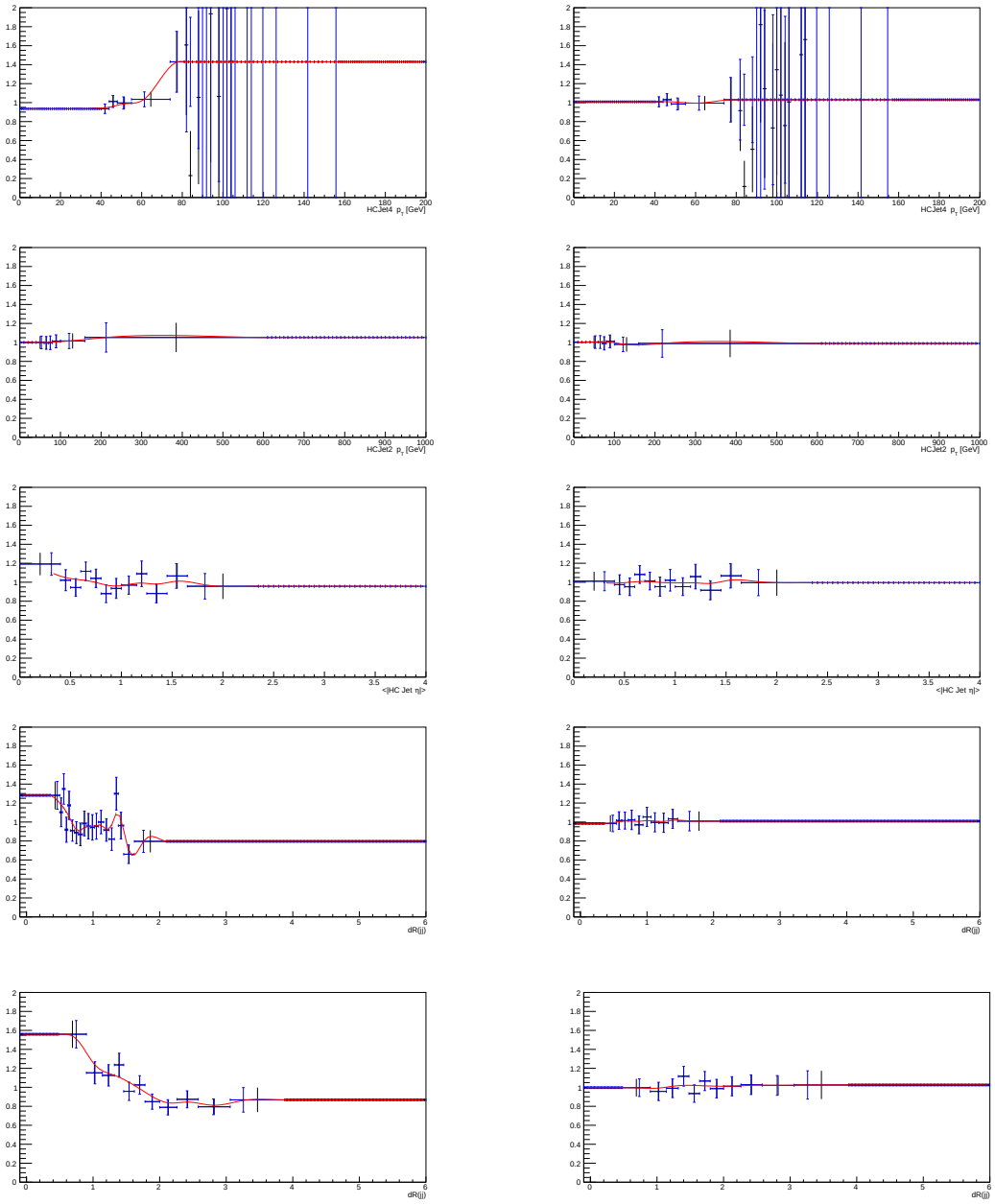

(a) Iteration 0

(b) Iteration 7

Figure E.1: The five reweighted ratios before and after the reweighting procedure had been applied. In black is the raw ratio, in blue is TGraph where the x values of the bins have been set to the mean of the background distribution in that bin and in red is the spline used for reweighting.

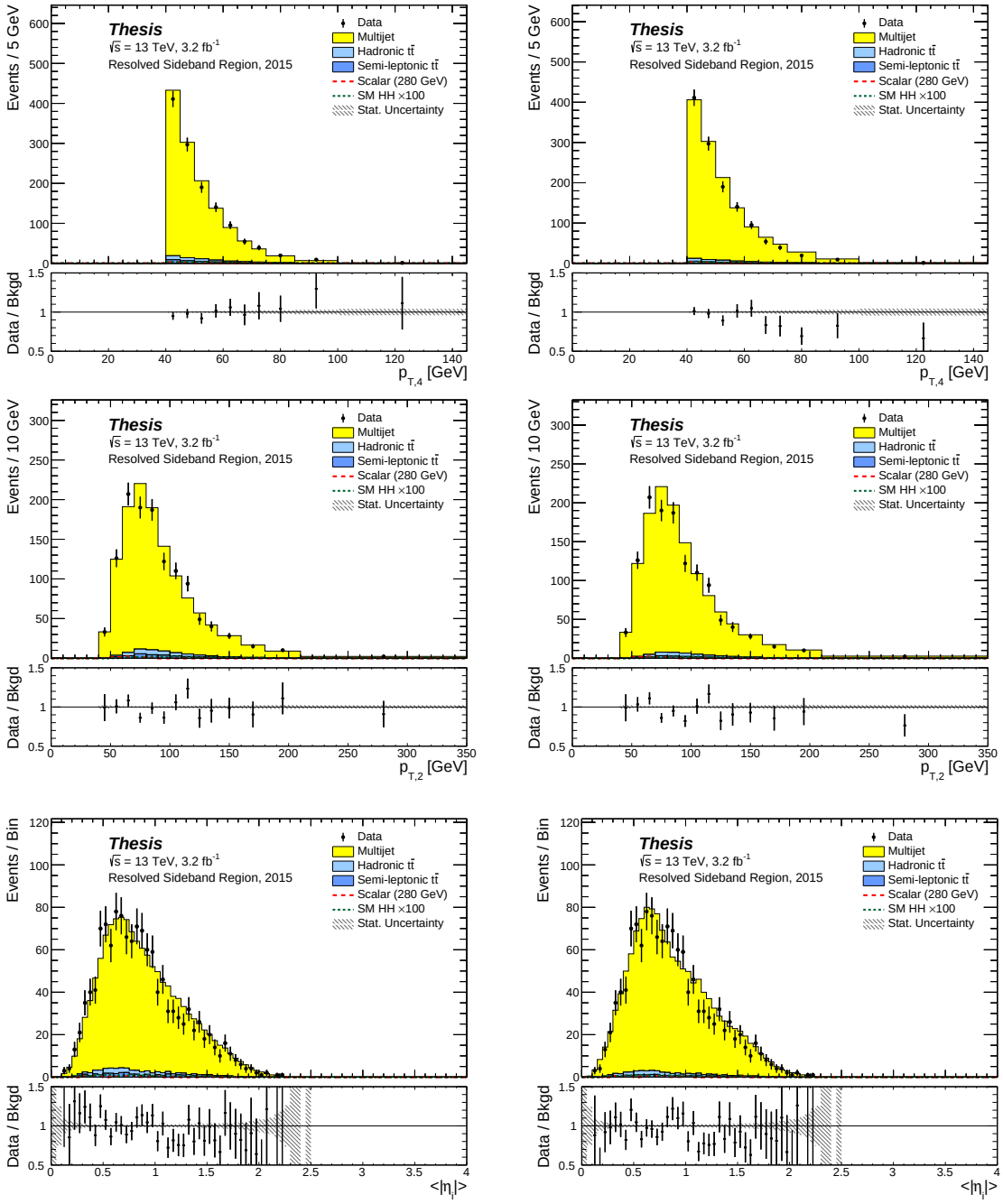

(a) Iteration 0

(b) Iteration 7

Figure E.2: The reweighted $p_{\mathrm{T}\ i}$ and $< |\eta_i| >$ distributions before and after the reweighting procedure had been applied.

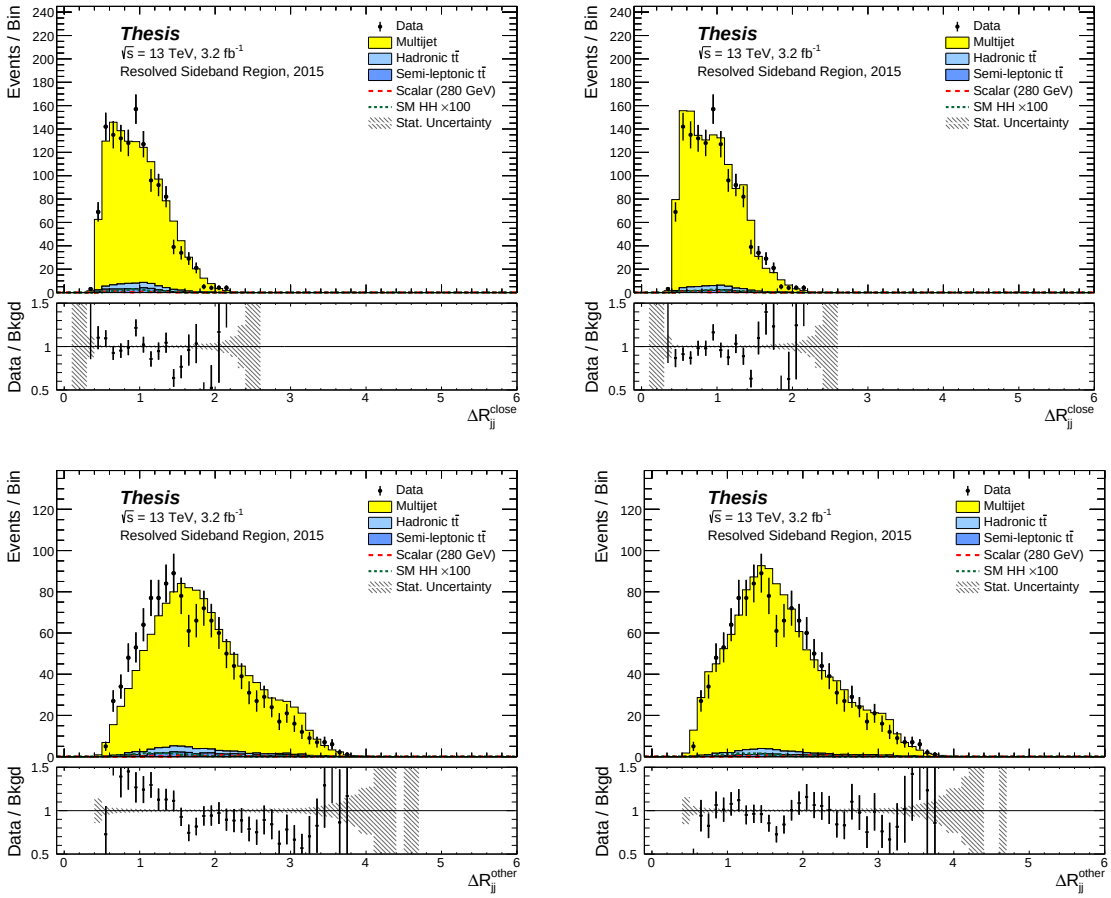

(a) Iteration 0

(b) Iteration 7

Figure E.3: The reweighted ΔR_{jj} distributions before and after the reweighting procedure had been applied.

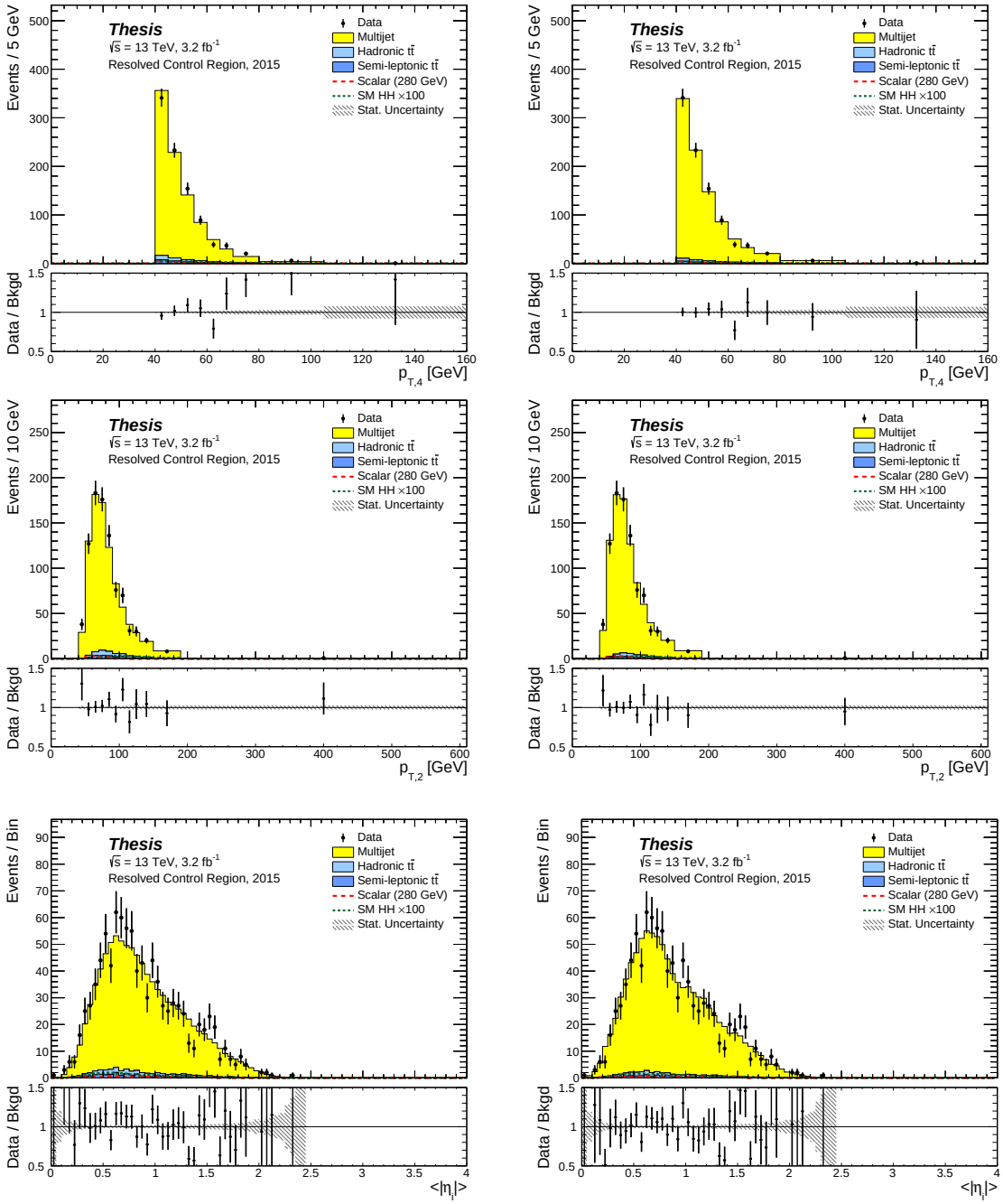

Figure E.4: The reweighted $p_{\mathrm{T}\ i}$ and $< |\eta_i| >$ distributions before and after the reweighting procedure had been applied.

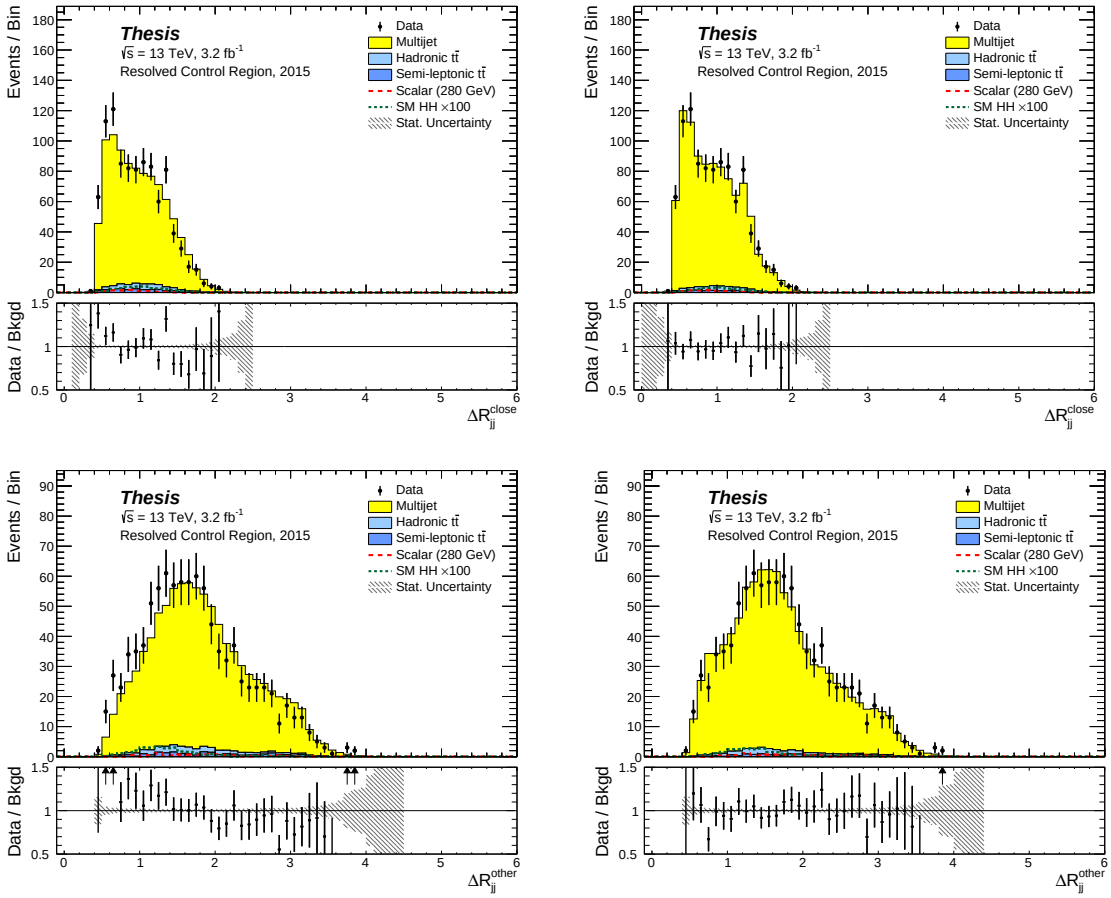

(a) Iteration 0

(b) Iteration 7

Figure E.5: The reweighted ΔR_{jj} distributions before and after the reweighting procedure had been applied.

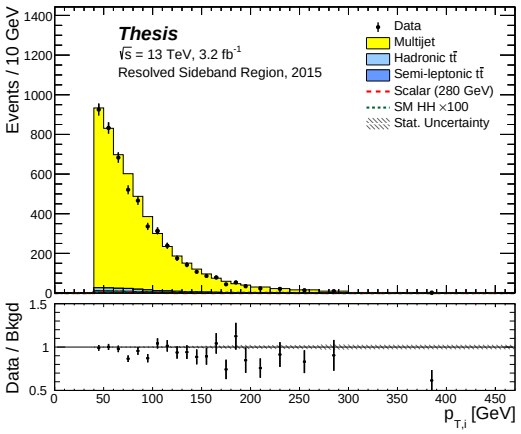

(a) p_{T} of all HC jets

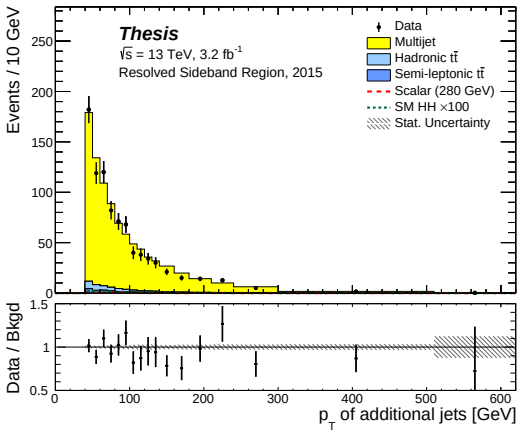

(b) p_{T} of all other jets in the event

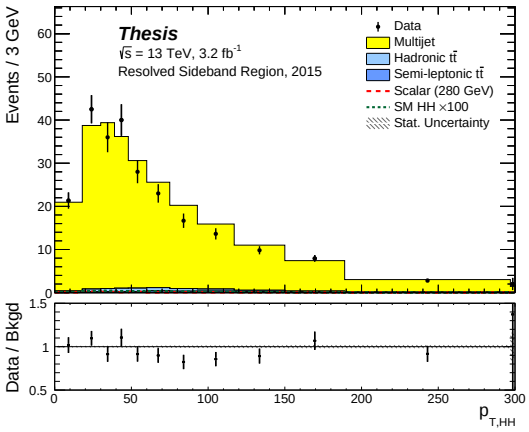

(c) p_{T} of the di-higgs candidate system

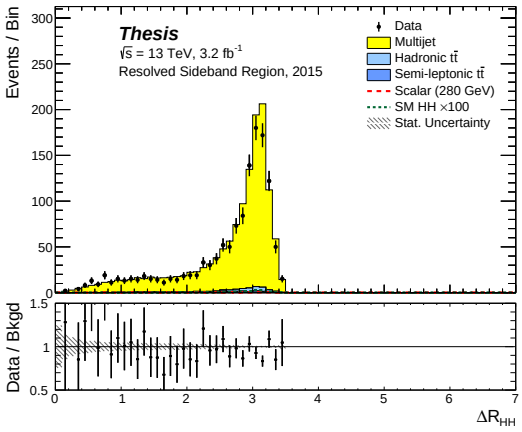

(d) ΔR between the two higgs candidates

Figure E.6: Figures a and b show that the p_{T} of both the higgs candidate jets and the other jets in the event are well modelled in the Sideband. Figures c and d show that higher level quantities like the p_{T} and openning angle of the di-higgs candidate system are also well modelled as a result.

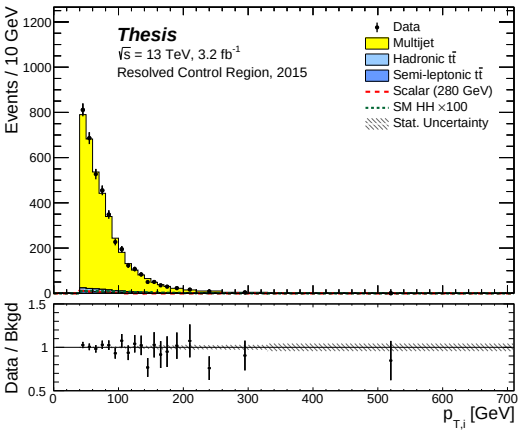

(a) p_{T} of all HC jets

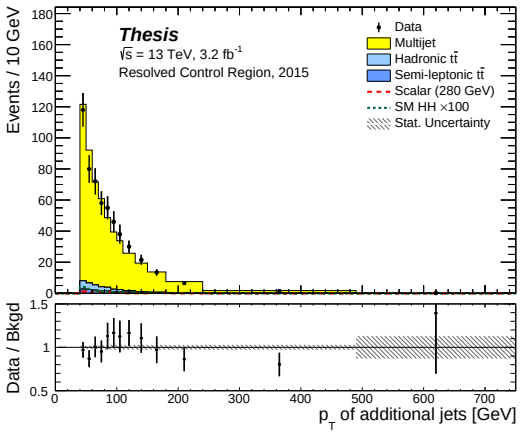

(b) p_{T} of all other jets in the event

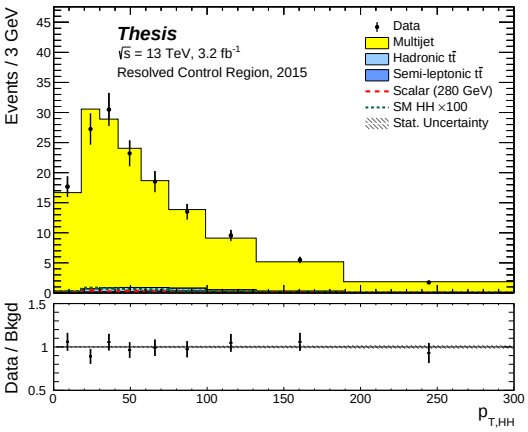

(c) p_{T} of the di-higgs candidate system

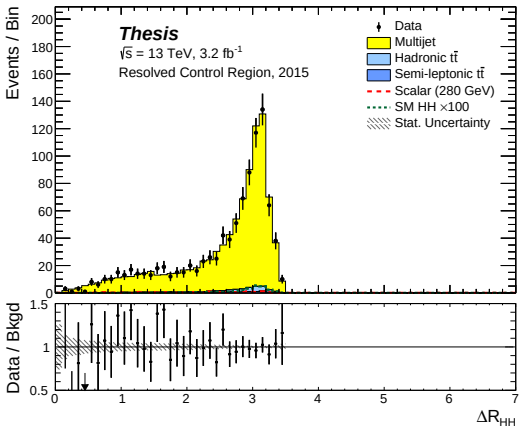

(d) ΔR between the two higgs candidates

Figure E.7: The same distributions as Figure E.6, but this time in the Control region to demonstrate that event level quantities remain well modelled as we move towards the Signal Region.

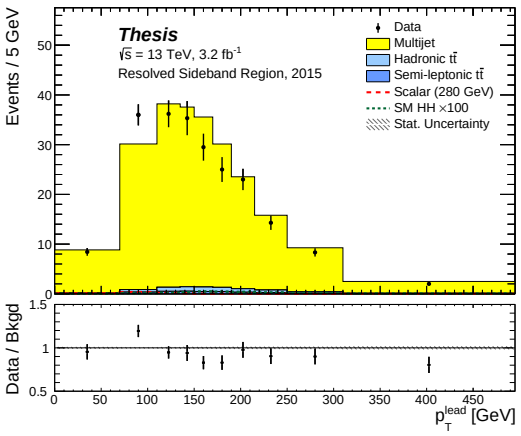

(a) Leading Higgs Candidate p_{T}

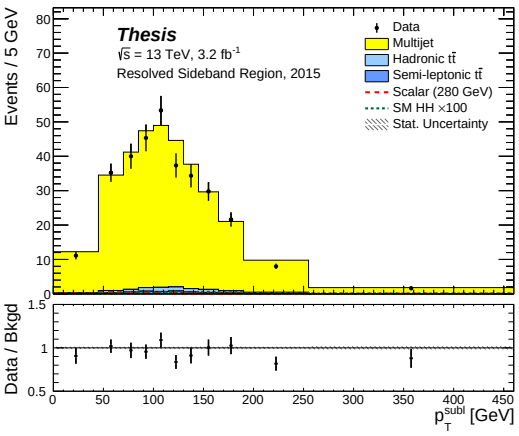

(b) Subleading Higgs Candidate p_{T}

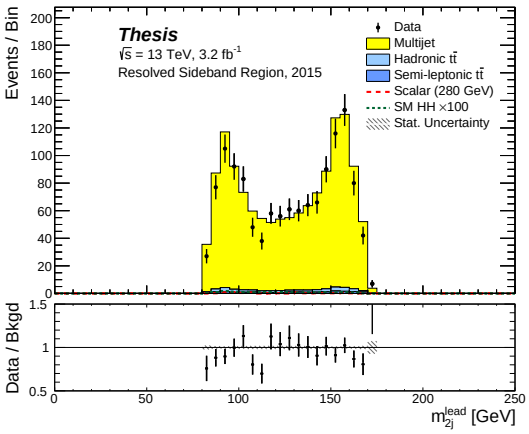

(c) Leading Higgs Candidate Mass

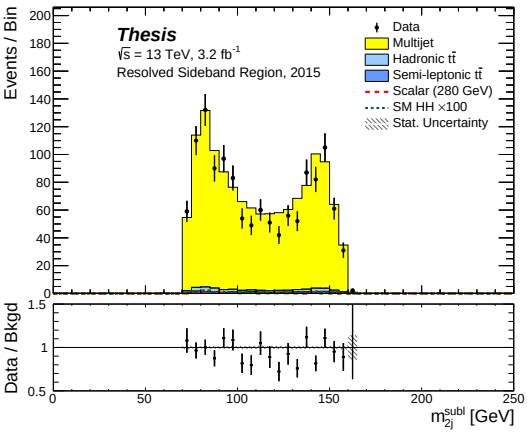

(d) Subleading Higgs Candidate Mass

Figure E.8: Modelling of Higgs Candidate kinematics in the Sideband.

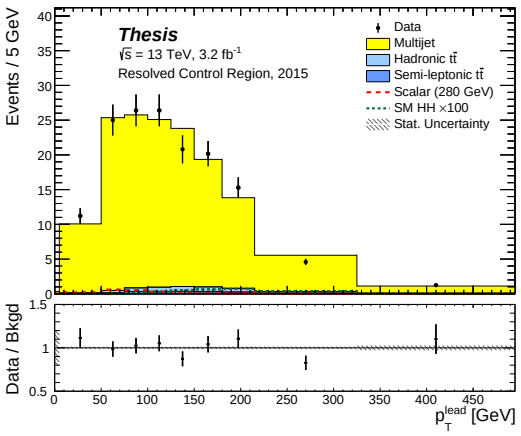

(a) Leading Higgs Candidate p_{T}

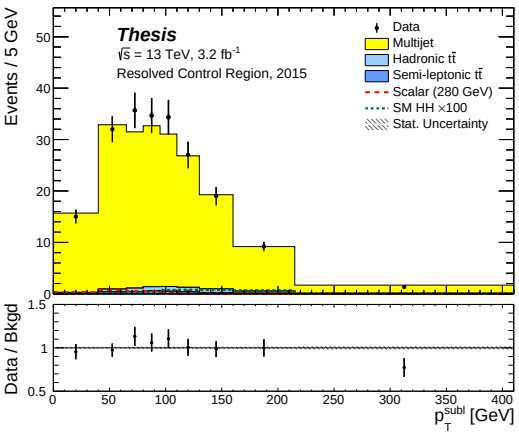

(b) Subleading Higgs Candidate p_{T}

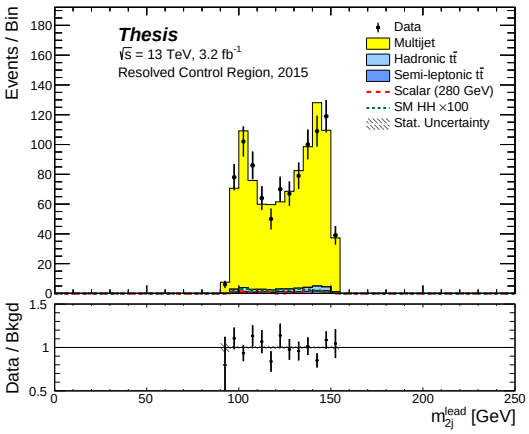

(c) Leading Higgs Candidate Mass

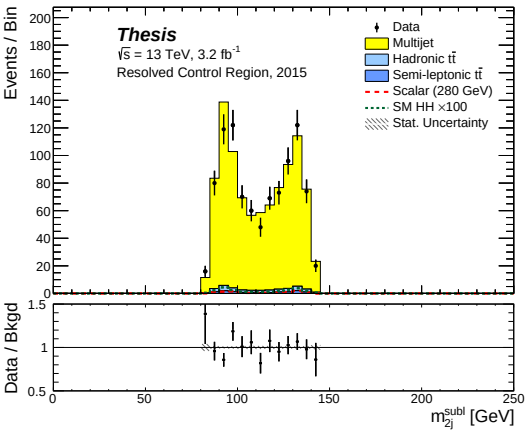

(d) Subleading Higgs Candidate Mass

Figure E.9: Modelling of Higgs Candidate kinematics in the Control Region.

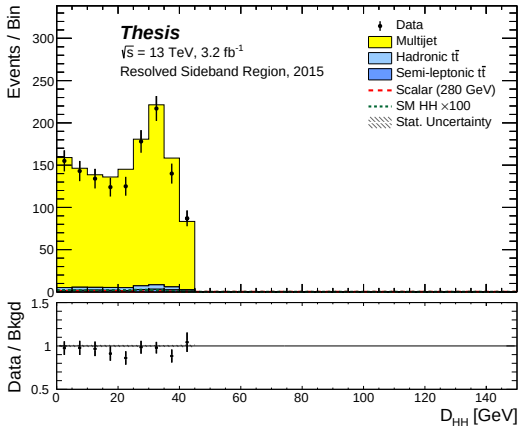

(a) The minimized jet pairing quantity D_{HH}

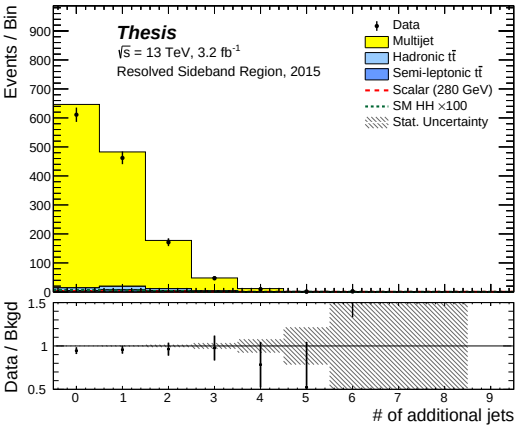

(b) The number of additional jets

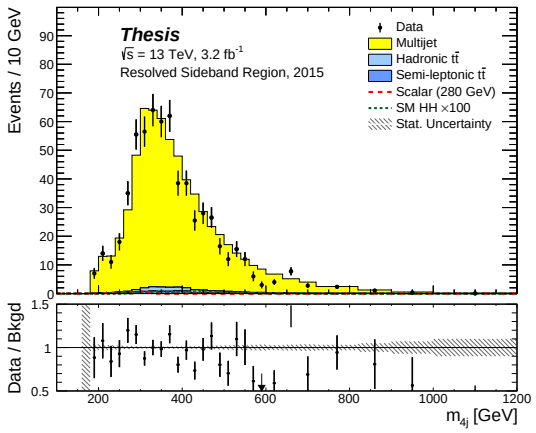

(c) The di-higgs candidate Mass

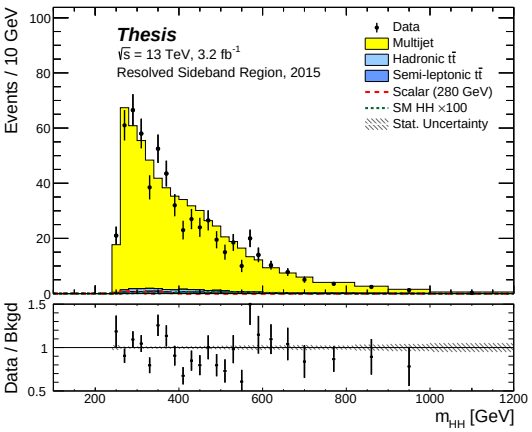

(d) The corrected di-higgs candidate Mass

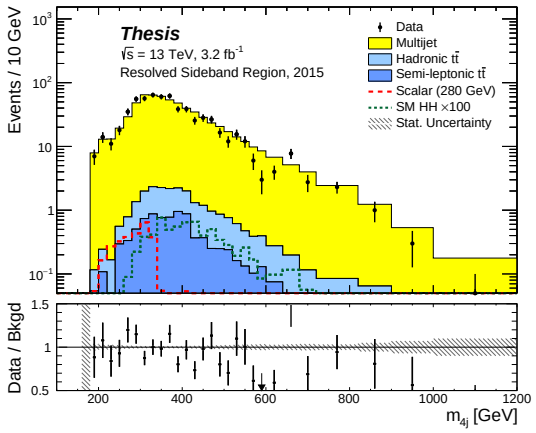

(e) Log scale of (c)

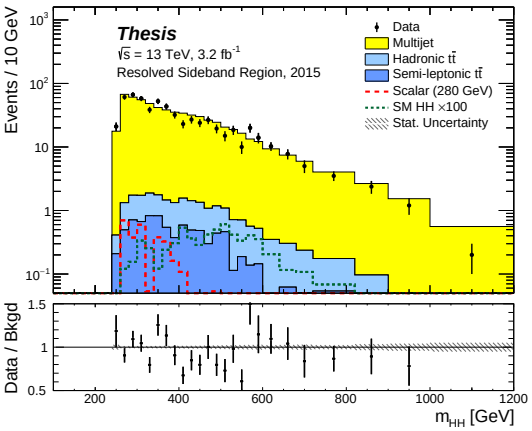

(f) Log scale of (d)

Figure E.10: Modelling of D_{HH}, the number of additional jets and the corrected and uncorrected di-higgs spectra. The corrected di-higgs mass is constructed by scaling the higgs candidate four vectors to have mass = 125 GeV and then computing the four body invariant mass.

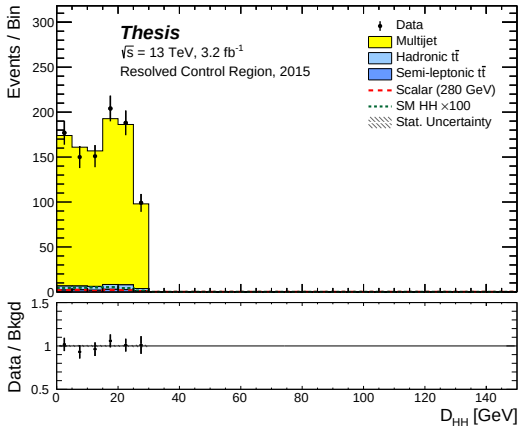

(a) The minimized jet pairing quantity D_{HH}

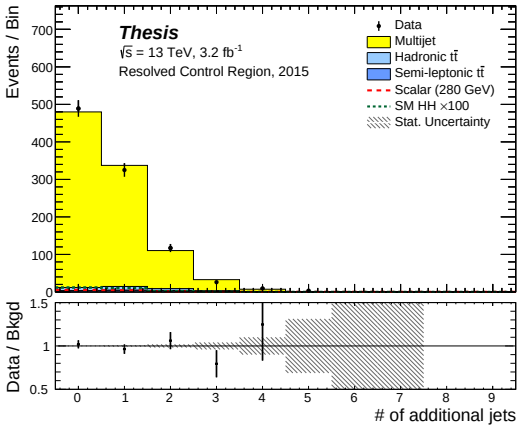

(b) The number of additional jets

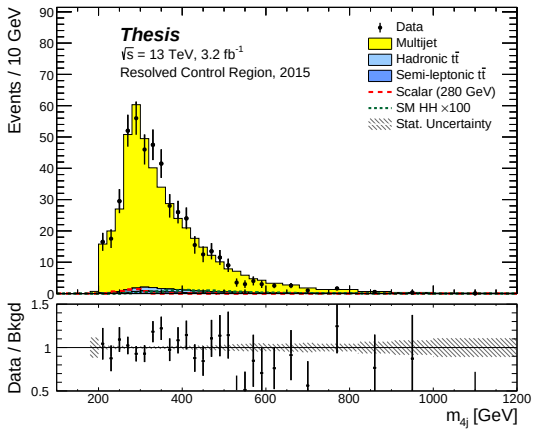

(c) The di-higgs candidate Mass

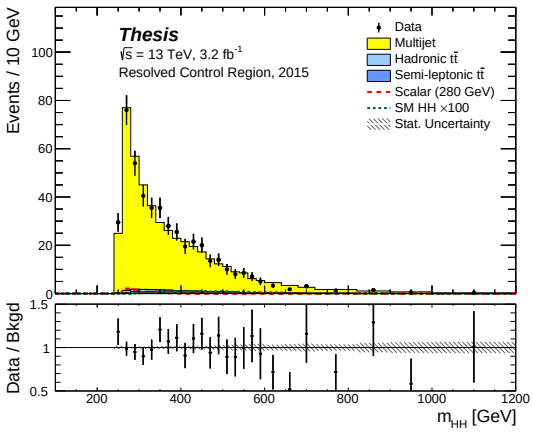

(d) The corrected di-higgs candidate Mass

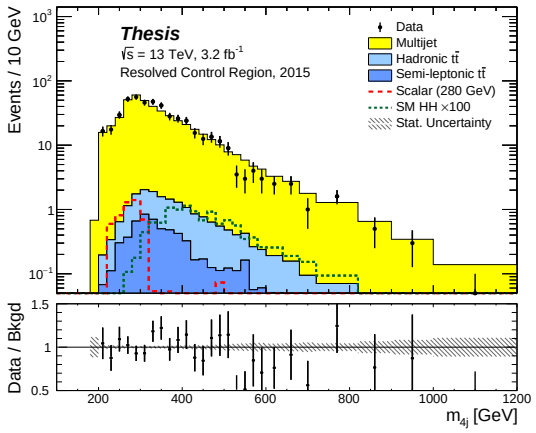

(e) Log scale of (c)

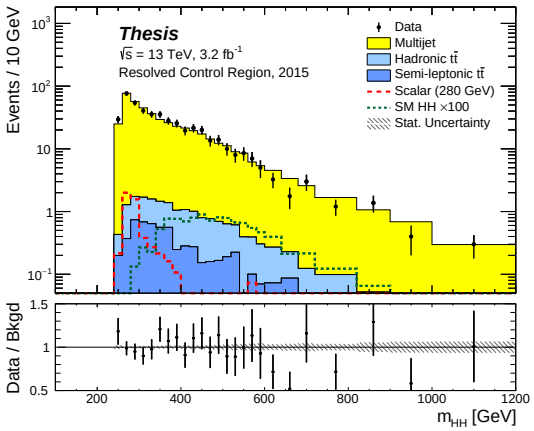

(f) Log scale of (d)

Figure E.11: Modelling of D_{HH}, the number of additional jets and the corrected and uncorrected di-higgs spectra. The corrected di-higgs mass is constructed by scaling the higgs candidate four vectors to have mass = 125 GeV and then computing the four body invariant mass.

Appendix F

TRIGGER EFFICIENCIES IN THE 2015 DATASET

Section 9 presents an overview of the trigger efficiency measurement and the results applied to the 2016 dataset. This section presents the corresponding results in the 2015 dataset. The triggers used in 2015 are presented in Table F.1. The efficiencies of the various items in MC and their combination is shown as a function of resonance mass for the various signal samples in Figure F.1.

Figure F.2 shows the jet-level uncertainties in data and MC as measured in the $t\bar{t}$ sample. Unlike the case in 2016, the MC efficiency in 2015 significantly underestimates the performance in data. This is a result of MC sample being frozen before the tuning of the b-tagging used for data was optimized. The jet-level uncertainties are taken to be 100% correlated.

The jet-level trigger efficiencies in the various 4b signal samples are shown in Figure F.3. Negligible variation is seen among the signal samples. In the following, the jet-level efficiencies are taken from the 4b MC and corrected to data using the scale factor measured in $t\bar{t}$ events.

The methodology presented in Section 9 is applied to the 2015 triggers. Figure F.4 validates the modeling of the individual and combined trigger efficiencies using Method-1. The non-closure from Methods-1 and 2 are shown for the combined trigger efficiency in Figure F.5.

2015
2j35_btight_2j35
j100_2j55_bmedium
j225_bloose

Table F.1: Triggers used in the 2015 analysis.

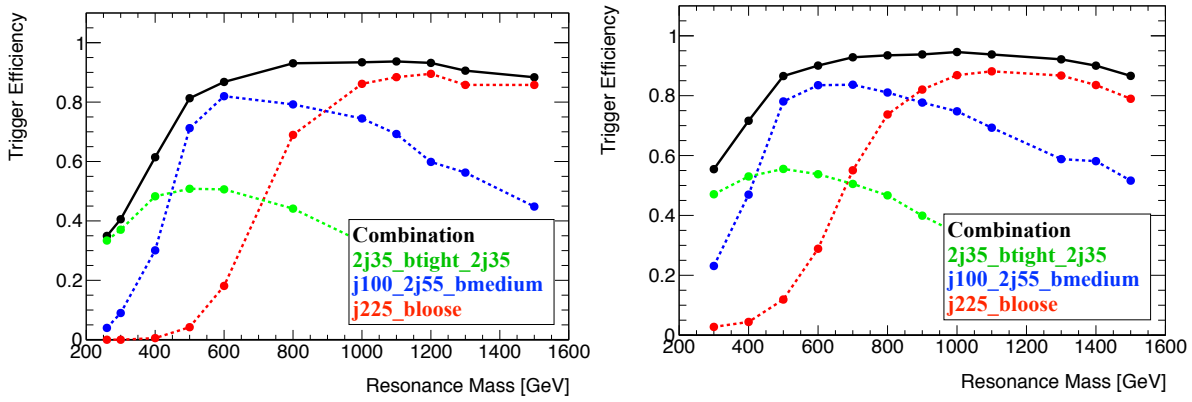

(a) Scalar (b) Spin-2

Figure F.1: MC Triggers efficiencies as a function of resonance mass for the signal samples.

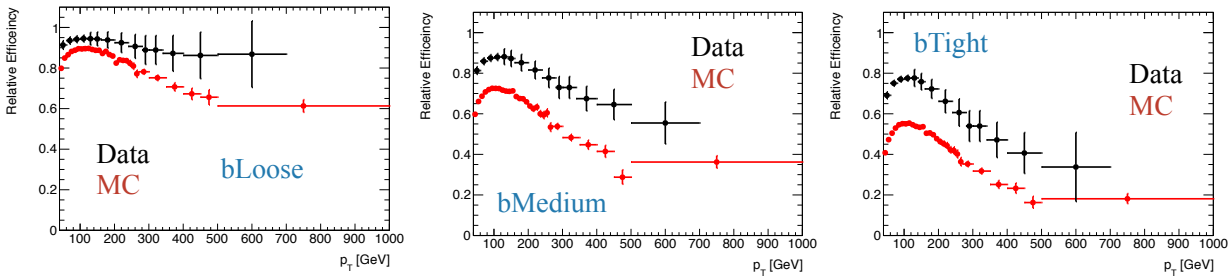

(a) bLoose (b) bMedium (c) bTight

Figure F.2: 2015 jet-level efficiencies measured in the $t\bar{t}$ sample.

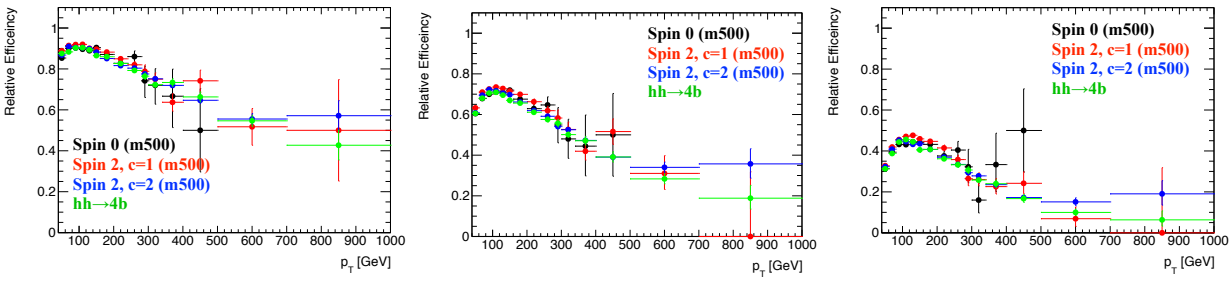

(a) bLoose (b) bMedium (c) bTight

Figure F.3: 2015 jet-level efficiencies measured in the 4b signal samples.

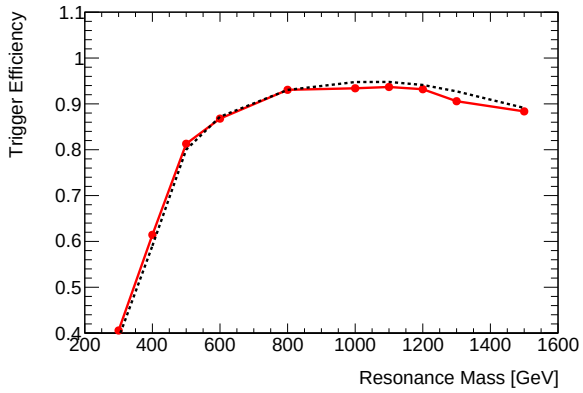

(a) HLT OR

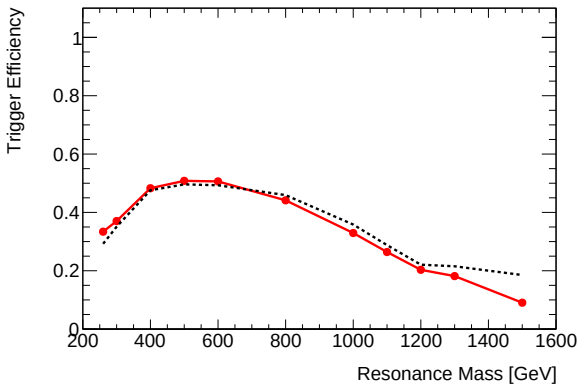

(b) 2j35_btight_2j35

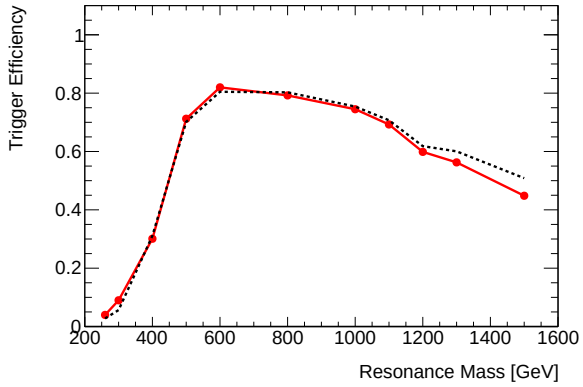

(c) j100_2j55_bmedium

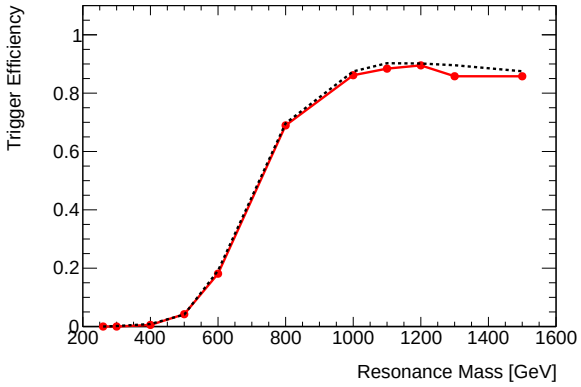

(d) j255_bloose

Figure F.4: Comparison of trigger efficiency in MC using the jet-level approximation to the MC decisions including the full correlation.

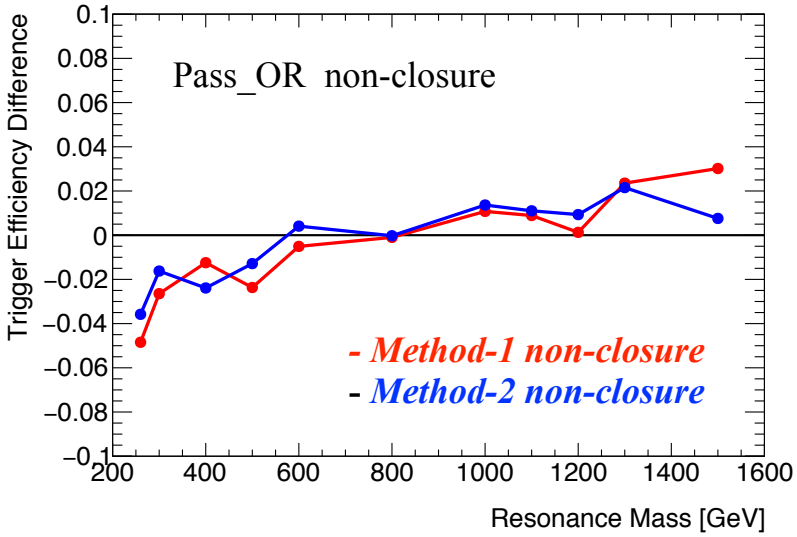

Figure F.5: Difference between the full combined event-level trigger efficiency in the MC and when the jet-level emulation of Method-1 and Method-2.

Figure F.6 shows the event-level trigger efficiencies for the various signal samples corrected for the jet-level efficiencies measured in data. The dashed lines indicate the systematic uncertainties on the trigger efficiency including all the components described here. The measured efficiency for the non-resonant signal is $94 \pm 2\%$.

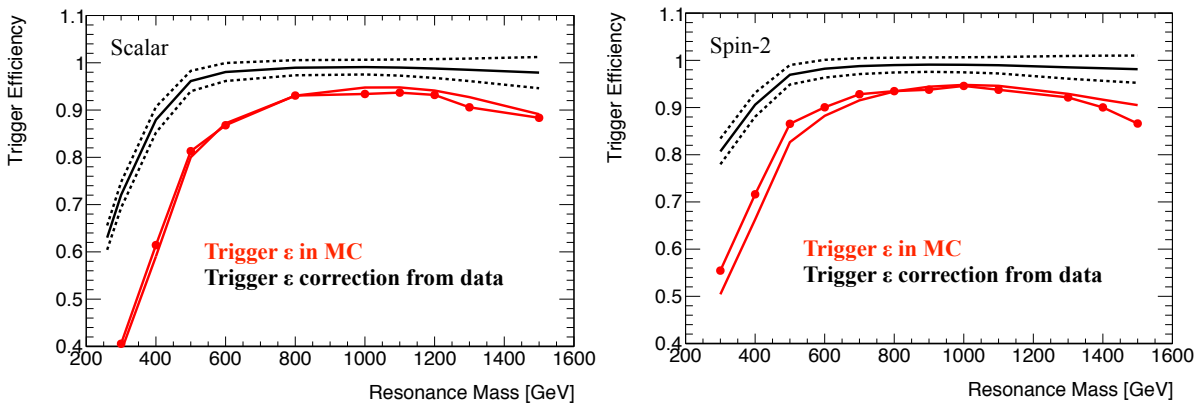

(a) Scalar Samples

(b) Spin-2 Samples

Figure F.6: 2015 event-level signal trigger efficiencies corrected for the efficiency in data.

Appendix G

LOW MASS VALIDATION REGION SCULPTING

As mentioned in Section 12, the shape of the low mass spectrum is a result of two effects:

1. The four body mass spectrum peaks lower for events with additional jets. With additional jets, the Higgs candidates can be closer in ΔR allowing $m_{4\mathrm{j}}$ to be closer to the sum of the Higgs candidate masses. In the LMVR this corresponds to $2 \times 90 = 180$ GeV.

2. The LMVR overlaps with the W boson mass used in the definition of X_{Wt} (Eqn. 8.4) for the top veto. At low $m_{4\mathrm{j}}$ the Higgs candidate ΔR_{jj} requirements have a large lower bound. This means the Higgs candidate mass is close to the sum of the constituent jet p_{T}'s. The combination of these constraints means that the X_{Wt} cut strongly suppresses events in the LMVR with exactly four jets and $m_{4\mathrm{j}} < 400$ GeV.

Despite this complex interplay of event and object level kinematics, the LMVR is modelled well at all stages of the cutflow, even after the top veto as shown in Figure G.3. This nicely demonstrates our ability to model the kinematics of the four Higgs candidate jets and the additional jet activity in the event.

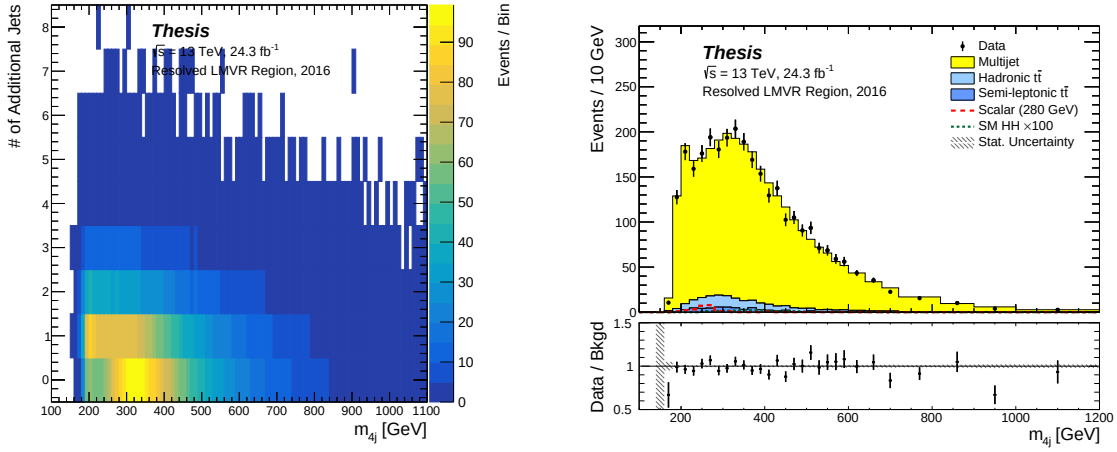

Figure G.1: The $m_{4\mathrm{j}}$ spectrum prior to the MDCs and top veto.

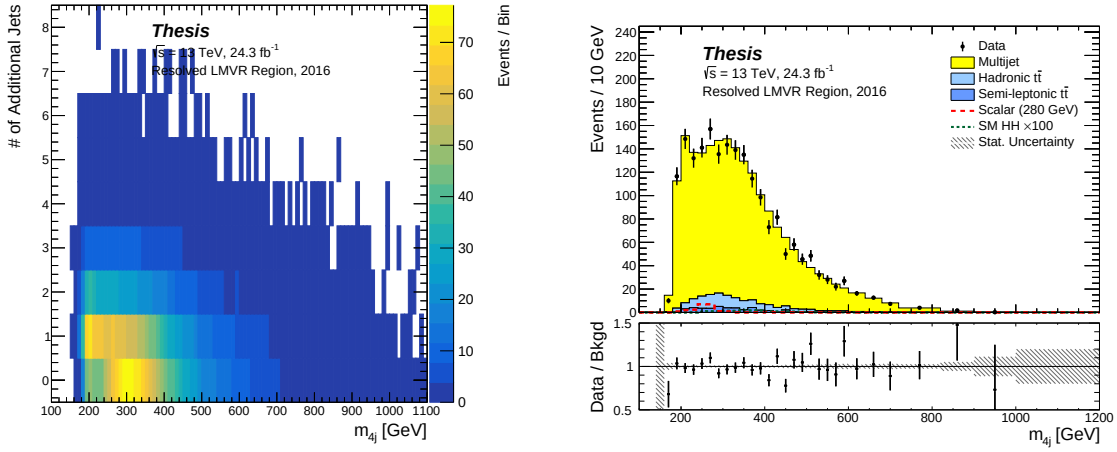

Figure G.2: The $m_{4\mathrm{j}}$ spectrum after the MDCs and prior to the top veto.

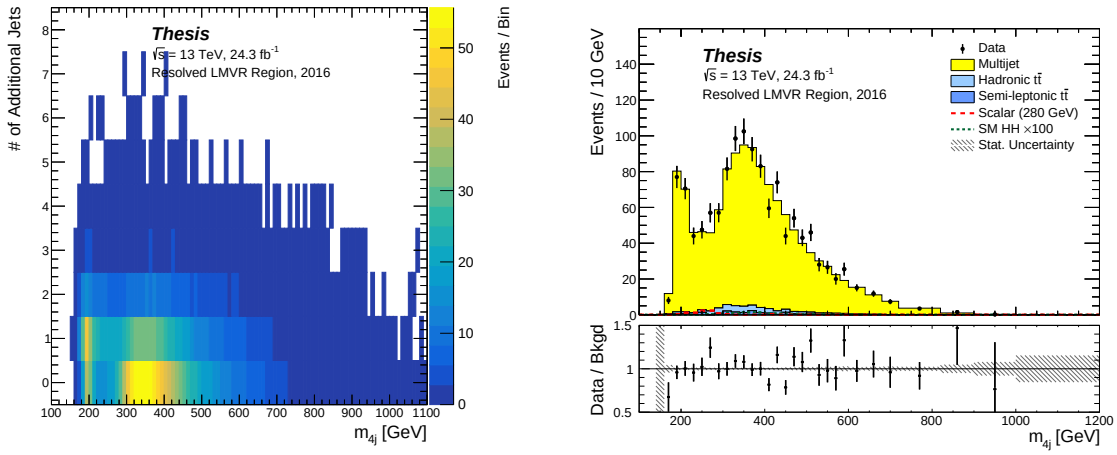

Figure G.3: The $m_{4\mathrm{j}}$ spectrum after the full event selection is applied.

Appendix H

STUDIES OF LOW MASS EXCESS

H.1 $Z + b\bar{b}$ Estimate from Data

The possible background contribution from Z+jets is estimated in data due to a lack of full simulation inclusive hadronically decaying Z+jets samples. By requiring two prompt isolated muons and two b-jets and selecting events with $81 < m_{\mu\mu} < 101$ we can get a relatively pure sample of Z+jets in data. These events are then scaled by the b-tag working point squared and the ratio of Z branching ratios to give the approximate expected Z+jets to $b\bar{b}b\bar{b}$ yield:

$$\mathrm{WP}^2 \times \frac{BR(Z \to b\bar{b})}{BR(Z \to \mu^+\mu^-)} = 0.7^2 \times \frac{0.15}{0.034} \approx 2.2$$

The prompt muon four-vectors are treated as b-jet four-vectors in the analysis of this selection. The events are then passed through the same b-trigger emulation used to emulate the trigger decisions for MC samples. This gives an expected Z+jets yield in the Signal region of 15 ± 6 events with only a few of those events expected under the excess. Using a truth level sample the expected Z+jets yield was found to be ≈ 20 events in the signal region.

This study shows that the neglected Z+jets background cannot account for the excess. The distribution in the signal region is shown in Figure H.1

H.2 Correlations in Reweighted Distributions

Another possible explanation for the excess would be a missed correlation in the background reweighting procedure. The one dimensional reweighted distributions are well modeled in

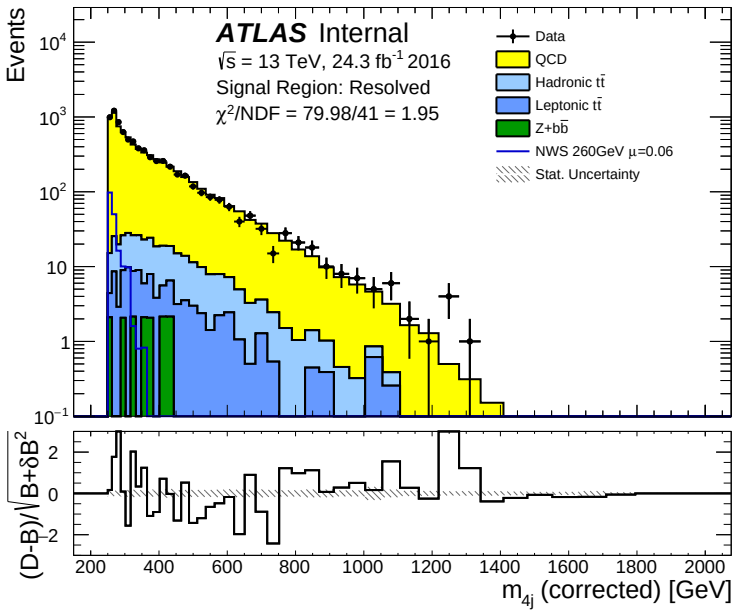

Figure H.1: The approximate Z+jets contribution to the signal region is shown in green where the other backgrounds are taken from the model derived in the Control Region. The ratio plot shows the approximate significance bin by bin of the data minus the total background using statistical uncertainty only.

the Sideband and Control regions, but it is possible that higher dimensional combinations of these distributions are poorly modeled. Studying multidimensional modeling is challenging and quickly becomes statistically limited as dimensions are added.

No significant evidence is found for poorly modeled correlations outside of the Signal Region. Three key 2D distributions and the significance of data minus background for events under the excess are shown in Figures H.2, H.3 and H.4. The excesses seen in the Signal Region are kinematically consistent with a low mass resonance and the same regions of phase space outside of the Signal Region do not show an excess. The distributions for a 280 GeV scalar are shown in Figure H.5

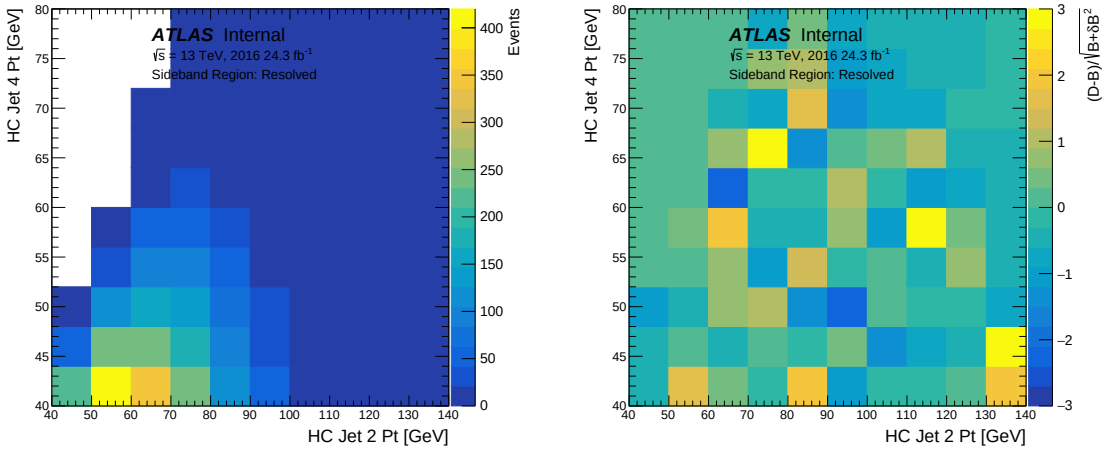

(a) Sideband

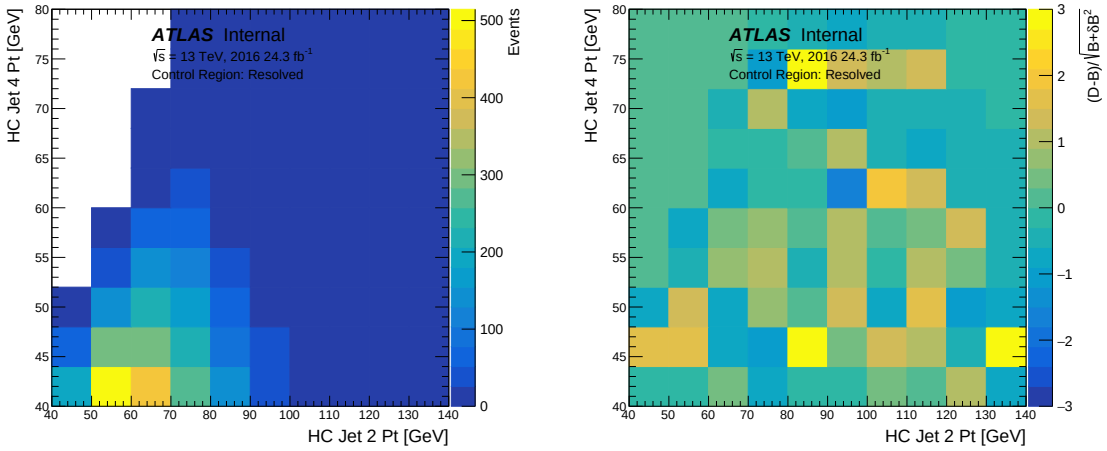

(b) Control

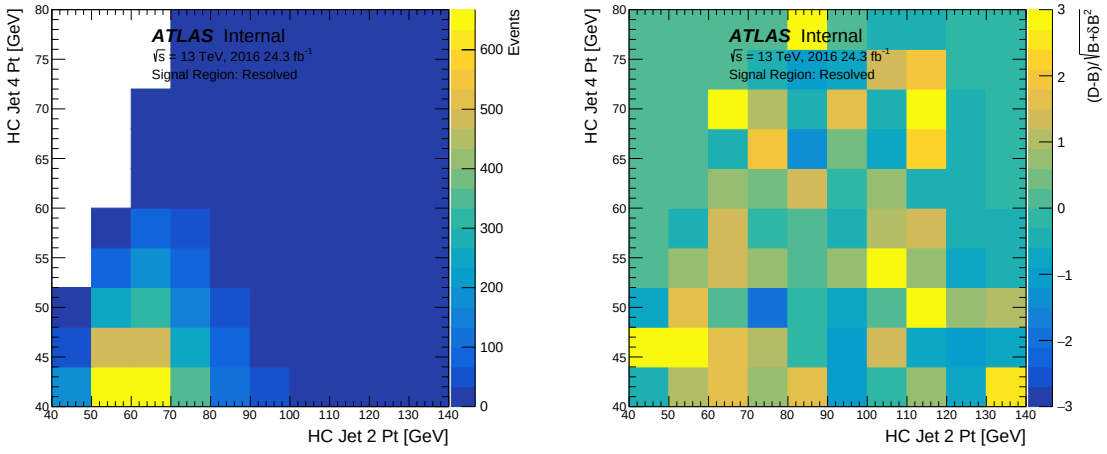

(c) Signal

Figure H.2: Correlation and modeling of the reweighted Higgs candidate jet p_{T}'s in the Sideband (top), Control (middle) and Signal (bottom) regions. Expected background on the left with data minus background divided by the background uncertainty on the right. Shown for events with $m_{4\mathrm{j}} < 320$ GeV

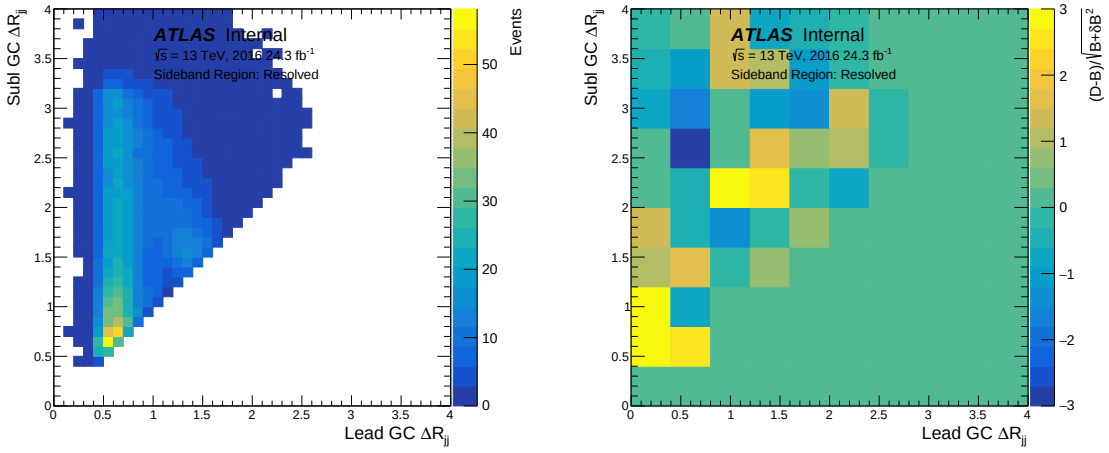

(a) Sideband

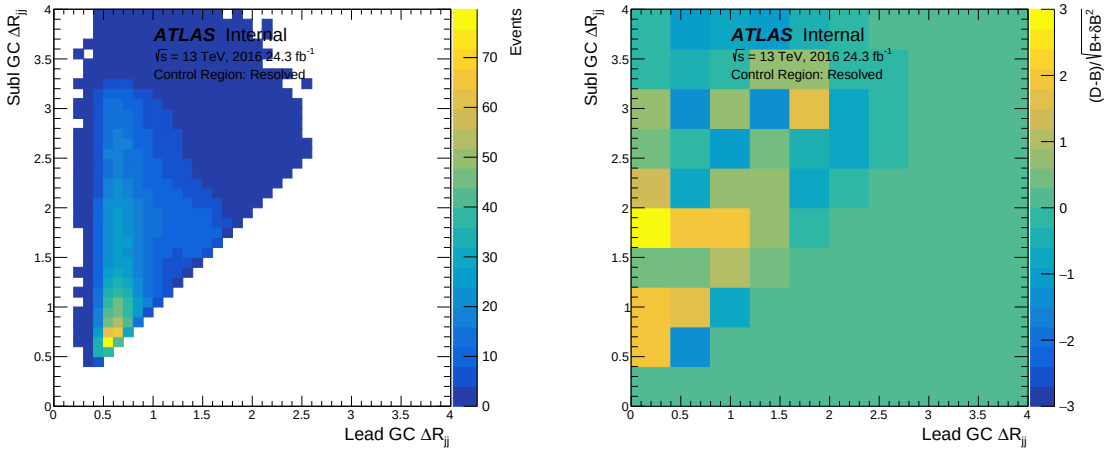

(b) Control

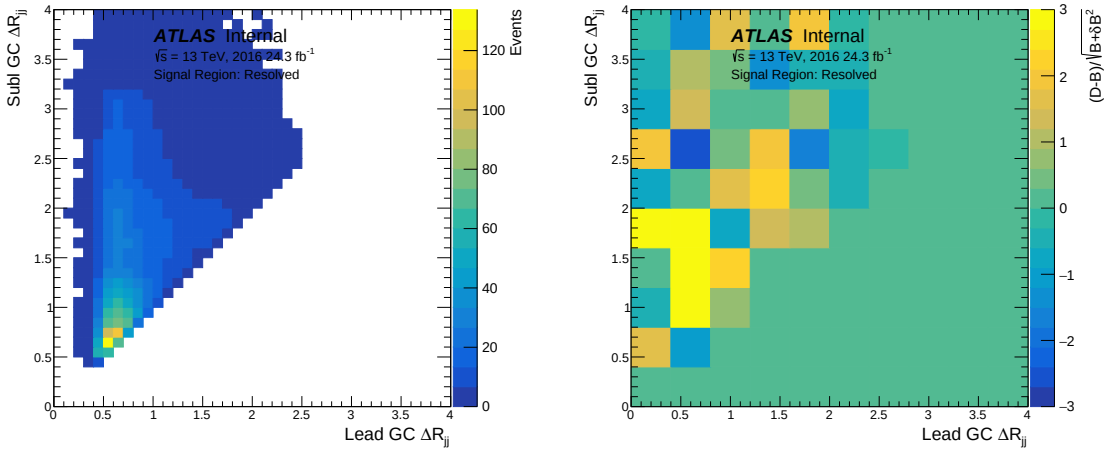

(c) Signal

Figure H.3: Correlation and modeling of the reweighted dijet ΔR_{jj}'s in the Sideband (top), Control (middle) and Signal (bottom) regions. Expected background on the left with data minus background divided by the background uncertainty on the right. Shown for events with $m_{4\mathrm{j}} < 320$ GeV

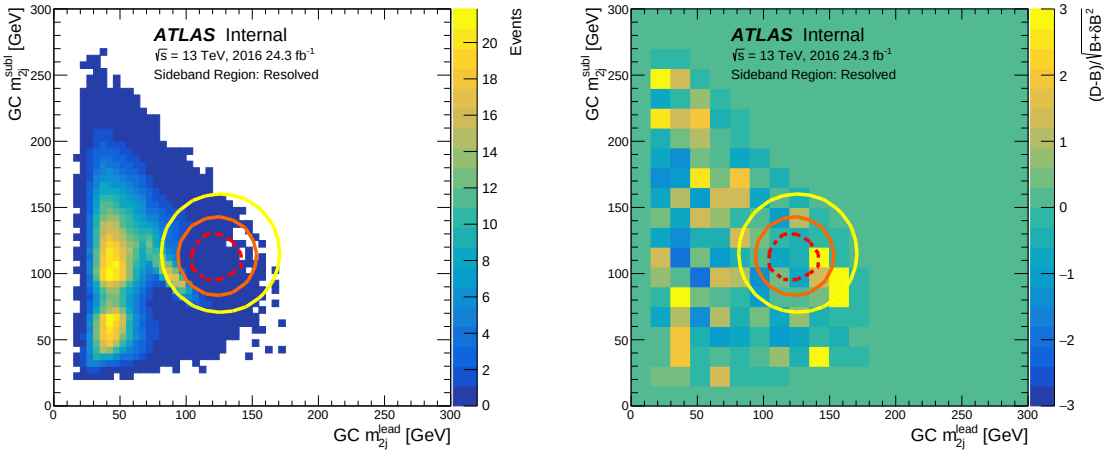

(a) Sideband

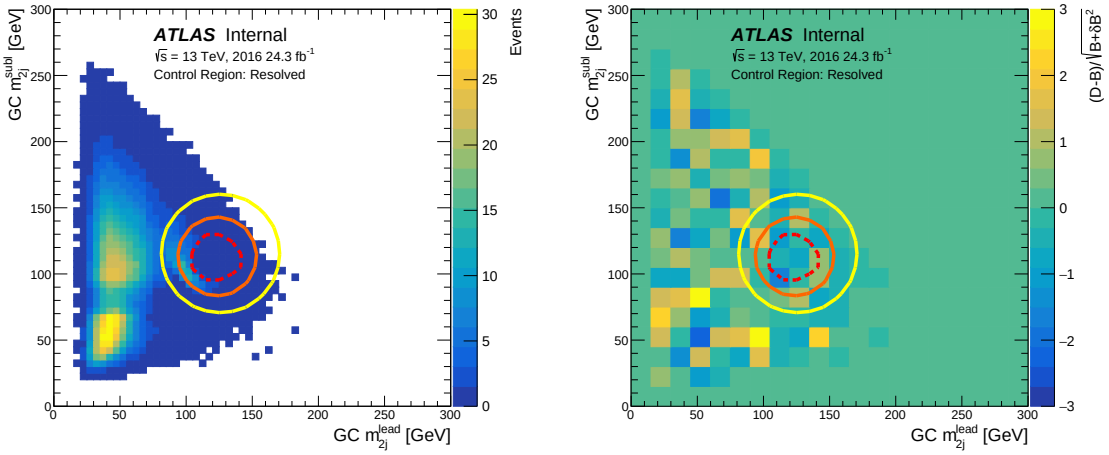

(b) Control

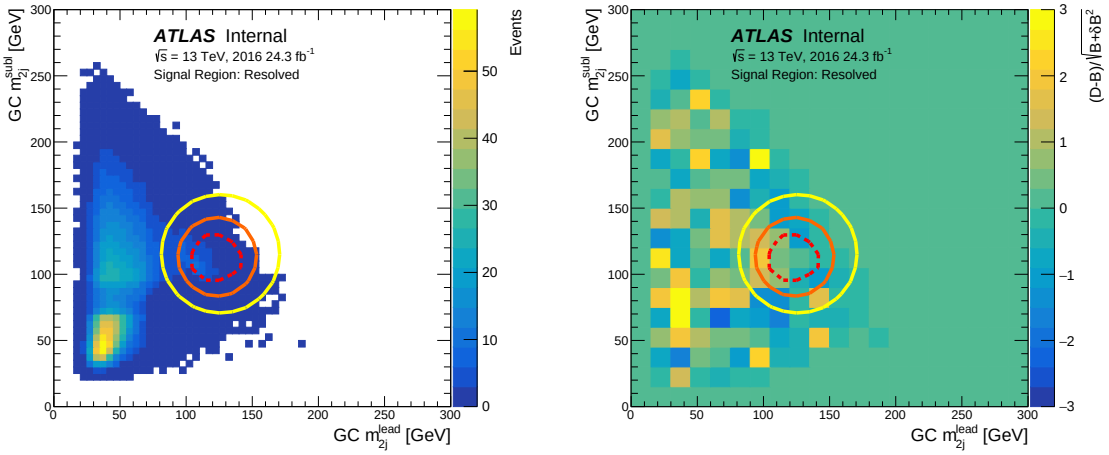

(c) Signal

Figure H.4: Correlation and modeling of the dijet masses in the Sideband (top), Control (middle) and Signal (bottom) regions. Expected background on the left with data minus background divided by the background uncertainty on the right. Shown for events with $m_{4\mathrm{j}} < 320$ GeV

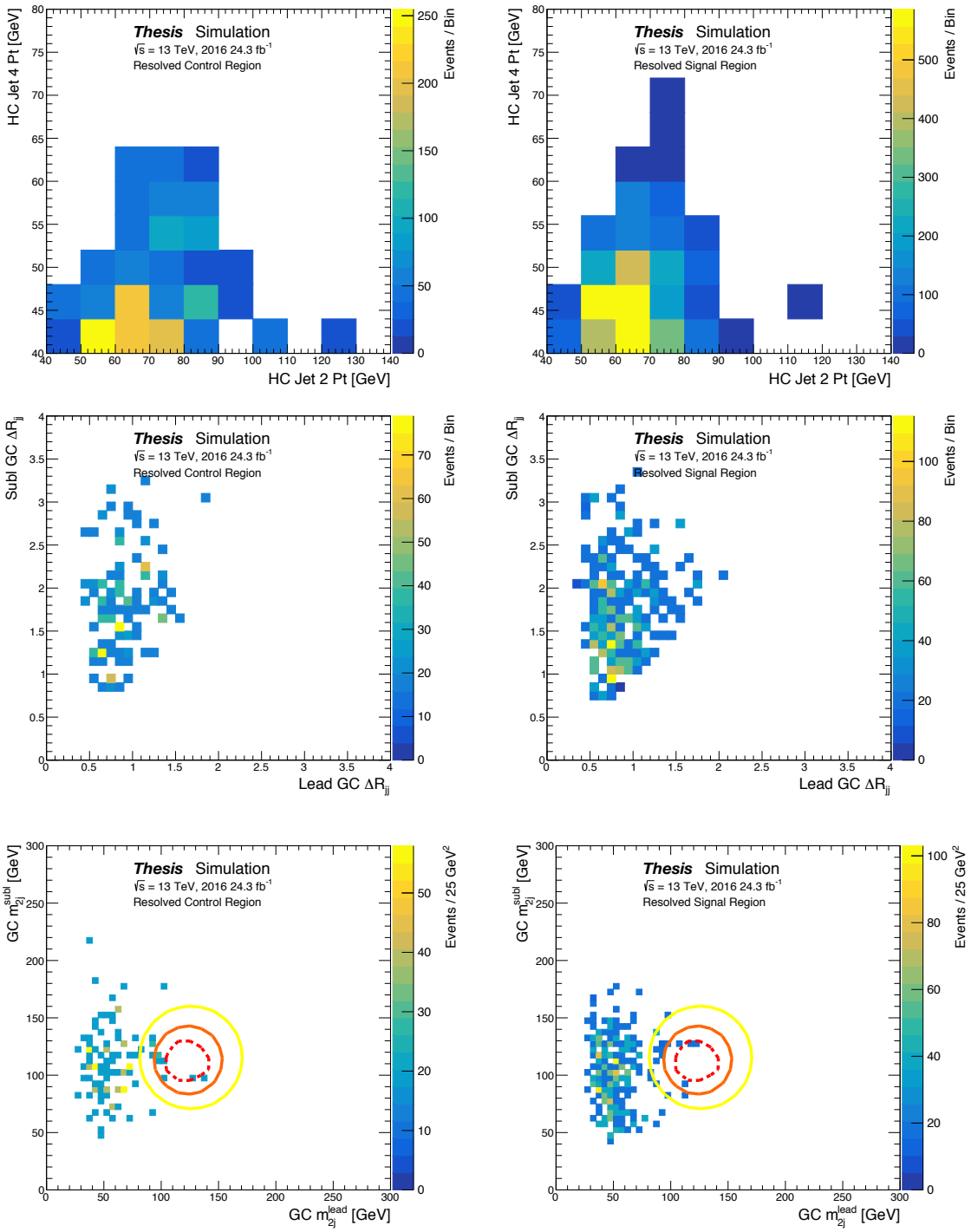

(a) Control (b) Signal

Figure H.5: The 2D distributions for the 280 GeV scalar sample in the Control (left) and Signal (right) regions. The regions with the largest excesses cover close to 50% of this signal model.

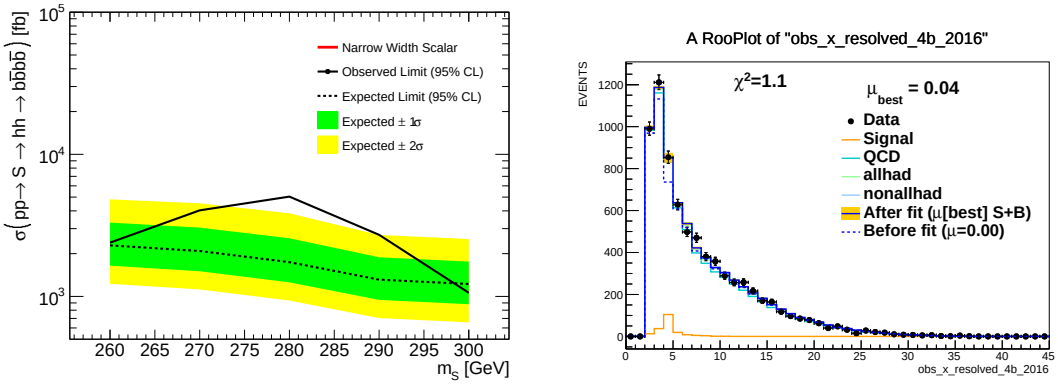

Figure H.6: On the left is the exclusion limit for the low mass scalar samples. On the right is the best fit signal shown for the 2016 dataset.

H.3 Best Fit Signal

The excess is fit well with a 280 GeV narrow width resonance, and progressively worse with wider resonances. For the 280 GeV scalar the best fit is with $\mu = 0.042 \pm 0.015$ which corresponds to $\sigma(pp \rightarrow S \rightarrow HH) = 9 \pm 3pb$. Figure H.6 shows the low mass scalar exclusion and best fit signal. Figure H.7 compares the pulls of the nuisance parameters in the fit between the background only and signal plus background fits. Figure H.8 shows the correlation matrix for the best fit signal. In the background only fit the low mass shape nuisance parameter is pulled significantly. This is not surprising because the low mass shape nuisance parameter is constrained by the data in the first several bins while the excess is in the second and third non-empty bins. The low mass shape nuisance parameter is compared to data in Figure H.9.

The result of fits to an Asimov dataset created with different values of injected signal is displayed in H.10, showing perfect linearity and no bias. Another test is displayed in H.11, after creating an Asimov dataset from the background-only fit condition, and then varying the pull of *LowHtCR*, which is a parameter largely anti-correlated with the signal strength. The resulting post-fit signal strength, however, is smaller than 10% of the excess observed.

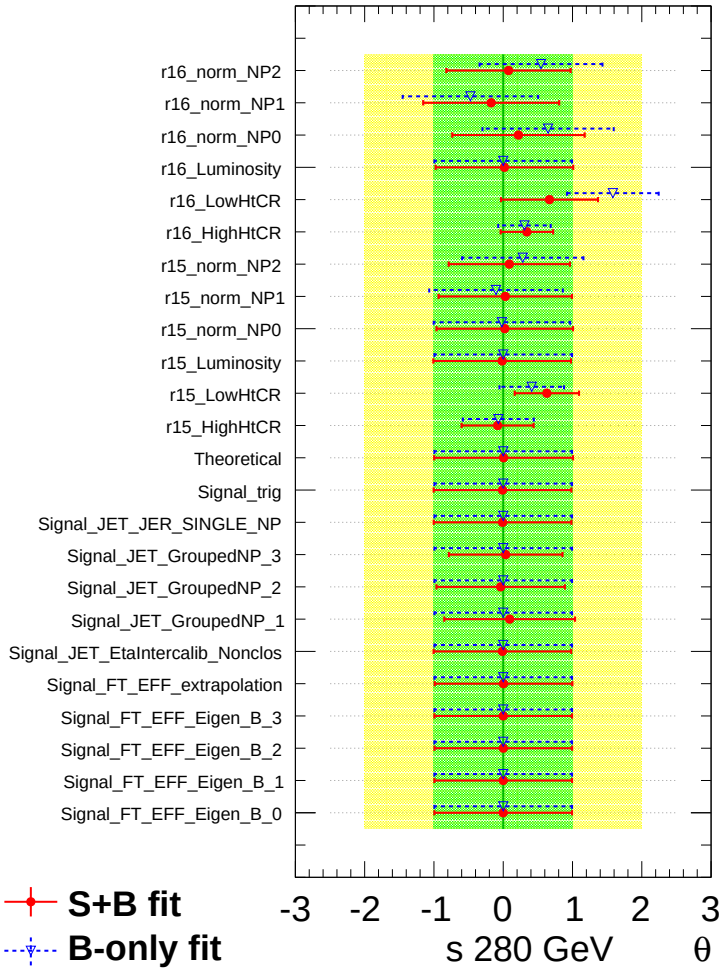

Figure H.7: Pulls of nuisance parameters in the background only fit versus the signal plus background fit.

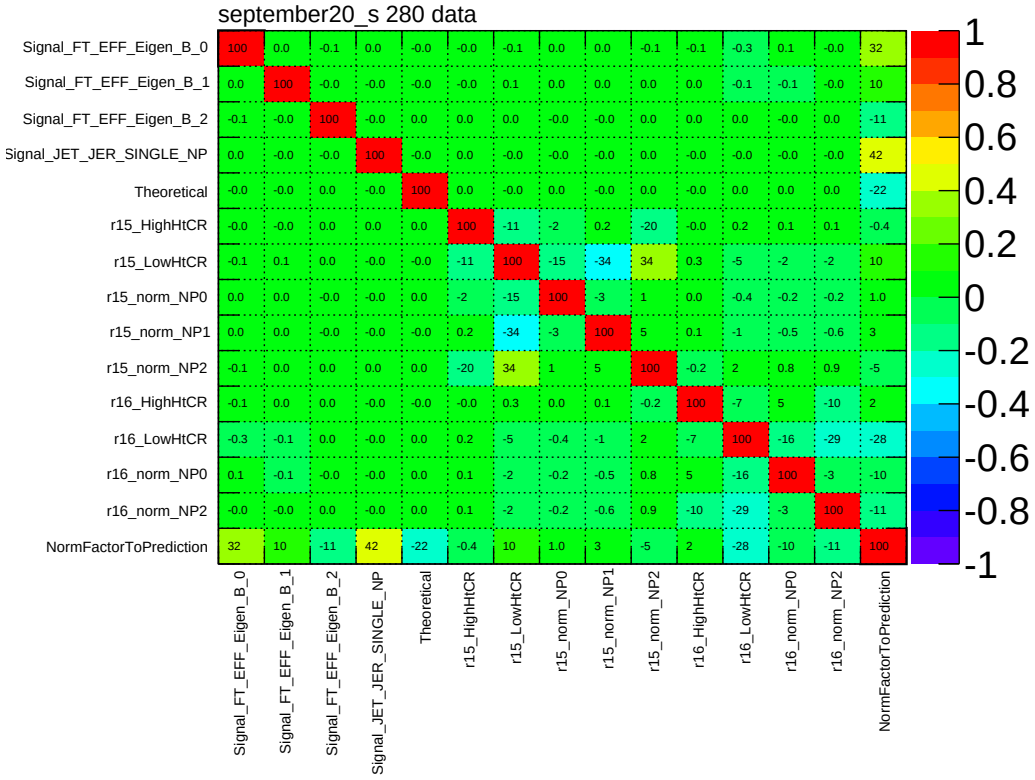

Figure H.8: Correlations of the nuisance parameters in the signal plus background fit.

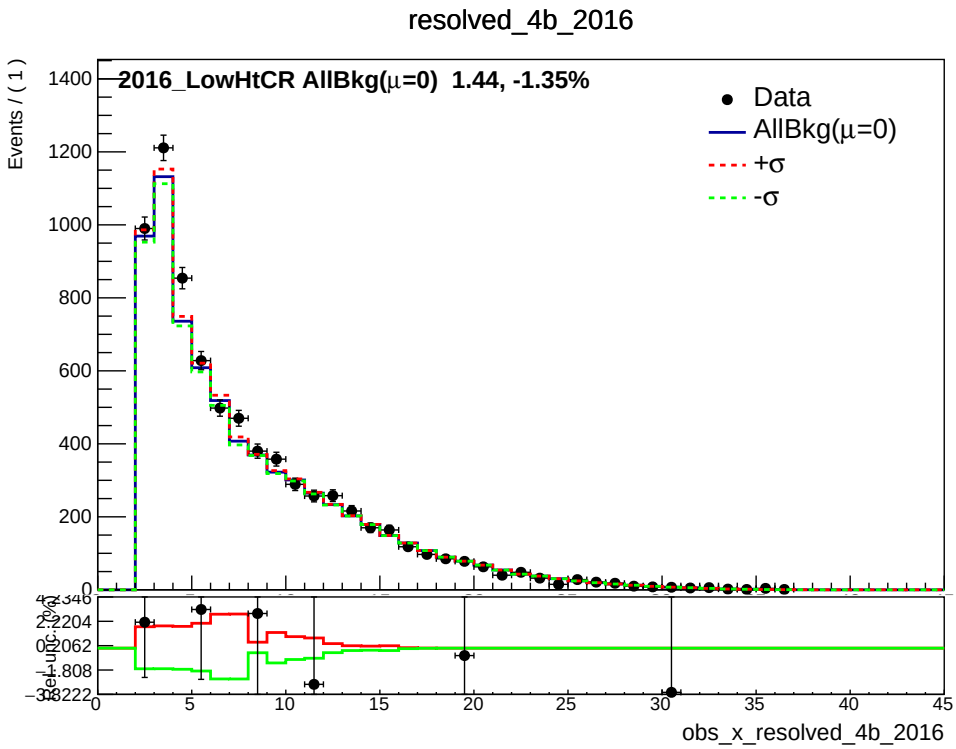

Figure H.9: The Low mass shape nuisance parameter compared with data in the 2016 signal region.

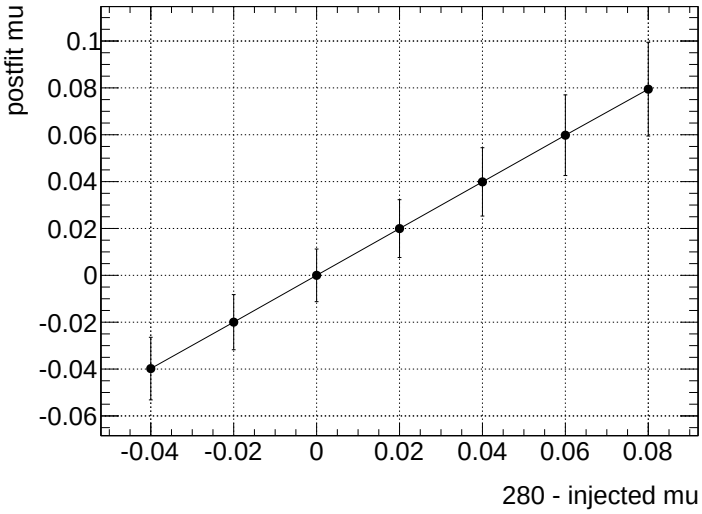

Figure H.10: Post-fit signal strength as a function of an injected signal. The Asimov dataset is created from nominal conditions.

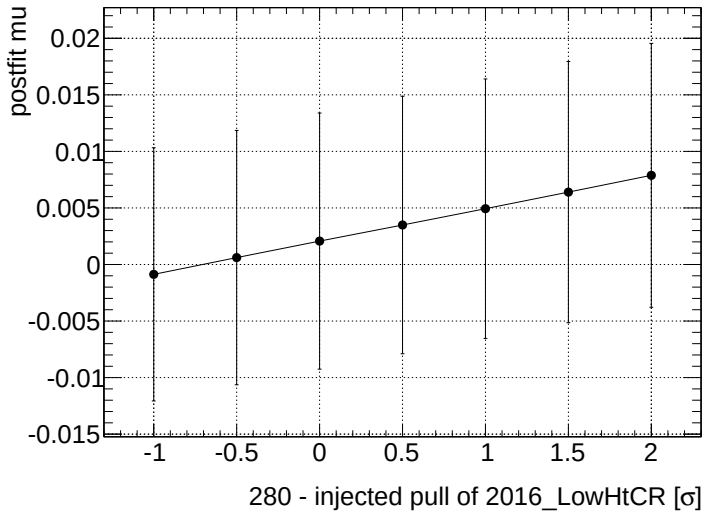

Figure H.11: Post-fit signal strength as a function of an injected pull of LowHtCR. The Asimov dataset is created from the background-only data fit conditions.

H.4 Impact of Injected Signal on Background Uncertainty

In the presence of a signal, it is important that the control region background derivation used to define the shape systematics is not significantly impacted by signal contamination. This has been explicitly verified by injecting the best fit signal during the derivation of the control region background model and checking the impact on the fit.

Injecting the best fit signal inflates the low mass shape systematic but has a negligible impact on the best fit signal or significance. The best fit before and after signal injection are compared in Figure H.12. For this study only the 2016 data was used. The 2015 data set does not contribute significantly to the sensitivity.

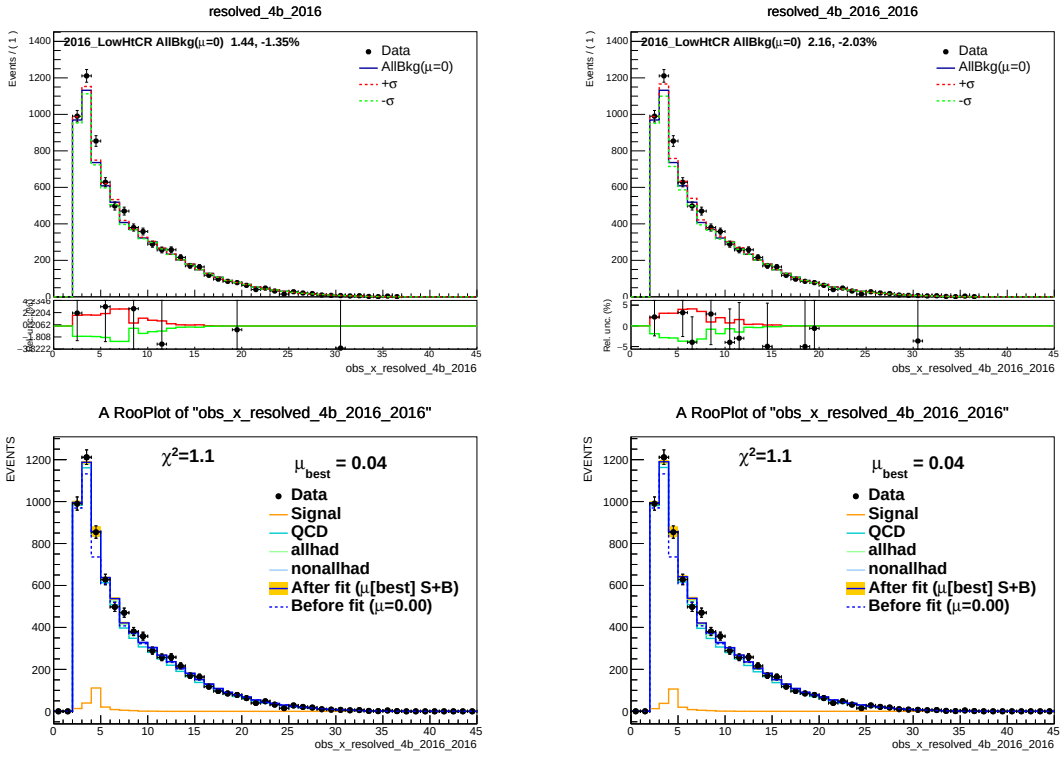

Figure H.12: Right: The nominal fit the best fit is $\mu = 0.044 \pm 0.016$. Left: The fit with the shape systematics derived with injected signal gives $\mu = 0.042 \pm 0.016$.

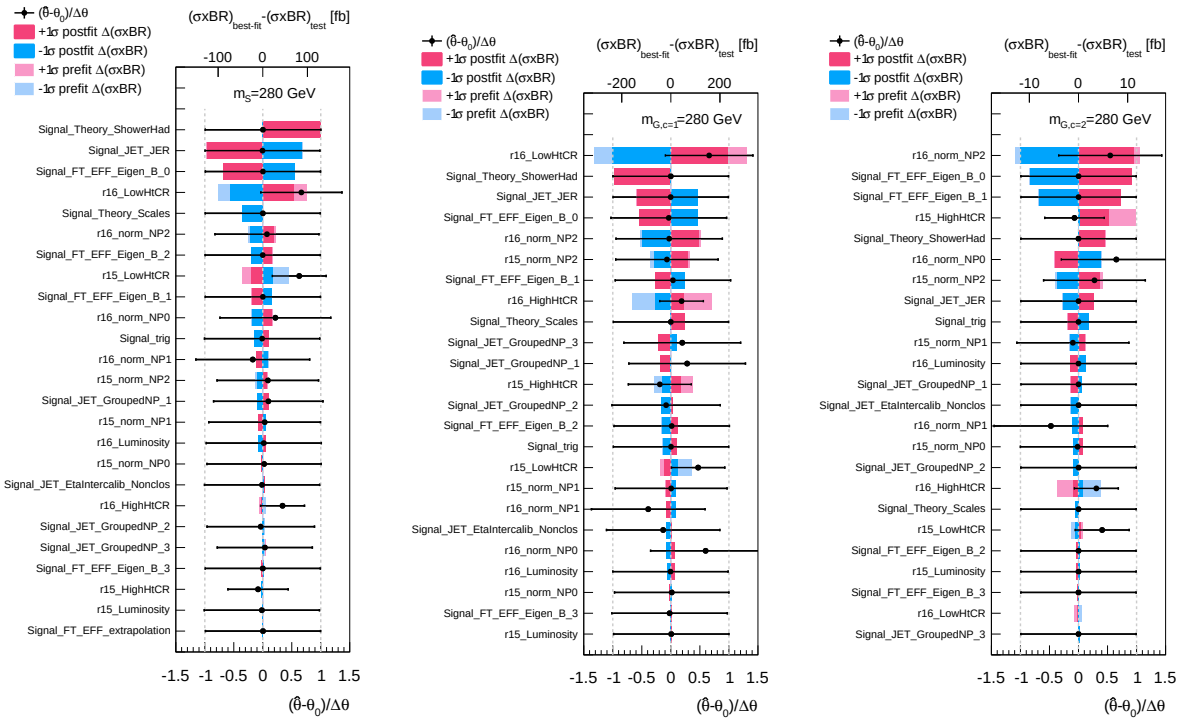

(a) (b) (c)

Figure H.13: Nuisance parameters ranked by their post-fit impact on the cross section [fb], (a) for the scalar, (b) for the c=1 Graviton, and (c) for the c=2 Graviton.

H.5 Impact of nuisance parameters on the fitted cross section

The impact of the various uncertainties on the fitted cross section is computed for each signal model at 280 GeV. The impact is evaluated for both prefit and postfit errors, for fits to the data and by varying each nuisance parameter by its best-fit value plus or minus its uncertainty. These ranking plots are depicted in Fig. H.13, where the change of cross section is given in units of fb.

H.6 Upper Limit on Global Significance Using BumpHunter

Upper limits on the global significance of the excess can be placed by using the model-independent BumpHunter algorithm. Unfortunately for this analysis it is not obvious how to include information about background systematics. For this reason we checked the BumpHunter significance for any excess in 2 or more bins of the 2015 plus 2016 data using four different background models:

1. Nominal background model as derived in the Sideband: Figure H.14
2. Background model variation as derived in the Control Region: Figure H.15
3. Background only fit using all background systematics: Figure H.16
4. Signal plus Background fit using the 280 GeV scalar model: Figure H.17

The results are somewhat inconclusive, but perhaps most enlightening is that the excess insignificant when using the background only fit. The nuisance parameter for the low mass shape is pulled about 1.7σ in the direction of the control region derived shape suggesting that the signal region is modelled well by the background model within the allowed systematic bias.

H.7 Event Rate Over Time

As a final check, the event count per pb^{-1} of luminosity in each run of the 2016 data set is checked for excesses in time. No Significant effects are seen as shown in figure H.18.

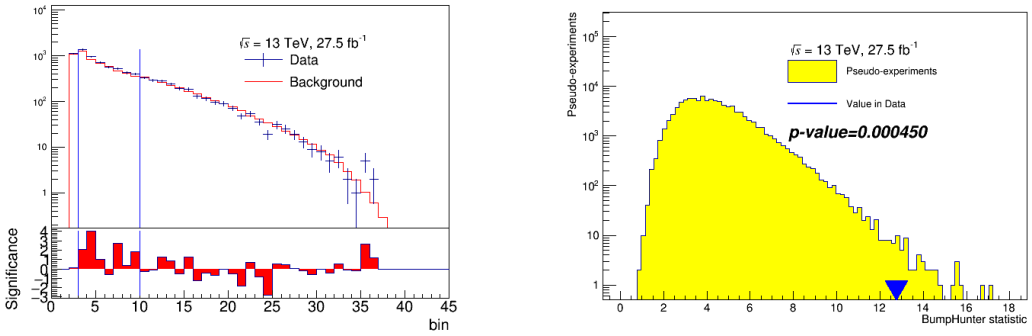

Figure H.14: Model derived in Sideband. Global significance 3.3σ

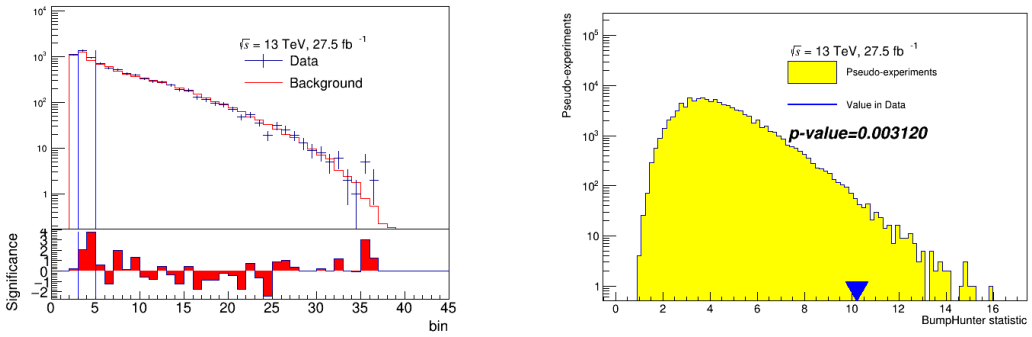

Figure H.15: Model derived in Control. Global significance 2.7σ

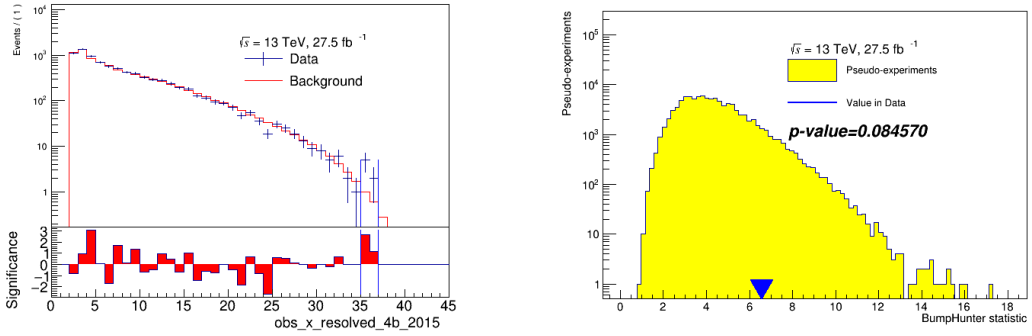

Figure H.16: Background only fit. Global significance $\leq 1.4\sigma$

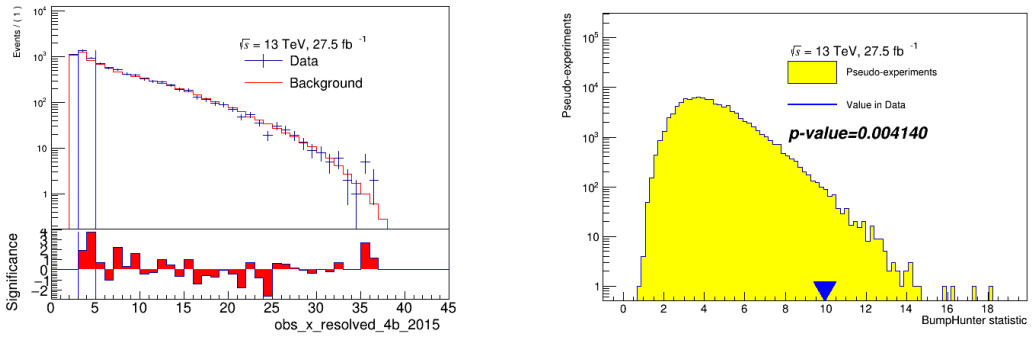

Figure H.17: Signal (280 GeV scalar) plus background fit. Global significance 2.6σ

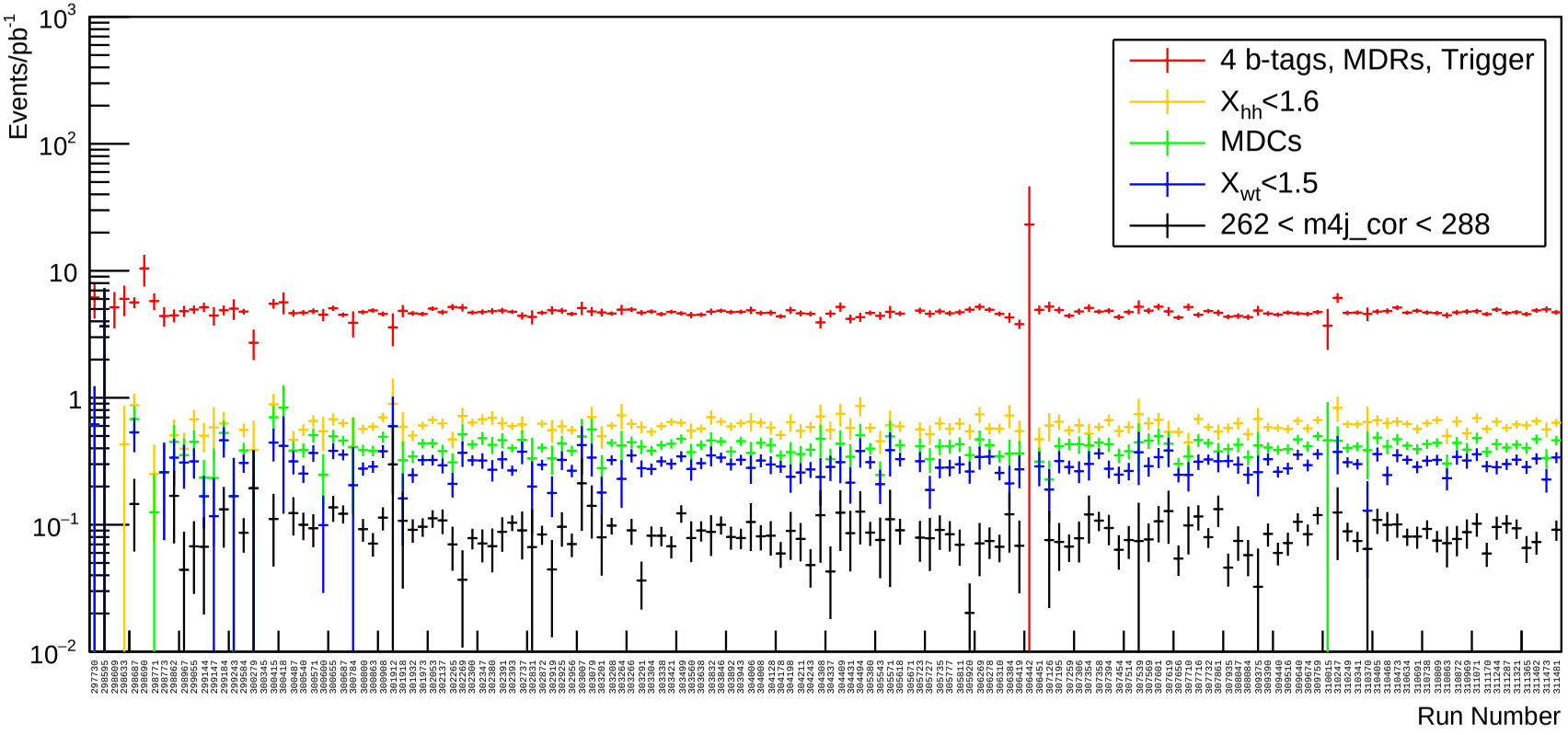

Figure H.18: Events per pb^{-1} per run in the 2016 data set at various stages of the cutflow. In red, the preselection of trigger, four jets passing cleaning, p_{T}, η and MV2c10 cuts and at least one jet pairing passing the $m_{4\mathrm{j}}$ dependent ΔR_{jj} requirements for Higgs candidate construction is applied. In orange the Signal Region window on the Higgs candidate masses is applied. In green the $m_{4\mathrm{j}}$ dependent cuts are applied. In blue the top veto is applied. Finally in Black, the two bins with the largest excess in the corrected $m_{4\mathrm{j}}$ spectrum are selected.